

**DESIGN, FABRICATION AND CHARACTERIZATION
OF AN OPTIMAL MAGNETORHEOLOGICAL (MR)
DAMPER FOR PROSTHETIC KNEE APPLICATION**

Thesis

Submitted in partial fulfillment of the requirements for the degree of

DOCTOR OF PHILOSOPHY

by

TAK RADHE SHYAM SAINI



DEPARTMENT OF MECHANICAL ENGINEERING
NATIONAL INSTITUTE OF TECHNOLOGY KARNATAKA,
SURATHKAL, MANGALORE – 575025

OCTOBER 2021

**DESIGN, FABRICATION AND CHARACTERIZATION
OF AN OPTIMAL MAGNETORHEOLOGICAL (MR)
DAMPER FOR PROSTHETIC KNEE APPLICATION**

Thesis

Submitted in partial fulfillment of the requirements for the degree of

DOCTOR OF PHILOSOPHY

by

TAK RADHE SHYAM SAINI

Under the guidance of

Dr. Hemantha Kumar

Associate Professor

Department of Mechanical Engineering
NITK, Surathkal

Dr. C. Sujatha

Professor,

Department of Mechanical Engineering
IIT Madras



DEPARTMENT OF MECHANICAL ENGINEERING
NATIONAL INSTITUTE OF TECHNOLOGY KARNATAKA,
SURATHKAL, MANGALORE – 575025


OCTOBER 2021

DECLARATION

I hereby *declare* that the Research Thesis entitled “**DESIGN, FABRICATION AND CHARACTERIZATION OF AN OPTIMAL MAGNETORHEOLOGICAL (MR) DAMPER FOR PROSTHETIC KNEE APPLICATION**” which is being submitted to the **National Institute of Technology Karnataka, Surathkal** in partial fulfillment of the requirements for the award of the Degree of **Doctor of Philosophy** in **Department of Mechanical Engineering** is a *bonafide report of the research work carried out by me*. The material contained in this Research Thesis has not been submitted to any University or Institution for the award of any degree.

Register Number : 177158 177ME026

Name of the Research Scholar : **Tak Radhe Shyam Saini**

Signature of the Research Scholar : 

Department of Mechanical Engineering

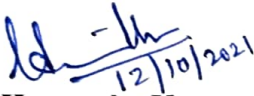
Place : NITK, Surathkal

Date: 12/10/2021

C E R T I F I C A T E

This is to *certify* that the Research Thesis entitled “**DESIGN, FABRICATION AND CHARACTERIZATION OF AN OPTIMAL MAGNETORHEOLOGICAL (MR) DAMPER FOR PROSTHETIC KNEE APPLICATION**” submitted by Mr. **Tak Radhe Shyam Saini (Register Number: 177158 177ME026)** as the record of the research work carried out by him, is *accepted as the Research Thesis submission* in partial fulfillment of the requirements for the award of degree of **Doctor of Philosophy**.

Research Guide(s)


12/10/2021

Dr. Hemantha Kumar

Associate Professor

Department of Mechanical Engineering

NITK, Surathkal



Dr. C. Sujatha

Professor,

Department of Mechanical Engineering,

IIT Madras



Chairman – DRPC

Department of Mechanical Engineering

Place: NITK, Surathkal

Date:

12 OCT 2021



ACKNOWLEDGEMENT

I am extremely thankful to my supervisors, Dr. Hemantha Kumar , Department of Mechanical Engineering, NITK Surathkal and Prof. C. Sujatha, Department of Mechanical Engineering, IIT Madras for their wonderful guidance, mentorship and patience over the course of this work. I would like to thank them for letting me pursue this area of research and for their constant encouragement from the early stages of this work. I am equally thankful to Prof. Sujatha Srinivasan, Department of Mechanical Engineering, IIT Madras for her valuable suggestions and support with the biomechanics part of this work.

I would like to thank my Doctoral committee members, Dr. Arun M, Department of Mechanical Engineering, NITK Surathkal and Dr. V. Murugan, Department of Mathematical and Computational Sciences, NITK Surathkal for their many helpful suggestions and critical review.

I acknowledge the funding support from IMPRINT Project No. IMPRINT/2016/7330 titled, “Development of Cost-effective Magneto rheological (MR) Fluid Damper in Two Wheelers and Four Wheelers Automobile to Improve Ride Comfort and Stability” sponsored by Ministry of Human Resource and Development and Ministry of Road Transport and Highways, Government of India. I also acknowledge the funding support from SPARC Project No. P/785 titled, “Design of Magneto Rheological Damper for Vehicular Applications” sponsored by Ministry of Human Resource and Development, Government of India.

I thank all my lab mates Puneet, Hussain, Suhaas, Ashok, Devi, Surya, Vishal, Surya Bhanu as well as Mr. Rangaraj, Mr. Subash, Mr. Ravi, Dr. Vipin, Dr. Manjeet and Dr. Guru for their help and support in carrying out many of the experimental works.

My sincere thanks are due to Mr. Gurudutt Kulkarni, Arya Technocats, Belgaum and Mr. Shivanandan Sahu, Sahau Engineering for their excellent work in the fabrication of all the prototype dampers in this work.

I am thankful to my parents for believing in me and to my father’s novel methods in making me study during childhood, which have helped me reach this stage. I am also thankful to my uncles, Gopal and Mahesh for all the support during my entire academic career.

ABSTRACT

A transfemoral amputation is the removal of lower limb above the knee joint in the thigh, through the femur bone. The design of any device which can make a transfemoral amputee's gait similar to a normal gait is a challenging problem. An even more challenging task is to make the prosthetic leg adapt to variable walking speeds, terrains and intents. Magnetorheological (MR) fluids with their magnetic field controllable rheological properties, along with their fast response have been applied to design prosthetic knee devices capable of assisting a transfemoral amputee in replicating a near-normal gait. In this study, various design configurations based on MR fluids are explored for their suitability in prosthetic knee domain and an optimal design is selected among them.

The device should be capable enough of producing the required knee braking torque sufficient for normal human walking and a low off-state resistance with a least possible mass, which forms a design optimization problem. The optimal design of any device configuration based on MR fluid involves coupling a mechanical design and an electromagnetic design. The mechanical design is based on the application of fluid constitutive models on the problem geometry. Equivalent magnetic methods (EMM) and finite element magnetostatics (FEM) are the two methods used in the electromagnetic design process. The former results in producing significant errors in magnetic field variables, whereas the latter requires a large computational time and effort. In this study, a combined magnetostatics approach is proposed which can address the various shortcomings associated with the available optimization methodologies. The proposed algorithm is compared with frequently used optimization methodologies based on FEM, EMM as well as neural network based data-driven methods. A statistical comparison of hypervolume indicator revealed that the proposed methodology produces similar design points compared to optimization based on FEM method and also substantially reduces the computational time.

Although there exists only one commercially available design based on MR fluid, many alternative knee design configurations have been studied by various researchers. However, not all the previously studied design configurations are optimally

designed specific to prosthetic knee applications. In this study, four design configurations based on MR fluids are selected based on intuition and also from models based on literature. The design configurations namely waveform arc boundary MR brake, multi-pole MR brake, twin rod MR damper and rotary vane MR damper are considered for a preliminary design process. The commercially available multi-plate MR brake has been extensively studied in the literature and thus is avoided from optimal design, although it is used in comparative studies at a later stage in this work. Among the chosen design configurations, twin rod MR damper and rotary vane MR damper are selected based on the criteria of producing normal human knee braking torque adequately. The multi-pole MR brake is found to produce a braking torque of 14 Nm, which is insufficient for normal human walking and thus is rejected for further testing. Although the waveform arc boundary MR brake is capable of producing the required braking torque, the design has limitations similar to that of commercially available multi-plate MR brakes and thus is also rejected for further testing.

A prototype of the other two dampers is fabricated with random dimensions so as to obtain a few insights into the working nature of the device. Later, optimal design of selected design configurations is performed using the developed optimization methodology. The twin rod MR damper is characterized on a linear dynamic testing machine using harmonic excitations of varying amplitudes, frequencies and currents. This device configuration is capable of producing a damping force of 1020 N (equivalent to 40.8 Nm at 40 mm force moment arm) at a current of 1 A and also has a mass of 0.71 kg. An equivalent test setup to characterize the rotary vane MR damper is developed. This device configuration is found to produce a damping torque of 33 Nm at a current of 1A and has a mass of 1.1 kg. Based on the experimental findings and a comparison of the dampers with the available commercial model and models based on literature, the twin rod MR damper is selected as the optimal design configuration for prosthetic knee application.

Finally, the twin rod MR damper is mathematically modelled using Bouc-Wen model with the model parameters evaluated by minimizing the error norms for time, displacement and velocity between the experimental and the model-generated results using a multi-objective genetic algorithm optimization. In the process, two different

experimental data sets are used, one for mathematical modeling and the other for assessing the accuracy of the fit model. Also, an inverse model based on the forward damper model is proposed and validated later. This model predicts the current directly and avoids the necessity of solving any quadratic equation, which is otherwise required in the case of inverse models based on the modified Bouc-Wen model.

The dynamic model of a single axis two segmental prosthetic knee is coupled with the forward Bouc-Wen model, the inverse model and a proportional derivative (PD) plus controlled torque (CT) controller to realize a complete semi-active prosthetic knee model. The parameters of PD plus CT controller are tuned to minimize the error between the desired and the controller-estimated torques. A closed loop control study is performed for the swing phase of the gait cycle. The results from the dynamic analysis predict that the damper is suitable for reproducing knee angle trajectories similar to those of normal gait and thus can be applied for prosthetic knee applications. Further, it was observed that the shank reaches full knee extension at the end of the swing phase with terminal velocity small enough to be handled by an extension stop.

Keywords: Twin rod MR damper, rotary vane MR damper, Semi-active prosthetic knee, combined magnetostatic approach, Inverse MR damper Model, PD plus CT controller.

TABLE OF CONTENTS

DECLARATION	
CERTIFICATE	
ACKNOWLEDGEMENT	i
ABSTRACT	ii
TABLE OF CONTENTS	v
LIST OF FIGURES	x
LIST OF TABLES	xiv
ABBREVIATIONS	xv
NOMENCLATURE	xvi
1. INTRODUCTION	1
1.1 BASIC ANATOMICAL TERMS	1
1.2 BONES IN THE LOWER LIMBS	3
1.3 GAIT CYCLE	3
1.4 TRANSFEMORAL AMPUTATION	4
1.5 PROSTHESIS	5
1.5.1 Classification of Prosthetic Knee	5
1.6 MAGNETORHEOLOGICAL (MR) FLUID	7
1.6.1 MR Fluid Modes	7
1.6.2 MR Damper	9
1.7 MR FLUID MODELS	13
1.8 MR DAMPER MODELS	16
1.8 SUMMARY	17
2. LITERATURE REVIEW AND METHODOLOGY	18
2.1 INTRODUCTION	18
2.2 TRANSFEMORAL PROSTHESIS	19
2.3 SEMI-ACTIVE KNEES BASED ON MR FLUIDS	27
2.3.1 MR Brakes	27

2.3.2	Limited Angle MR Dampers	31
2.3.3	Linear MR Damper	33
2.3.4	Control Logics	35
2.3.5	Design Optimization Strategies	37
2.4	SUMMARY OF LITERATURE	39
2.5	MOTIVATION	40
2.6	OBJECTIVES	42
2.7	SCOPE OF RESEARCH WORK	43
2.8	METHODOLOGY	43
2.9	SUMMARY	45
3.	OPTIMAL DESIGN METHODOLOGIES FOR MR DAMPER	46
3.1	INTRODUCTION	46
3.2	COMBINED MAGNETOSTATIC APPROACH	47
3.3	MECHANICAL DESIGN OF MR DAMPER	50
3.3.1	Dynamic Range	51
3.3.2	Inductive Time Constant	52
3.3.3	Mass	53
3.4	MAGNETOSTATIC ANALYSIS	53
3.4.1	Finite Element Magnetostatics (FEM)	53
3.4.2	Equivalent Magnetic Model (EMM)	54
3.5	DESIGN PROBLEMS	56
3.5.1	Design Problem 1	56
3.5.2	Design Problem 2	56
3.6	OPTIMIZATION ROUTINE	57
3.7	MAGNETOSTATIC METHODOLOGIES FOR OPTIMIZATION	59
3.7.1	O-FEM	59
3.7.2	O-EMM	59
3.7.3	O-NN	59
3.7.4	O-COM	60
3.8	PARETO COMPARISON	63
3.9	RESULTS AND DISCUSSION	63

3.9.1	Comparative Studies	65
3.10	SUMMARY	72
4.	PROSTHETIC KNEE DAMPERS –	
	PRELIMINARY DESIGN STUDY	73
4.1	INTRODUCTION	73
4.2	MULTI-POLE ROTARY DRUM BRAKE	73
4.2.1	Geometry	74
4.2.2	Design Parameters	75
4.2.3	Design of Experiments	77
4.2.4	Optimal Design	78
4.2.5	Results and Discussion	80
4.3	TWIN ROD MR DAMPER	83
4.3.1	Formulation of Total Damping Force	84
4.3.2	Formulation of the Electromagnetic Circuit	85
4.3.3	Constrained Optimization Problem Formulation	86
4.3.4	Results and Discussion	88
4.4	ROTARY VANE MR DAMPER	89
4.4.1	Design of Rotary Chamber	90
4.4.2	Design of MR Valve	92
4.4.3	Electromagnetic Circuit Design	93
4.4.4	Formulation of MR Valve Mass	95
4.4.5	Materials Used in Damper	96
4.4.6	Optimization of MR Valve	98
4.4.7	Multi Objective Genetic Algorithm (MOGA)	99
4.4.8	Results and Discussion	100
4.4.9	Magnetostatic Analysis	102
4.5	INVERTED DRUM WAVEFORM ARC MR BRAKE	103
4.5.1	Waveform Arc Parameters	104
4.5.2	Mathematical Formulation	107
4.5.3	Optimization Problem Formulation	111
4.5.4	Finite Element Method Magnetics	112

4.5.5	Equivalent Magnetic Circuit Method	114
4.5.6	Results and Discussion	117
4.6	SUMMARY	119
5. DESIGN, FABRICATION AND CHARACTERIZATION		
OF TWIN ROD MR DAMPER		120
5.1	INTRODUCTION	120
5.2	INITIAL PROTOTYPE OF TWIN-ROD MR DAMPER	120
5.2.1	Experimental Test Rig	122
5.2.2	Characterization of MR Damper	123
5.3	OPTIMAL DESIGN OF TWIN ROD MR DAMPER	126
5.4	CHARACTERIZATION OF TWIN ROD MR DAMPER	130
5.5	DESIGN VALIDATION	132
5.6	SUMMARY	134
6. DESIGN, FABRICATION AND CHARACTERIZATION		
OF ROTARY VANE MR DAMPER		135
6.1	INTRODUCTION	135
6.2	INITIAL PROTOTYPE OF ROTARY VANE MR DAMPER	135
6.3	OPTIMAL DESIGN OF ROTARY VANE MR DAMPER	137
6.4	DEVELOPMENT OF EXPERIMENTAL TEST RIG	142
6.5	CHARACTERIZATION OF ROTARY VANE DAMPER	144
6.6	DESIGN VALIDATION	146
6.7	COMPARISON OF VARIOUS PROSTHETIC KNEE SYSTEMS	150
6.8	SUMMARY	153
7. SEMI-ACTIVE PROSTHETIC KNEE MODEL –		
A CLOSED LOOP CONTROL STUDY		154
7.1	INTRODUCTION	154
7.2	MATHEMATICAL MODELING OF TWIN ROD MR DAMPER	155
7.3	OPTIMIZATION OF BOUC – WEN MODEL PARAMETERS	156
7.4	MATHEMATICAL MODELING OF PROSTHETIC LIMB	162

7.5	SEMI-ACTIVE KNEE WITH TWIN ROD MR DAMPER	164
7.6	PD PLUS CT CONTROL	166
7.7	RESULTS AND DISCUSSION	167
7.8	VALIDATION OF THE INVERSE MODEL	171
7.9	SUMMARY	173
8.	SUMMARY AND CONCLUSIONS	175
8.1.	SUMMARY	175
8.2.	CONTRIBUTIONS	177
8.3.	CONCLUSIONS	177
8.4	SCOPE OF FUTURE WORK	178
	REFERENCES	180
	Appendix I	190
	Appendix II	199
	Appendix III	210

LIST OF FIGURES

Fig. 1.1	(a) Reference planes and 6 fundamental directions in the basic anatomical position and (b) Movements about the major joints of lower limbs	2
Fig 1.2	2D kinematics of normal gait cycle	4
Fig 1.3	Behavior of MR fluids (a) No applied magnetic field, $H = 0$ and (b) Applied magnetic field, $H > 0$	8
Fig 1.4	MR fluid modes	8
Fig 1.5	Classification of MR dampers	9
Fig 1.6	(a) Disc type MR brake and (b) Drum type MR brake	10
Fig 1.7	Rotary vane damper with internal MR valve	11
Fig 1.8	(a) Single tube MR damper, (b) Twin tube MR damper And (c) Twin rod MR damper	12
Fig 1.9	Shear stress versus shear strain for (a) Bingham, Herschel-Bulkley and Casson models (b) Biviscous model, (c) Biplastic model, and (d) Papanastasiou model	15
Fig 2.1	Typical prosthetic knee system	19
Fig 2.2	Evolution of knee prostheses	21
Fig 2.3	Schematic representation of (a) C – Leg 4 and (b) Rheo knee XC	26
Fig 2.4	Common configurations of MR brake (a) Drum, (b) Inverted drum, (c) T-shaped rotor, (d) Disk and (e) Multiple disk	29
Fig 2.5	Exploded view of multi-plate MR brake	30
Fig 2.6	Waveform arc boundary on rotor	31
Fig 2.7	Rotary vane damper with (a) Servo motor controlled Permanent magnet and (b) Electromagnet controlled	32
Fig 2.8	Lord Corporation damper RD-8040-1	34
Fig 2.9	Twin rod MR damper designs	35
Fig 2.10	Block diagram of controller hierarchy	36
Fig 2.11	Methodology of current work	44
Fig 3.1	Combined magnetostatic analysis	48

Fig 3.2	Cross-section of a typical flow mode MR damper	51
Fig 3.3	Axisymmetric model of piston in FEMM software	54
Fig 3.4	Pseudo MATLAB code to perform magnetostatic analysis in FEMM	54
Fig 3.5	Lumped parametric magnetic model	55
Fig 3.6	Basic structure of PSO	58
Fig 3.7	Architecture of feed-forward neural network	61
Fig 3.8	Constrained MDPL-MOPSO in MATLAB coupled with FEMM	62
Fig 3.9	DP1 Pareto fronts of (a) O-EMM and corrected O-EMM and (b) O-NN and corrected O-NN	64
Fig 3.10	DP2 Pareto fronts of (a) O-EMM and corrected O-EMM and (b) O-NN and corrected O-NN	65
Fig 3.11	Q-Q graphic plots of DP1 for (a) O-FEM, (b) O-EMM, (c) O-COM and (d) O-NN	67
Fig 3.12	Q-Q graphic plots of DP2 for (a) O-FEM, (b) O-EMM, (c) O-COM and (d) O-NN	68
Fig 3.13	Box plots of hypervolume measures for (a) DP1 and (b) DP2	69
Fig 4.1	Cross-section of multi-coil inverted drum brake	74
Fig 4.2	2D axisymmetric model of (a) single coil brake and (b) multi-coil brake	80
Fig 4.3	Magnetostatic analysis of (a) Single coil rotary brake and (b) multi-coil rotary brake	81
Fig 4.4	Normal magnetic flux distribution in single coil and multi-coil brake	82
Fig 4.5	Twin rod MR damper in flow mode	84
Fig 4.6	Equivalent electromagnetic circuit of piston	86
Fig 4.7	(a) Axisymmetric model of piston assembly including cylinder and (b) Magnetic field strength in the model	88
Fig 4.8	Rotary vane MR damper	89
Fig 4.9	Geometry of rotary chamber	90
Fig 4.10	MR valve geometry	93
Fig 4.11	(a) Magnetic circuit with equivalent links (b) Equivalent magnetic circuit model	94

Fig 4.12	B-H Curves of SAE 1020, SAE 1018 and MRF-132DG	97
Fig 4.13	Pareto optimal set of (a) Off-state and total damping torque and (b) Mass and total damping torque	101
Fig 4.14	(a) Axisymmetric model of piston assembly and (b) Contours of magnetic flux densities	102
Fig 4.15	(a) Cross-sectional view of inverted drum MR brake and (b) Section view of A-A showing waveform arc boundary	104
Fig 4.16	Geometrical parameters of inverted rotary drum brake	105
Fig 4.17	Various waveform arc boundary configurations of MR brake	106
Fig 4.18	(a) FEMM model and (b) axisymmetric model with equivalent links and (c) lumped parametric equivalent magnetic circuit model	115
Fig 4.19	Pareto front showing non-dominated solutions	117
Fig 5.1	Cross-section of twin rod MR damper	121
Fig 5.2	Fabricated prototype damper components	122
Fig 5.3	Schematic of damper testing machine	123
Fig 5.4	Experimental testing of fabricated MR damper	124
Fig 5.5	Force-displacement and force-velocity curves at varying (a) – (b) currents, (c) – (d) frequencies and (e) – (f) displacements respectively	125
Fig 5.6	Piston core assembly	127
Fig 5.7	Geometry of twin rod MR damper in flow mode configuration	128
Fig 5.8	(a) Pareto front of twin rod flow mode damper and (b) Magnetostatic analysis of optimal design	130
Fig 5.9	Twin rod damper fabricated components	131
Fig 5.10	Piston core assembly	131
Fig 5.11	Force-displacement and force-velocity curves at varying (a) – (b) currents, (c) – (d) frequencies and (e) – (f) displacements respectively	133
Fig 6.1	3D model of rotary vane damper prototype	136
Fig 6.2	Fabricated components of initial rotary vane MR damper	137
Fig 6.3	Modified rotary vane MR damper	138

Fig 6.4	Geometric variables of rotary vane MR damper	138
Fig 6.5	(a) Pareto front of rotary vane MR damper and (b) Magnetostatic analysis of MR valve	141
Fig 6.6	Fabricated components of optimal design of rotary vane damper	142
Fig 6.7	Schematic of rotary damper experimental test setup	143
Fig 6.8	Rotary damper experimental test setup	144
Fig 6.9	MR fluid filling process	145
Fig 6.10	Rotary chamber filled with MR fluid	146
Fig 6.11	Force-displacement and force-velocity curves for varying (a) – (b) currents, (c) – (d) amplitudes and (e) – (f) frequencies respectively	147
Fig 6.12	Magnetif flux density in fluid gap	148
Fig 7.1	Force-displacement and force-velocity curves for experimental and model-predicted values for varying (a) – (b) currents, (c) – (d) amplitudes and (e) – (f) frequencies respectively	159
Fig 7.2	Free body diagram of lower limb model in swing phase	163
Fig 7.3	Knee joint line diagram	164
Fig 7.4	Block diagram of simulation model	168
Fig 7.5	Estimated and obtained torque curves	169
Fig 7.6	Desired and simulated knee angle trajectories	169
Fig 7.7	Power generated and power dissipated at knee joint	170
Fig 7.8	Current input supplied to MR damper	170
Fig 7.9	Estimated and obtained damping force curves	173

LIST OF TABLES

Table 2.1	Types of microprocessor controlled prosthetic knees	22
Table 3.1	Design variables and their bounds	57
Table 3.2	Hyper-parameters of the ANN model	60
Table 3.3	Shapiro – Wilk tests for DP1 and DP2	66
Table 3.4	Bonferroni tests for DP1 and DP2	70
Table 3.5	Dunnett C tests for DP1 and DP2	71
Table 3.6	Comparison of computational time	72
Table 4.1	Parameters and their levels	77
Table 4.2	Response parameters for different geometric variable combinations	79
Table 4.3	Bounds and optimized values of parameters	87
Table 4.4	Parameters of rotary chamber	91
Table 4.5	Material properties	97
Table 4.6	Design variables with bounds	99
Table 4.7	Design variables and their bounds	112
Table 4.8	Materials of the components	113
Table 4.9	Constant design parameters	113
Table 4.10	Variables for vertical equivalent links	116
Table 4.11	Variables for horizontal equivalent links	117
Table 4.12	Optimal dimensions of waveform inverted rotary brake	118
Table 4.13	Preliminary design configuration assessment	119
Table 5.1	Parameters of twin rod MR damper	122
Table 5.2	Variables, bounds and optimized values of twin rod MR damper	129
Table 6.1	Bounds and optimum values of design variables	142
Table 6.2	Comparison of prosthetic knee MR devices	152
Table 7.1	Parameter bounds and optimized values of the mathematical model of MR damper	158
Table 7.2	Error norms of data sets used in optimized problem	160
Table 7.3	Error norms averaged across varying currents	161
Table 7.4	Parameters of subjects' lower limb	164

ABBREVIATIONS

ANN	Artificial Neural network
CFD	Computational fluid dynamics
CT	Controlled torque
DoE	Design of experiments
EMM	Equivalent magnetic method
FEM	Finite element magnetostatics
FEMM	Finite element method magnetics
GA	Genetic algorithm
MDPL	Minimum distance from point to line
MOGA	Multi objective genetic algorithm
MOPSO	Multi objective particle swarm optimization
MR	Magnetorheological
O-COM	Optimization based on combined magnetostatics approach
O-EMM	Optimization based on equivalent magnetic method
O-FEM	Optimization based on finite element magnetostatics
O-NN	Optimization based on neural network
PD	Proportional derivative
PSO	Particle swarm optimization
SA	Simulated annealing

NOMENCLATURE

τ	shear stress
η_r	elastic fluid property
w_t	average circumference of fluid gap
λ	dynamic range
A_p	effective cross-sectional area
w_C	mean circumference of annular gap
r_0	radius of piston rod
T_C	inductive time constant
L_{in}	inductance of the coil
R_w	resistance of coil wire
Φ	magnetic flux
ρ	resistivity of the coil
d_c	diameter of coil
d_{avg}	average diameter of coil cross-section
ρ_{core}	density of core
ρ_{MRF}	density of MRF
ρ_{coil}	density of coil
V_{MRF}	volume of MR fluid
V_{coil}	volume of coil
A_p	piston cross-section area
L_a	active pole length
η	fluid viscosity
τ_y	fluid yield stress
F_{MR}	controllable MR force
F_{draw}	drawing force per unit width
\bar{F}_{exp}	average experimental force
F_{xh}, F_{yh}	forces acting at the hip joint
r_0	piston rod radius

\dot{u}	velocity of piston
B_{\max}	maximum magnetic flux density
L_r	height of rotary vane
w_r	width of rotary vane along radial direction
R_r, R_{vane}	radial distance from shaft axis to centroid of rotary vane
r_c	radius of MR valve core
w_t	average circumference of MR flow channel
c_t	outer cylinder thickness
ω	angular speed
R_0	rotor shaft radius
Ω	angular velocity of knee joint
p_f	packing factor
T_d	damping torque
A_{vane}	cross-sectional area of rotary vane
N_{arc}	number of circumferential arcs
r_{arc}	radius of arc
w_{arc}	total width of the annular pole region
ε	effective coefficient
P_e	maximum electrical power consumed by brake
μ_0	permeability of air
F_d	damping force of MR damper
μ	scaling parameter
f_0	force offset
E_t	error norm for time
E_x	error norm for displacement
E_v	error norm for velocity
θ_1	absolute angular displacement of hip
θ_2	absolute angular displacement of knee
L_1	thigh segment length
L_2	shank segment length
I_1	moment of inertias of thigh

I_2	moment of inertias of shank mass including foot
τ_k	torque at knee joint
τ_c	control input torque
K_p	proportional gain
K_d	derivative gain
θ_{2d}	desired knee angle
F_{vis}, F_v	viscous force
F_{Total}, F_t	total damping force
T_{MR}, T_τ	controllable torque
T_{vis}, T_0, T_η	viscous torque or off-state torque
B	magnetic flux density
g	fluid gap
h	coil height
K	consistency index
L	total piston length
n	flow behavior index
Q	flow velocity
T	total braking torque
w	coil width
z	hysteresis operator

CHAPTER 1

INTRODUCTION

Normal human walking seems so effortless and devoid of conscious effort, but it involves immense underlying complexities. Therefore, the design of any device that can make a transfemoral amputee's prosthetic gait similar to normal gait is a challenging problem. An even more challenging task is to make the prosthetic component adapt to varying walking speeds, terrains and intents. In this regard, smart materials with their controllable properties prove themselves to be very much effective. The present work intends to design a prosthetic knee damper based on magnetorheological (MR) fluid, a smart fluid with magnetic field controllable rheological properties. The device should be capable enough to support the amputee in achieving stance phase stability and also allow him/her to perform a smooth swing phase. In this work, the criterion of "Stability in Stance and Agility in Swing" is assessed in terms of the device's ability to generate the required knee braking torque.

This chapter introduces the basic anatomical terms and the relevant terminology pertaining to human walking which is followed by a brief description of transfemoral amputation and a classification of knee prostheses. Later, a brief introduction of the MR fluid and its controllable rheological behavior is provided. A classification of semi-active device configurations is presented next. Finally, a few mathematical models of the MR fluid and MR dampers are disclosed.

1.1 BASIC ANATOMICAL TERMS

The basic anatomical position of the body is standing erect with feet together and arms by the sides of the body, with the palms facing front. The reference planes and the fundamental directions in the anatomical position are as shown in Figure 1.1 (a). The transverse plane divides the body into upper and lower portions. The sagittal plane divides the body into left and right portions and the coronal plane divides it into front and back portions. The movements about the major joints of the lower limbs are

as shown in Figure 1.1 (b). Flexion and extension movements occur in the sagittal plane and exist both at hip and knee joints. They are referred to as dorsiflexion and plantarflexion in the case of the ankle joint. Abduction and adduction movements exist at all three joints of the lower limb. The internal and external rotation exists in hip and knee joints and for the ankle joint, they are called pronation and supination.

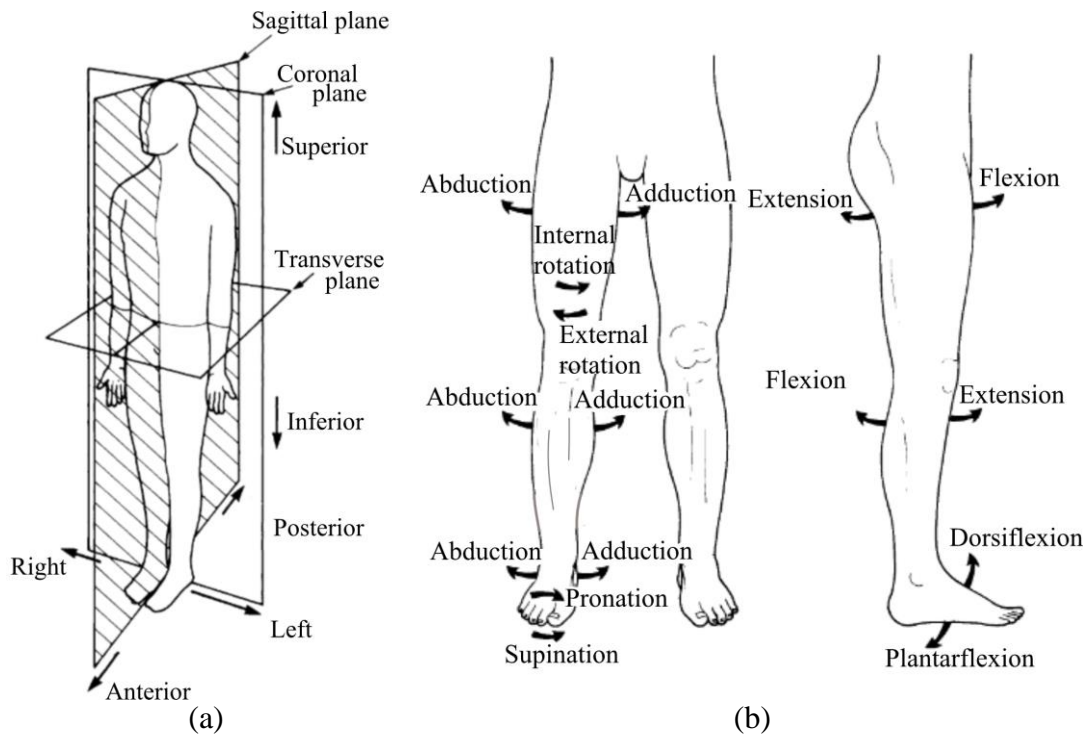


Figure 1.1 (a) Reference planes and 6 fundamental directions in the basic anatomical position and (b) Movements about the major joints of lower limbs (Whittle 2007)

A few additional terms which describe anatomical relationships are:

1. Medial implies towards the midline of the body, while lateral means away from the midline of the body. For instance, in anatomical position, the little finger is on the medial side of hand while the thumb is on the lateral side of the hand.
2. Proximal means towards the rest of the body, while distal implies away from the rest of the body. A shoulder is a proximal part of the arm and fingers are a distal part of the hand.
3. Superficial structures are close to the surface and deep structures are far from the surface.

1.2 BONES IN THE LOWER LIMBS

Although every bone in the body plays a minor role in the walking process, from a practical point of view it is only necessary to consider the bones of the pelvis and legs. The femur is the longest bone in the body extending between the hip and knee joints. The part of the leg between the knee and ankle joint, referred to as shank, consists of two bones, tibia and fibula. The former exists on the medial side of the leg while the latter extends on the lateral side of tibia. The two bones are in contact with each other at both the upper and lower ends, but only tibia is in contact with the femur. The patella or the kneecap is a sesamoid bone, that it is embedded within a tendon. A groove exists at the knee joint on the femur which articulates with the patella and forms a patellofemoral joint. The lower ends of the tibia and fibula form an ankle joint. The foot is also a complicated structure and the walking process sees a good amount of participation from the foot bones, roughly classified as hindfoot, midfoot and forefoot.

1.3 GAIT CYCLE

Gait is defined as the manner of walking. A gait cycle can be broadly divided into two phases, stance and swing phase. Stance phase is the one in which the leg supports a part of the body weight and swing phase is the one in which the leg is in the air swinging from one end to the start of the next stance phase. Further, it can be classified into many ways using various events happening during the cycle. Figure 1.2 shows the stance and swing phases of the gait cycle. The sagittal plane kinematics of ankle, knee and hip joints during a normal human gait cycle are also shown in the figure.

Any event can be used to initiate the gait cycle; in general it starts with a heel strike. Consider the right foot for the cycle, the cycle begins and ends with a heel strike as seen in Figure 1.2. Since the events happen in an order and are independent of time, the cycle can be explained in terms of percentages or time, thus permitting normalizing the data for large group of subjects. The duration of one complete gait cycle is called stride time; this has both stance time and swing time. Stance constitutes approximately 62% of the gait cycle, while swing phase is composed of the left over 38%. Stride length refers to the distance between the two successive placements of the same foot. Cadence is the number of steps taken in a given time, the usual units being steps per minute.

Velocity of walking is the total distance covered by the whole body in a given time and can be calculated using stride length and cadence using equation (1.1).

$$velocity(m/s) = \frac{stride\ length(m) \times cadence\ (steps/min)}{120} \quad (1.1)$$

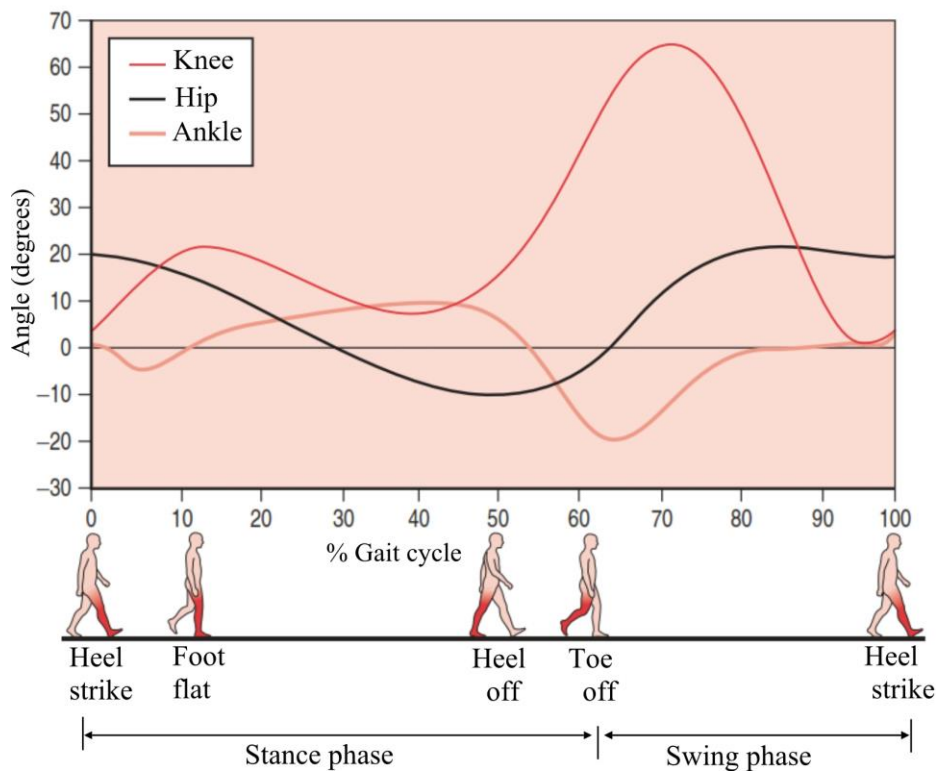


Figure 1.2 2D kinematics of normal gait cycle (Kirtley 2006)

1.4 TRANSFEMORAL AMPUTATION

Amputation is the removal of a limb by trauma, medical illness, or by surgery. Transfemoral amputation is the removal of the lower limb above the knee joint in the thigh, through the femur bone. The level of amputation depends on where there is the greatest blood flow and, therefore, the greatest possibility of healing. The surgeon often attempts to save the knee, because the energy cost of walking with an intact knee is much less than without it. The most common problems during the immediate post-surgery period are wound healing, infections, limited range of motion, swelling, and pain in the residual limb. The goals of this part of recovery are adequate healing of the

residual limb, optimizing nutrition, minimizing pain and swelling, and slowly starting the rehabilitation process (Cristian 2005).

Following the amputation, the prosthesis user begins the rehabilitation process which involves the surgeon, prosthetist and therapist. The surgeon's main task is to leave as much as residual limb as possible, preserving musculature, and effective suturing of the remaining soft tissue. The residual limb is housed in a customized socket and is integrated with a prosthesis.

1.5 PROSTHESIS

Prosthesis is a device which is used to replace a missing part of the body. Prosthetic technology is emerging with advanced use of new lightweight materials and designs that are biomimetic. Micro-processor based prosthetics are used nowadays for effective functioning and to show real life response. In the case of transfemoral amputees, the knee joint which is an active joint for gait, is replaced by a prosthetic leg with a mechanical joint. The main function of the prosthesis is to provide the structural support in the stance phase and a smooth swing phase. A well designed prosthesis should be able to improve the user's ability to participate in physical activities resulting in higher quality of life.

1.5.1 Classification of Prosthetic Knee

There are many manufacturers supplying various kinds of prostheses. The knee joint is the primary component on which the various models available in the market can be classified. Based on the geometry, the knees can be classified as follows. A few examples of commercially available prosthetic knees are also provided.

- 1. Single axis knee:** This is a compact design based on a hinge joint and is ideal for moderately active patients. The knee supports the weight of the patients in stance phase and flexes and extends in swing phase. For example, single axis friction knee (Make: Hosmer), 3R41 (Make: Otto Bock), Rheo Knee (Make: Össur), etc.
- 2. Polycentric knees:** These are knees based on linkage mechanisms to allow multiple axes of rotation. These will have polycentric behavior and are good at mimicking real life gait motion. These can be designed to offer stability in early

stance phase and flex in late stance to commence the swing phase. Examples of this type of knee are Total knee (Make: Össur), SpectrumEX 4-Bar Knee (Make: Hosmer), Stanford-Jaipur Knee (Make: Jaipurfoot), etc.

Based on the function, the knees can be classified as follows:

- 1. Manual locking knee:** This type of knee is locked during the gait cycle and the patient releases the lock in order to perform other tasks such as sitting down. For example, 3R33 (Make: Otto Bock), Locking Knee (Make: Össur) etc.
- 2. Free moving knees:** This type of knees maybe of self-locking in nature or of variable damping. They are further classified as follows:
 - a. Stance controlled knees:* The knee locks itself in stance phase when the patient exerts weight on the prosthetic leg and releases itself when the weight is removed in the swing phase. Examples of this type of knee are 3R49 (Make: Otto Bock), Stabilized Pyramid knee (Make: Hosmer), Endolite ESK + MKL (Make: Endolite) etc.
 - b. Friction controlled knees:* The friction between the rubbing parts dampen the swing action of the shank. An example of this type of knee is Stanford-Jaipur knee.
 - c. Pneumatic damper controlled knees:* The damping effect is provided by the pneumatic dampers equipped in this knee. An example of this type of knee is OP5 Knee (Make: Össur).
 - d. Hydraulic damper controlled knees:* In this type of knee joint, the damping is achieved by using a liquid filled damper. Examples of this type of knees are Mauch SNS knee (Make: Össur), Endurance 160 Hydraulic unit (Make: Fillauer), etc.
 - e. MR fluid based knees:* Smart fluids, such as MR fluid is used to achieve variable damping in this type of knee. An example of this type of knee is Rheo knee (Make: Össur).

Based on the type of damping, the knee joints can be classified as follows:

- 1. Passive knee:** In this type of knee joint, the movement of the shank is being controlled by the thigh alone. Examples of this type of knees are Mauch SNS knee (Make: Össur), 3R41 (Make: Otto Bock), etc.

2. **Active knee:** In this type of knee joint, the movement of the shank is being controlled by the thigh along with other actuating elements such as hydraulic power pack, DC motor, etc. The actuating elements supply positive power as well as dissipate the power (damping) from the knee joint. An example of this type is Power Knee (Make: Össur). They are also referred to in the literature as active microprocessor controlled knees or intelligent active knees.
3. **Semi-active knee:** This type of knee joint does not add energy to the system, but can dissipate energy from the system. This can be achieved using elements such as variable orifice dampers, smart fluids, etc. Examples of this type of knees are Rheo knee (Make: Össur), C-leg 4 (Make: Otto Bock), etc. They are also referred to as passive microprocessor controlled knees or intelligent passive knees.

1.6 MAGNETORHEOLOGICAL (MR) FLUID

This is a class of smart fluid which consists of soft ferromagnetic or paramagnetic particles suspended in a base carrier oil. Usually the ferromagnetic particles are pure iron, carbonyl iron, or cobalt powder and the carrier fluid may be silicone or mineral oil. Other additives for anti-settling or dispersing agents may also be added to the fluid. When no magnetic field is applied, the particles are distributed randomly in the fluid as shown in Figure 1.3 (a). However, an application of magnetic field induces a dipole moment in the particles and they tend to align themselves along the external field. This chain formation as shown in Figure 1.3 (b) induces a reversible yield stress in the fluid.

1.6.1 MR Fluid Modes

There are four different operational modes of the MR fluid which depends on the fluid flow, application of magnetic field and motion of plates. They are described as follows:

1. **Flow mode:** In this mode, the MR fluid flows between two stationary plates. Also, the magnetic field is applied perpendicular to the direction of flow as

shown in Figure 1.4 (a). Applications based on this mode include MR dampers and MR Powertrain mounts.

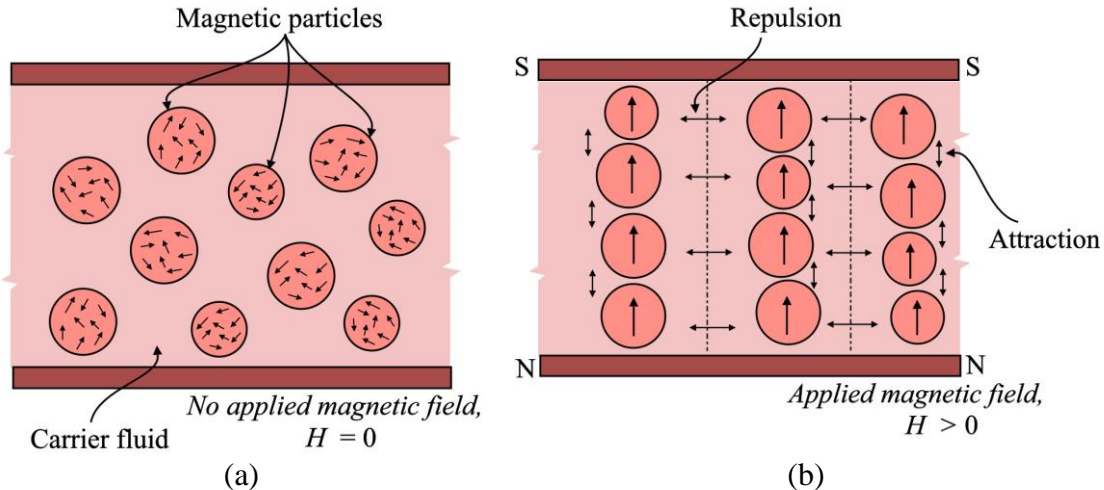


Figure 1.3 Behavior of MR fluids (a) No applied magnetic field, $H = 0$ and (b) Applied magnetic field, $H > 0$

2. Shear mode: In this mode, the MR fluid flows between two plates of which one is stationary and the other is in relative motion along the flow direction as shown in Figure 1.4 (b). Also, the magnetic field is applied perpendicular to the flow direction. Devices which are based on this mode are rotary dampers, brakes and clutches.

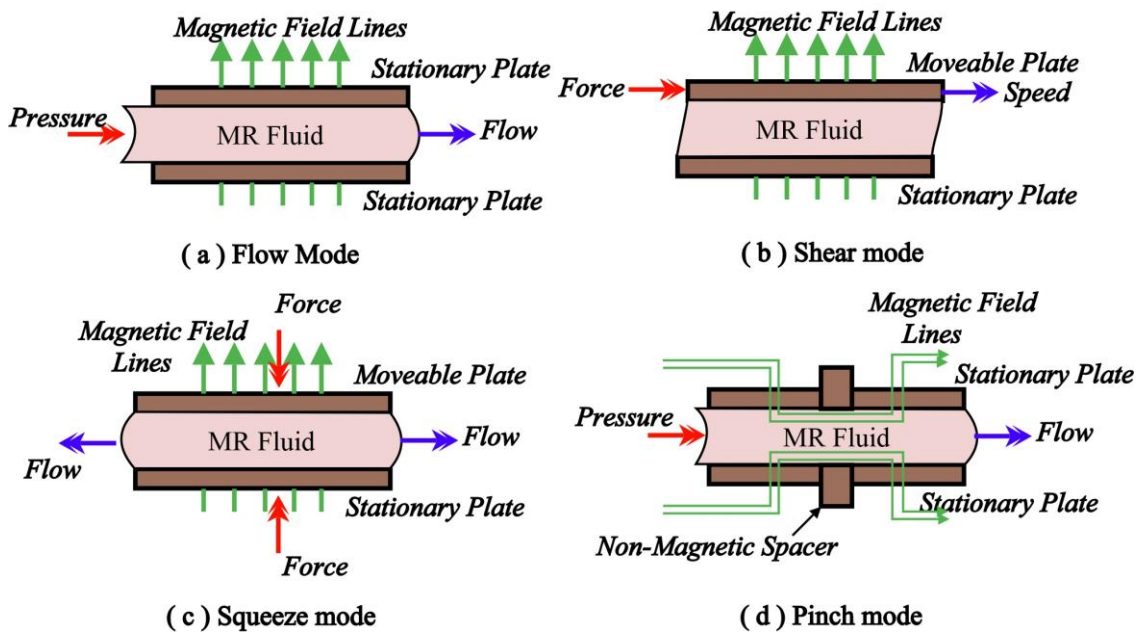


Figure 1.4 MR fluid modes

3. **Squeeze mode:** In this mode, the MR fluid is sandwiched between two plates. One of the plates is in motion towards or away from the other plate such that it creates a squeeze effect on the MR fluid. The magnetic field lines are also applied along the direction of plates as shown in Figure 1.4 (c). This is restricted to applications in which the vibration amplitudes are small.
4. **Pinch mode:** Both the plates are stationary in this mode. The MR fluid flow and the magnetic field lines are in parallel direction as shown in Figure 1.4 (d). This arrangement of magnetic field creates an orifice with a controllable diameter. This configuration is recently explored and has very limited studies.

1.6.2 MR Damper

An MR damper is a device which uses the variable rheological properties of the MR fluid and dissipates energy from the system. This device can use any of the fluid working modes described in the previous section. However, device configurations primarily use flow and shear working modes. A broad classification of MR dampers is shown in Figure 1.5.

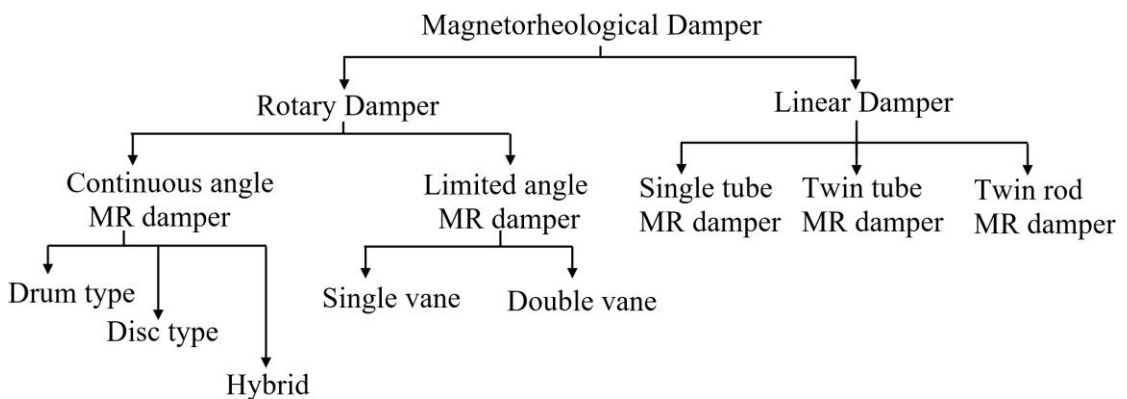


Figure 1.5 Classification of MR damper (Adapted from Imaduddin et al. (2013))

1. Rotary MR Damper

This is a class of damper which is operated based on angular velocity and uses any of MR fluid working modes for its operation. Based on the range of motion, this can be further classified into two types namely, continuous angle damper and limited angle rotation damper.

a. *Continuous angle MR damper*: This type of rotary MR damper can trace a complete rotation. Examples of this type of damper are rotary MR brakes. Generally, brakes and dampers are two different devices. The former defined as a device intended to slow or completely stop the motion and the latter serves to dampen the motion by removing energy from the system. However, in the context of applications of MR fluid devices specifically to prosthetic knee, they are used synonymously here in this study. This can be further classified into drum, disc and hybrid types based on the arrangement of rotor, stator, magnetic coil etc.

In the disc type design configuration, the effective area of shear is the axial face of the rotor as shown in Figure 1.6 (a). In the drum type, the effective area of shear is the radial face of the rotor as shown in Figure 1.6 (b). In a hybrid type configuration, shearing action takes place at both the axial as well as radial faces. Other continuous angle MR brake configurations also exists such as T-shaped rotor, inverted drum type, waveform boundary, etc. and are described in the following chapter with the help of supporting literature.

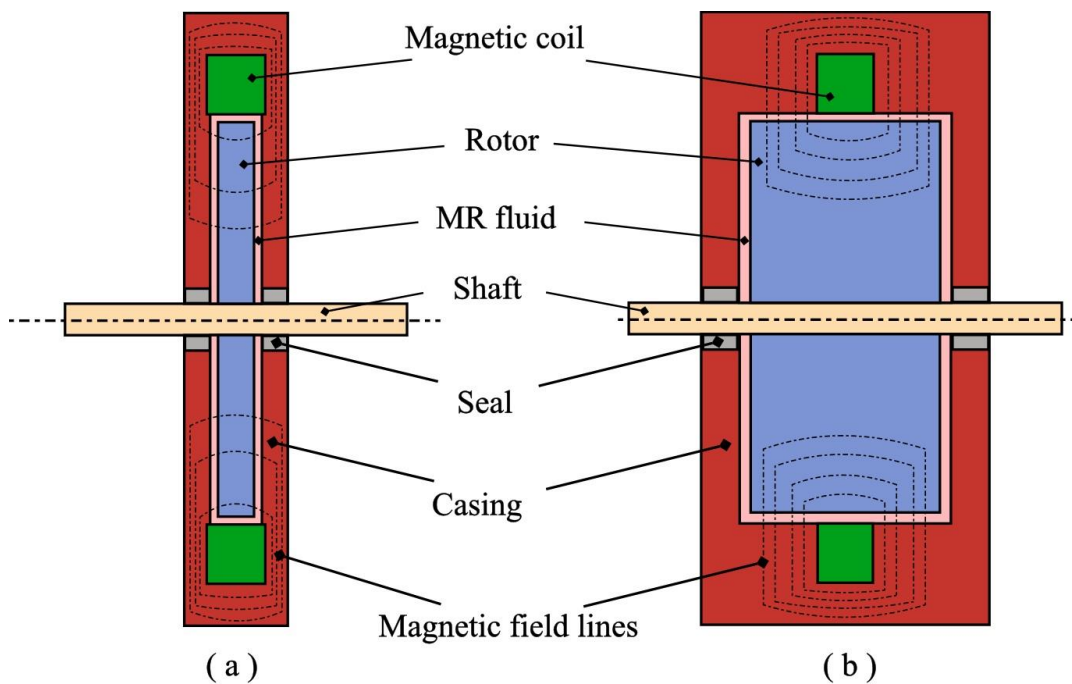


Figure 1.6 (a) Disc type MR brake and (b) Drum type MR brake

b. *Limited angle motion MR damper*: This type of damper cannot make a continuous rotation but is suitable for applications involving limited rotation. Structurally, this design configuration consists of a rotary chamber containing MR fluid. Rotary and static vanes divide the rotary chamber into multiple volumes. Motion of the rotary vane generates a fluid flow from one chamber to the other and the use of MR valve in the fluid flow path creates a variable resistance. A rotary vane damper with an internal MR valve is shown in Figure 1.7. Based on the number of vanes, it can be further classified as single vane and double vane rotary damper.

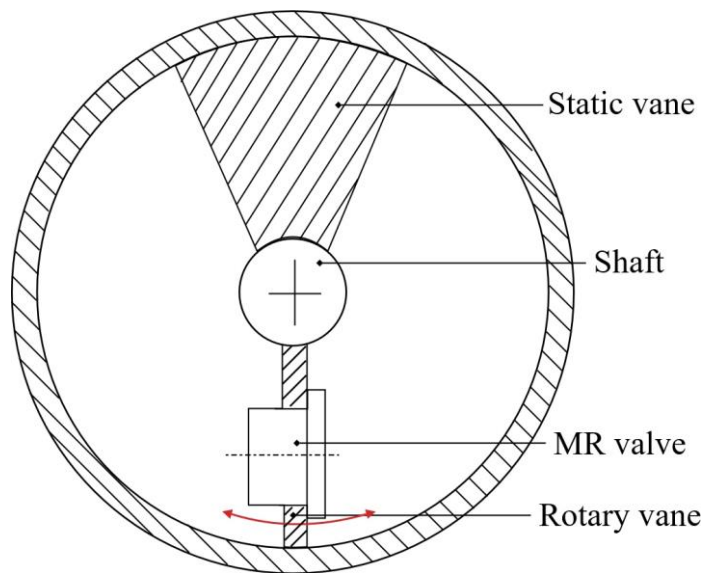


Figure 1.7 Rotary vane damper with internal MR valve

2. Linear MR damper

This is a class of damper which is operated based on linear velocity and uses any of MR fluid working modes for its operation. They can be further classified into single tube, twin tube and twin rod MR dampers.

a. *Single tube MR damper*: This design configuration consists of single cylinder tube. The piston itself acts as the MR valve and depending on the flow of MR fluid through an annular channel or via a shear gap between cylinder and piston, it can be considered as flow mode or shear mode device. An example of single tube MR damper is shown in Figure 1.8 (a). Since fluid flows through the small gap between the piston and cylinder, this can be assumed as a shear mode

device. Also, to accommodate the volumetric changes due to the motion of the piston rod, to avoid cavitation and to compensate for thermal expansion, a small accumulator chamber is employed. The high pressurized gas in the accumulator can be separated using arrangements such as floating piston, bellows etc. The hollow piston rod allows the electromagnetic coil terminals to be accessed easily outside the damper.

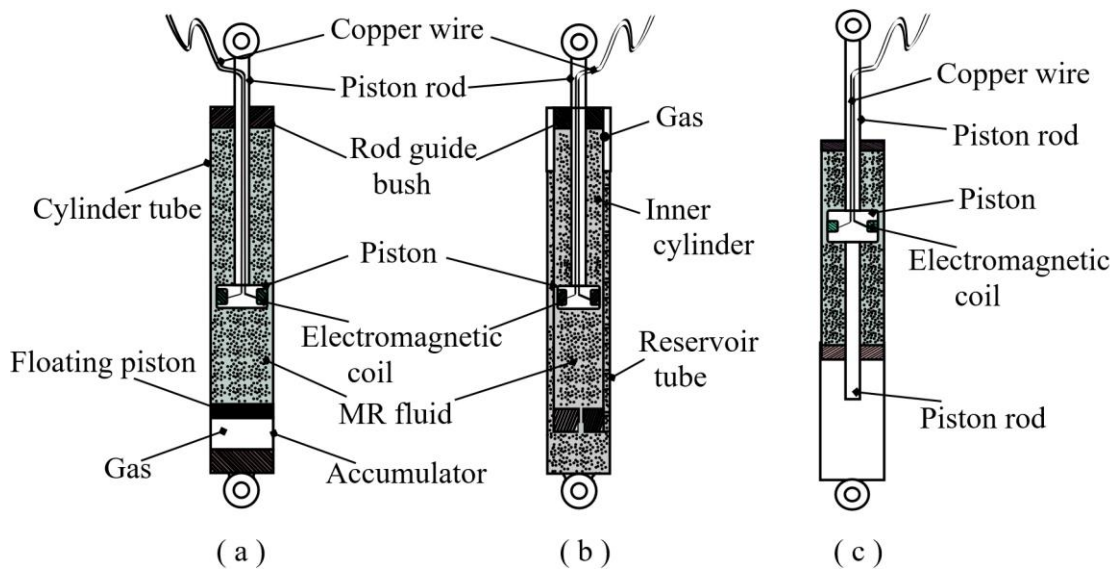


Figure 1.8 (a) Single tube MR damper, (b) Twin tube MR damper and (c) Twin rod MR damper (Goldasz and Sapiński 2015)

b. Twin tube MR damper: Mono tube dampers require highly charged accumulators to avoid cavitation problems. Therefore, this arrangement of twin concentric cylinders allows the MR damper to work with a relatively low pressured gas. The piston rod and MR valve in the piston can exist similar to that of mono tube damper. However, this damper consists a base valve which regulates the flow of MR fluid from the inner cylinder to the outer reservoir. Use of gas without any (usually) separating component restricts the damper to work in upright or in low inclination angular positions. A schematic of this design configuration with a shear mode working for MR fluid is shown in Figure 1.8 (b).

- c. *Twin rod MR damper*: This is by far the simplest design configuration of linear MR dampers. The piston with MR valve is attached to piston rods on either side as shown in Figure 1.8 (c). If both the piston rods are of same diameter, volumetric changes due to piston rod displacement does not exist. However, in situations with large damping force, an accumulator for thermal compensation can be maintained.

1.7 MR FLUID MODELS

The characteristics of MR fluids depends on various factors such as particle volume fraction, base oil viscosity, additives, induced magnetic field etc. The induced field, also called as MR effect, may appear as changes in viscosity or appearance of a yield stress. There exists pre-yield and post-yield regions of behavior of MR fluids. In the pre-yield region, the MR fluid behaves as a semi-solid with no flow. Once the applied force crosses the yield stress level, the liquid starts flowing and this is considered as a post-yield region where MR fluids mostly work in. The flow behavior of the MR fluids can be estimated using various models proposed in previous studies. Although many models based on structuration of MR fluids, discrete approaches considering various forces such as fluid-particle, particle-particle interaction forces, inter-particle magnetic forces, etc. are studied in previous studies, the design of MR fluid based devices is mostly based on rheological models. Some of the most conveniently reported rheological models for MR fluids are provided below.

- 1. Bingham – Plastic model**: This model contains a variable shear stress parameter in parallel to a Newtonian viscosity. The behavior of the fluid is shown in Figure 1.9 (a) and the shear stress applied on the fluid can be estimated using Equation (1.2) (Mitsoulis 2007),

$$\tau = \tau_y + \eta \dot{\gamma} \quad |\tau| > \tau_y \quad (1.2)$$

Here, τ_y is the field dependent yield stress of the fluid, η is the apparent viscosity or off-state viscosity of the fluid and $\dot{\gamma}$ is the shear rate.

- 2. Herschel – Bulkley model:** This model takes into consideration the post-yield shear thickening or thinning nature of MR fluids. The shear stress in this model can be expressed as (Mitsoulis 2007),

$$\tau = \tau_y + K(\dot{\gamma})^n \quad |\tau| > \tau_y \quad (1.3)$$

Here, τ_y is the field dependent yield stress of the fluid, $\dot{\gamma}$ is the shear rate, K is the consistency index and n is the flow behavior index. For the case of $n = 1$, this model reduces to Bingham model. The shear stress versus strain curve for the model is shown in Figure 1.9 (a).

- 3. Casson model:** The behavior of the fluid is shown in Figure 1.9 (a) and the fluid shear stress can be modeled according to the equation (Mitsoulis 2007),

$$\sqrt{\tau} = \sqrt{\tau_y} + \sqrt{\eta\dot{\gamma}}, \quad \text{for } |\tau| > \tau_y \quad (1.4)$$

- 4. Biviscous model:** In this model, the rheology of MR fluid is characterized in terms of pre-yield and post-yield behavior as shown in Figure 1.9 (b). The shear stress can be estimated by the following equation (Goldasz and Sapiński 2015),

$$\tau = \begin{cases} \eta_r \dot{\gamma} & \tau \leq \tau_1 \\ \tau_y + \eta \dot{\gamma} & \tau > \tau_1 \end{cases} \quad (1.5)$$

Here, η_r and η are the elastic and viscous fluid properties. It can be noticed that in a limiting case of $\eta_r \rightarrow \infty$, this model tends to Bingham model.

- 5. Biplastic Bingham model:** This model also takes into consideration the pre and post-yield behavior of MR fluids with the shear stress varying according to the equation (Goldasz and Sapiński 2015),

$$\tau = \begin{cases} \tau_1 + \eta_r \dot{\gamma} & \tau \leq \tau_2 \\ \tau_y + \eta \dot{\gamma} & \tau > \tau_2 \end{cases} \quad (1.6)$$

The behavior of MR fluids in this model can be seen in Figure 1.9 (c).

6. Papanastasiou model: To avoid using discontinuity relations between pre-yield and post-yield relations, an exponential stress growth term was considered in the fluid model as given by the following equation (Papanastasiou and Boudouvis 1997),

$$\tau(\dot{\gamma}) = \tau_N(\dot{\gamma})W_1(\dot{\gamma}) + \tau_{Bn}(\dot{\gamma})W_2(\dot{\gamma}) \quad (1.7)$$

Here, τ_N and τ_{Bn} are the Newtonian and the Bingham shear stress respectively, W_1 and W_2 are the weight functions. The fluid behavior can be seen in Figure 1.9 (d).

For a more detailed review on modelling of MR fluids, the study by Ghaffari et al. (2015) can be referred.

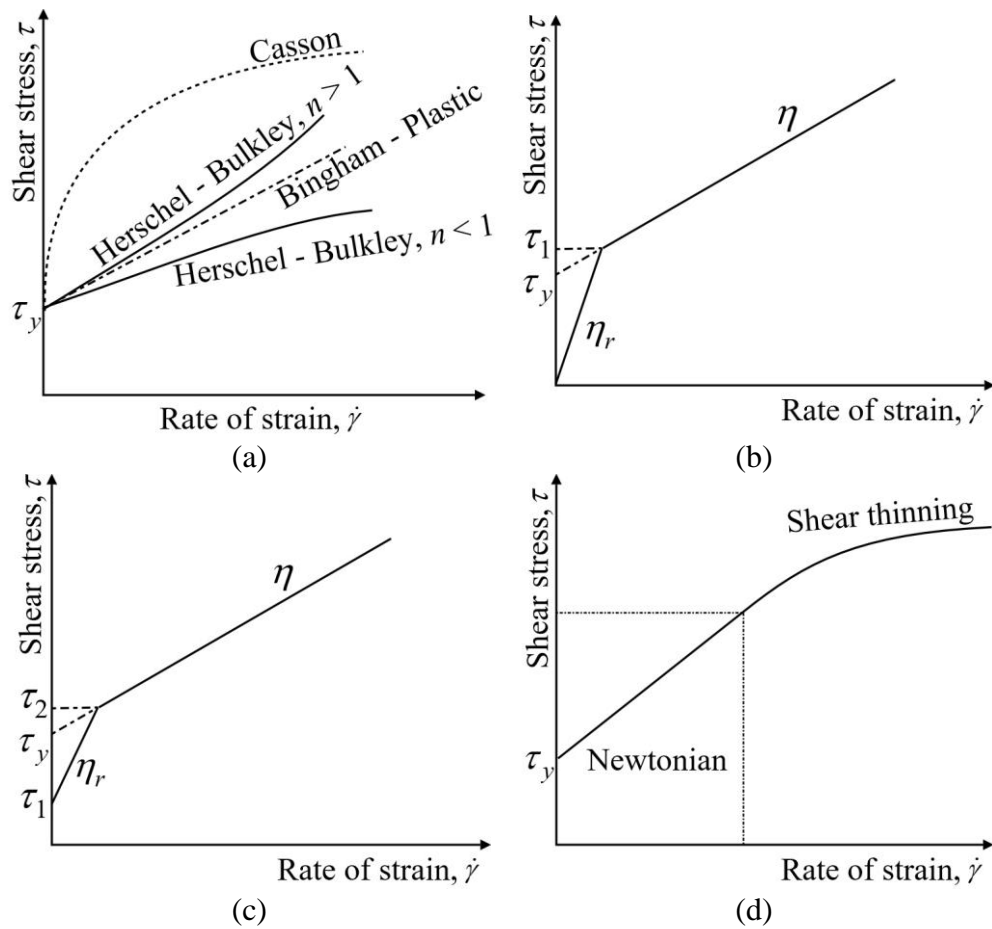


Figure 1.9 Shear stress versus shear strain curves for (a) Bingham, Herschel-Bulkley and Casson models, (b) Biviscous model, (c) Biplastic model and (d) Papanastasiou model (Ghaffari et al. 2015).

1.8 MR DAMPER MODELS

Mathematical modeling of the MR damper helps in the design process of the damper, to understand the non-linear behavior, to perform simulation studies and also to study feedback control strategies. Various models have been developed in the previous studies and according to the model property, they can be classified into two main types.

1. **Quasi-static models:** In this modeling approach, the MR fluid models described in section 1.7 are used to develop mathematical equations specific to the geometry of the damper under study. Generally, linear MR damper models are developed using Bingham-Plastic model while rotary MR brake are modeled using Herschel-Bulkley model. This modeling approach is extensively used in the optimal design studies of MR dampers.
2. **Dynamic models:** The quasi-static models cannot sufficiently describe the nonlinear behavior of MR dampers under dynamic loading. Therefore, dynamic models are proposed which can predict the non-linear behavior of MR dampers, especially the force-velocity characteristics. For example, Bouc-Wen models, Dahl models, Tangent models, etc.

According to the modeling methods, the dynamic models can be further classified into two types.

- a. *Parametric models:* This modeling technique characterizes the device using a set of linear and/or nonlinear springs, dampers and other physical elements. Examples of this modeling approach are Bouc-wen models, Dahl operator based models, sigmoid function based models, Bingham-plastic based dynamic models, etc. The model parameters are evaluated by fitting the model to the experimental data using optimization methods.
- b. *Non-parametric models:* This modeling technique employs analytical expressions to describe the damper behavior. Examples of this modeling techniques are polynomial models, black-box model, neural network model and fuzzy models.

Based on the model reversibility, the dynamic models can be classified into two types.

- a. *Forward dynamic models*: These models evaluate the damping forces given the displacements, velocities and currents as inputs. They can help in studying the dynamic responses of MR dampers or systems coupled with them.
- b. *Inverse dynamic models*: These models predict the applied current/voltage for the given inputs of displacements, velocities and force. They are beneficial to the studies based on feedback control strategies.

1.9 SUMMARY

In this chapter, the anatomical terminology has been introduced. A brief discussion of transfemoral amputation, prosthetic knee devices used by transfemoral amputee and their classifications have been presented. Later, a brief introduction of MR fluids and the various damping devices based on such fluids has been provided. Finally, rheological models of MR fluids and mathematical models of MR dampers have been presented.

The present chapter provides the terminology necessary to understand the remaining part of this work. A few other required elements are described upon their introduction in subsequent chapters, while others are supported by related material in the Appendix. The next chapter focuses on the literature review of many aspects related to design of MR fluid based devices in prosthetic knee application.

CHAPTER 2

LITERATURE REVIEW AND METHODOLOGY

2.1 INTRODUCTION

The process by which the human body activates different muscles and provides adequate torque at the respective joints for normal walking is almost automatic and performed subconsciously. Although it can be argued that every bone in the body plays a minor role in the walking process, from a practical point of view it is only necessary to consider the bones of the pelvis and legs. Also, the center of mass of the body moves in all the three anatomical planes of the body. However, transfemoral amputee gait study is concerned predominantly with the sagittal plane motion of the human body and thus is only considered in the present work.

The earlier works in body movement were based on a knowledge of anatomy and observations of the way in which the human body was used in various activities. The lack of equipment restricted them to measure the patterns of movement or the forces developed in the motion. A review of musculoskeletal modeling by Paul (2005) reports about the series of events or work done by various investigators in the field of human body motion. To summarize, the interest began with investigators trying to obtain kinematic patterns of human gait, obtaining angular displacements and inter-segmental forces in swing phases, to the use of force plate data for calculating the same in stance phases and to the extent of using musculoskeletal modeling to obtain the muscle activation patterns in the human gait cycle. Quantifying the human walking is in itself a difficulty, while reproducing the normal gait for an amputee is almost an impossible task. There are many compromises to be made for designing assistive or wearable devices so as to perform the intended task as normally as possible.

Smart fluids, particularly MR fluids have gained a lot of popularity in the past few decades and have been applied in many areas where controllability, adaptability and fast response times are desirable. Of these applications, vehicular suspension seems to be one area which has seen major research contribution with the implementation of

MR fluids in dampers, brakes, etc. The quest for variable walking speed, fast response time, low power requirements and a dynamic torque range attracted the use of these smart fluids in semi-active prosthetic knee domain too. Although there exists only one commercially available design based on MR fluid, many alternative knee design configurations have been studied by various researchers. A review of literature by a few of them organized as per the device configuration is briefed in the following sections. Before proceeding with the design configurations and their design methodologies, a systematic literature review starting with the use of semi-active devices in prosthetic knee domain, advantages and limitations of semi-active devices compared to active knee devices is provided next.

2.2 TRANSFEMORAL PROSTHESIS

A prosthesis is a device which is used to replace a missing part of the body. A typical knee prosthesis consists of a socket which houses the stump of the amputee, a knee joint, a shank attachment, an ankle joint and a prosthetic foot as shown in Figure 2.1. Although each component is a part of ongoing research undergoing with many improvements, the knee joint is the one component which has attracted the maximum effort in terms of development. This is because it plays a stellar role during the whole gait cycle, articulating between the thigh and the shank and making human gait the most efficient mode of moving body from one position to another (Torrealba et al. 2008).

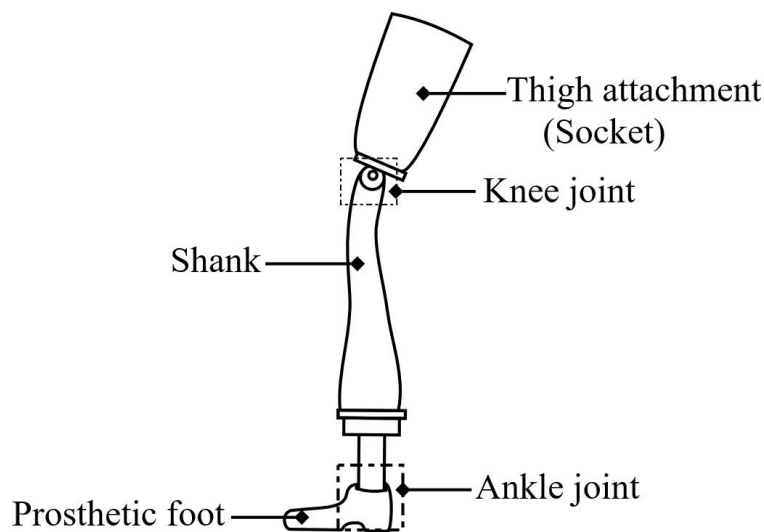


Figure 2.1 Typical prosthetic knee system

Prosthetic technology has emerged from the first introduction of peg leg to an advanced use of new light-weight materials and designs that are biomimetic. An evolution of knee prosthesis can be seen in Figure 2.2. The scientific research that took place in Europe after the end of World War I helped in commercialization of mechanically passive prostheses such as 3R22 and 3R15 by Ottobock (Radcliffe 1977). Later with the introduction of fluid controlled prostheses during the 1950s by Hans Mauch (Mauch 1968), the knees with hydraulic cylinders such as GaitMaster and Mauch SNS knee were commercialized by Össur and exist even today. The introduction of hydraulic prostheses provided high resistive torques to the knee system giving the user the security and stability in the stance phase. Also, knee flexion and extensions during the swing phase are smooth for a large range of cadences. With the advancement in electronics, attempts to realize a fully active knee were made in the 1970s; however, the approaches were experimental trials and microprocessor controlled or intelligent passive (or semi-active) prostheses were introduced in the market only during the 1990s (Torrealba et al. 2008).

The first introduction of microprocessor controlled knee was the “Intelligent Prosthesis” by Blatchford & Sons Ltd. in 1993. The knee featured a weight activated stance control along with a pneumatic swing phase control. The diameter of a variable orifice in the pneumatic damper was adjusted according to the swing speed. The knee got substituted by many improved versions and is currently being marketed as “SmartIP”. The earlier versions of intelligent knees did not offer any stance phase control; however, this feature was initiated by C – Leg (Make: Ottobock) and Rheo Knee (Make: Össur), the former launched in 1997 and the latter in 2001. Further, the only active knee commercially available in the market is Power knee, launched by Össur in 2007. Table 2.1 provides a few microprocessor controlled prosthetic knees currently available in the market and their various features in stance and swing phase control. As can be seen in the table, semi-active prostheses are also capable of providing swing and stance phase resistances similar to an active knee (Power knee). However, the real benefits of an active knee can be seen in activities such as sit to stand tasks, where it delivers powered extension when standing up and controlled resistance while descending.



Figure 2.2 Evolution of knee prostheses (Source: ¹www.ottobock.com, ²www.ossur.com, ³www.blatchfordus.com)

Table 2.1: Types of microprocessor controlled prosthetic knees (Henrikson et al. 2011)

Prosthetic knee (Manufacturer)	Stance control system	Swing control system	Function of microprocessor			
			Adjusts knee resistance during stance	Adjusts knee resistance during swing	Switch to stance	Switch to swing
Power (Össur)	Motor powered	Motor powered	Yes	Yes	Yes	Yes
Rheo (Össur)	MR fluid	MR Fluid	Yes	Yes	Yes	Yes
Genium (Ottobock)	Hydraulic fluid	Hydraulic fluid	Yes	Yes	Yes	Yes
C-Leg (Ottobock)	Hydraulic fluid	Hydraulic fluid	Yes	Yes	Yes	Yes
Compact (Ottobock)	Hydraulic fluid	Hydraulic fluid	No	No	Yes	Yes
Orion (Endolite)	Hydraulic / Pneumatic fluid	Pneumatic fluid	Yes	Yes	Yes	Yes
Smart Adaptive (Endolite)	Hydraulic / Pneumatic fluid	Pneumatic fluid	Yes	Yes	Yes	Yes
SmartIP (Endolite)	Mechanical friction (Weight - activated)	Pneumatic fluid	No	Yes	No	No
IP+ (Endolite)	Mechanical friction (Weight - activated)	Pneumatic fluid	No	Yes	No	No
Single axis Power/Intelligent (Trulife)/(Nabtesco)	Mechanical friction (Weight - activated)	Pneumatic fluid	No	Yes	No	No
4 bar power /Intelligent (Trulife) / (Nabtesco)	Geometric	Pneumatic fluid	No	Yes	No	No
Fusion power / Hybrid (Trulife)/(Nabtesco)	Hydraulic fluid	Pneumatic fluid	No	Yes	No	No
Plie (Freedom Innovations)	Hydraulic fluid	Hydraulic fluid	No	No	Yes	Yes
REL-K (Fillauer)	Hydraulic fluid	Hydraulic fluid	Yes	Yes	Yes	Yes

Comparative studies between normal and transfemoral subjects indicate that the latter have lower walking speeds, larger stride lengths, asymmetrical walking patterns and extreme lateral bending (Jaegers et al. 1995). Further, transfemoral amputees cannot shift smooth trajectories of gravity points like healthy subjects, the reasons being impossibility of flexion in the amputated leg as supporting leg and the higher velocity of the sound limb in swing phase (Hayashi et al. 2014). Many studies showed that unilateral transfemoral amputees have asymmetric gait patterns; however, the use of prosthesis with even a slight modification or a technological advancement may bring significant improvements in the transfemoral amputees' gait and provide the user satisfaction and a sense of stability. Thus it is worthwhile to brief here a few comparative studies which have been performed showing the relative advantages and limitations among various commercially available prosthetic knee systems.

A clinical comparison of polycentric (3R20) and single axis knee (3R15) was performed by Taheri and Karimi (2012). Based on the spatiotemporal parameters such as step length, cadence, and walking velocity, the study concluded that the performance of above knee amputees while walking with 3R20 may be better than that of 3R15, as the walking speed with polycentric knee joint was more than that with the single axis joint. Moreover, walking with polycentric knee was found to be more symmetrical compared to a single axis knee. The study however suffers from a limited number of subjects.

A simulation study on the swing phase behavior of a single axis knee and an indigenously developed polycentric knee was considered by Sudeesh et al. (2020). A negative heel clearance was found with the polycentric knee suggesting a requirement of hip compensation strategies. Nevertheless, the design was found to be superior to that of a single axis knee in terms of achieving knee extension in preparation for the next stance, even without any extension assist and also with a lower hip effort. Polycentric knees, as a low cost solution for developing countries, can improve stance phase stability; however, the increase in the extent of stability delays the initiation of the swing phase proportionately. This results in abnormal gaits implying that the excessive focus on cost reduction alone cannot serve the desired purpose and low cost

prostheses must also have the ability to provide a gait kinematics closer to that of healthy gait (Pandit et al. 2018).

On the other hand, intelligent passive knees provide sensory feedback to the prosthetic knee system and enable swing phase initiation more easily (Schmalz et al. 2002). Variable damping knees (C-Leg and Rheo knee) are observed to show biomechanical advantages over the passive knee (Mauch SNS) in terms of an enhanced smoothness of gait, a decrease in hip work production, lower peak hip flexion moment at terminal stance and a reduction in peak hip power generation at toe-off (Johansson et al. 2005). Further, an obstacle course performance and a quality of life survey showed that C- Leg performed better and provides increased functional mobility and ease of performance in home and community environment compared to non-microprocessor controlled knees (Seymour et al. 2007).

Although fluid controlled passive knees can allow the amputee to adjust the level of damping specific to the task, the tasks of meeting real world physical demands such as carrying extra loads (like picking up groceries which is not very uncommon) and the load-adaptive powered knee controllers in intelligent prostheses could be beneficial to the amputees (Brandt et al. 2017). However, a systematic review of literature by Sawers and Hafner (2013) shows that only a low evidence exists indicating that microprocessor controlled knees offer increased walking speed on uneven terrain, improved gait patterns in stair descent and decreased rate of oxygen consumption while walking. Nevertheless, a simulation model over a 10 year time period for unilateral transfemoral amputees demonstrated that microprocessor controlled knees result in a fewer major and minor injurious falls, fewer incidences of osteoarthritis, lives saved on a per person per year basis compared to non-microprocessor knees. Also, microprocessor controlled knees result in a total cost increment of just \$1702 for the 10 year period including direct and indirect healthcare costs, device acquisition and repair costs as compared to their counterparts (Chen et al. 2018).

Compared to intelligent passive prostheses, active prostheses (such as Power Knee) can provide resistance as well as active torque using an electric motor. This allows the prosthetic device to actively flex into swing phase and provide a gait dependent pre-flexed positioning ($4-12^\circ$) at initial contact via active extension at the

end of swing. Also, the use of active knees resulted in diminishing of hip torque differences between the prosthetic leg and sound leg, indicating a more symmetric gait (Creylman et al. 2016). On the other hand, in spite of the power generating capacity of Power Knee, no significant reduction in intact knee power generation was observed (Wolf et al. 2013). Furthermore, to provide a significant amount of energy to the amputee, the device requires a considerable amount of motor and battery pack which increases the overall weight of the prosthetic knee system. For instance, the reported mass of Power Knee is 3.2 kg including batteries (Power knee 2011) whereas, it is around 1.6 kg for Rheo knee (Rheo Knee 2011) and 1.2 kg for C-Leg (C-Leg 2016).

Among various semi-active knees, the ones which provide both swing and stance phase damping offers clear advantages during walking at various speeds, especially at higher walking speeds (Bellmann et al. 2010). The two semi-active knees by Ottobock, Genium and C-Leg are similar in designs, both with a hydraulic actuator and minor modifications such as stance locking feature in the former component. Even a few tasks such as stair descent showed no significant differences on subjects using the two prostheses (Lura et al. 2017). The other most comparative studies performed are between C-Leg and Rheo knee, both differing majorly in their torque producing strategies. The current version, C-Leg 4 generates knee resistance using control of two separate motorized valves (servo valve flexion and extension in Figure 2.3(a)). This enables continuous variations in hydraulic resistance in both directions. A compensation reservoir stores energy due to flexion using a steel spring, which helps in subsequent extension. The spring (a) in Figure 2.3(a) along with the hydraulic channel (b) provides a smooth extension stop.

The Rheo knee generates resistances in both flexion and extension directions using MR fluids. An Iron-Cobalt alloy forms the magnetic core of the device on which electromagnetic coil is wound as shown in Figure 2.3(b). Thin steel blades are attached alternatively on the inner core (rotor) and the outer core (stator) and a rotary motion of the outer cover creates a shearing motion between the plates. The design consists of around 70 plates coupled tightly with a gap size of nearly 30 μm between the blades. The magnetic field generated in the core radiates outwards by the side covers of the brake and is forced to pass through the coupled steel blades. The MR fluid is filled in

the gap between the plates and any change in magnetic field alters the rheological properties of the fluid which affects the torque dissipated by the MR brake.

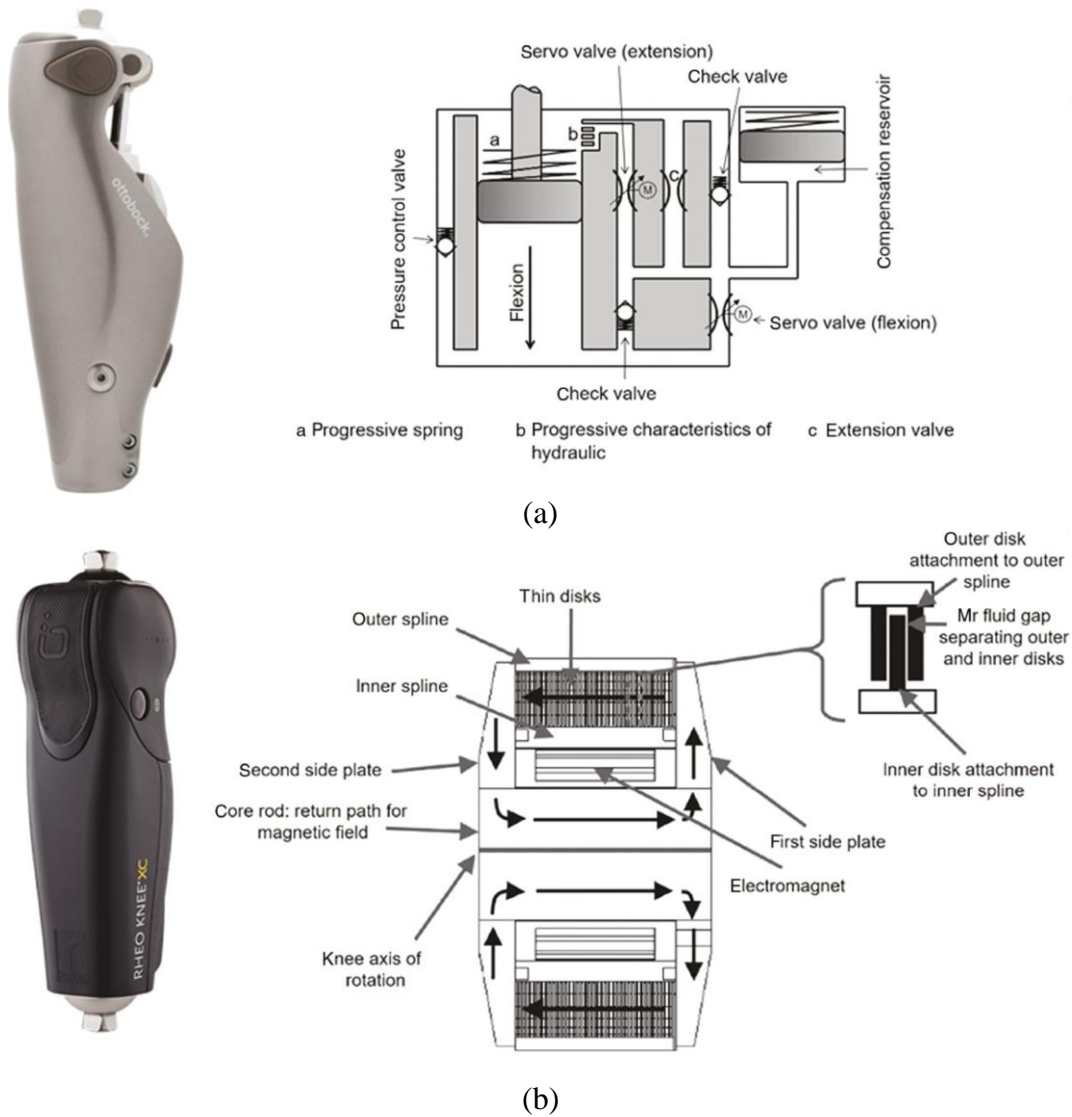


Figure 2.3 Schematic representation of (a) C-Leg 4 and (b) Rheo Knee XC (Bellmann et al. 2019)

The comparative study involving Rheo knee by Johansson et al. (2005) showed an average decrease of oxygen consumption rates, a lower peak hip extension torque during late swing, and a greater peak foot compression during early stance when compared with the C-Leg. On the other hand, C-Leg showed the most natural knee function when compared to the contralateral side of the amputee (Thiele et al. 2019). However, the studies suffer from a very small group of subjects. In any case, inclusion

of a microprocessor control is believed to provide a number of theoretical benefits to the user, including improvements in balance, confidence, uneven terrain ambulation, stair descent, incline negotiation, and overall activity, as well as a reduction in adverse events such as stumbles and falls (Sawers and Hafner 2013). Despite availability of a large variety of prosthetic knee designs, no knee exists which fits any patient (Torrealba et al. 2008). Therefore, there exists a list of technical specifications of various prosthetic systems which guides the prosthetist to recommend to the final user a particular component, depending upon his/her mobility grade, weight and other factors. Due to these reasons, researchers are still exploring low cost solutions along with alternative knee designs.

Drifting away from the commercial perspective on the prosthetic knee systems, the following review is provided with an academic research perspective which explores various possible alternative design configurations with a scope of being applied for prosthetic knee applications. The discussion is limited to devices based on MR fluids and is categorized according to the device configuration classifications provided in the previous chapter.

2.3 SEMI-ACTIVE KNEES BASED ON MR FLUIDS

MR fluid is a smart fluid which consists of soft iron particles suspended in a base oil along with a few additives. Upon introduction of a magnetic field, the particles align themselves in the direction of the external field which induces a reversible yield stress in the fluid. An MR damper is a device which uses these variable rheological properties and dissipates energy from the system. Based on the classification of dampers shown in Figure 1.5, a review of literature on various design configurations applied to knee prosthetic systems is provided next.

2.3.1 MR Brakes

In the literature, the term MR brake is used interchangeably with continuous angle MR dampers and is followed in this work too. The primary classification of MR brakes involves drum and disc type of brakes. Depending on the placement of coil(s), shape of rotor, number of disks, various MR brake configurations as shown in Figure

2.4 can be developed. In the comparative study of various rotor configurations by Nguyen et al. (2015), it was shown that the disc type brakes are the most suitable for braking torque less than 15 Nm and for torque greater than 15 Nm, T-shaped rotor provides the most compact size. Applying a design braking torque of 5 Nm, MR brakes with various rotor configurations such as disc type, drum type, T-type, etc. were considered in their study. It was observed that the disc type rotor brake results in the least mass of 0.65 kg to produce the design torque. However, the evaluated torque range is very less for prosthetic knee application. A normal human of weight 56.7 kg requires a knee braking torque of at least 35 Nm (Winter 2009). An optimal design to reduce the mass of MR brake with a maximum braking torque of at least more than 10 Nm was considered by Nguyen et al. (2014). Various shapes for MR brake envelope such as rectangular, polygonal or spline shape were considered to reduce the uneven distribution of magnetic field in the fluid gap, which can ultimately increase the braking torque of the device. The results indicated that a spline type configuration can produce the design torque with a least mass of 1.029 kg. The above studies have not been performed specifically for prosthetic knee application, however, the optimal designs with the objectives of maximizing braking torque and minimizing mass of the device closely match to that for prosthetic knee application. Based on the above results, it can be concluded that the most common configurations similar to the ones shown in Figure 2.4 cannot be applied directly for prosthetic knee application.

Similarly, Arteaga et al. (2020) considered a single disc type MR brake; however, the device was capable only of producing a maximum torque of 4 Nm. Thus, they have considered a transmission system of ratio 6.25:1 to increase the torque capacity of the device. Even with the use of such a transmission, the system was capable of providing a torque of 25 Nm which again, was insufficient for an average human knee. Also, the mass of the overall system was not reported.

The problem of increasing torque to mass ratio of the semi-active MR brake has been attempted by a research group at Massachusetts Institute of Technology, developing an MR brake with multi-plate configurations (Herr and Wilkenfeld 2003). This is the design on which the current commercial brake, Rheo knee is based. An exploded view of the multi-plate MR brake is shown in Figure 2.5. A number of thin

plates are stacked together and alternately attached to the rotor and the outer cylinder. This design increases the shearing area substantially, producing the required braking torque of more than 35 Nm (Thorarinsson et al. 2006).

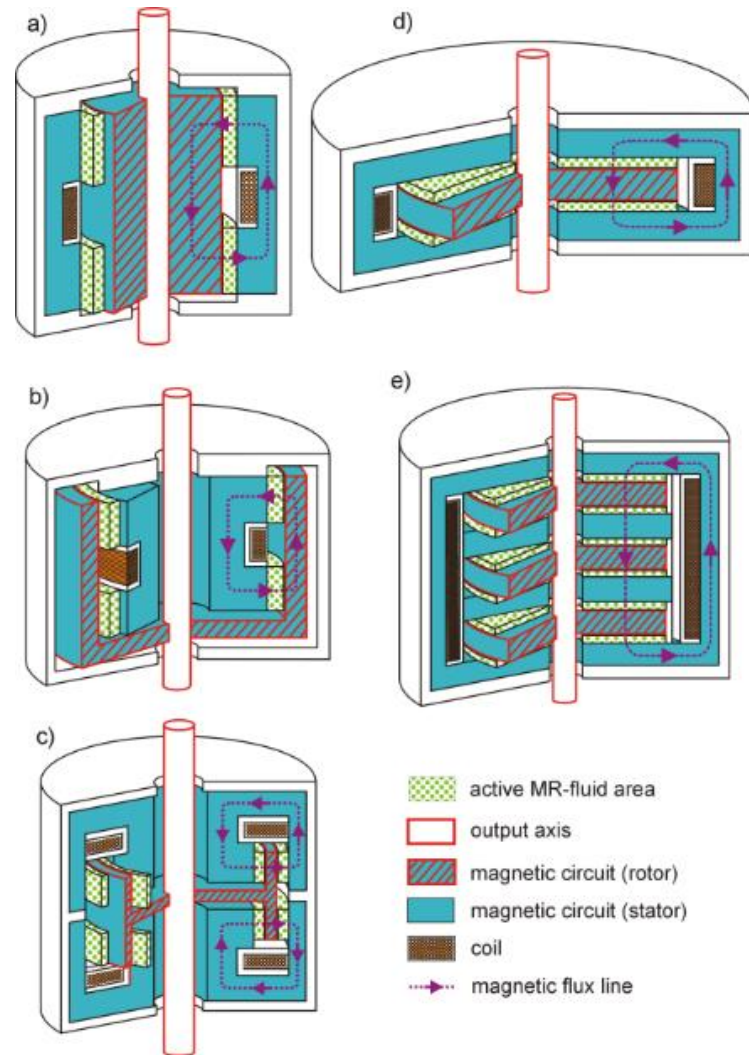


Figure 2.4 Common configurations of MR Brake (a) Drum, (b) Inverted drum, (c) T-Shaped rotor, (d) Disk, and (e) Multiple disk (Avraam et al. 2010)

The original design of MR brake with multi-plate rotor configuration has been improved in a series of studies. A parametric study is conducted to optimize the magnetic flow which further increases the efficiency of the prosthetic knee (Thorarinsson et al. 2006). Also, an increased core size was considered to allow the design to be used by heavier amputees as well (Jonsdottir et al. 2009). A geometric optimization is performed considering reducing on-state and off-state braking torques and mass as the objectives which resulted in producing a design capable of generating

a braking torque of 60 Nm at 1.5 A (Gudmundsson et al. 2010). A few studies also concentrated on designing MR fluids specifically for this application. Gudmundsson et al. (2011) investigated field induced shear yield stress and off-state viscosity of selected unimodal and bimodal distributed MR fluids. A bimodal distribution with a 75% coarse powder and 25% fine powder resulted in the highest ratio between on-state and off-state viscosity and is selected as the best for multi-plate MR brake in their work.

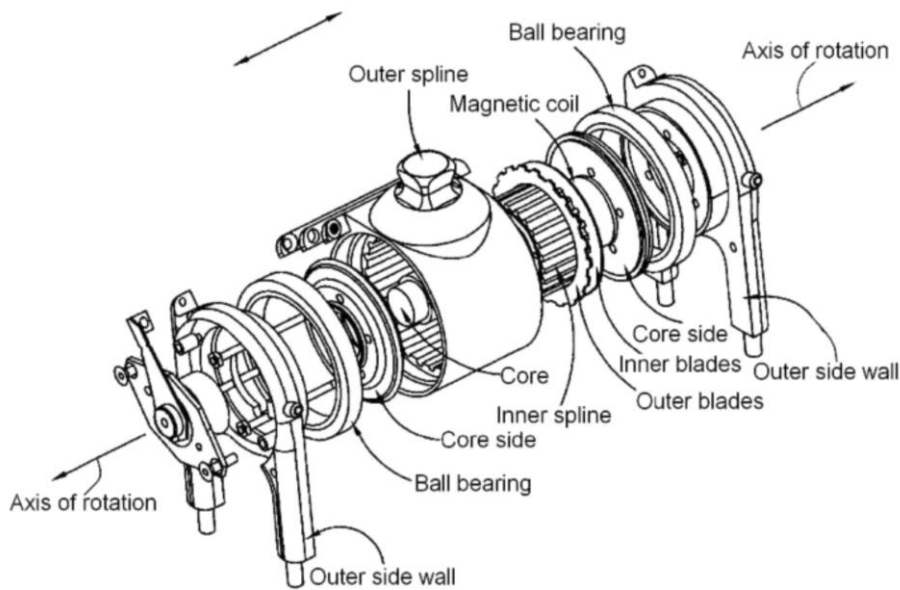


Figure 2.5 Exploded view of multi-plate MR brake (Deffenbaugh and Herr 2004)

Also, a few researchers combined an active element such as DC motor with the semi-active multi-plate MR brake to realize an active prosthetic knee. Ma et al. (2017) designed an MR actuator with MR brake working in parallel with a DC motor. Andrade et al. (2018) considered a similar multi-plate design and designed an active prosthetic knee element comprising an EC motor, a harmonic drive, a multi-plate clutch and brake. The complete assembly resulted in a mass of 2 kg and was capable of producing an active torque of 40.4 Nm and 85.4 Nm of braking torque. One of the disadvantages in the designs based on multi-plate MR brake is the shearing gap which is in the range of 20 – 35 μm . The small shear gap together with an average angular speed of knee of around 8 rpm would result in shear rates larger than 700/s. The amount of deterioration generally depends on the shear rate, temperature and duration (Carlson 2002), thus affecting the durability of the device. The second disadvantage is that the use of novel

fluid with bimodal distribution in commercial models increases the cost of the device. Further, the design is highly sensitive to surrounding shocks and impacts due to the small tolerance between the blades.

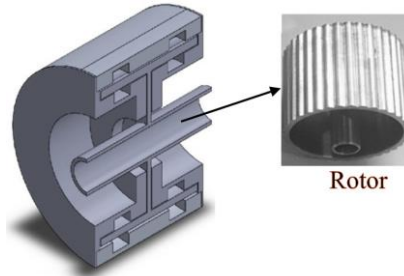


Figure 2.6 Waveform arc boundary on rotor (Mousavi and Sayyaadi 2018)

Another design configuration to achieve higher torque to weight ratio is the novel hybrid MR brake with waveform boundary surface developed by Mousavi and Sayyaadi (2018). They have considered a T-shaped rotor configuration, the outermost surface of the rotor being modified to be of arc waveform as shown in Figure 2.6. This design has a fluid gap tolerance of at least 0.4 mm which is relatively larger than the multi-plate design. Also, this design reduces the number of components in the brake configuration.

2.3.2 Limited Angle MR Dampers

In terms of research publications, not much is available related to the design of vane type MR damper and their applications to prosthetic knee. Kim and Oh (2002) designed a rotary vane damper for knee prosthesis. They have considered a rotary damper in which fluid exists in two chambers separated by a rotary and a static vane. The fluid from one chamber flows into the second chamber through an MR valve with rectangular channel. The magnetic field applied in the MR valve controls the resistance developed by the device. The amount of magnetic field in the valve depends on the exposure caused due to the permanent magnet which is controlled by the servo motor. The use of servo motor as shown in Figure 2.7(a) introduces a time delay in the system and increases the response time. To overcome this, they have considered an electromagnetic valve as shown in Figure 2.7(b) (Kim and Oh 2001). The final design with a fluid rectangular channel gap of 2 mm was able to produce a maximum damping

torque of around 20 Nm. This design has not been developed further to be applied for prosthetic knee applications in any of the future studies.

Due to the lack of relevant literature in the application of rotary vane design for prosthetic knee applications, it is worth mentioning the studies which applied this design for other applications, such as vehicular suspension. Zhang et al. (2009) designed a vane type MR damper based on a conventional hydraulic vane damper. The static vane was made hollow to accommodate the electromagnetic coil. Only the theoretical design of the damper was presented and no data related to the performance was published. Giorgetti et al. (2010) proposed and designed a rotary damper for vehicular applications. The designed damper was comparatively better than the linear dampers in terms of space requirements, quantity of fluid, sedimentation etc. Imaduddin et al. (2014) made a simulation study of double vane bypass rotary MR damper. The damper was characterized using torque-angular velocity curves. The theoretical study revealed that the damper was capable of producing a torque of 1000 Nm at an angular velocity of 1.5 rad/s with a supply current of 1 A.

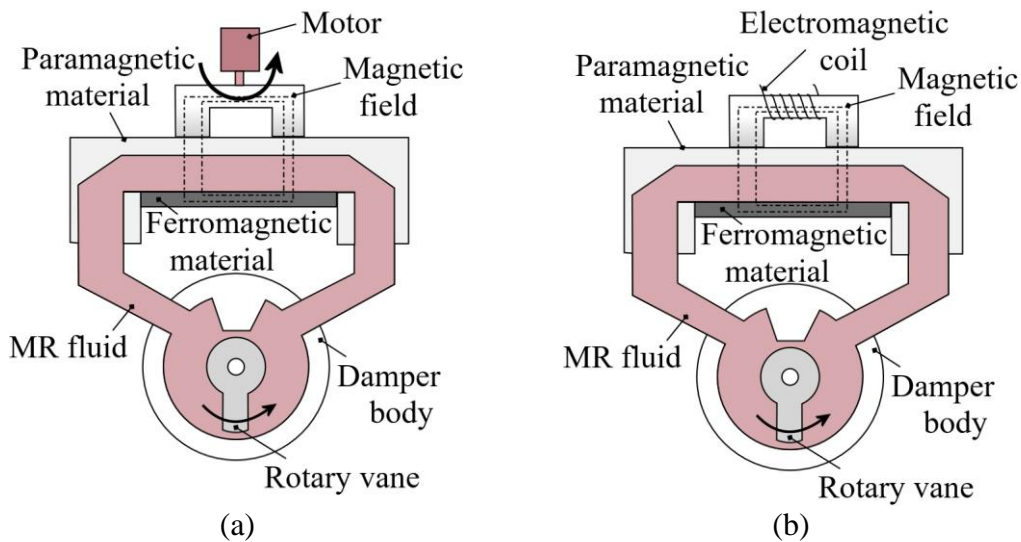


Figure 2.7 Rotary vane damper with (a) Servo motor controlled Permanent magnet and (b) Electromagnet controlled (Adapted from Kim and Oh (2001, 2002))

It can be observed that the rotary vane damper is capable of producing very high torques and has several other advantages in terms of space requirements, weight, etc. but the work carried out and published by applying this design for prosthetic application or any other application is very limited.

2.3.3 Linear MR Damper

Compared to the other designs of MR damper and their applications in prosthetic knee devices, the work done in the use of linear MR damper is relatively much higher. There exist a large number of publications related to the design, analysis and control of MR damper and thus only the ones which relate to the prosthetic applications will be discussed further. The research on the use of linear MR dampers for prosthetic knee applications can be classified into two major themes. The first one is based on the use of commercial dampers, while the other one is based on designing a damper specifically for knee applications. However, both the research areas explore majorly the kinetic, kinematic and control related aspects of the semi-active prosthetic knee system. From the three classifications of linear MR damper shown in Figure 1.5, twin tube MR damper results in higher mass for a given damping force compared to single tube damper due to the use of multiple cylinders and thus was not considered for prosthetic knee applications in any of the previous studies. Further, commercial dampers (such as RD-1003-5 and RD-8040-1) are single tube dampers with inherent accumulator, while the research based dampers are largely twin rod MR dampers, which result in a much more compact design for a given damping force.

RD-1036 MR damper, originally designed for truck seat applications by Lord Corporation, USA, was the first MR damper to be used for prosthetic knee applications by Biedermann Motech GmbH (Carlson et al. 2001). However, the damper and the prosthetic device “Smart Magnetix knee” is currently not listed in any of the supplier’s website. Another variant of damper such as RD-8040 (shown in Figure 2.8) is listed on the manufacturer’s website and is the one which is most often used in semi-active prosthetic knee studies. However, the semi-active prosthetic knee system based on commercial damper RD-1036 is presumably out of production (based on a web search on Smart Magnetix knee or any other variant based on commercial MR Damper).

Ochoa-Diaz et al. (2014) designed a variable damping prosthesis using a commercially available RD-8040 damper and a four bar based knee mechanism. They conducted preliminary tests on amputees in passive mode (with no applied current). A similar study on the application of a commercial damper using a polycentric knee joint was considered by Attia et al. (2016). However, only simulation studies were performed

on an open loop prosthetic knee model which resulted in the prediction of various input current profiles for tasks such as walking, stair ascent and descent. Pandit et al. (2018) proposed a novel and affordable lower limb prosthesis based on RD-8040. Cost analysis of the designed prosthesis was performed which shows its suitability to the amputee population in developing nations.



Figure 2.8 Lord corporation RD – 8040 – 1 (“Lord Corporation” 2001)

Not relying on commercial MR dampers alone, many studies were performed which considered designing an MR damper specifically for prosthetic knee applications. Park et al. (2016) designed and developed an active prosthetic knee using twin rod MR damper shown in Figure 2.9 (a) and a DC motor and tested it in both semi-active and active configurations. Gao et al. (2017) designed an optimal MR damper as shown in Figure 2.9 (b) with cost functions as total energy consumption and weight of the damper. A smart prosthetic knee was developed which hosts a DC motor, MR damper and springs. The complete prototype was not developed, but the MR damper was developed and compared with the simulation results. Fu et al. (2017) studied the effect of hysteresis on MR lower limb prosthesis by comparing an MR damper with hysteresis Bouc – Wen model and an ideal model with no hysteresis. Co-simulation models in MATLAB and Adams software were also performed to measure the swing phase trajectories of the prosthesis. Xu et al. (2016) developed a prosthetic knee utilizing a double ended MR damper with a four bar linkage prosthetic knee. A prototype for the same was developed and experimentally tested by applying constant currents and also by controlled currents using a control logic.

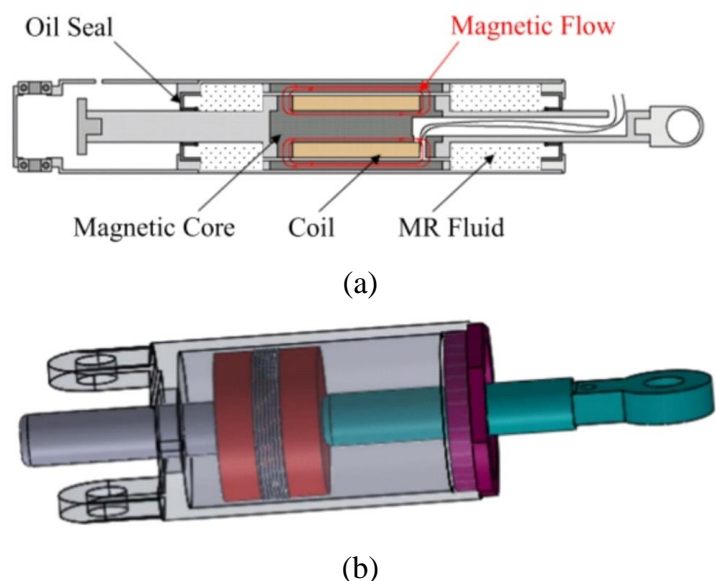


Figure 2.9 Twin rod MR damper design by (a) Park et al. (2016) and (b) Gao et al. (2017)

2.3.4 Control Logics

The control system in both the commercial knee systems and the research knee systems follows the architecture shown in Figure 2.10. The highest level is the perception layer which recognizes the user's intent. Different terrains like level ground, stair or ramps are recognized using various sensory information and a set of transition rules (Fluit et al. 2020). The mid layer is the translation layer which maps the locomotion modes to the desired state outputs of the device. For example, if the higher level detects the user's intent of level ground walking, the mid-level can map this locomotive mode into a set of different phases of level walking which are swing and stance phase and any intermediate phases in between. Finally the low level is the execution layer which acts on the torque commands set for various phases and minimizes the error between the current state and the reference.

Commercial prosthetic knee and few research based active knee prosthetic systems (such as Vanderbilt prosthesis (Lawson et al. 2014), CYBERLEGS-Beta (Flynn et al. 2018), etc.) focus on the whole architecture of control system shown in Figure 2.10. However, studies which focus on developing alternative knee actuators of semi-active or active nature focus mainly on the walking controller (which comprises both mid and low level layers). These studies test their prototype knee actuators using

various methods such as simulation studies, testing on gait motion simulators (Yilmaz and Orhanli 2015), testing on normal human wearing an able-bodied adapter (Park et al. 2016). Since the present study is based on developing an alternative semi-active knee actuator, the studies related to low level execution layer are detailed next. However, for a detailed review on various control architectures including information related to the various sensors employed on commercial as well as research based knees, the studies by Fluit et al. (2020), Lara-Barrios et al. (2018), Spanias et al. (2018) and Tschiedel et al. (2020) can be referred.

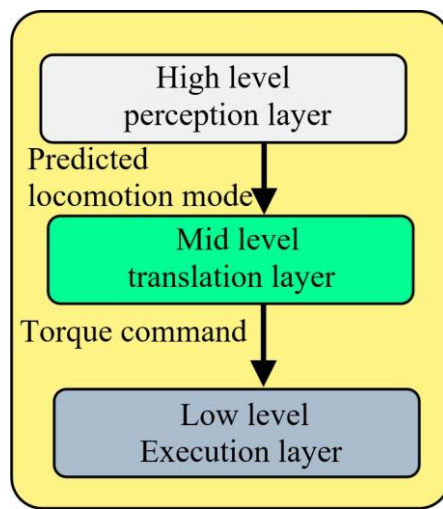


Figure 2.10 Block diagram of controller hierarchy (Spanias et al. 2018; Tschiedel et al. 2020)

Various studies have used different control laws to supply the input current to the electromagnet. Lawson et al. (2013) presented a finite state control system for subjects with powered prosthesis to provide stair ascent and stair descent capability and has compared it with passive prosthesis, along with gait kinematics of healthy subjects. Results show that both passive and powered prostheses provide appropriate knee joint kinematics, while the powered prosthesis provides ankle joint kinematics considerably more reflective of healthy joint kinematics. Ochoa-Diaz et al. (2014) used a finite state machine controller to modulate the damping level according to the gait cycle. Pandit et al. (2018) also used a finite state controller to apply suitable action to the RD-8040 damper which they used in the prosthetic device. Herr and Wilkenfeld (2003) also used finite state controller by dividing the entire normal walking gait cycle into five different phases and supplying a constant set values of currents in these phases. A disadvantage

with finite state controller is that the constant currents need to be adjusted by the prosthetist specific to the amputees, which results in a larger number of tuning parameters. However, changes in cadences during prosthetic gait would not affect the assistance since the mathematical model of finite state controllers is not time-dependent, rather is phase dependent (Lara-Barrios et al. 2018). If sensory information correctly identifies the gait phases, the smoothest damping profiles can be obtained.

Many researchers also used continuous controllers which adapt to the prosthetic gait. Kim and Oh (2001) used Proportional Derivative (PD) + Computed Torque (CT) law to control the rotary damper used in their prosthetic design. Fu et al. (2017) used a sliding mode based controller and compared the results with that of PD + CT control law. Kim and Oh (2002) used a PID Controller to supply the input to the servo motor. The permanent magnet connected to the servo motor applies the required magnetic field in the MR valve. Ekkachai et al. (2014) designed a controller using a neural network predictive control for MR damper prosthetic knee with a focus on only the swing phase of the gait cycle. The simulation results show that the controller used with the prosthesis can track the knee trajectory with minimal errors. Fu et al. (2017) designed a sliding mode controller for the semi-active prosthetic knee system based on MR damper. The model is designed based on the mathematical model of the MR damper and thus, it effectively captures the hysteresis in the system. Also, this strategy requires fewer tuning parameters. Further, continuous control strategies make an excellent choice for simulation based studies. Therefore, in the current work, a PD + CT control strategy is used to perform a dynamic analysis of the semi-active prosthetic knee model. An inverse model which can predict the required current inputs given the damping force, displacement and velocity as inputs is also developed.

2.3.5 Design Optimization Strategies

A semi-active device based on MR fluid requires the design of two components: mechanical design and the electromagnetic circuit design. The mechanical design involves the application of constitutive fluid models on the problem geometry. Equivalent magnetic methods (EMM) and the finite element magnetostatics (FEM) are the two primary methods used for solving the magnetostatic problem over the model domain.

FEM is a numerical method for solving a boundary value problem involving partial differential equations generated using Maxwell's equations. This method is more suitable for problems with complex geometry or complex physical properties (Wang 2013). This is the most accurate method and can determine magnetic flux densities at any location in the model. Also, complex geometries considering surrounding areas of the model can be modeled to simulate any possible flux leakages. On the other hand, EMM method simplifies the problem domain into constant magnetic flux links. Applying Gauss's law and Ampere's law on the simplified equivalent magnetic circuit produces a set of equations, which upon solving, yield the required magnetic variables. A disadvantage of this method is that it can produce significant amounts of error when estimating magnetic flux densities. Also, it lacks in providing any information about the localized saturation. However, this is the most commonly used method in design optimizations of MR devices because of its simplistic and computationally less expensive nature. Using the above methods, optimization routines use the following methodologies to evaluate the optimal designs of various semi-active devices based on MR fluids.

2.3.5.1 Optimization based on finite element Magnetostatics (O-FEM)

In this design methodology, the electromagnetic circuit design component is solved using FEM method. Search based optimization routines can require an order of 10^6 solutions; therefore, use of FEM for each solution can be a prohibitive task (Batdorff and Lumkes 2009). For instance, Nguyen and Choi (2011) reported that the use of particle swarm optimization (PSO) algorithm along with this approach required more than 8 hours of computational time. Many studies thus used first-order optimization method using a combination of the golden-section algorithm and a local quadratic fitting technique (Nguyen and Choi 2009, 2010; Nguyen et al. 2007, 2008). The initial point is evaluated using equivalent magnetic methodology, and subsequent iterations were performed using O-FEM. Based on the convergence criteria, this methodology yields an optimum solution in fewer iterations. However, traditional gradient-based methods are difficult to extend for constrained multi-objective optimization problems and for the same reason, a weighted approximation of objectives is considered in such problems. Also, the optimization routine has its own limitations,

such as the requirement of sufficient gradient information and appropriate initialization (Zhang et al. 2015).

2.3.5.2 Optimization based on equivalent magnetic method (O-EMM)

In this approach, optimal design of a semi-active device is performed by using EMM method. Despite many drawbacks, this is the most commonly used method. Many studies have been conducted on the optimal design of MR valves (Nguyen et al. 2009), MR dampers (Gao et al. 2017; Gavin et al. 2001; Xu et al. 2013), MR brakes (Mousavi and Sayyaadi 2018; Nguyen and Choi 2011), etc. To further improve the accuracy of the method, polynomial models to estimate relative magnetic permeability of core and MR fluid have also been considered in many studies (Gavin et al. 2001; Manjeet and Sujatha 2019). However, due to the simplification of geometry by constant magnetic flux links, localized saturation information cannot be obtained. Due to the low computational cost, this method has been coupled with various non-gradient or heuristic optimization routines such as genetic algorithm, PSO, etc.

2.3.5.3 Optimization based on data-driven modeling

This approach uses FEM methods for magnetostatic analysis; however, to limit the number of FEM evaluations, a design of experiments (DoE) table is constructed. A response function is fit based on the DoE table, which is an analytical function predicting the magnetic flux densities for various geometric configurations of MR device. This function is later used in gradient or non-gradient based optimization algorithms (Erol and Gurocak 2011; Seid 2017). Various models have been used in previous studies such as cubic polynomial (Hadadian 2011), neural network models (Keshav and Chandramohan 2019) etc.

2.4 SUMMARY OF LITERATURE

An extensive literature review of MR devices and their design methodologies has been conducted. Various semi-active design configurations based on MR fluids particularly for prosthetic knee applications have been discussed in previous sections. From the review, it was observed that multi-plate MR brake is the most studied design for prosthetic knee application. A few studies even coupled the semi-active MR brake

with active elements such as DC motor and realized an active knee joint. However, the high cost of commercially available MR brake makes it impossible to use for population in developing countries. Few other limitations of MR brake are low fluid gap clearances resulting in large shear rates and fluid degradation, manufacturing complexity due to large number of components. Therefore, in this study various alternative design configurations are explored.

Also, to reduce the computational cost of design optimization process, many studies used equivalent magnetic methods for optimal design of MR dampers. Over simplification of geometry, unavailability of localized saturation information and inaccuracies in reporting magnetic field variables are few of the drawbacks of this methods. On the other hand, FEM based methods are accurate in evaluating magnetic flux variables, but are computationally expensive. Consequently, a new design optimization methodology which reduces the computational cost along with producing accurate design solutions is developed in this study. This methodology is later used in the optimal design studies of design configurations. Additionally, the optimal damper designs are fabricated and characterized for various inputs. The optimal damper design is selected after performing a comparison study between the dampers developed from this study and with various prosthetic knee dampers developed in previous studies along with the commercial MR damper. Finally, a mathematical model of damper is developed and coupled with a prosthetic knee model and simulated for swing phase of gait cycle. The knee angular trajectories of simulation studies have been compared with normal human knee angular data to determine the suitability of design in practical application.

2.5 MOTIVATION

Although the MR fluid technology seems to have been a much researched one over the past two decades, it can be said that the application of this technology to the prosthetic knee seems still fresh. It is also seen that most of the MR damper applications explored seem to be in the vehicular vibration domain. Lord Corporation, USA is one of the leading manufacturers supplying MR dampers for truck seat applications and vehicular damping in high-end cars. Most of the work done in the area of prosthetic

knee used the truck seat MR damper produced by Lord Corporation. Thus the damper design and the required forces are fixed, restricting the kinematic design of the prosthetic knee. To overcome this, a damper should be designed specifically for the prosthetic knee. The inputs to the damper design will be based on the weight requirements, accommodating space and the load requirements of the knee.

Many semi-active device configurations using MR fluid have been studied over in the past. A few of them show a good potential of being applied to prosthetics based on their high torque to weight ratio. The various primary classifications of an MR brake such as disc type, drum type, hybrid type designs are found to be insufficient in generating the required damping torque. Increasing the shear area by increasing the number of discs resulted in a brake configuration which is already available commercially. In a drum type brake design, it was noticed that a uniform magnetic field distribution is not produced on the radial face of the rotor. Keeping this in mind and based on intuition, a multi-pole drum brake MR design is identified which is expected to produce a much uniform field distribution on the radial face of rotor. This is considered as one of the design configurations for a preliminary design process in this work.

The multi-plate MR brake design is studied rigorously and is even coupled with many active elements such as DC motor to realize an active prosthetic knee. Therefore, this design is not considered in the present study, however, it is used for comparative studies later in this work. The other MR brake configuration which contains a T-shaped rotor with a waveform arc boundary on the radial face of the rotor has a few drawbacks associated with the design. Four electromagnetic coils were placed on the inner and outer regions of the T-shaped leg as shown in Figure 2.6. One of the drawbacks with this arrangement is that it reduces the effective pole length as the coil covers some of the leg portion. Further, the use of an electromagnetic coil on the outer region of the T-shaped leg restricts the outermost radius of the rotor and thus decreases the overall braking torque. Therefore, an inverted drum brake design with a single electromagnetic coil is considered as the second design configuration for further study in this work.

On the other hand, the studies on a rotary vane MR damper are very much limited both theoretically and experimentally. The design by Kim and Oh (2001, 2002)

is capable of producing a damping torque of around 20 Nm, which is insufficient for normal human walking. Also, the rotary chamber used was a retrofit pneumatic component, thus creating a scope for an optimal design. Further, bypass MR valve results in a much simpler design compared to valves located in static or rotary vanes (Imaduddin et al. 2013, 2014). Therefore, a single rotary vane damper with a bypass MR valve is considered as the third design configuration for further study in this work.

Finally, it can be noticed that the twin rod MR damper has been studied previously in many studies (Fu et al. 2017; Gao et al. 2017; Park and Choi 2015). However, the optimal design methodologies are based on EMM method, which can produce significant errors in calculating magnetic flux densities in the model. The designs from the previous studies, along with a prototype design, were used to modify the twin rod MR damper geometry considered in this work. The modified piston core assembly helps to reduce fluid leakages from the damper. Furthermore, maintaining similar objectives and constraints in the optimization procedure allows the optimal design to be easily compared to other design configurations for prosthetic knee. Therefore, a twin rod MR damper is considered as the fourth design configuration in this work.

Therefore, in this research work, the four identified design configurations will be considered for a preliminary design. Further, the designs which show true potential of being applied for prosthetic knee domain will be selected. The primary requirement of the device will be to sufficiently produce the required braking torque or an equivalent force. The secondary requirement is simplifying the design addressing the limitations of a multi-plate MR brake model.

Observing the trends of the previous researches and to address the above shortcomings, the following objectives are formulated.

2.6 OBJECTIVES

1. To develop an optimization strategy for designing semi-active devices based on MR fluid to reduce computational time and to improve the accuracy of design points.

2. To conduct a preliminary design study considering various design configurations of semi-active devices based on MR fluid with the aim of determining suitability for prosthetic knee application.
3. To design, fabricate and characterize a twin rod MR damper for prosthetic knee application using the developed optimization methodology.
4. To design and fabricate a rotary vane MR damper for prosthetic knee application and to characterize the vane damper using a developed test setup.
5. To select an optimal design and to perform a dynamic analysis of the semi-active prosthetic knee model coupled with a developed control strategy.

2.7 SCOPE OF RESEARCH WORK

1. A multi-objective constrained particle swarm optimization algorithm is developed. This algorithm is initially applied on various test problems and the performance is evaluated.
2. The developed algorithm is coupled with combined magnetostatic approach and its performance is evaluated using the most commonly considered optimization problems. The performance metrics used in the comparison are hypervolume indicator and computational cost.
3. Various optimization methodologies have been considered for the preliminary design study. The suitability of design configurations for prosthetic knee application is determined based on maximum braking torque and device mass.
4. MR fluid characterization studies have not been performed in this study and in-house samples of MR fluids were prepared based on published literature.
5. Dynamic analysis of the semi-active prosthetic knee model is performed for the swing phase of gait cycle.

2.8 METHODOLOGY

To achieve the proposed objectives, the methodology shown in Figure 2.11 is followed. A multi-objective particle swarm optimization combining many features from previous studies is developed and its performance is evaluated for various test functions. This algorithm is later coupled with the combined magnetostatic approach to

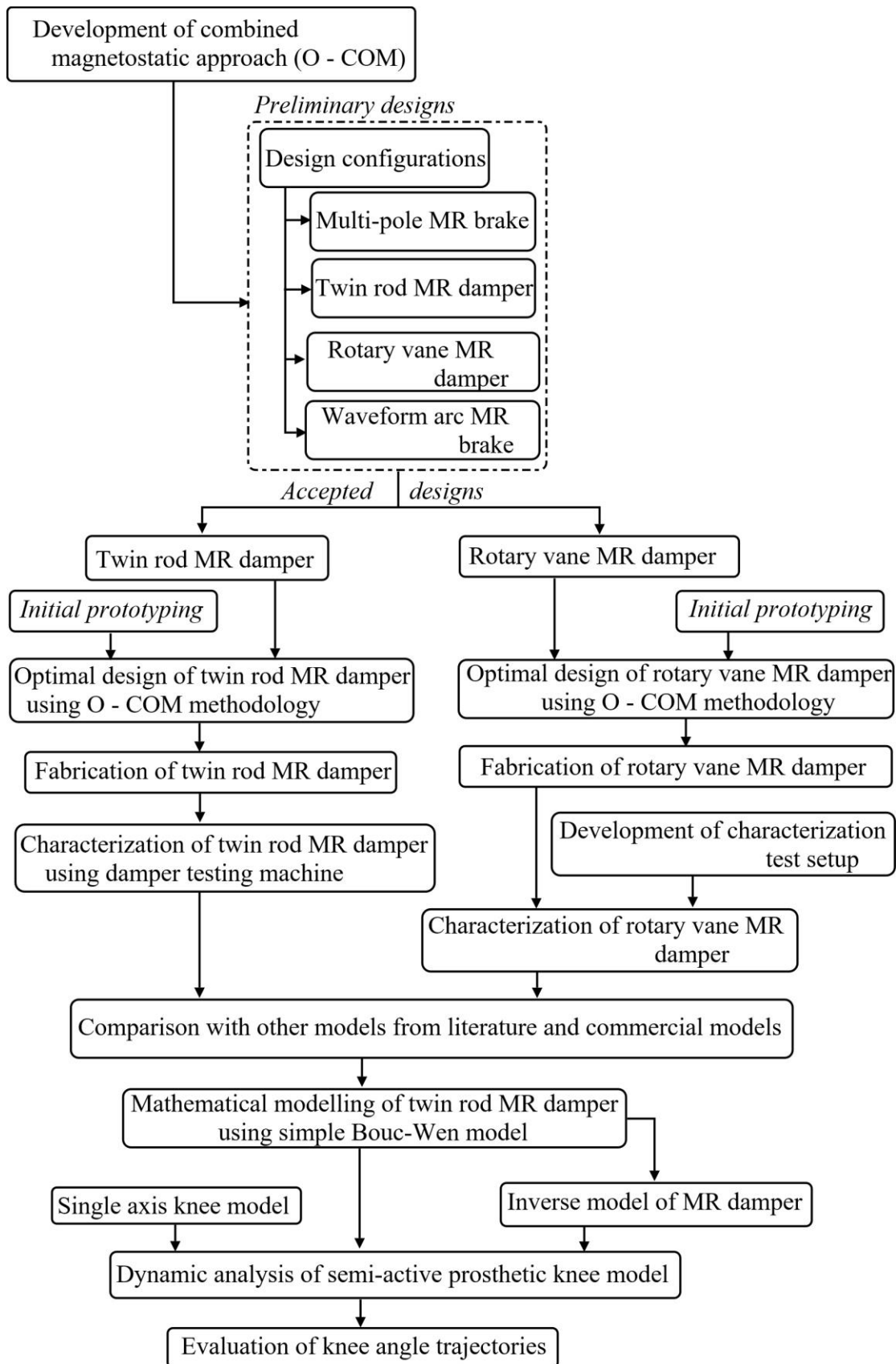


Figure 2.11 Methodology of current work

develop an optimization methodology which can reduce a few of the limitations associated with other frequently used optimization methodologies. Later, a preliminary design process is performed on the selected four design configurations. Based on the criteria of producing the required braking torque/force sufficient for prosthetic knee application, a twin rod MR damper and rotary vane MR damper are selected for further optimal design and experimentation. Initial prototyping using random dimensions is performed which can provide a few insights into the working nature of the damper. Optimal design, fabrication and characterization of both the designs is performed next. The characterization of the twin rod MR damper is performed on an available linear damper test facility, while the test setup to characterize the vane damper is developed as part of this study.

Later, comparative studies of two design configurations with literature and commercial models are conducted. A mathematical model of the optimal design configuration is developed using a simple Bouc-Wen model. Further, an inverse model is developed which can predict the required current, given the inputs such as displacement, velocity and force. A semi-active closed loop control study is implemented for the swing phase of the gait cycle and the knee angular trajectories are evaluated.

2.9 SUMMARY

In the present chapter, a review of literature on the use of various commercially available passive, semi-active and active knees was provided. Later, scientific research on the use of MR fluid based devices and the various device configurations was briefed. Based on the various shortcomings associated with both the design configurations and their optimization methods, the objectives and scope of the current study have been proposed.

CHAPTER 3

OPTIMAL DESIGN METHODOLOGIES FOR MR DAMPER

3.1 INTRODUCTION

The various methodologies used in the literature for the optimal design of MR device are:

1. Optimization based on finite element magnetostatics (O-FEM)
2. Optimization based on equivalent magnetic method (O-EMM)
3. Optimization based on data-driven modeling

Among those, O-FEM methodology is the most accurate one since it solves each design point using FEM analysis. This analysis method also results in providing a localized saturation information which can be used as a constraint in optimal design problems so as to avoid core saturation, but the method has its drawbacks in terms of computational time required. In many studies, this has been avoided by considering first-order optimization algorithms such as golden-section algorithm and a local quadratic fitting technique. However, the algorithm results are highly influenced by the initial design point and they cannot conduct a complete search of the design variable space. Furthermore, optimization design problems based on search based optimization algorithms are often repeated multiple times so as to reasonably conclude the final Pareto front vector to be the optimal one. This, together with the high computational cost renders this methodology as the least preferred one in optimal design problems.

An equivalent magnetic method (EMM) which assumes the magnetic path to be composed of equivalent magnetic links has been considered by many researchers. Owing to its simplistic and computationally inexpensive nature, this method is often coupled with search based optimization routines such as particle swarm optimization, genetic algorithm, etc. However, this method can produce significant amounts of error in estimating magnetic flux densities. Also, core saturation information is lost due to

the assumption of constant magnetic links. Further, increase in equivalent magnetic loops, which is often the case in MR brake devices results in higher inaccuracies in producing magnetic flux densities.

Data-driven modeling is the one compromise between computationally expensive FEM method and its counterpart EMM method. In this method, a design of experiments (DoE) table is initialized and is solved for magnetostatic analysis using FEM method. A response function is fit based on the DoE table, which is an analytical function predicting the magnetic flux densities for various geometric configurations of the MR device. This function is later used in gradient or non-gradient based optimization algorithms (Erol and Gurocak 2011; Seid 2017). Various data-driven models have been used in previous studies such as cubic polynomial (Hadadian 2011), neural network models (Keshav and Chandramohan 2019) etc. However, the model's accuracy in predicting magnetic flux densities in core and fluid regions depends on the number of design variable combinations used in the DoE table. Also, any change in the design variable ranges may require the DoE to be constructed again, thereby repeating the whole model fitting process again.

In general, a search based optimization algorithm involves a random population vector and the cost function values are evaluated for each particle in the population. Later, the candidate vector which produces the best cost function values is selected as the elite candidate vector and subsequent populations are initialized based on this elite group. It may be noticed that in the process of selection, the non-dominated individuals form only a small subset of a large population vector. In O-FEM methodology, magnetostatic analysis is performed for each particle in the population vector. If somehow, the magnetostatic analysis using FEM method is allowed only for this subset of population, then the computational time required in the optimization process can be substantially reduced. Using this notion, a combined magnetostatic approach which uses both FEM and EMM method is formulated and is detailed in the following section.

3.2 COMBINED MAGNETOSTATIC APPROACH

In this approach, both EMM and FEM methods are coupled together to reduce the number of FEM evaluations. The process of obtaining elite candidates is shown in

Figure 3.1. Each filter consists of the said magnetostatic analysis method followed by the selection of elite candidates. At first, the objective function for each particle in an n^{th} generation is evaluated choosing EMM as the magnetostatic method. Non-dominated individuals are selected from the pool of particles using the concept of Pareto-dominance. Later, the objective function of these individuals is re-evaluated choosing FEM as the magnetostatic analysis method followed by the selection of the best individuals. At this stage, the particles in the objective space observe a shift and since magnetic fields are not linear systems, the shift of each particle may not be same for all particles. In the process, a few individuals may be removed if found infeasible (if they violate any design constraints). Therefore, this approach reduces the computational cost by effectively reducing the overall population and also improves the accuracy of the design points.

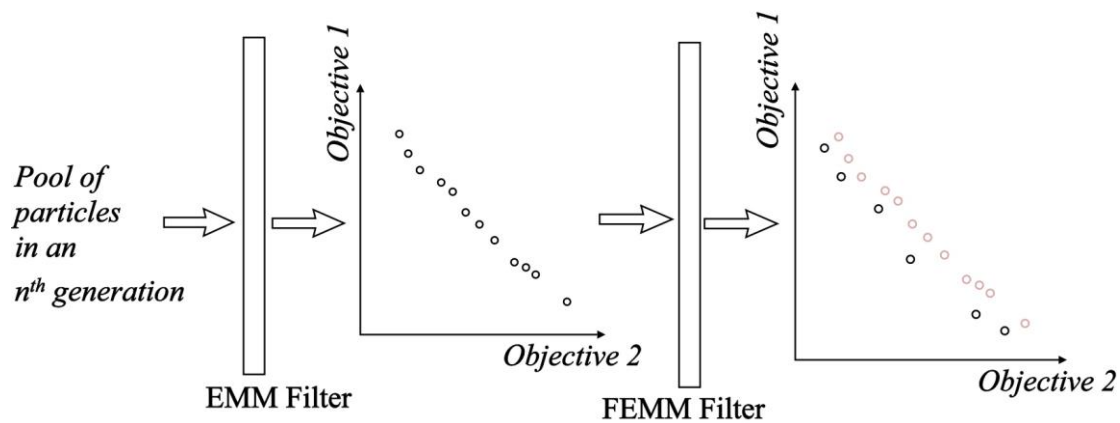


Figure 3.1 Combined magnetostatic analysis

In order to assess the performance of O-COM methodology, a quantitative comparison of various optimization methodologies is considered. In data-driven modeling, various response function models such as cubic polynomial, neural networks, etc. have been used in the previous studies. Neural network models are found to capture well the non-linear nature of the data sets, and therefore, will be used in data-driven modeling. Further, the optimization methodology based on neural network data-driven model will be referred as O-NN, from this point forward.

Previous optimization studies considered a wide range of objective functions such as dynamic range, on-state dynamic torque/force, off-state dynamic torque/force, mass, induction time constant, power dissipation, etc. They can be broadly classified as

objectives directly affected by magnetic flux density of fluid gap and those which are unaffected by magnetic field strength. For example, mass and off-state dynamic torque/force of MR damper are not affected by magnetic flux densities in the semi-active device, whereas on-state dynamic torque/force depends on the magnetic field strength in the fluid gap. Although the choice of objectives was either device or application-specific, the selection of these objectives has an impact on the optimal Pareto front produced. In this study, a bi-objective optimization problem is considered with two different objective combinations. In the first combination, only one objective is taken as flux dependent, and in the second one, both objectives are considered flux dependent. As will be seen later, the choice of objectives using the O-EMM and O-NN methodologies shifts the Pareto front and may lose optimal design points during the optimization process.

A quantitative comparison between the design optimal methodologies such as O-FEM, O-EMM, O-NN and O-COM can be helpful in selecting the optimal design methodology without compromising the accuracy of the design points. A comparison of various optimization algorithms such as genetic algorithm, simulated annealing along with a proposed algorithm has been performed by Younis et al. (2011). The study uses computational time and convergence as two performance metrics to compare different algorithms for a semi-active MR brake optimization problem. They also reported that their proposed surrogate model is computationally less expensive compared to simulated annealing (SA) and genetic algorithm (GA) based optimization methods. However, the accuracy of SA is 24% and 17% better than GA and their proposed method respectively. Furthermore, all chosen algorithms use FEM as a magnetostatic analysis method and thus can be classified as O-FEM methodologies. Here, in the present work, various optimization methodologies are considered rather than optimization algorithms for an effective comparison. Therefore, a quantitative comparison using the hypervolume indicator is provided for state-of-the-art magnetostatic methods used in the design optimization of MR dampers.

In the scope of computationally expensive optimization problems, it is worthwhile to mention another class of algorithms known as surrogate assisted evolutionary algorithms (SAEA) which decrease the optimization cost by reducing the

number of calls to objective functions (Chugh et al. 2017; Xia et al. 2020). In this technique, an approximate model is used as a surrogate model to construct simpler and lower computational cost models. This modelling technique has also been applied to design problems on MR devices, but has not been clearly identified as their member. For example, optimization based on data-driven modeling is a type of SAEA method. Since the original fitness function (which is to be evaluated using FEM method) is completely replaced by a data driven model, this approach can be further classified as direct fitness replacement method with no evolution control strategy (Díaz-Manríquez et al. 2016). Also, O – COM methodology can be classified as an indirect fitness replacement method, a sub-classification of surrogate assisted modeling method. In this method, a surrogate model (EMM Filter) returns the best n solutions which will be further evaluated using the real fitness function (FEM filter). Other surrogate models such as Kriging models, radial basis functions etc. have not been applied in design optimization of MR devices as far as the author’s knowledge is concerned. Therefore, in this work, a comparison is performed on the four methodologies which have been applied earlier on MR device design.

The remainder of this chapter is organized as follows. A description of MR damper design based on the most commonly chosen optimization problems is provided next. A detailed procedure on performing magnetostatic analysis on the axisymmetric geometry of the damper piston using FEM and EMM methods is explained. A brief description of the optimization routine is provided. Later, two different design problems are described and are optimized using the four methodologies. Lastly, parametric and non-parametric statistical analysis techniques are used in comparison of Pareto optimal sets generated in the four methodologies and in both the design problems. The algorithms are also compared in terms of computational time required.

3.3 MECHANICAL DESIGN OF MR DAMPER

A cross-section of a typical flow mode piston in an MR damper is shown in Figure 3.2. The arrangement consists of a piston connected to a hollow piston rod. The piston is made of the inner core and outer core with an electromagnetic coil wound on the inner core. Additionally, the piston equips an annular channel for the flow of MR

fluid. The electromagnetic setup creates a magnetic field across the flow channel. This changes the rheological properties of the MR fluid, affecting the overall damping force.

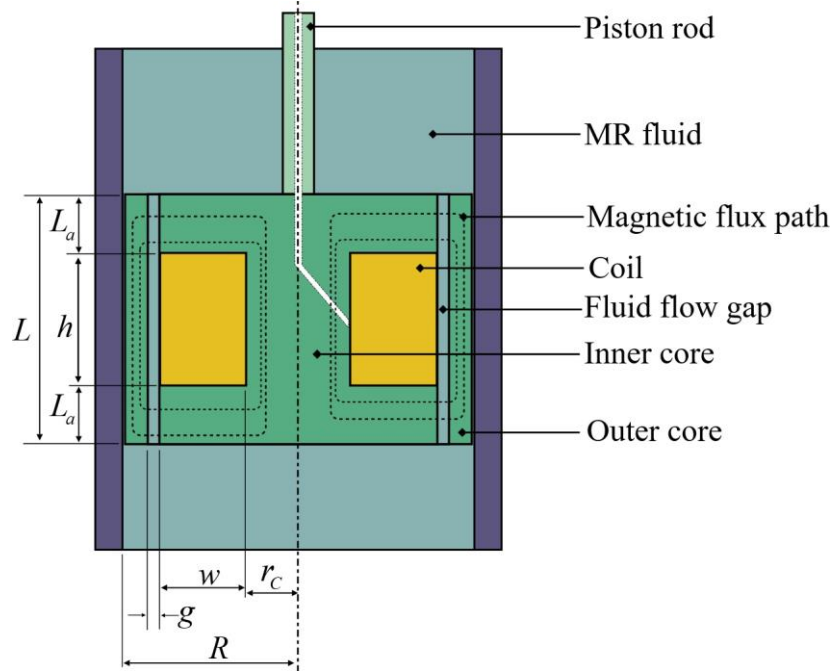


Figure 3.2 Cross-section of a typical flow mode MR damper

3.3.1 Dynamic Range

Dynamic range is the ratio of the total resisting force of the damper to the viscous force. This is one of the important parameters of the damper and a higher value is expected such that the damper can possess a large operating range. The dynamic range of the damper can be calculated using Equation (3.1).

$$\lambda = \frac{F_t}{F_v} \quad (3.1)$$

Here, F_t is the total damping force produced and F_v represents the viscous or the off-state force produced. Neglecting frictional forces, the total damping force can be calculated using Equation (3.2).

$$F_t = F_v + F_{MR} \quad (3.2)$$

Here, F_{MR} represents the controllable MR force. The controllable and viscous forces can be calculated using the following equations (Yang et al. 2002).

$$F_v = \frac{12\eta QLA_p}{w_c g^3} \quad (3.3)$$

$$F_{MR} = \left(2.07 + \frac{12Q\eta}{12Q\eta + 0.4w_c g^2 \tau_y} \right) \frac{2\tau_y L_a A_p}{g} \quad (3.4)$$

Here, η is the off-state viscosity of the MR fluid, Q is the flow rate, L is the total length of the piston, A_p is the effective cross-sectional area of piston, w_c is the mean circumference of the annular gap, τ_y is the field-dependent yield stress of the MR fluid, and g is the fluid gap thickness. The parameters for the given geometry in Figure 3.2 can be calculated using the following equations.

$$A_p = \pi(R^2 - r_0^2) \quad (3.5)$$

$$Q = A_p \dot{u} \quad (3.6)$$

$$w_c = 2\pi(w + r_c + 0.5g) \quad (3.7)$$

Here, r_0 is the radius of the piston rod and \dot{u} is the velocity of the piston. Based on previous studies, a piston rod radius of 5 mm and a velocity of 0.1 m/s is chosen. In this study, MRF-132DG fluid is selected and the field-dependent yield stress (in kPa) can be calculated using Equation (3.8) (Nguyen et al. 2007). The relation is obtained by curve fitting the data provided by the supplier shown in Appendix I.

$$\tau_y = 52.96B^4 - 176.51B^3 + 158.79B^2 + 13.708B + 0.1442 \quad (3.8)$$

Here, B is the average magnetic flux density in the fluid gap.

3.3.2 Inductive Time Constant

The inductive time constant of the MR valve can be calculated using Equation (3.9),

$$T_c = \frac{L_{in}}{R_w} \quad (3.9)$$

Here, L_{in} is the inductance of the coil and R_w is the resistance of the coil wire which can be evaluated using the following equations.

$$L_{in} = \frac{N_{turns}\Phi}{I} \quad (3.10)$$

$$R_w = \frac{4N_{turns}d_{avg}\rho}{d_c^2} \quad (3.11)$$

Here, N_{turns} is the number of turns of the coil, Φ is the magnetic flux in the circuit, I is the current, d_{avg} is the average diameter of coil cross-section, ρ is the resistivity of the coil and d_c is the diameter of the coil.

3.3.3 Mass

The mass of the MR valve can be calculated using the equation,

$$M = \rho_{core}V_{core} + \rho_{MRF}V_{MRF} + \rho_{coil}V_{coil} \quad (3.12)$$

Here, ρ_{core} , ρ_{MRF} and ρ_{coil} are the densities of the core, MR fluid and coil material respectively and V_{core} , V_{MRF} and V_{coil} are the volume of the core, MR fluid, and coil respectively. The volume of the materials can be calculated as follows.

$$V_{coil} = \pi \left[(r_c + w)^2 - r_c^2 \right] h \quad (3.13)$$

$$V_{MR} = \pi \left[(r_c + w + g)^2 - (r_c + w)^2 \right] L \quad (3.14)$$

$$V_{core} = \pi R^2 L - V_{coil} - V_{MR} \quad (3.15)$$

3.4 MAGNETOSTATIC ANALYSIS

The average magnetic flux density in the fluid gap, the magnetic flux in the circuit and the maximum magnetic flux density in the core (constraint to avoid core saturation) are required in order to evaluate the dynamic range and the inductive time constant. The methods of magnetostatic analysis for calculating the required magnetic variables are detailed next.

3.4.1 Finite Element Magnetostatics (FEM)

In this method, an axisymmetric model of the piston as shown in Figure 3.3 is considered. In order to obtain the magnetic field distribution in the damper, Maxwell

equations are solved over the entire domain by discretizing it into small elements. To perform this task, finite element method magnetics (FEMM) software is used (Meeker 2009). This is an open source finite element analysis software which also offers operation using a set of MATLAB functions via OctaveFEMM interface (Meeker 2010). The pseudo MATLAB code which evaluates the magnetic flux density and maximum magnetic flux in the piston for a specific geometry is shown in Figure 3.4.

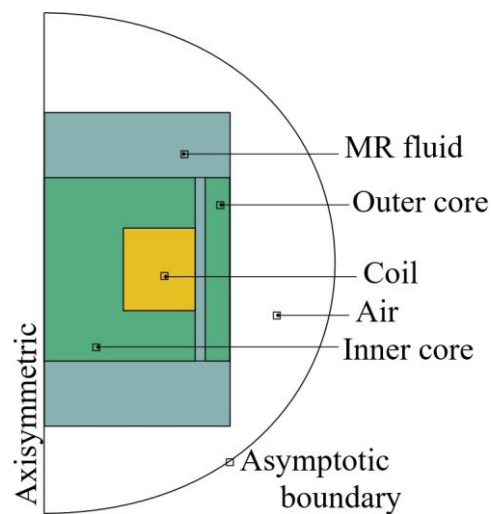


Figure 3.3 Axisymmetric model of piston in FEMM software

```
function [ B_fluid, B_max ] = Model_FEMM(param)
% initialize parameters
openfemm;
newdocument(0);
mi_probdef(0, 'millimeters', 'axi', 13-8, 0, 30);
% draw geometry and add block labels
% Add and apply materials
mi_analyze|
mi_loadsolution
% calculate B_fluid and B_max
end
```

Figure 3.4 Pseudo MATLAB code to perform magnetostatic analysis in FEMM

3.4.2 Equivalent Magnetic Model (EMM)

A lumped parametric model of the axisymmetric model of the piston is shown in Figure 3.5. Application of Ohm's law around the magnetic loop yields the following equation.

$$N_{turns}I = \Phi(R_1 + 2R_2 + 2R_3 + R_4) \quad (3.16)$$

Here, R_i is the reluctance of the i^{th} link and can be calculated as follows:

$$R_1 = \frac{L - L_a}{\pi\mu_{core}r_c^2} \quad (3.17)$$

$$R_2 = \frac{\ln\left(\frac{r_c + w}{0.5r_c}\right)}{2\pi\mu_{core}L_a} \quad (3.18)$$

$$R_3 = \frac{\ln\left(\frac{r_c + w + g}{r_c + w}\right)}{2\pi\mu_{MRF}L_a} \quad (3.19)$$

$$R_4 = \frac{L - L_a}{\pi\mu_{core}\left[R^2 - (r_c + w + g)^2\right]} \quad (3.20)$$

Here, μ_{core} and μ_{MRF} are the magnetic permeabilities of the core and MR fluid respectively. High magnetic permeability is a desirable material property for the core material. Considering other factors such as material costs and ease of availability along with magnetic permeability, 1020 steel is selected as inner and outer core material.

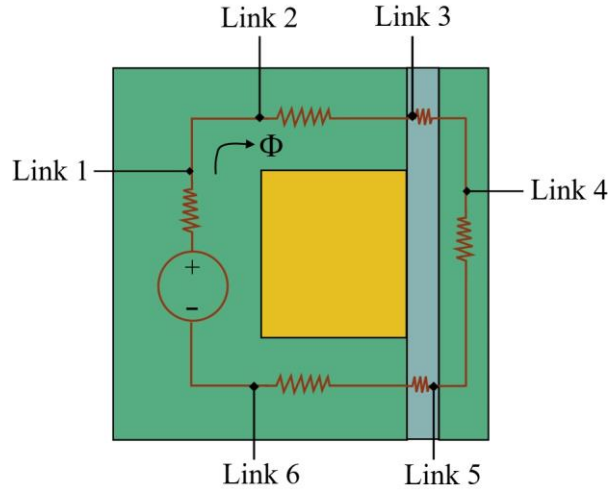


Figure 3.5 Lumped parametric magnetic model

The magnetic flux in the circuit and the number of turns of the coil can be calculated using the following equations.

$$\Phi = 2\pi BL_a(r_c + w + 0.5g) \quad (3.21)$$

$$N_{turns} = \frac{4p_f wh}{\pi d_c^2} \quad (3.22)$$

Here, p_f is the packing factor, which is taken as 0.6. Also, 24 AWG copper coil with a diameter of 0.51 mm is selected.

3.5 DESIGN PROBLEMS

Previous studies have used a variety of design problems considering single, multiple or weighted aggregate of various objective functions. Also, the design variables along with the constraints imposed are problem-specific. In this study, two most commonly used design problems which are constrained volume optimization and the constrained force optimization are considered.

3.5.1 Design Problem 1

One of the most common problems considered in many previous studies is a constrained volume optimization problem. In this problem, the largest possible dimensions of the piston which are R and L are constrained. In the present study, R and L are constrained to be 30 mm and 50 mm respectively. Potential applications of this device are retrofitting the existing dampers with a semi-active piston, vehicular applications, prosthetic applications, etc. Therefore, a constrained volume optimization problem with dynamic range and inductive time constant as the two objective functions is chosen as the first design problem and from hereafter will be referred to as “DP1”. The design variables are $\{r_c, w, g, L_a, I\}$.

Objective function: Minimization of objectives $[-\lambda, T_c]$

Constraints: $B_{max} \leq 1.8$ T and $F_v \leq 100$ N

3.5.2 Design Problem 2

Another common problem used in many optimal design studies is to constrain the total damping force. For example, earthquake mitigation dampers with a damping force more than 200 kN are reported in Xu et al. (2013). Also, minimization of mass of the device is one of the most used non-magnetic flux dependent objective. Therefore,

dynamic range and mass are considered as the two objectives in the second design problem and from hereafter will be referred as “DP2”. The design variables are $\{r_c, w, h, g, L_a, I, t\}$ and the bounds are listed in Table 3.1. The common design variables have been given similar bounds in both design problems, DP1 and DP2. The largest possible dimensions, R and L are not constrained in this problem.

Objective function: Minimization of objectives $[-\lambda, M]$

Constraints: $B_{\max} \leq 1.8$ T and $F_T \geq 1000$ N

Table 3.1: Design variables and its bounds

Variable	Name	Bounds	
		Lower (mm)	Upper (mm)
r_c	Core radius	6	16
w	Coil width	2	8
h	Coil height	2	10
g	Fluid gap	0.5	2
L_a	Active pole length	8	21
I	Current	0.5	1.5
t	Thickness of outer cylinder	2	10

3.6 OPTIMIZATION ROUTINE

In this study, particle swarm optimization (PSO) is used as the common optimization routine for all methodologies. PSO is a search-based algorithm which is based on the movement of a flock of birds. Many previous studies have used this algorithm for optimal designs because of its easier implementation and faster convergence (Bahiuddin et al. 2019; Gao et al. 2017; Gudmundsson et al. 2010; Nguyen and Choi 2011). Also, many PSO algorithms are available in the literature differing in aspects such as handling objectives, constraints, mutation, external archive maintenance etc. A recent advancement using the concept of the minimum distance of point to line (MDPL) to obtain the global best has been proposed and comparative studies have been conducted showing the superiority of this algorithm (Fan et al. 2017). However, only unconstrained problems have been used as test functions and the performance of the algorithm with respect to constrained problems remains an open question. Therefore, the constraint handling method from the study by Woldeesenbet et

al. (2009) is used to extend the proposed MDPL – multi objective particle swarm optimization (MOPSO) algorithm and performance metrics are evaluated for constrained test functions. To evaluate the performance of this extended algorithm, four representative constrained test functions are chosen and performance metrics are compared to previous studies. The results of comparison are presented in Appendix II. From the results, it can be concluded that the proposed constrained MDPL-MOPSO algorithm shows a significant reduction in performance metrics apart from a few deviations.

Figure 3.6 shows the basic structure of the PSO. The general methodology used in an optimization process requires the evaluation of magnetic flux density for each particle in the population and based on that, the objective functions are calculated. The four methodologies differ in their way of performing magnetostatic analysis and selection of the elitist population.

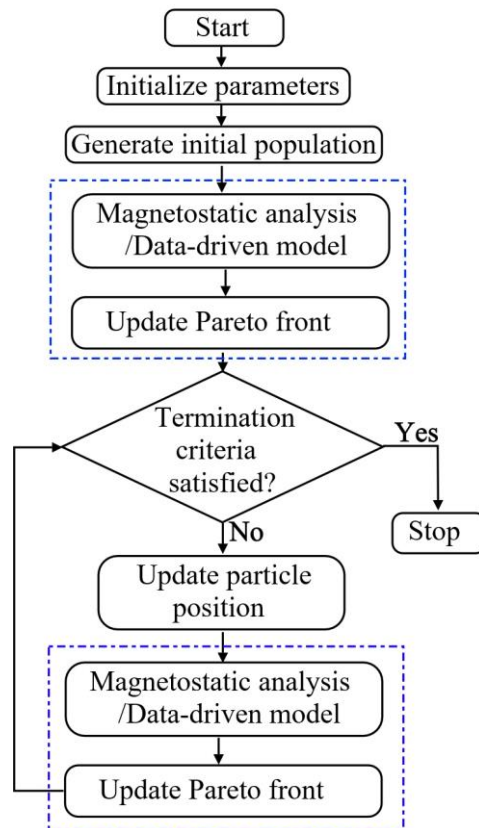


Figure 3.6 Basic structure of PSO

3.7 MAGNETOSTATIC METHODOLOGIES FOR OPTIMIZATION

A few studies have also considered the design of mechanical and the electromagnetic part of the semi-active device by coupling computational fluid dynamics (CFD) and FEM analysis (Bompos and Nikolakopoulos 2011; Omidbeygi and Hashemabadi 2012; Park et al. 2008; Parlak et al. 2012). The methodology is more suitable for studies which consider temperature distribution and heat dissipation as their objectives and, therefore, is omitted from a comparison in this study. The four methodologies used in the optimal design of MR dampers are formulated in this section.

3.7.1 O-FEM

In this approach, the magnetostatic analysis is performed using FEMM software for all the particles in the population. Later, the concept of elitism is applied based on Pareto dominance.

3.7.2 O-EMM

In this approach, the magnetostatic analysis is performed using EMM for all particles in each iteration. Pareto dominance is used later to select elite candidates.

3.7.3 O-NN

In this approach, a data-driven artificial neural network (ANN) model is used to predict magnetic flux density in the fluid gap and the maximum flux density in the valve model. An ANN is a network of neurons derived from the analogy of neurons in the brain. Each neuron processes the input data using the weights, bias, and the activation functions as shown in Figure 3.7. The training of ANN model refers to optimally adjusting the weights and bias parameters such that the final empirical model can correlate well between the input and output data. There also exists variables such as the number of hidden layers, number of neurons in each layer etc. which are termed as hyper-parameters of the ANN.

In the present study, a DoE table is constructed at first for both design problems, viz., DP1 and DP2. For DP1, five levels are chosen for each of the five design variables;

whereas for DP2, three levels are chosen for each of the seven design variables. The lower and upper bounds of the design variables chosen are listed in Table 3.1. A full factorial experiment is considered with a total of 3125 data points for DP1 and 2187 data points for DP2. Now, for each data point, the FEMM model is built and the average magnetic flux density at the fluid gap and maximum magnetic flux density in the valve model are stored.

For the current problem, feed forward-type architecture as shown in Figure 3.7 is chosen and two ANN models for each design problem are fitted. The hyper-parameters as listed in Table 3.2 are selected based on the mean square error (MSE) criteria. MSE refers to the mean of the squares of the error difference between the model estimated magnetic flux values and the FEM estimated values. By minimizing this criteria, the fitness of the model with the data has been estimated. By observing the trends of MSE values for variations in neurons and hidden layers, the hyper-parameters were tuned. For more information on model fitting and hyper-parameter tuning, the study by Keshav and Chandramohan (2019) can be referred. The available data is split into train, test and validation data in the ratio of 70:15:15 and the final model showed a fitness level of around 99%. This model is later used as the data-driven model in the optimization process.

Table 3.2: Hyper-parameters of the ANN model

Design problem	DP1		DP2	
	B	B_{\max}	B	B_{\max}
Number of layers	2	2	3	3
Number of neurons in each layer	{19, 1}	{20, 1}	{20, 16, 1}	{19, 18, 1}

3.7.4 O-COM

In this approach, both EMM and FEM methods are coupled together to reduce the number of FEM evaluations. Finite element method magnetics (FEMM) is an open source finite element analysis software for solving electromagnetic problems (Meeker 2009). The constrained MDPL-MOPSO code is implemented in MATLAB software and FEMM is communicated for all the non-dominated solutions found at each iteration

using OctaveFEMM interface (Meeker 2010). The methodology and the flow of information between the various stages of optimization algorithm in MATLAB and FEM analysis in FEMM software is shown in Figure 3.8. A sample code of objective function with FEMM script file, EMM and NN methods is provided in Appendix III for the design problem “DP1”. The code can be modified to execute DP2 optimization with a minor modification in objective functions, constraints and variable values based on the data provided in sections 3.3 and 3.5.2.

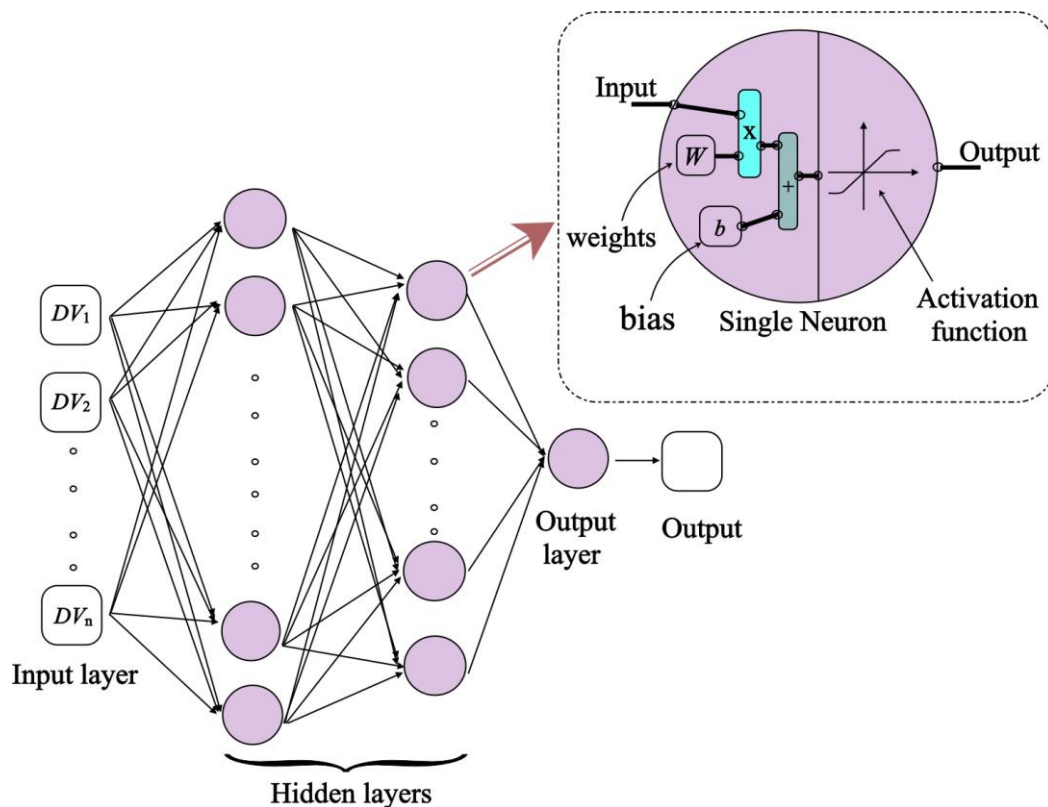


Figure 3.7 Architecture of feed-forward neural network

In each function call, FEMM executes the statements shown in Figure 3.8. Average magnetic flux densities in radial and annular gaps are calculated after the analysis. At present, FEMM has no dedicated manual operation or programmatic function which returns the maximum flux density. Therefore, magnetic flux densities at each node were calculated and a maximum value was found. To reduce the computational load, nodes on only top half of the axisymmetric model were considered. Each call to FEMM module ends with return of the three required flux densities to the main MOPSO function.

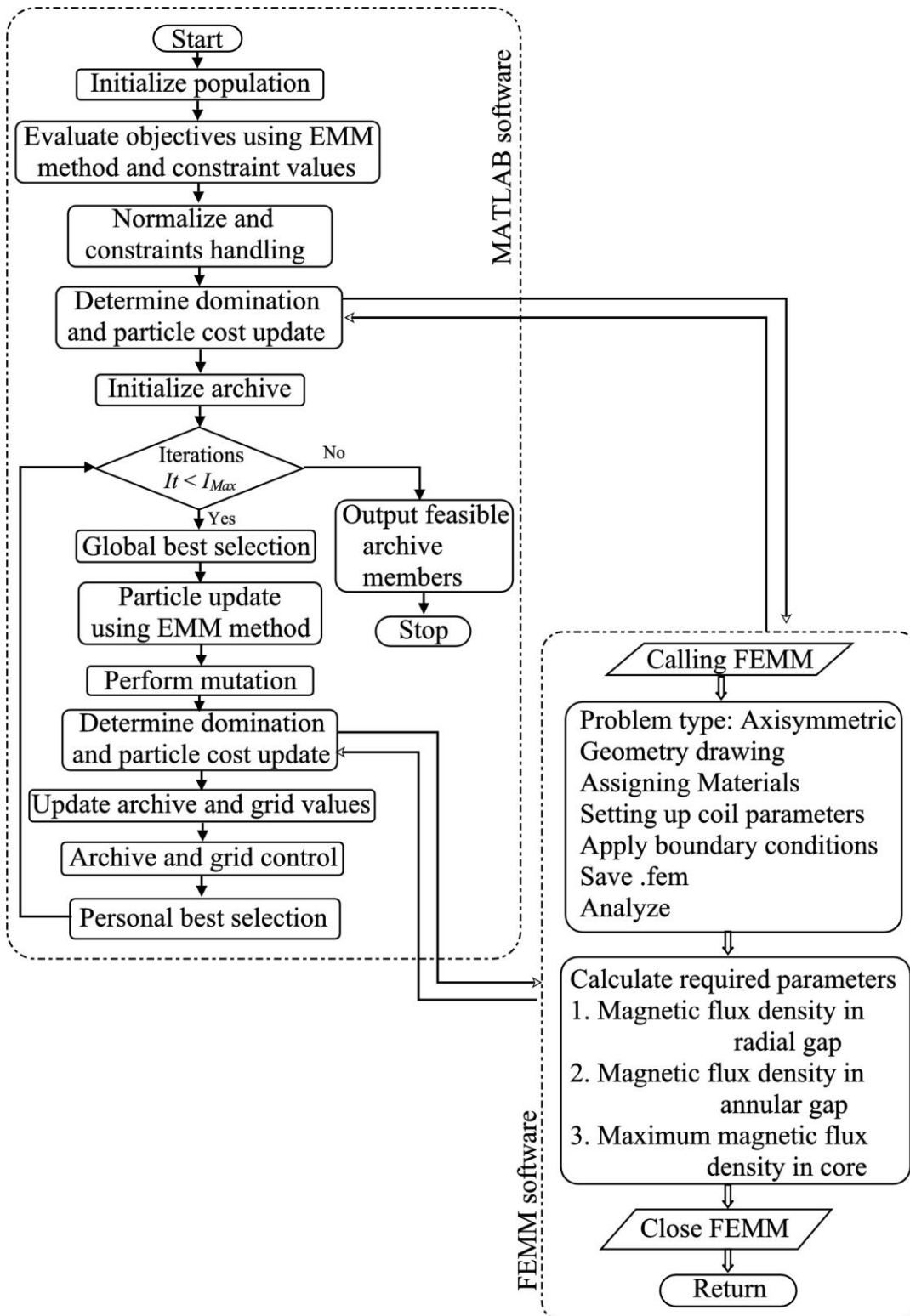


Figure 3.8 Constrained MDPL- MOSPO in MATLAB coupled with FEMM

3.8 PARETO COMPARISON

Many quality indicators are available in literature for comparing Pareto front approximations of different optimization routines. In general, these indicators provide varied information such as diversity of Pareto points, uniformity of points, proximity to Pareto front or other set of points, etc. (Coello et al. 2007). In the present study, hypervolume indicator is used for quantitative comparison of Pareto fronts. Hypervolume is a unary quality indicator which assigns a real number to the specific Pareto approximation set (Pareto front). This is a measure of the volume of the portion of objective space that is weakly dominated by the Pareto approximation set (Zitzler et al. 2008). In a bi-objective design optimization problem, hypervolume is the area enclosed by all optimal design points and a reference point. The objective function values of individual Pareto approximation sets are normalized in the range [0, 1] using equation (3.23).

$$\tilde{f}_i(x) = \frac{f_i(x) - f_{\min}}{f_{\max} - f_{\min}}, \quad i = 1, 2, \dots, l \quad (3.23)$$

Here, f_{\max} and f_{\min} are the maximum and the minimum value of the objective function values respectively, $f_i(x)$ is the objective function value in the i^{th} dimension of the objective space and l is the number of objectives. A surrogate Pareto front vector comprising all non-dominated sets from the four methodologies is evaluated and f_{\max} and f_{\min} are calculated using this surrogate vector. In this step, all individual Pareto fronts are also normalized. A reference point vector of [1, 1] is selected and hypervolume of each Pareto approximation set is calculated. The selected reference point is dominated by all Pareto approximation sets (Knowles et al. 2006).

3.9 RESULTS AND DISCUSSION

Based on the above description, the optimization process is performed for both the designs DP1 and DP2 using the four methodologies. A population of 50 and a number of iterations of 100 have been used for all the cases. Each optimization problem is repeated over 30 times.

A disadvantage of EMM method is that it under or over estimates the magnetic flux in the model. Therefore, for an accurate comparison, the objective functions of the final non-dominated Pareto front obtained using O-EMM and O-NN methodologies are re-evaluated using FEM analysis. The re-evaluated front is termed as “Corrected-O-EMM” and “Corrected-O-NN” respectively. Figure 3.9 shows the original Pareto fronts and the corrected fronts of O-EMM and O-NN of a sample run of DP1.

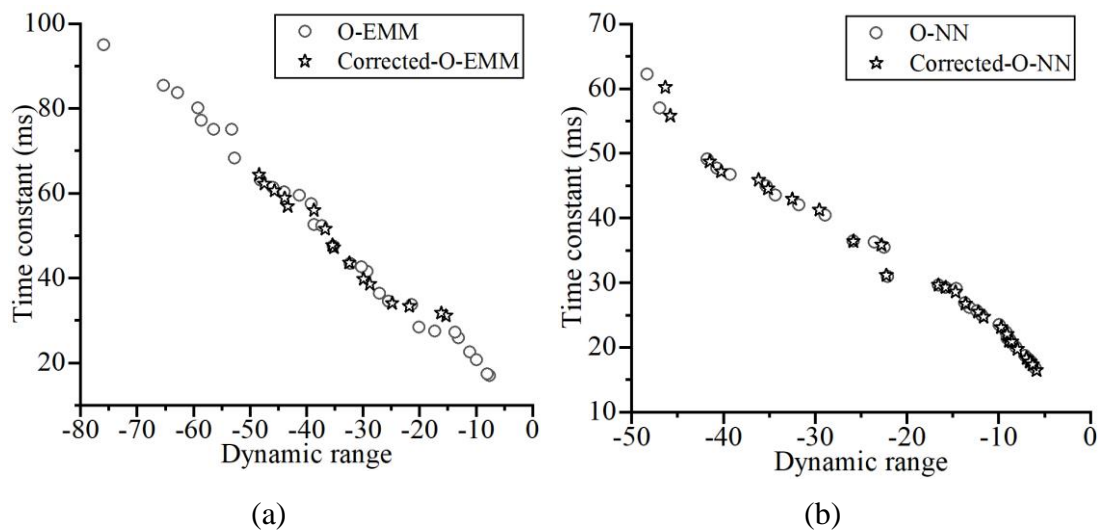


Figure 3.9 DP1 Pareto fronts of (a) O-EMM and Corrected O-EMM (b) O-NN and Corrected O-NN

The reduction in the number of design points (infeasible due to the violation of saturation constraint) in both cases may be noted. The difference in the number of design points for O-EMM in Figure 3.9 (a) can be attributed to the inaccuracy of the EMM model. Although O-NN uses FEM magnetostatic analysis, the optimization methodology uses a neural network model. As compared to O-EMM, the reduction in design points in the case of O-NN is far less because the neural network model has been fit with an accuracy of around 99% for the FEM data.

For each design point, magnetic flux densities in the fluid gap, overall magnetic flux in the model and the maximum flux in the model are evaluated. The infeasibility of design points due to violation of saturation constraint is apparent from Figure 3.9 because of the reduction in number of design points. The inaccuracy in magnetic field distribution will produce inaccurate objective function values. Thus the corrected front should observe a shift from the original Pareto front. Since both the objectives in DP1

are dependent on magnetic flux distribution, the shift in the front is approximately diagonal which can be noticed in Figure 3.9. Figure 3.10 shows the original Pareto fronts and the corrected fronts of O-EMM and O-NN for a sample evaluation of DP2. In this case, only one of the objectives is dependent on magnetic flux distribution and therefore, the Pareto front shift can be noticed clearly. This non-linear shift in Pareto front will affect the selection of best individuals during the process of optimization. Therefore, there remains a possibility with O-EMM and O-NN that they retain infeasible particles and may lose the best optimal candidates during the optimization process. In the subsequent comparison process, only corrected design points of O-EMM and O-NN are used.

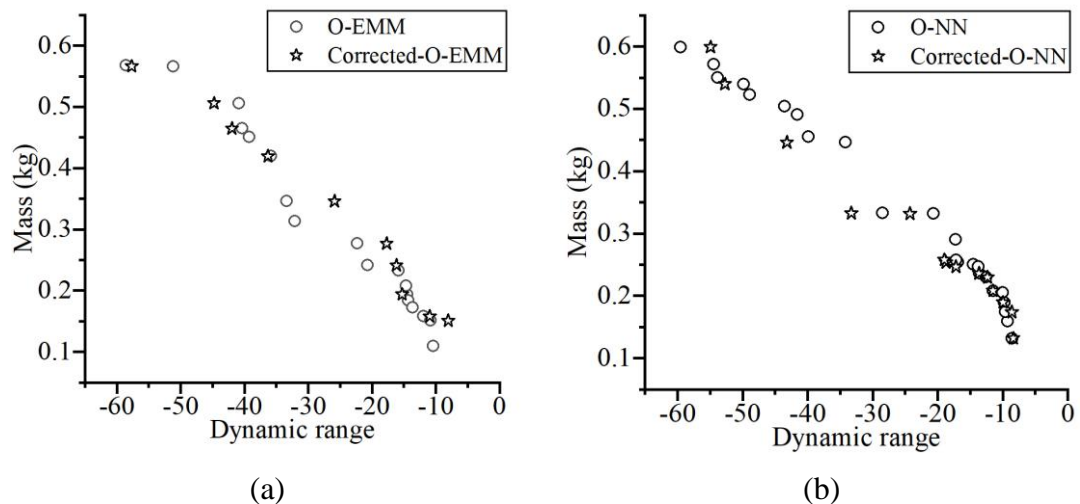


Figure 3.10 DP2 Pareto fronts of (a) O-EMM and Corrected O-EMM and (b) O-NN and Corrected O-NN

3.9.1 Comparative Studies

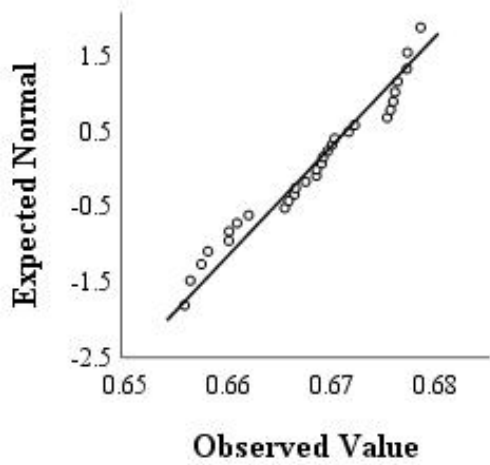
Each algorithm is run 30 times independently and the hypervolume for each Pareto approximation set is calculated. In this study, both parametric and non-parametric studies are performed, the detailed usage and assumptions behind these tests can be found in Weaver et al. (2017). The parametric tests assume that the data distribution is normal while the non-parametric tests do not assume any sampling distribution. At first, to determine the normality of samples, Shapiro – Wilk test has been performed. This test is available when the variables are continuous in nature. The null hypothesis assumes that the data is normally distributed for a chosen level of

significance. The test results suggested that O-NN from DP1 and O-FEM, O-NN from DP2 deviate from normal distributions. Therefore, for performing parametric testing, an outlier from each group is skipped to convert the data into a normal distribution (García et al. 2009). The Shapiro – Wilk test results after data conversion are shown in Table 3.3. From the results, it can be verified that the hypervolume measures of each individual algorithm in both the design problems follow a normal distribution ($p > 0.05$). A one way ANOVA is performed to determine the differences in the distribution. ANOVA allows comparison of more than two sampling distributions at the same time. In the case of DP1, the average hypervolume measure is statistically different, $F(3,115) = 201.483, p < 0.05$. In the case of DP2 also, the average hypervolume measures are statistically different, $F(3,114) = 88.974, p < 0.05$. The Q-Q plots for all algorithms in the design problems DP1 and DP2 are shown in Figures 3.11 and 3.12 respectively. As can be seen, the datasets of both the design problems fall on the reference line. This signifies that the design methodologies from both the design problems (after removing outliers) conform to normal distribution.

Table 3.3: Shapiro – Wilk tests for DP1 and DP2

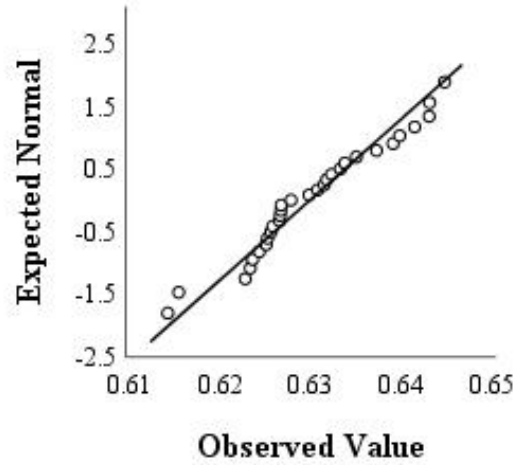
Algorithm	Shapiro – Wilk					
	DP1			DP2		
	Statistic	df	p - value	Statistic	df	p - value
O – FEM	0.943	30	0.110	0.952	29	0.212
O – EMM	0.960	30	0.303	0.939	30	0.088
O – COM	0.958	30	0.279	0.972	30	0.602
O – NN	0.935	29	0.073	0.961	29	0.349

Normal Q-Q plot for O - FEM (DP1)



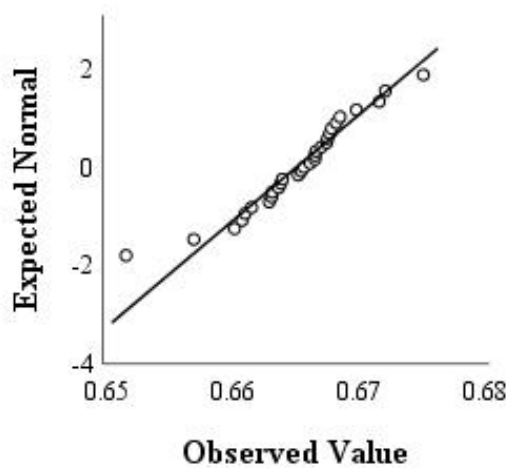
(a)

Normal Q-Q Plot for O - EMM (DP1)



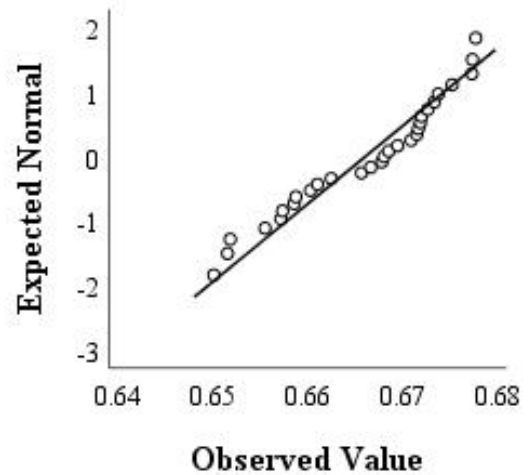
(b)

Normal Q-Q plot for O - COM (DP1)



(c)

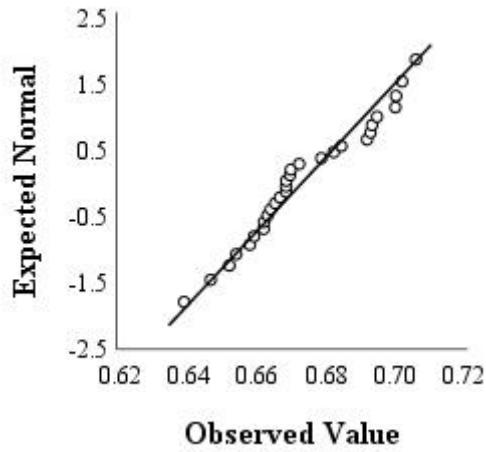
Normal Q-Q plot for O - NN (DP1)



(d)

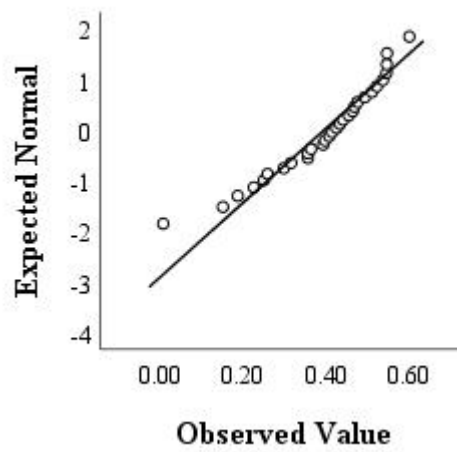
Figure 3.11 Q-Q graphic plots of DP1 for (a) O – FEM, (b) O – EMM, (c) O – COM and (d) O – NN

Normal Q-Q plot for O - FEM (DP2)



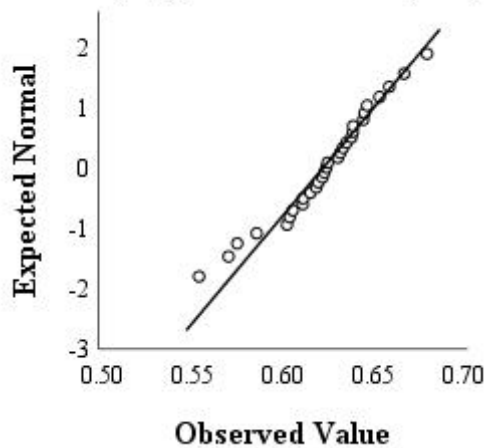
(a)

Normal Q-Q plot for O - EMM (DP2)



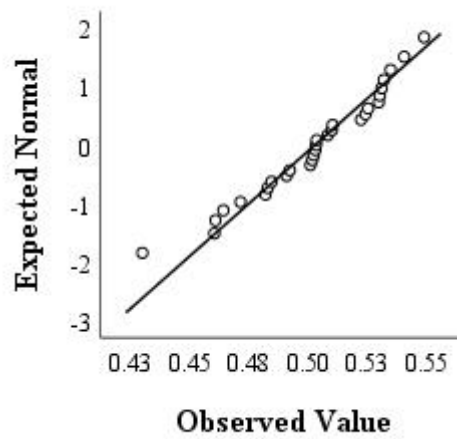
(b)

Normal Q-Q plot for O - COM(DP2)



(c)

Normal Q-Q plot for O - NN(DP2)



(d)

Figure 3.12 Q-Q graphic plots of DP2 for (a) O – FEM, (b) O – EMM, (c) O – COM and (d) O – NN

Also, non-parametric tests have been performed to determine the differences in original data (including outliers). Kruskal – Wallis test is the non-parametric alternative to ANOVA test and determines if there are any significant differences between two or more groups. An independent samples Kruskal - Wallis test resulted in rejection of null

hypothesis which stated that the distributions are similar across all categories in DP1 and DP2 independently. Therefore, the hypervolume measures across all algorithms in DP1 and DP2 are significantly different. The box plots for DP1 and DP2 are shown in Figure 3.13.

Both the ANOVA test and the Kruskal – Wallis tests predict only about the significant differences among two or more groups. However, to determine which group is statistically different from others, a post-hoc analysis has to be performed. There are many post-hoc analyses which are used in the literature. In this study, Bonferroni test and Dunnett C test are performed which are commonly used in similar comparative studies.

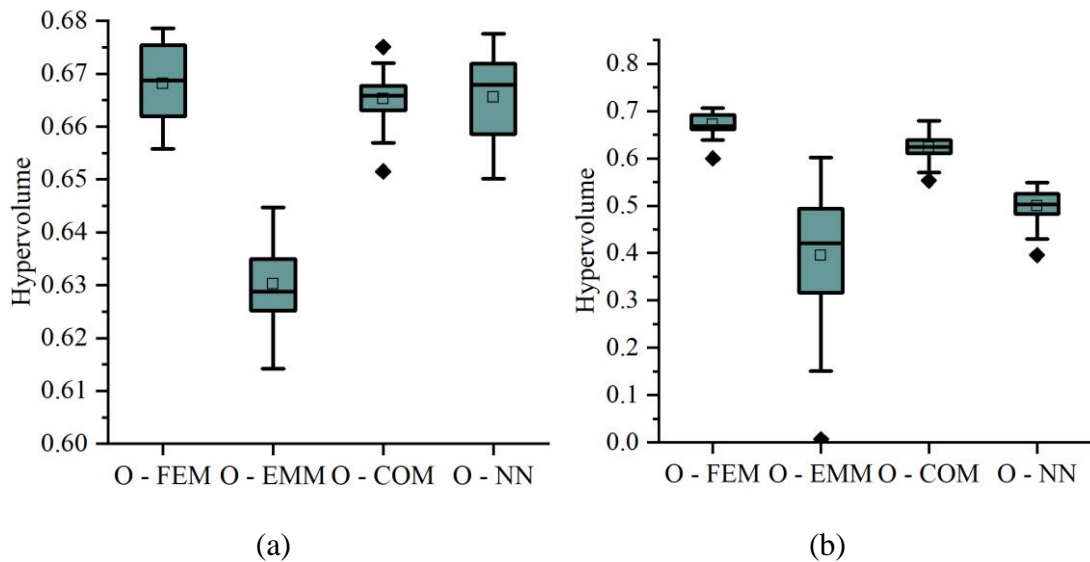


Figure 3.13 Box plots of hypervolume measures for (a) DP1 and (b) DP2

A post hoc analysis is conducted to determine the differences that lie between the individual methodologies. A Bonferroni test is performed for both the design problems and the results are shown in Table 3.4. For DP1, the test predicts no significant difference in the hypervolume measures between O-FEM, O-COM (p – value = 0.655) and O-FEM and O-NN (p – value = 1.00). Also, based on the mean difference values, it is clear that O-NN predicts similar hypervolume measures as that of O-FEM followed by O-COM. However, there is a significant difference between O-FEM and O-EMM results with a p – value < 0.05. In the case of DP2, the tests predict

significant differences between all individual algorithms with a p – value < 0.05 . However, based on mean difference values, the greatest difference is between O-FEM and O-EMM, followed by O-FEM and O-NN and finally between O-FEM and O-COM. Also, similar conclusions were obtained when using Dunnett C test results shown in Table 3.5. Therefore, it can be concluded that O-COM methodology performs similar to the O-FEM methodology with respect to hypervolume indicator.

Table 3.4: Bonferroni tests for DP1 and DP2

(I)	(J)	DP1		DP2	
		Mean difference (I – J)	p - value	Mean difference (I – J)	p - value
O-FEM	O-EMM	0.0379	0.000	0.2782	0.000
	O-COM	0.0029	0.655	0.05	0.053
	O-NN	0.0021	1.000	0.1706	0.000
O-EMM	O-FEM	-0.0379	0.000	-0.2782	0.000
	O-COM	-0.035	0.000	-0.2282	0.000
	O-NN	-0.0358	0.000	-0.1076	0.000
O-COM	O-FEM	-0.0029	0.655	-0.05	0.053
	O-EMM	0.035	0.000	0.2282	0.000
	O-NN	-0.0008	1.000	0.1206	0.000
O-NN	O-FEM	-0.0021	1.000	-0.1706	0.000
	O-EMM	0.0358	0.000	0.1076	0.000
	O-COM	0.0008	1.000	-0.1206	0.000

Table 3.6 lists the computational time taken by different methodologies. All the work has been performed on a machine with i7 processor, 16 GB RAM and 1 TB HDD. The time taken by O-FEM is nearly 6 hours while the O-EMM and O-NN utilize under 2 minutes of computational time. Although the combined magnetostatic approach requires relatively more computational time than that of O-EMM and O-NN, it requires substantially less time compared to O-FEM. It may be noted that O-FEM requires similar time in both the design problems. This is due to the fact that magnetostatic analysis is performed for all the particles in each population of the PSO in O-FEM.

However, the combined approach requires less time in DP2 than in DP1, nearly 50% reduction in time from DP1. This is because the Pareto approximation set in DP2 is less populated than in DP1 and therefore, the non-dominated candidates in each iteration are less. This also indicates that the reduction in computational time is due to the reduction in the number of FEM evaluations made during the optimization process. Any better programming skills or an advanced FEMM software might reduce the computational runtime of each FEM evaluation, but O-COM directly influences the number of FEM runs and thus reduces the overall computational time of the design problem.

Table 3.5: Dunnett C tests for DP1 and DP2

(I)	(J)	DP1		DP2	
		Mean difference (I – J)	<i>p</i> - value	Mean difference (I – J)	<i>p</i> - value
O-FEM	O-EMM	0.0379	0.0019	0.2758	0.0252
	O-COM	0.0029	0.0015	0.0476	0.0065
	O-NN	0.0026	0.002	0.1717	0.0074
O-EMM	O-FEM	-0.0379	0.0019	-0.2758	0.0252
	O-COM	-0.035	0.0016	-0.2282	0.0254
	O-NN	-0.0353	0.0021	-0.104	0.0256
O-COM	O-FEM	-0.0029	0.0015	-0.0476	0.0065
	O-EMM	0.035	0.0016	0.2282	0.0254
	O-NN	-0.0003	0.0018	0.1241	0.008
O-NN	O-FEM	-0.0026	0.002	-0.1717	0.0074
	O-EMM	0.0353	0.0021	0.104	0.0256
	O-COM	0.0003	0.0018	-0.1241	0.008

It is noted that from the previous results of comparison of hypervolume measures, O-NN also performs similar to O-FEM methodology with a major reduction in computational time. However, the computational time required during the preliminary process in generating data sets related to DoE table, fitting a neural network model and hyper parameter tuning were not considered. Therefore, based on the above

results, it can be concluded that O-COM methodology performs similar to O-FEM in predicting the optimal design points and also offers a huge reduction in computational cost.

Table 3.6. Comparison of Computational time

	DP1	DP2
O-EMM	7.6 ± 0.7 s	7.3 ± 0.9 s
O-NN	1.41 ± 0.02 mins	1.7 ± 0.03 mins
O-COM	65.6 ± 13.8 mins	28.4 ± 1.5 mins
O-FEM	354 ± 3 mins	322 ± 1.42 mins

3.10 SUMMARY

In this chapter, a quantitative comparison of the different methodologies used in the optimal design of semi-active MR dampers is presented. The most commonly considered design problems which are constrained volume optimization and the constrained force optimization are chosen for comparison. Also, the choice of objective functions and their effect on the Pareto optimal points when considering O-EMM and O-NN methodologies is studied. A hypervolume indicator is selected for effective comparison of various Pareto front approximations. A search-based PSO algorithm is used for all four methodologies operating on both the design problems. From the results, it can be concluded that the combined magnetostatic approach provides comparable design points as that of O-FEM with respect to hypervolume indicator. Along with accuracy, O-COM methodology also offers a substantial reduction in computational time when compared with O-FEM methods. Therefore, this methodology can be used to optimally design other semi-active devices based on MR fluids.

CHAPTER 4

PROSTHETIC KNEE DAMPERS – PRELIMINARY DESIGN STUDY

4.1 INTRODUCTION

In this chapter, four different device configurations namely multi-pole rotary drum brake, inverted drum waveform arc brake, rotary vane MR damper and linear twin rod MR damper are considered for a preliminary design process and feasibility check in prosthetic knee domain. The device configurations are optimally designed by choosing relevant but simple optimization methodology. As and when required, O-EMM methodology is preferred at this stage, however, depending on the complexity of the problem, other methodologies are also applied. The primary criteria for selection of design is based on its ability to generate the required knee braking torque or equivalent force.

The preliminary optimal designs performed in this chapter are also used to show the various optimization methodologies and objective functions and constraint combinations commonly employed in the literature in designing a damper for prosthetic knee domain. Although the methodologies and objective functions are chosen as different for all four designs, further experimental analysis of the design configuration is performed only if the preliminary device is capable of producing the required knee braking torque or equivalent force.

4.2 MULTI-POLE ROTARY DRUM BRAKE

In this section, at first the geometry of the multi-pole brake design and the geometric variables are described. Later, the design parameters are defined in terms of geometric variables. The design consist of multiple electromagnetic poles on the radial face of the rotor. Optimization based on a data driven model is selected for optimal design of this damper. Four influencing variables are selected and a design of

experiments method is used to formulate a set of combinations of these variables. Magnetostatic analysis at each design point is performed to calculate the average magnetic field in the annular and radial gaps which are then used to calculate the design parameters. Regression analysis is used later to obtain braking torque as a function of geometric variables. A genetic algorithm optimization from the MATLAB toolbox is performed to obtain the optimum geometric dimensions of the brake.

4.2.1 Geometry

The multi-pole inverted drum brake consists of more than one coil area wound around the rotor. A total of 11 coil areas are considered to get an even distribution of the magnetic field on the active pole length around the axial face of the rotor. Further, the whole casing is considered to be made of magnetic material, which helps in achieving the magnetic field on both the radial and axial faces of the rotor. MR fluid occupies the narrow gap of 0.5 mm between the rotor and the casing. The shaft is assumed to be made of aluminum material to reduce any flux leakages through it. The cross-section of the drum brake along with the geometric variables are shown in Figure 4.1.

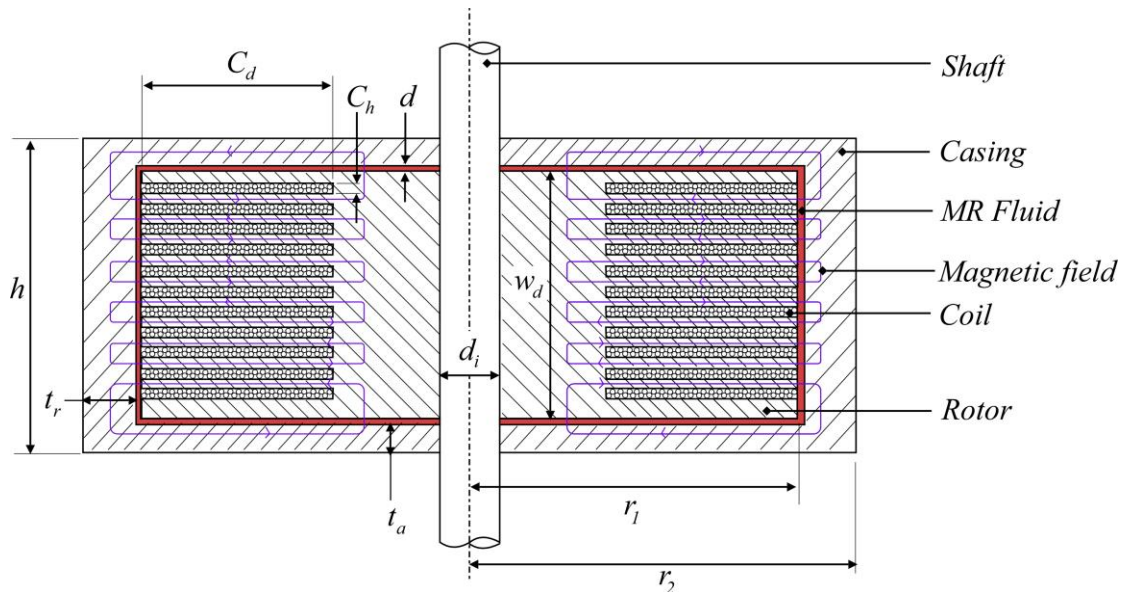


Figure 4.1 Cross-section of multi-coil inverted drum brake

Here, C_d is the coil width, C_h is height of each coil cross-section, h is the height of brake, w_d is width of brake, d is fluid gap, t_r is casing radial thickness, t_a is casing axial thickness, r_1 is radius of rotor, r_2 is radius of casing and d_i is diameter of shaft.

4.2.2 Design Parameters

The MR fluid occupying the narrow gap is modeled using a Herschel-Bulkley model given by Equation (4.1) (Nguyen and Choi 2010).

$$\tau = \tau_y + K\dot{\gamma}^n \quad (4.1)$$

Here, τ_y is field dependent yield stress, K is the fluid consistency index and n is the flow behavior index. All the variables in the model are considered to be field dependent and can be calculated using Equation (4.2).

$$Y = Y_\infty + (Y_0 - Y_\infty) \left(2e^{-B\alpha_{sy}} - e^{-2B\alpha_{sy}} \right) \quad (4.2)$$

Here, Y can represent the variables τ_y , K and n . The value of Y is considered to vary from zero applied value, Y_0 to saturation value, Y_∞ . Also, B represents the magnetic flux at the corresponding location and α_{sy} is the saturation moment index. In this dissertation, MRF-132 DG (low off-state viscosity and high yield stress MR fluid) is considered for all optimization problems. However, an initial optimal design of this device configuration resulted in a much lower knee torque. Therefore, the design was repeated considering MRF-140 CG, an alternative to MRF-132DG but with a relatively higher yield stress and a higher off-state viscosity. The parameters for MRF 140CG are: $K_0 = 0.65 \text{ Pa} \cdot \text{s}^n$, $K_\infty = 5400 \text{ Pa} \cdot \text{s}^n$, $\alpha_{sk} = 5 \text{ T}^{-1}$, $\alpha_{sn} = 35 \text{ T}^{-1}$, $\tau_{y0} = 25 \text{ Pa}$, $\tau_{y\infty} = 39000 \text{ Pa}$, $\alpha_{s\tau_y} = 2 \text{ T}^{-1}$, $n_0 = 0.915$ and $n_\infty = 0.24$ (Nguyen and Choi 2010).

When the brake is not supplied with any current, the off-state torque generated by the brake can be calculated using Equations (4.3) and (4.4) (Nguyen et al. 2015).

$$T_0 = \left\{ \begin{array}{l} \frac{4\pi\mu_{eq0}r_1^4}{(n_0+3)d} \left[1 - \left(\frac{d_i}{2r_1} \right)^{n_0+3} \right] \Omega + \frac{4\pi\tau_0}{3} (r_1^3 - r_0^3) \\ + 2\pi r_1^2 w_d \left[\tau_0 + K_0 \left(\frac{\Omega r_1}{d} \right)^{n_0} \right] \end{array} \right\} \quad (4.3)$$

$$\mu_{eq0} = K_0 \left(\frac{r_1 \Omega}{d} \right)^{n_0-1} \quad (4.4)$$

Here, Ω is the angular velocity at the knee joint. Current supply produces a magnetic field which passes through the core, crosses the MR fluid gap expands through the casing and returns into the core. It should be noted that the adjacent areas of the coil should be wound alternating between clockwise and anticlockwise direction so as to produce the magnetic field shown in Figure 4.1. The total on-state torque generated by the brake can be calculated using Equations (4.5) and (4.6) (Nguyen and Choi 2010).

$$T_B = \left\{ \begin{array}{l} \frac{4\pi\mu_{eq}r_1^4}{(n_e+3)d} \left[1 - \left(\frac{d_i}{2r_1} \right)^{n_e+3} \right] \Omega + \frac{4\pi\tau_{ye}}{3} (r_1^3 - r_0^3) \\ + 2\pi r_1^2 L_a \left[\tau_{ya} + K_a \left(\frac{\Omega r_1}{d} \right)^{n_a} \right] \end{array} \right\} \quad (4.5)$$

$$\mu_{eq} = K_e \left(\frac{r_1 \Omega}{d} \right)^{n_e-1} \quad (4.6)$$

Here, τ_{ye} is the torque in the end (or radial) surface of the brake and τ_{ya} is the torque in the annular surface of brake. The total torque generated is the sum of both on-state and off-state torques.

$$T = T_0 + T_B \quad (4.7)$$

The magnetic flux in the gap varies with distance and thus in Equations (4.3) – (4.7), an average magnetic flux in the annular and radial gaps given by Equations (4.8) and (4.9) is considered.

$$B_a = \frac{1}{L_a} \int_0^{L_a} B dl \quad (4.8)$$

$$B_r = \frac{1}{(r_1 - 0.5d_i)} \int_{0.5d_i}^{r_1} Bdr \quad (4.9)$$

4.2.3 Design of Experiments

The outermost dimensions of the rotary brake namely maximum height, h and the radius of the casing, r_2 are constrained such that the whole knee joint can be contained within the geometrical limits of a normal adult human knee. Therefore, the maximum height is restricted to 90 mm, while the maximum radius of the casing is limited to 35 mm. Further, a fluid gap size of 0.5 mm and a shaft diameter of 8 mm is considered in the analysis. The remaining parameters show a non-linear variation in the total torque generated by the brake. Increasing the coil height may help accommodate a larger number of turns of the coil, but reduces the pole length, thus affecting the torque. The axial and radial casing thicknesses also show a major effect on the braking torque. Therefore, the brake is designed considering the coil height, coil width, casing radial thickness and casing axial thickness as design variables and three levels are considered for each parameter as listed in Table 4.1.

Table 4.1. Parameters and their levels

	Coil depth, C_d (mm)	Coil height, C_h (mm)	Casing radial thickness, t_r (mm)	Casing axial thickness, t_a (mm)
Low level	10	2	3	3
Medium level	15	3	5	5
High level	20	4	7	7

All the combinations of design parameters will result in 81 combinations and performing magnetostatic analysis for each will take up a lot of CPU time. Thus, an L27 orthogonal array method is used to determine the various combinations of design variables. For each combination of design variables, an axisymmetric quarter model is used to perform magnetostatic analysis. Low carbon SAE1020 steel is chosen for both casing and rotor because of its high relative permeability and a magnetic saturation flux

of 2.3 T (Gudmundsson et al. 2010). The number of turns in each coil cross-section is determined using Equation (4.10).

$$N = \frac{p_f (C_d C_h)}{\left(\frac{\pi}{4} d_c^2 \right)} \quad (4.10)$$

Here, p_f is the packing factor and d_c is the coil diameter. Copper coil of 24 AWG gage is chosen with a packing factor of 0.7. The analysis is performed at 12 V and a current supply of 2 A. Due to simplicity in parameterization of brake design and an easy approach in performing magnetostatic analysis of all design points, ANSYS Workbench was preferred at this stage. Fluid properties of MRF140CG referred from the datasheet (“Lord Corporation” 2001) were given as inputs to ANSYS, while the rest of the material properties were obtained from ANSYS library. A one fourth of brake model was analyzed for each combination of dimensions and average magnetic fields were determined in both annular and radial gaps using Equations (4.8) and (4.9). Further, the total torque generated by the brake was calculated using Equation (4.7). A design speed of 8.4 rpm was selected for the analysis (Gudmundsson et al. 2010). The combinations of geometric parameters, along with their output torque calculated using the above mentioned procedure are listed in Table 4.2.

4.2.4 Optimal Design

The calculated mass of the brake for all design points varied in the range of 2.7 kg to 2.9 kg. This small variation is because of the restrictions in the outer most dimensions. Owing to this small variation and to simplify the optimization process, mass was not considered as an objective function. Therefore the optimal design is the one which will yield the maximum total braking torque for the given geometric dimensions.

Since magnetostatic analysis was performed for only discrete values of the dimensions, there may exist an optimum design value in the considered range. To determine this optimum, a regression analysis is performed to obtain the total braking torque as a function of the four design variables. The variation of torque with design variables is given by Equation (4.11).

$$T = \left\{ \begin{array}{l} 3.88 + 1.357C_d - 1.48C_h - 0.64t_r + 1.54t_a - 0.0392C_d^2 \\ +0.252C_h^2 - 0.028t_r^2 - 0.1362t_a^2 - 0.0407C_dC_h - 0.029C_d t_r \\ -0.0112C_d t_a + 0.144C_h t_r - 0.202C_h t_a + 0.0379t_r t_a \end{array} \right\} \quad (4.11)$$

Table 4.2. Response parameters for different geometric variable combinations

Sl. No.	Coil depth, C_d (mm)	Coil height, C_h (mm)	Casing radial thickness, t_r (mm)	Casing axial thickness, t_a (mm)	Total braking torque, T (Nm)
1	10	4	5	5	8.64
2	10	3	3	5	9.05
3	15	2	3	5	12
4	15	3	5	5	9.85
5	15	4	3	5	9.89
6	15	3	3	7	8.58
7	20	2	5	5	7.91
8	10	3	5	3	8.4
9	10	3	5	7	7.49
10	20	3	7	5	5.69
11	20	3	3	5	8.77
12	15	2	5	7	8.71
13	15	3	3	3	10.35
14	15	3	5	5	8.33
15	15	4	5	7	5.9
16	15	3	7	7	6.24
17	15	2	7	5	7.75
18	15	4	7	5	6.79
19	20	3	5	7	6.26
20	15	4	5	3	9.01
21	10	3	7	5	7.12
22	15	2	5	3	10.21
23	20	3	5	3	7.61
24	10	2	5	5	9.91
25	20	4	5	5	5.83
26	15	3	5	5	8.33
27	15	3	7	3	7.41

A genetic algorithm optimization is performed with an objective function of maximizing braking torque for the given dimensional constraints using MATLAB. The optimum geometric dimensions obtained are coil depth of 14.59 mm, coil height of 2 mm, casing radial thickness of 3 mm and casing axial thickness 3.98 mm. The optimum braking torque obtained for this design is 11.78 Nm. It can be observed that this value is less than the maximum braking torque shown in Table 4.2, which is 12 Nm. This difference in value can be attributed to the accuracy with which the regression equation was fit. Magnetostatic analysis using the optimal designs will predict more accurate braking torque value.

4.2.5 Results and Discussion

The advantage of multi-pole design over a single coil design is that the former gives a more uniform magnetic field over the activated length. To show this effect, a magnetostatic analysis of a 2D axisymmetric model is performed considering only a single coil of the total area of cross-section similar to the multi-coil design. The individual coil area in multi-coil design is $(C_h \times C_d)$ which implies a coil cross-section of $(11 \times C_h \times C_d)$ for the single coil design. Therefore, the activated lengths of both the designs are similar. Models of the multi-coil and single coil designs considered in FEMM software are shown in Figure 4.2.

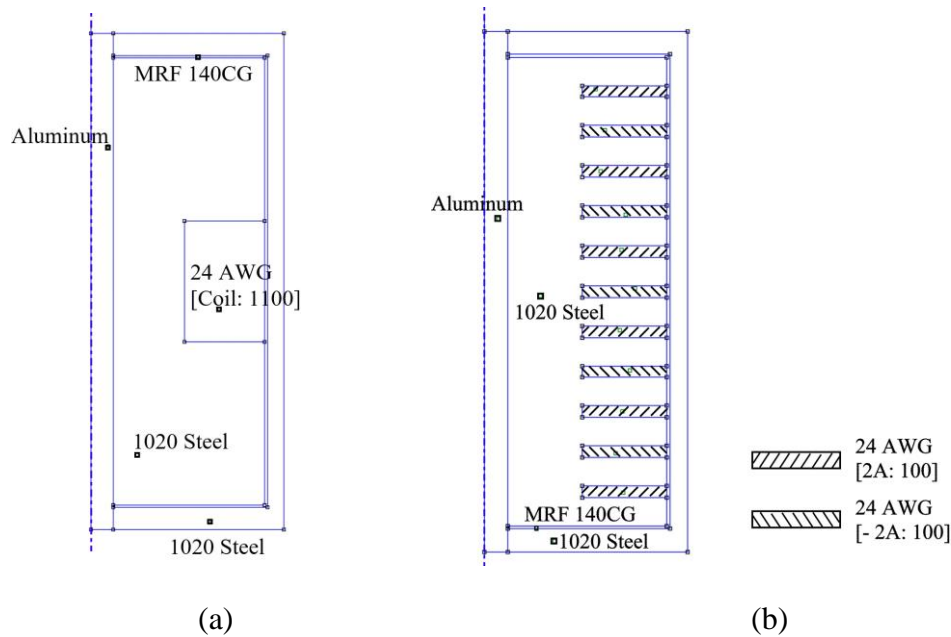
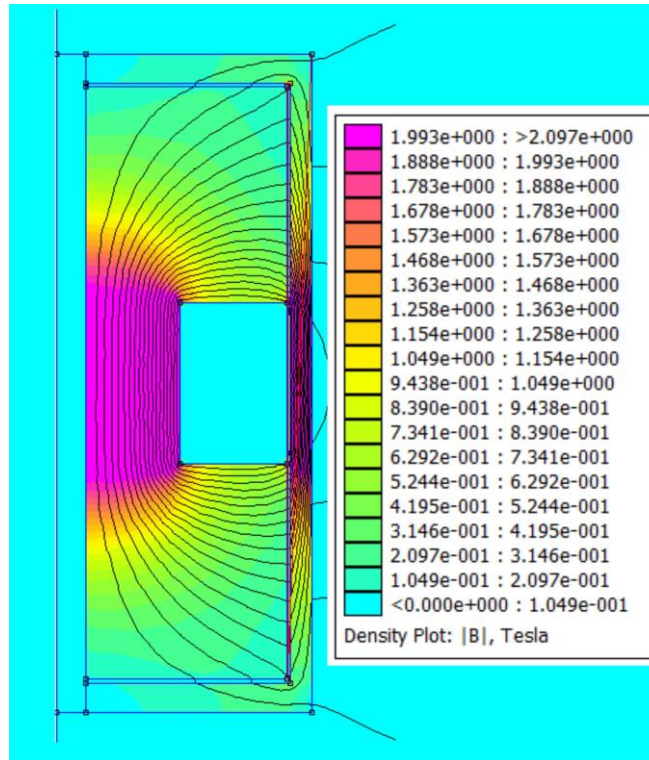
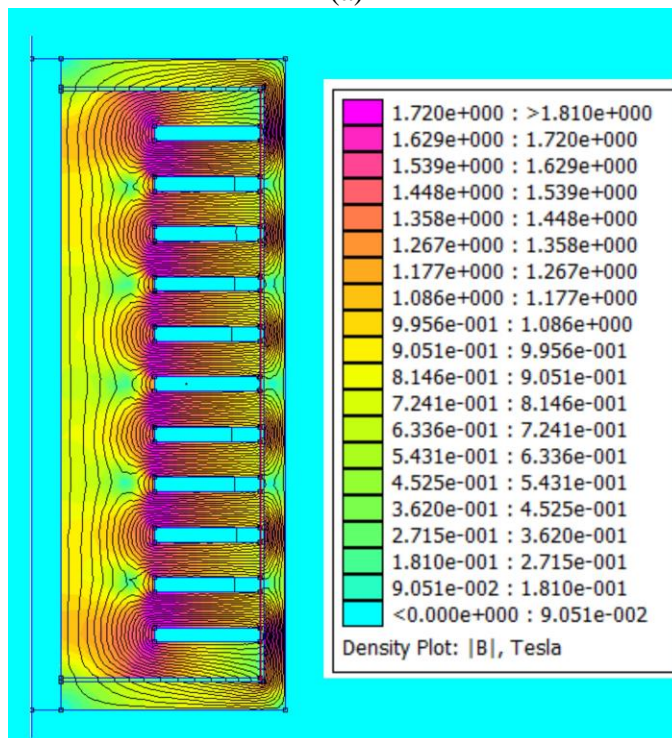


Figure 4.2 2D axisymmetric model of (a) single coil brake and (b) multi-coil brake



(a)



(b)

Figure 4.3 Magnetostatic analysis of (a) Single coil rotary brake and (b) Multi-coil rotary brake

It can be seen from Figure 4.2(b) that the coil cross-sections are supplied with 2 A and -2 A current alternatively. The number of turns in the coil cross-section is calculated using Equation (4.10) and a constant current of 2 A is used in both the analysis. Magnetostatic analysis is performed on both the models. Magnetic flux distribution of both models is shown in Figure 4.3. It can be clearly seen that the multi-pole design has larger uniform flux density distribution compared to the single coil design. Further, in both the designs, the maximum flux density is less than the saturation field strength of 2.3 T.

The magnitudes of the normal magnetic flux density in the fluid gap plotted for both the configurations is shown in Figure 4.4. As seen in the figure, the multi-pole design resulted in a much more uniform magnetic field in the activated pole length, region while the single coil drum brake resulted in a varying one. The magnetic field distribution of the multi-coil brake in both the annular as well as radial faces results in a total braking torque of 13.4 Nm.

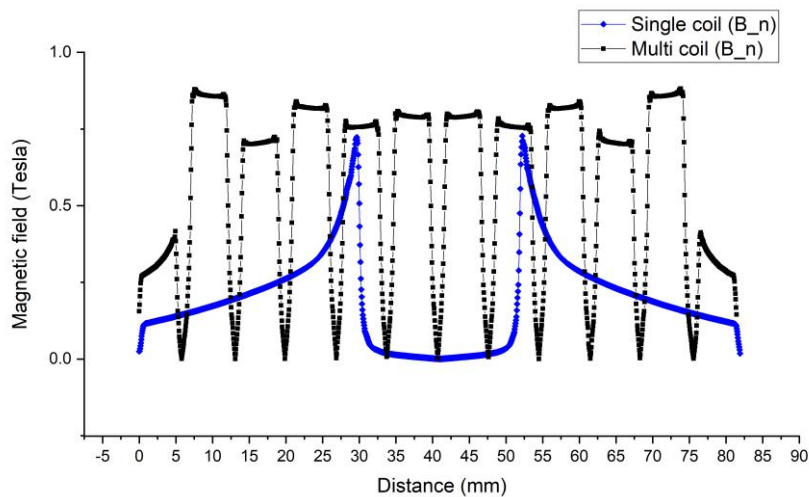


Figure 4.4 Normal magnetic flux distribution in single coil and multi-coil brake

Although, normal human gait requires a torque of up to 35 Nm, the designed brake can satisfy the swing phase knee requirements of an average human. However, the mass of the optimal design is around 2.7 kg which is very high for prosthetic knee applications. The use of multi-pole design resulted in a much more uniform distribution of magnetic field strength, however, this increase in strength is insufficient for producing the required knee braking torque. Based on the criteria of insufficiency of

producing adequate knee braking torque along with a large device mass, this design configuration is rejected from further optimal design and experimental testing.

4.3 TWIN ROD MR DAMPER

The proposed design of twin rod MR damper consists of a cylinder, piston assembly, piston rod, an electromagnetic coil, and a cylinder attachment. A cross-sectional view of the damper along with geometrical parameters are shown in Figure 4.5. An electromagnetic coil is wound around the piston and an outer sleeve is attached on top of it. A narrow gap along the whole length is maintained between the outer sleeve and the piston flange portion. Two piston rods are connected on either side of the piston. MR fluid occupies the remaining volume inside the cylinder in which the piston rod assembly is placed. To provide relative motion between the cylinder and piston, one of the rods is connected with an eye while the other end of the cylinder is connected with a suitable attachment. To keep the optimization process simple, O-EMM methodology is used as the design procedure. The formulation of objective functions and the electromagnetic circuit design procedure are similar to design problems (DP1 and DP2) from Chapter 3, and are repeated here briefly for the design variables in the present case.

In the flow mode, the piston core, MR fluid, and the outer sleeve form an essential part of the magnetic circuit. To obtain a high damping force, the materials used for piston core and outer sleeve should be of high relative permeability and also to avoid saturation, the saturation field density should be higher than that of the MR fluid. Here, 1018 steel is proposed as a material for piston core, outer sleeve, piston rod, and cylinder. Further, lord MRF -132DG is selected as the MR fluid in this design.

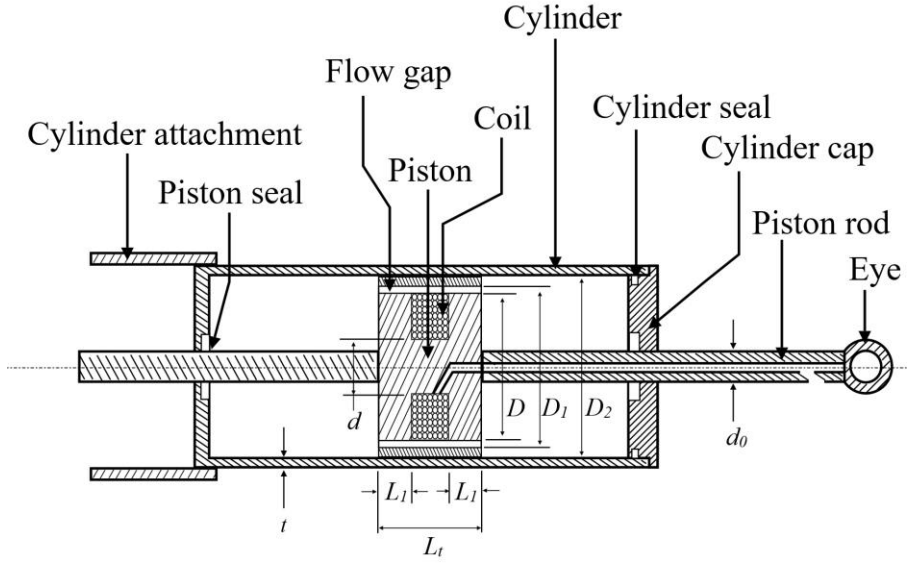


Figure 4.5 Twin rod MR damper in flow mode

4.3.1 Formulation of Total Damping Force

The total damping force produced consists of viscous forces, controllable MR forces, and friction forces. Neglecting the friction forces, the total damping force is given by Equation (4.12).

$$F = F_{vis} + F_{MR} \quad (4.12)$$

Here, F_{MR} is the controllable MR force and F_{vis} is viscous damping force.

Assuming a parallel plate Bingham model, the damping forces for a positive piston velocity are given by Equations (4.13) and (4.14),

$$F_{vis} = \frac{12\eta QL_t A_p}{wh^3} \quad (4.13)$$

$$F_{MR} = \left(2.07 + \frac{12Q\eta}{12Q\eta + 0.4wh^2\tau_y} \right) \frac{\tau_y LA_p}{h} \quad (4.14)$$

Here, η is the apparent viscosity of the fluid, Q is the volumetric flow rate, A_p is the effective cross-section of the piston, τ_y is the field dependent yield strength of the fluid and w is the mean circumference of the annular gap. For the given geometry shown in Figure 4.5, the variables are related as follows.

$$A_p = \frac{\pi(D_2^2 - d_0^2)}{4} \quad (4.15)$$

$$Q = A_p \dot{u} \quad (4.16)$$

$$w = \pi(D + h) \quad (4.17)$$

Here, \dot{u} is the velocity of the piston.

4.3.2 Formulation of the Electromagnetic Circuit

The yield stress is a function of the magnetic field which is controlled by the current supplied to the electromagnetic circuit. The strength of the magnetic field depends on various parameters such as coil diameter, number of turns, core material, etc. For an approximate solution of the magnetic circuit, the structure of the circuit is assumed to be constituted of various links of the constant magnetic field as shown in Figure 4.6. Applying Ohm's law to the magnetic circuit yields Equation (4.18).

$$Ni = \Phi(R_1 + 2R_2 + 2R_3 + R_4) \quad (4.18)$$

Here, N is the number of turns of coil wound, i is the current in the coil, Φ is the magnetic flux, and R_1 , R_2 , R_3 and R_4 are the reluctances of the links 1, 2, 3 and 4 respectively.

Based on the geometry of the piston, the reluctances of the links can be calculated using Equations (4.19) to (4.22).

$$R_1 = \frac{4L_t}{\pi\mu_{steel}d^2} \quad (4.19)$$

$$R_2 = \frac{\ln(D/d)}{\pi\mu_{steel}L} \quad (4.20)$$

$$R_3 = \frac{\ln(D_1/D)}{\pi\mu_{MRF}L} \quad (4.21)$$

$$R_4 = \frac{4L_t}{\pi\mu_{steel}(D_2^2 - D_1^2)} \quad (4.22)$$

Here, μ_{steel} and μ_{MRF} are the magnetic permeabilities of 1018 steel and MR fluid respectively.

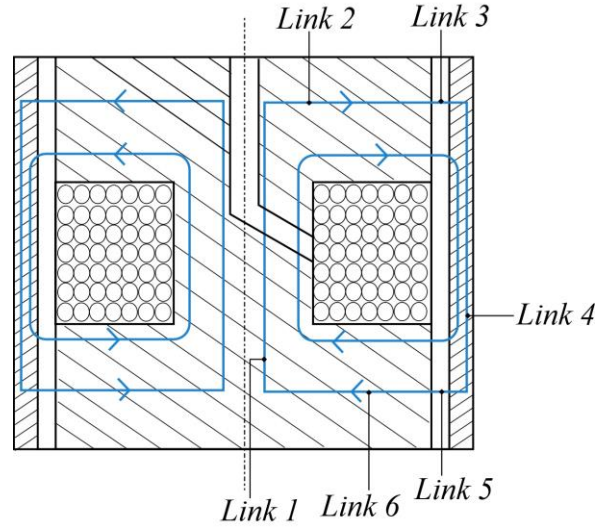


Figure 4.6 Equivalent electromagnetic circuit of piston

Further, the number of turns of coil can be approximated using Equation (4.23).

$$N = \frac{2p_f(D-d)(L_t-L)}{\pi d_c^2} \quad (4.23)$$

Here, d_c is the diameter of the coil and p_f is the packing factor constant. A value of 0.7 is considered as the packing factor constant. Applying the flux conservation rule and considering average surface cross-section areas for the links, the following relation can be deduced.

$$\Phi = B_1 \frac{\pi d^2}{4} = B_2 \frac{\pi(D+d)L_2}{2} = B_3 \pi(D+h)L_2 = B_4 \frac{\pi}{4}(D_2^2 - D_1^2) \quad (4.24)$$

4.3.3 Constrained Optimization Problem Formulation

The maximum knee torque requirement increases with increase in human weight. Therefore, optimal design studies of MR damper are usually done on an average human with a torque requirement of around 35 Nm (Gao et al. 2017; Gudmundsson et al. 2010). Further, the off-state damping should be as low as possible since it determines the rotation of the knee in a no-load condition. Maximum off-state torque of 2.4 Nm at

a rotation speed of 8.4 rpm is considered as a design constraint. Converting the rotational motion into linear damping force and velocity assuming a force moment arm of 40 mm, the damper should be capable of producing a maximum off-state damping force of 60 N, the total damping force of 800 N at a speed of 0.1 m/s. A magnetic field strength of 0.6 T is assumed in the annular gap, thus the yield strength of the MR fluid in the gap is 34.27 kPa for the assumed field strength. To limit the material in the core reach saturation point, magnetic field strengths are calculated using Equations (4.24) and nonlinear constraints are applied. Also, a 24 gage coil is considered for the design, which has a maximum ampacity of 2.1 A and a coil diameter of 0.51 mm. However, a current limit of 1.6 A is considered for analysis. The relative permeabilities of 1018 steel and MR fluid are taken as 800 and 2.78 respectively (Meeker 2009). Therefore, a constrained force optimization is formulated to determine the geometric variables $\{D, d, L, L_t, D_2\}$.

Objective function: maximizing dynamic range, $\frac{F_{MR}}{F_{vis}}$

Constraints: $i \leq 1.6$ A,

$$B_1, B_2, B_3 \leq 1.5 \text{ T}, F_h \leq 60 \text{ N},$$

$$F_{MR} + F_{vis} \geq 800 \text{ N} \quad @ \dot{u} = 0.1 \text{ m/s}$$

A constrained nonlinear minimization problem is solved using the MATLAB optimization toolbox with the bounds of design variables shown in Table 4.3. The optimized values are also listed in Table 4.3. For these dimensions, the off-state damping force obtained is 56.8 N and the maximum on-state damping force at a current of 1.6 A is 1582 N with a dynamic range of 26.

Table 4.3 Bounds and optimized values of parameters

Parameter	Bounds		Optimized value (mm)
	Lower (mm)	Upper (mm)	
D	22	38	35.25
d	12	25	18.73
L	12	20	12.10
L_t	20	36	21.40
D_2	30	45	41.7

4.3.4 Results and Discussion

The electromagnetic circuit was designed assuming constant magnetic field intensities in the links. Further, a constant relative permeability was assumed for the materials which is not true since the materials exhibit a nonlinear B-H curve. Therefore, a magnetostatic analysis using FEMM software for the optimized values of the piston assembly and considering a cylinder thickness of 5 mm is performed. An axisymmetric model of the piston assembly and the outer cylinder is considered for the analysis as shown in Figure 4.7(a). The magnetic field strength obtained in the piston assembly as a result of the analysis is shown in Figure 4.7(b).

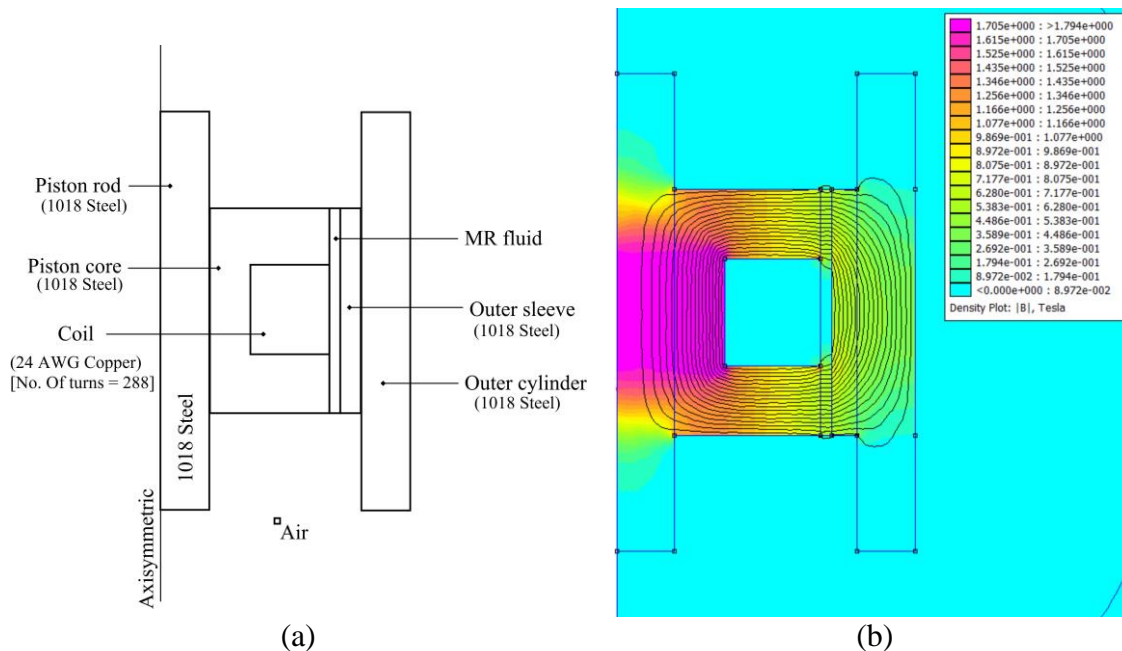


Figure 4.7 (a) Axisymmetric model of piston assembly including cylinder and (b) Magnetic field strength in the model

The results in Figure 4.7(b) show a magnetic strength of 1.8 T in the piston core and a strength of 0.62 T in the annular fluid gap. Therefore, the annular gap is exposed to a magnetic field strength more than 0.6 T as assumed. However, the strength in the piston core exceeds a value of 1.5 T, which may not pose a problem since the saturation field intensity of the material used for piston parts is around 2.1 T. This analysis also depicts the inaccuracies produced by EMM methods in producing maximum magnetic field in core and also magnetic flux density in fluid gaps. Also, use of magnetic material

for outer cylinder increases the cross-section of link 4 in Figure 4.6 and thus reduces the magnetic field strength in that link as verified by Figure 4.7(b).

The optimum dimensions of the damper yielded an off state damping force of 56.8 N and a maximum on-state damping force of 1582 N with a dynamic range of 26. Therefore, the design is capable of producing the required equivalent braking force and is considered further for optimal design and experimentation in the subsequent chapters.

4.4 ROTARY VANE MR DAMPER

The cross-sectional view of the proposed rotary vane damper with a bypass MR valve is shown in Figure 4.8. The two primary elements in this design are the rotary chamber and the bypass MR valve. The rotary chamber contains a static and a rotary vane which separates the hydraulic chamber into two volumes. Two fluid ports are located near the static vane, each opening into separate fluid regions. Hydraulic cables connect the two fluid regions with an MR valve located in-between the cables. In the bypass valve, the MR fluid flows through the narrow passage between the piston and the cylinder, realizing a flow mode. An electromagnetic coil is wound on the piston with the terminals pulled out through the piston shaft. Current supply to the coil produces a magnetic field across the annular gap, thus influencing the rheological parameters of the MR fluid.

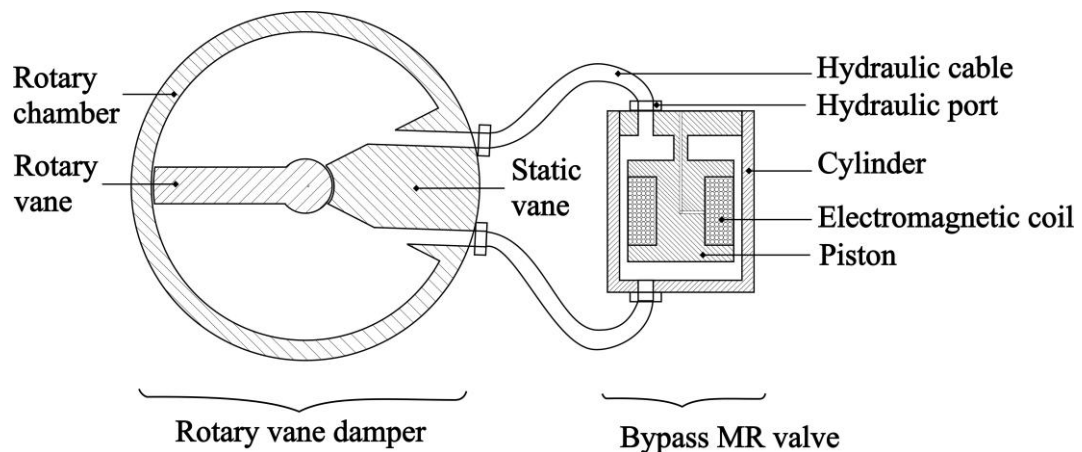


Figure 4.8 Rotary vane MR damper

4.4.1 Design of Rotary Chamber

The geometrical variables of the rotary chamber are shown in Figure 4.9. The resisting torque is produced by the pressure difference between the two separated fluid regions. Neglecting the friction forces due to seals and the flow tube pressure drops, the damping torque can be evaluated using Equation (4.25).

$$T_d = T_\eta + T_\tau \quad (4.25)$$

Here, T_η and T_τ are the off-state torque and the total controllable torque given by Equations (4.26) and (4.27), respectively.

$$T_\eta = \Delta P_\eta A_{vane} R_{vane} \quad (4.26)$$

$$T_\tau = \Delta P_\tau A_{vane} R_{vane} \quad (4.27)$$

Here, ΔP_η is the pressure drop due to viscous forces in the MR valve, ΔP_τ is the pressure drop due to the controllable shear forces, A_{vane} is the cross-sectional area of the rotary vane and R_{vane} is the distance between the centroid of the vane area cross-section and the rotary axis.

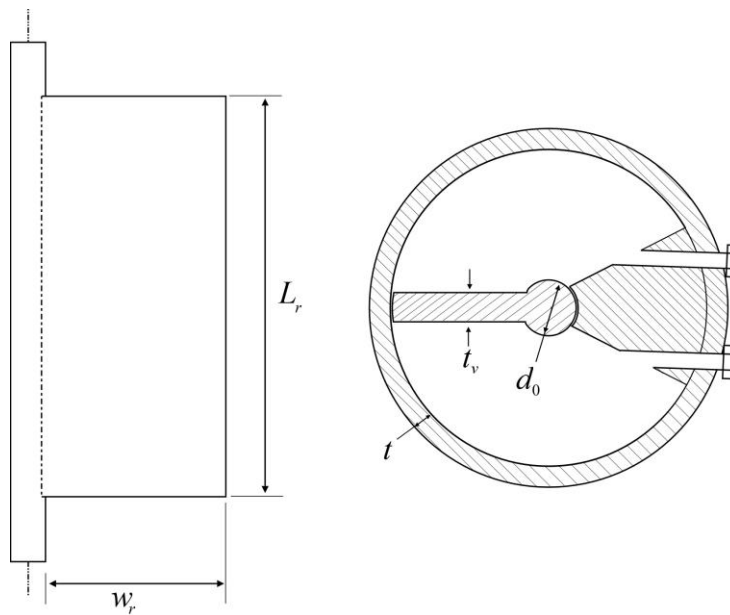


Figure 4.9 Geometry of rotary chamber

Considering Equation (4.27), the component affecting the variability in damping torque is given by ΔP_τ and the geometrical dimensions, A_{vane} and R_{vane} have no effect on it. However, the total damping torque produced is directly proportional to these two parameters. Owing to this proportionality and also to simplify the design process, the geometrical parameters are selected such that the rotary chamber can be contained well within the limits of an average sized human knee. The selected parameters are shown in Table 4.4. The selected dimensions would result in a device of approximately 75 mm \times 70 mm which lies well within the envelope of an average human knee.

The rotary chamber consists of the static and rotary vanes, of which static vane plays no major functional role other than separating the volume into two chambers and allowing hydraulic ports into each of them. During a normal walking, the knee observes a peak flexion between 60° and 70°, and a full range of motion of around 135° can allow the knee to carry out most of the daily activities (Whittle 2007). Therefore, to reduce the overall weight of the rotary chamber, the static vane is assumed to occupy half of the rotary chamber volume and the remaining volume is allowed for the motion of the rotary vane.

Table 4.4. Parameters of rotary chamber

Parameter	Definition	Value (mm)
L_r	Length of rotary vane (along axial direction)	66
w_r	Width of rotary vane (along radial direction)	26
t	Thickness of rotary cylinder	5
d_0	Shaft diameter	8
t_1	Thickness of cylinder cover plate	5
t_v	Thickness of rotary vane	6

The mass of the rotary vane, MRF fluid in the rotary chamber and overall enclosure can be calculated using Equations (4.28) – (4.30), respectively.

$$m_{RotaryVane} = \rho_{RotaryVane} \left[\frac{\pi d_0^2 (L_r + 2t_1)}{4} + w_r L_r t_v \right] \quad (4.28)$$

$$m_{RotaryMRF} = \rho_{MRF} \left\{ \frac{\pi}{2} \left[(0.5d_0 + w_r)^2 - (0.5d_0)^2 \right] L_r - w_r L_r t_v \right\} \quad (4.29)$$

$$m_{Enclosure} = \rho_{Enclosure} \left\{ \begin{aligned} &\pi \left[(0.5d_0 + w_r + t)^2 - (0.5d_0 + w_r)^2 \right] L_r \\ &+ 2\pi t_1 (0.5d_0 + w_r + t)^2 \end{aligned} \right\} \quad (4.30)$$

Here, $\rho_{RotaryVane}$ is the density of rotary vane material, ρ_{MRF} is the density of MR fluid, and $\rho_{Enclosure}$ is the density of the cylinder material. The total mass of the rotary chamber can be estimated using Equation (4.31),

$$M_{rotary} = m_{RotaryVane} + m_{RotaryMRF} + m_{Enclosure} \quad (4.31)$$

The static vane can be made using low density filler materials such as polypropylene along with a hollow structural design and thus its mass is neglected. Note that the static vane can be completely eliminated by using a semicircular cross-section design for the rotary chamber, however for manufacturing ease, a circular cross-section was used.

4.4.2 Design of MR Valve

The cross-sectional view of the MR valve is shown in Figure 4.10. This component consists of a cylinder, piston, cap, and a copper coil. The coil is wound on the piston and the end terminals are pulled out through the piston shaft. The piston and the cap form a single component with a hydraulic port located on the top. Another hydraulic port is located at the bottom of the cylinder. When connected with the rotary chamber, the fluid enters through one port, passes through the fluid gap and leaves the valve through the other port. Any change in magnetic field in the fluid gap affects the rheological parameters of the fluid, thus influencing the resisting torque.

For flow mode condition, the pressure drop due to viscous and controllable forces can be calculated using Equations (4.32) and (4.33),

$$\Delta P_\eta = \frac{12\eta QL_t}{wh^3} \quad (4.32)$$

$$\Delta P_{\tau} = \left(2.07 + \frac{12Q\eta}{12Q\eta + 0.4wh^2\tau_y} \right) \frac{\tau_y L}{h} \quad (4.33)$$

Here, w is the mean circumference of the annular flow path, Q is the flow rate of the fluid in the gap, h is the fluid gap, L is the effective pole length, L_t is the total axial length of the piston, η is the apparent viscosity, and τ_y is the yield strength of the MR fluid.

Neglecting flow tube pressure drop, the fluid flow rate in the annular gap will be equal to the flow rate in the vane chamber and is given by Equation (4.34).

$$Q = A_{vane} R_{vane} \omega \quad (4.34)$$

Here, ω is the rotational velocity of the shaft.

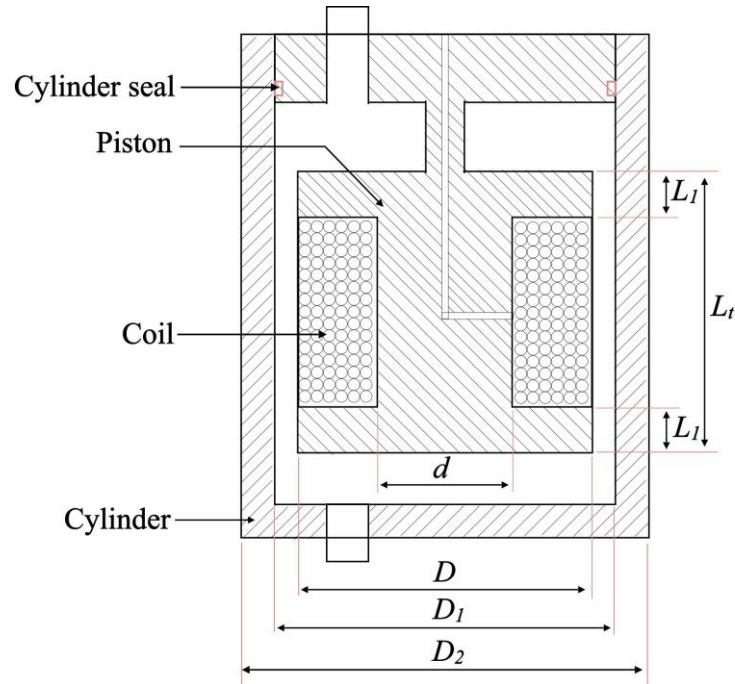


Figure 4.10 MR valve geometry

4.4.3 Electromagnetic Circuit Design

The controllable pressure drop given by Equation (4.33) depends on the yield strength of the MR fluid which is a function of the magnetic flux density in the gap. In the present design of the MR valve, the field produced in the core passes across the

fluid gap, expands through the outer cylinder and returns to the core, thus completing a magnetic circuit. The equivalent model of the MR valve to solve magnetostatic analysis is shown in Figure 4.11(a).

The equivalent magnetic circuit is shown in Figure 4.11(b). In the Figure, R_n represents the reluctance of the respective link, n . Application of Ohm's law to the magnetic circuit yields Equation (4.35).

$$Ni = \Phi \sum_{n=1}^6 R_n \quad (4.35)$$

Here, N is the number of turns of copper coil, i is the current supply to the coil and Φ is the magnetic flux in the circuit.

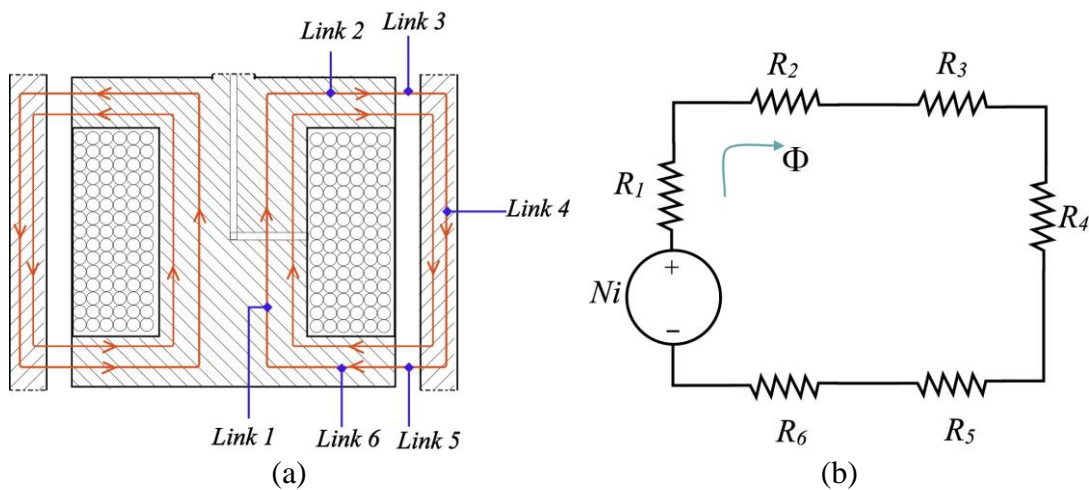


Figure 4.11 (a) Magnetic circuit with equivalent links (b) Equivalent magnetic circuit model

Based on the geometry shown in Figure 4.10, the reluctances of the various links and the number of turns of coil can be calculated using Equations (4.36) to (4.40) (Xu et al. 2013).

$$R_1 = \frac{4L_t}{\pi\mu_1 d^2} \quad (4.36)$$

$$R_2 = R_6 = \frac{\ln(D/d)}{2\pi\mu_1 L_1} \quad (4.37)$$

$$R_3 = R_5 = \frac{\ln(D_1 / D)}{2\pi\mu_{MRF}L_1} \quad (4.38)$$

$$R_4 = \frac{4L_t}{\pi\mu_4(D_2^2 - D_1^2)} \quad (4.39)$$

$$N = \frac{2p_f(D-d)(L_t - 2L_1)}{\pi d_c^2} \quad (4.40)$$

Here, μ_1 and μ_4 are the magnetic permeabilities of the piston and cylinder materials respectively, μ_{MRF} is the magnetic permeability of the MR fluid, p_f is the packing factor and d_c is the diameter of the coil.

Applying the flux conservation rule, the following relations can be obtained. For links 2, 3, 5, and 6, average surface cross-sections are considered. The magnetic flux densities in links 2 and 6 (also in links 3 and 5) are opposite in direction and the following relations calculate only the magnitude of the quantity.

$$B_1 = \frac{4\Phi}{\pi d^2} \quad (4.41)$$

$$B_2 = B_6 = \frac{2\Phi}{\pi(D+d)L_1} \quad (4.42)$$

$$B_3 = B_5 = \frac{\Phi}{\pi(D+h)L_1} \quad (4.43)$$

$$B_4 = \frac{4\Phi}{\pi(D_2^2 - D_1^2)} \quad (4.44)$$

4.4.4 Formulation of MR Valve Mass

The weight of the MR valve includes the combined weight of the piston and cap assembly, copper coil, MR fluid, and the outer cylinder. Here, for the optimization process, the section of the MR valve shown in Figure 4.11(a) is used. The rationale behind this is that the remaining upper and lower sections of the MR valve are approximately an extrusion of this section and any weight minimization of this section

will also affect the weight of the remaining sections resulting in an optimal weight. Although other components such as seals, ports still remain a variable, their role in weight minimization can be safely neglected. Equations (4.45) – (4.48) can be used to calculate the mass of the core, coil, MR fluid and cylinder components.

$$m_{core} = \rho_{core} \frac{\pi \left[D^2 L_t - (D^2 - d^2)(L_t - 2L_1) \right]}{4} \quad (4.45)$$

$$m_{coil} = \rho_c \frac{\pi (D^2 - d^2)(L_t - 2L_1)}{4} \quad (4.46)$$

$$m_{MRF} = \rho_{MRF} \pi (D_1^2 - D^2) L_t \quad (4.47)$$

$$m_{cyl} = \rho_{cyl} \pi (D_2^2 - D_1^2) L_t \quad (4.48)$$

Here, ρ_{core} is the density of the piston core, ρ_c is the density of copper and ρ_{cyl} is the density of cylinder. The total mass is the sum of the individual masses given by Equation (4.49).

$$M = m_{core} + m_{coil} + m_{MRF} + m_{cyl} \quad (4.49)$$

4.4.5 Materials Used in Damper

Relative permeability of the material is one of the key factors affecting the magnetic field strength in the circuit. High damping torque requires a large pressure drop across the piston, which depends on the magnetic flux density in the fluid gap. SAE 1020 material is chosen for both the cylinder and the piston core. Further, in this study, commercial MR fluid, MRF 132DG (Make: Lord Corporation) is used. The fluid specifications provided by Lord Corporation are curve-fit and the approximate polynomial given by Equation (4.50) is used to evaluate the yield stress in the fluid gap (Nguyen et al. 2007). The B-H curves of the fluid, 1018 and 1020 materials are shown in Figure 4.12. It can be seen that materials 1018 and 1020 have similar properties except for the saturation point.

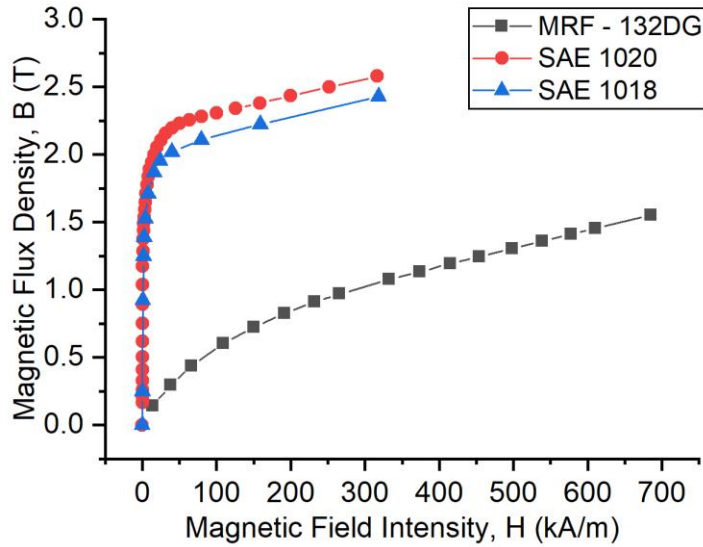


Figure 4.12 B - H curves of SAE 1020, SAE 1018 (Meeker 2009) and MRF – 132DG (Lord Corporation, 2003)

For optimization purposes, a constant relative permeability of 2.78 was used for MRF – 132DG. Also, the magnetic flux density in the fluid gap was assumed to be 0.6 T. Therefore, any design solution should be able to produce this value. After obtaining an optimal solution, a magnetostatic analysis is performed to verify this assumption. The yield stress of the MR fluid (in kPa) at the chosen magnetic flux density is calculated using Equation (4.50) and is listed in Table 4.5 along with other required material properties.

$$\tau_y = 52.962B^4 - 176.51B^3 + 158.79B^2 + 13.708B + 0.1442 \quad (4.50)$$

Table 4.5: Material Properties

Material	Parameter	Value (units)	Units
Air	μ_0	$4\pi \times 10^{-7}$	H/m
SAE 1020	$\rho_{core} (= \rho_{cyl})$	7870	kg/m ³
	$\mu_1 (= \mu_4)$	$800\mu_0$	H/m
Copper	ρ_c	8960	kg/m ³
MRF 132DG	ρ_{MRF}	3640	kg/m ³
	μ_{MRF}	$2.78\mu_0$	H/m
	τ_y (@ 0.6 T)	34.27	kPa

4.4.6 Optimization of MR Valve

The design of rotary vane MR damper should be able to satisfy all the torque requirements of a transfemoral prosthesis user. The maximum torque required by a normal human weighing around 90 kg is approximately 45 Nm in normal walking (Gudmundsson et al. 2010). The selected knee braking torque in most studies is scaled for an average person of mass 56.7 kg and it is around 35 Nm. This general requirement is considered in optimal design studies in Chapters 5 and 6 for an effective comparison among various commercial and literature models. However, the current vane damper design objectives and constraints in this section are kept similar to that of Gudmundsson et al. (2010).

Any external component aiding the prosthetic gait should be able to satisfy this normal torque requirement. Also, the off-state torque should be kept a minimum. In the current design, three objectives are considered: (i) minimization of total off-state torque, (ii) maximization of total on-state torque and (iii) minimization of the mass of the MR valve. The following multi-objective problem is formulated to determine the 6 geometric variables $\{D, d, L_1, L_2, D_2, h\}$.

$$\begin{aligned} \text{Objective function: Minimization of } \{T_n, M\} \text{ and} \\ \text{Maximization of } \{T_\tau\} \end{aligned} \tag{4.51}$$

4.4.6.1 Constraints

In the present study, 24 AWG copper coil is chosen for the electromagnet; this has a diameter, d_c of 0.51 mm. For the present analysis, a maximum current of 2 A is considered.

$$i \leq 2 \text{ A} \tag{4.52}$$

Table 4.6 shows that the magnetic permeabilities of the core and cylinder materials are much larger than that of the MR fluid. Therefore, the magnetic reluctance of the core and cylinder components are much lower compared to that of MR fluid, which implies that they are subjected to larger flux densities. If the flux density reaches the saturation limit of the material, the core will possess some magnetic retentivity and

the MR valve may not perform as intended. Therefore, a saturation limit constraint is imposed for the piston and cylinder materials.

$$B_1, B_2, B_4, B_6 \leq 1.8 \text{ T} \quad (4.53)$$

Table 4.6: Design variables with bounds

Variable	Name	Bounds		Optimized values (mm)
		Lower (mm)	Upper (mm)	
D	Diameter of piston	35	45	36.4
d	Diameter of core	25	30	25.6
$L (= 2L_1)$	Total pole length	15	30	15.3
L_t	Total piston length	20	36	20.8
D_2	Diameter of outer cylinder	40	56	42.1
h	Fluid gap	0.2	1	0.47

The prosthetic knee employed with the vane type MR damper should be able to satisfy the torque requirements of the amputee in both the phases of the gait cycle. The stance phase should offer complete stability to the subject such that the knee should not buckle on loading and therefore, requires a high damping torque. During the swing phase, the knee reaches maximum extension and prepares itself for the next heel strike. This phase requires comparatively less damping. Therefore, the following two constraints are imposed at a considered design speed of 8.4 rpm. Further, these constraints allow the multi-objective optimization to converge on the required particular part of the Pareto front.

$$T_\eta \leq 5 \text{ Nm} \quad (4.54)$$

$$T_r \geq 45 \text{ Nm} \quad (4.55)$$

4.4.7 Multi Objective Genetic Algorithm (MOGA)

The current optimization problem has a 6-dimensional design variable space to achieve 3 objectives. Here, genetic algorithm is utilized to obtain the optimum solution set. The algorithm tries to mimic the natural evolution process in order to solve an optimization problem. The operations such as selection, mutation and cross-over are implemented over each generation to create new population vectors (individuals). The

concept of elitism is applied based on the fitness value of each individual. This process is repeated till a convergence criterion is met. The design variables are provided with bounds listed in Table 4.6. The bounds to these variables are chosen based on the geometrical limitations of the component. A closer look at the bounds indicates that some of the design variables have overlapping bounds. Therefore, the following nonlinear inequalities are applied to avoid any unrealistic designs in MOGA search optimization.

$$L - L_t \leq -\varepsilon \quad (4.56)$$

$$D + 2h - D_2 \leq -\varepsilon \quad (4.57)$$

Here, ε is a small value which is chosen as 1 mm.

Therefore, the MOGA problem is defined as follows: “Minimization of $\{-T_\tau, T_\eta, M\}$ subject to constraints given by Equations (4.54) – (4.57) with the design variables $\{D, d, L_1, L_t, D_2, h\}$ within the bounds specified in Table 4.6.” The optimization is performed in MATLAB software using *gamultiobj* solver. A population size of 50 with a number of generations of 100 was chosen. A bi-tournament selection method, adaptive feasible mutation scheme and a scattered crossover function were selected based on previous optimization studies (Assadsangabi et al. 2011). The remaining options were retained as default values provided by the solver.

4.4.8 Results and Discussion

An objective function and a non-linear constraint function are supplied as inputs to the optimization toolbox in MATLAB software. With conflicting objectives, there can possibly be no single optimum solution for a MOGA problem. The multi-objective optimization problem solves for a set of solutions expected to be the best with regard to all the considered objectives. Figure 4.13(a) shows the optimal Pareto front for the objectives, off-state damping torque, and the total damping torque. It can be observed that the limitation constraints for off-state and total damping torque are totally satisfied. Figure 4.13 (b) shows the optimal front for mass and total damping torque. The results

displayed in Figures 4.13 (a) and 4.13 (b) show a clear trade-off between the three objectives.

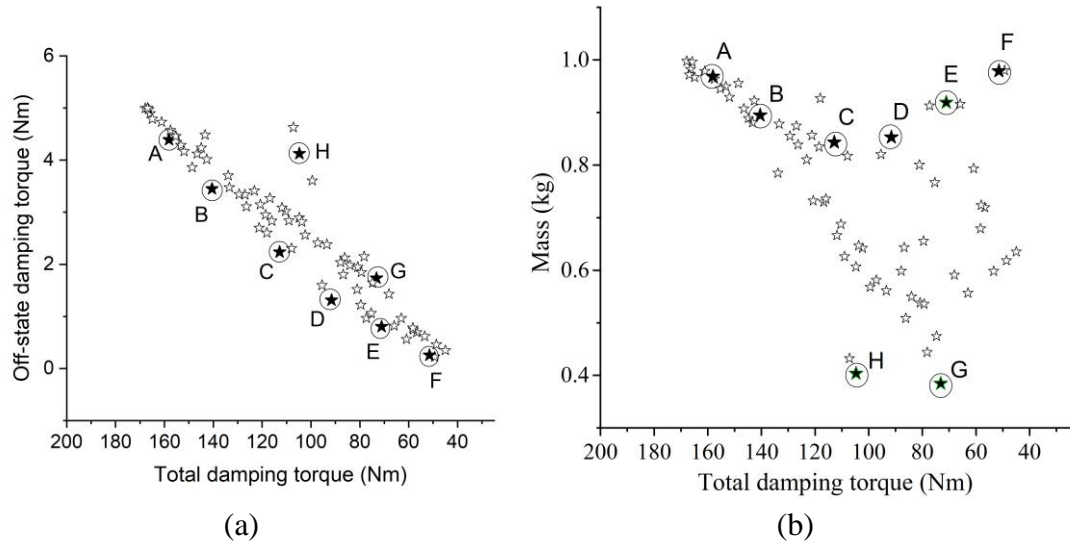


Figure 4.13 Pareto optimal set of (a) off-state and total damping torque and (b) Mass and total damping torque

Many literature studies based on the design of semi-active components like MR brakes or dampers for prosthetic knee application suggest a maximum off-state torque of 2 – 5 Nm at design speeds of 5 – 60 rpm (Gudmundsson et al. 2010; Park et al. 2016; Thorarinsson et al. 2006). Further, the current design of vane-type MR damper needs many other auxiliary components such as batteries, controllers, shank, foot assembly, etc.; hence a higher priority can be assigned to the minimization of the mass of the semi-active device. Based on this, the design solution represented by point *G* in Figure 4.13 is chosen as the optimal one. Note that point *H* offers more than 40% increase in total damping torque with a marginal increase of just 5% in weight. However, off-state braking torque is also increased by more than 200% compared to point *G*. The optimized values of the design variables represented by the point *G* are listed in Table 4.7.

The optimal mass of the MR valve is obtained as 0.38 kg. However, this is the mass of the section of the MR valve shown in Figure 4.11 (a). Unlike MR dampers, the piston in the MR valve has no stroke and the top and bottom covers of the MR valve can be kept as small as possible since the seals or thick guide ways for the piston rod are unnecessary. The primary function of the rotary chamber is to contain the MR fluid,

although the device must be able to withstand large pressure differences. The optimal design can provide a braking torque up to 73 Nm at the design speed and at a current of 1.9 A. Using Equations (4.25) – (4.27) and the optimal design parameters, the pressure differences in the rotary chamber can be calculated up to 24 bar. Based on thin shell pressure theory, a cylinder thickness of 4 mm can easily withstand this pressure assuming that the cylinder and rotary vane are made of aluminum material. Further, the total mass of the vane damper which is the sum of rotary chamber mass, given by Equation (4.31) and the optimal MR valve mass of 0.35 kg can be estimated to be around 1 kg. The weights of hydraulic ports, cables, seals are not taken into account due to uncertainty.

4.4.9 Magnetostatic Analysis

To verify the assumed magnetic flux density of 0.6 T in the gap, a magnetostatic analysis of the axisymmetric model of the piston and cylinder arrangement is carried out. The optimization is carried out using relative permeabilities of the materials employed, but in reality the materials show nonlinear B-H curves. The B-H curves of 1020 steel and that of MR fluid are shown in Figure 4.12. An axisymmetric model shown in Figure 4.14 (a) is modeled using FEMM software (Meeker 2009). For the given geometry and using Equation (4.40), the number of turns is calculated as 116. A current supply of 1.9 A is specified. The surrounding MR fluid above and below the piston is also modeled to simulate any flux leakages.

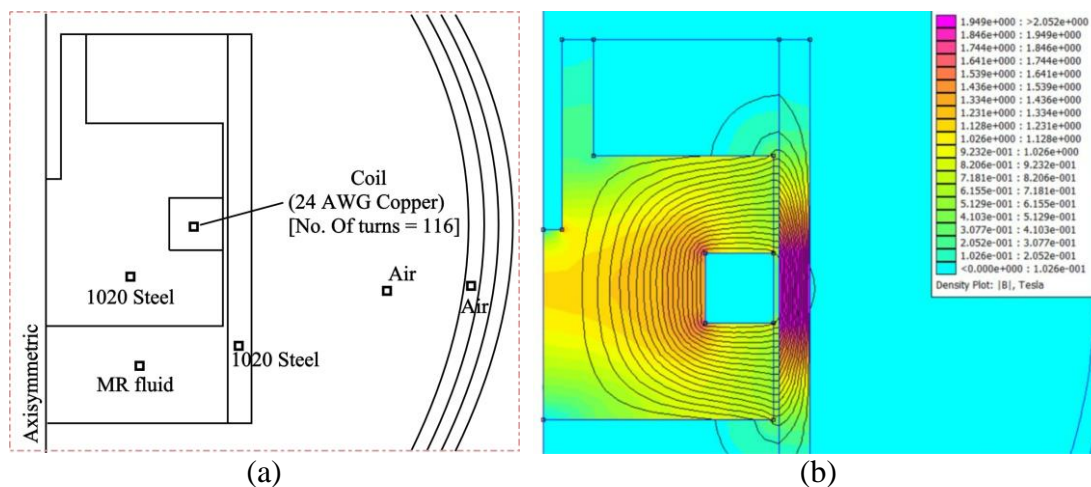


Figure 4.14 (a) Axisymmetric model of piston assembly and (b) Contours of magnetic flux densities

As seen in Figure 4.14 (b), the magnetic flux density turned out to be 0.58 T which is very close to the assumed value of 0.6 T. However the magnetic flux densities in the outer cylinder reach a value of 2.0 T crossing the set limitation of 1.8 T. This may not pose a problem since the saturation density of 1020 steel is as high as 2.3 T. Therefore, it is verified that the present design process produces a necessary magnetic flux density in the fluid gap.

The braking torque is directly proportional to the vane dimensions of the rotary cylinder and owing to this proportionality, the largest possible dimensions were selected for the same. Previous studies show that the flow mode MR valves are capable of achieving large damping force to weight ratio. Therefore, it is hypothesized that a design optimization problem combining the rotary cylinder and the MR valve can yield much better results and a reduction in weight, and thus an optimal design and experimentation will be carried out for this design configuration in the subsequent chapters.

4.5 INVERTED DRUM WAVEFORM ARC MR BRAKE

The rotary brake consists of more than one magnetic loop and thus considering EMM method will result in inaccurate magnetic flux densities in the gap, thus O-EMM methodology is not considered for this design. Also, optimization based on data driven modeling requires a large amount of data to fit a reasonably accurate data driven model. Therefore, O-COM methodology is considered for the present design configuration.

The structure of the proposed inverted drum brake with waveform arc boundary is shown in Figure 4.15 (a). The inverted drum brake consists of an inverted drum rotor which accommodates an electromagnetic coil around its hub. MR fluid is filled in the gap between the rotor and the casing. Magnetic field lines cross both the radial and the annular faces of the rotary drum and thus MR effect occurs in both these regions. In this study, the annular face of the rotary drum is provided with a waveform arc boundary as shown in Figure 4.15 (b). Owing to this surface texture, many local MR zones are formed and braking torque is produced from not just the shear effect, but a hybrid effect resulting from crushing of magnetic fibrils together.

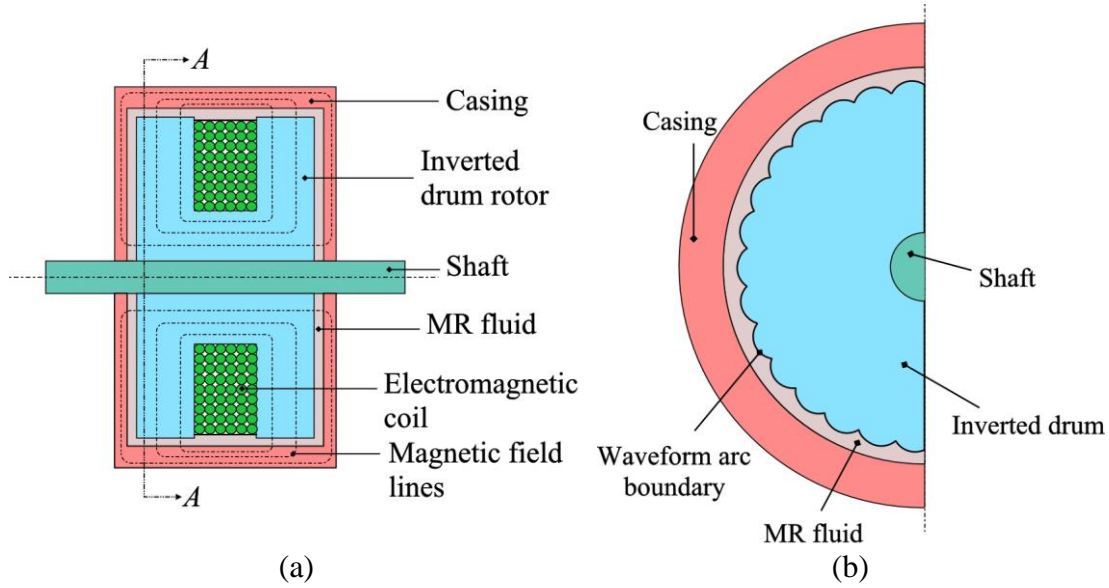


Figure 4.15 (a) Cross-sectional view of inverted drum MR brake and (b) Section view of A-A showing waveform arc boundary

4.5.1 Waveform Arc Parameters

The geometrical parameters of the inverted drum brake are shown in Figure 4.16. In the present design of waveform brake, four other geometrical parameters which are N_{arc} , r_{arc} , α and h_1 also need to be defined. The interdependency among these parameters varies with the geometric configuration of the arc. The maximum number of smaller circles that can be inscribed in a circle being tangential to each other can be calculated using Equation (4.58),

$$N_{\max} = \frac{\pi}{\sin^{-1}\left(\frac{r_{arc}}{r_1 - r_{arc}}\right)}, \quad r_{arc} < 0.5r_1 \quad (4.58)$$

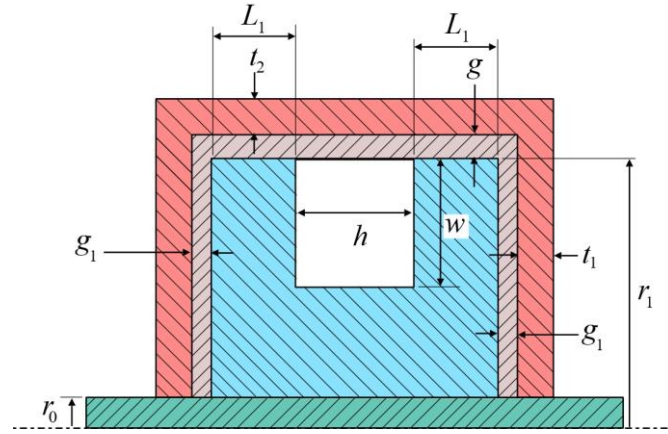


Figure 4.16 Geometrical parameters of inverted rotary drum brake

Based on the number of circumferential arcs, the following four cases can be defined.

$$\text{Case 1: } N_{arc} = N_{max}$$

The following parametric relations can be derived using the geometry in Figure 4.17 (a).

$$\sin\left(\frac{\pi}{N_{arc}}\right) = \frac{r_{arc}}{r_1 - r_{arc}} \quad (4.59)$$

$$h_1 = r_1 + g - \sqrt{r_1^2 - 2r_1 r_{arc}} \quad (4.60)$$

$$\alpha = \pi - \cos^{-1}\left(\frac{r_{arc}}{r_1 - r_{arc}}\right) \quad (4.61)$$

$$\text{Case 2: } N_{arc} < N_{max}$$

In this case, the number of arcs is an independent parameter and requires any two parameters out of $\{r_{arc}, \alpha, h_1\}$ to be defined. The following parametric relations can be derived using the geometry in Figure 4.17 (b).

$$\sin(\alpha - \theta) = \frac{r_1 - r_{arc}}{r_{arc}} \sin \theta \quad (4.62)$$

$$\cos \alpha = \frac{r_1 + g - h_1}{r_{arc}} \sin \theta \quad (4.63)$$

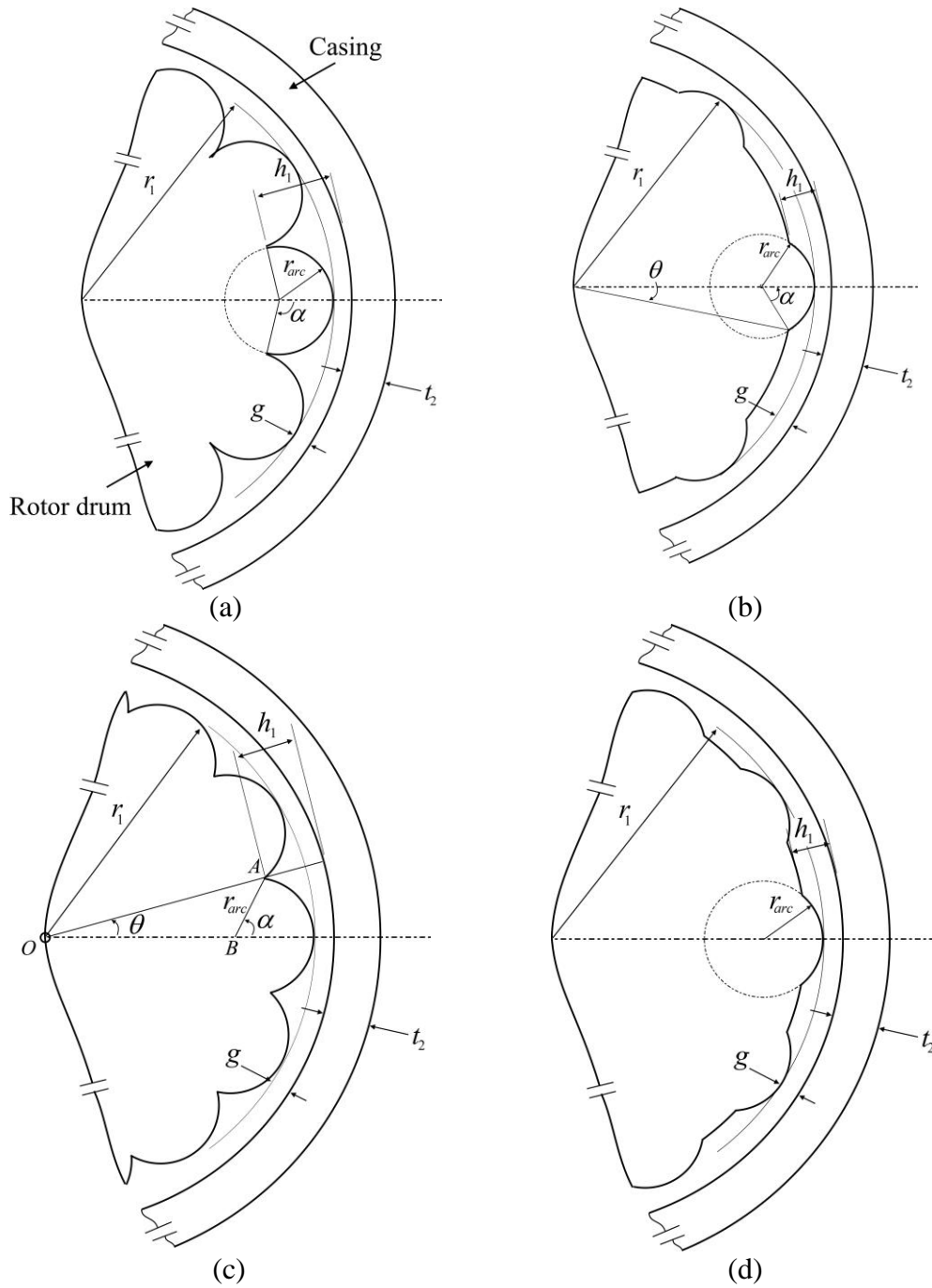


Figure 4.17 Various waveform arc boundary configurations of MR brake

Case 3: $N_{arc} > N_{max}$

This configuration is shown in Figure 4.17 (c) and the following parametric relations can be defined.

$$\theta = \frac{\pi}{N_{arc}} \quad (4.64)$$

$$\alpha = \sin^{-1} \left(\frac{r_1 - r_{arc}}{r_{arc}} \sin \theta \right) + \theta \quad (4.65)$$

$$h_1 = r_1 + g - \sqrt{(r_1 - r_{arc} + r_{arc} \cos \alpha)^2 + (r_{arc} \sin \alpha)^2} \quad (4.66)$$

Case 4: Other configurations may also be achieved by setting h_1 as an independent parameter like the one shown in Figure 4.17 (d). This configuration is similar to Case 1 with $h_1 < r_1 + g - \sqrt{r_1^2 - 2r_1r_{arc}}$. The slit angle, α can be derived based on the geometry.

In the waveform configuration many localized MR zones are created with relatively high magnetic field being concentrated on the convex part of each arc than at the intersection of two arcs. The total resistance torque is directly proportional to the number of arcs on the surface. Since a mean value of surface shear stress is considered, waveform configuration in case 3 can be shown to produce better average magnetic field on the radial surface when compared to case 1. This is due to the reason that the slit angle in case 1 is greater than 90° and owing to low permeability of the MR fluid, the magnetic flux concentrates on the convex hull of the waveform producing dispersed magnetic field lines across the arc. Further, case 2 and 4 configurations result in a lesser number of waveform arcs compared to the other two cases. Therefore, in this design, waveform arc configuration shown in case 3 is considered for further analysis with N_{arc} being the only parameter to be defined. To reduce variables in the optimization process, the radius of arc is chosen as $0.3r_1$ similar to that in previous studies (Mousavi and Sayyaadi 2018; Nam and Ahn 2009).

4.5.2 Mathematical Formulation

The total braking torque is calculated from the forces resulting from two main components. A mathematical proof in deriving the forces is presented by Nam and Ahn (2009). The first component is a result of formation of localized MR zones and to create motion, a critical minimum value is required to break the hardened MR zone. The total drawing force which is a function of the variable yield stress of the MR fluid is calculated using a slab method based on the theory of plasticity. Assuming the surface

shear stress, k to have a mean value equal to the yield stress of the MR fluid at a particular magnetic field ($\bar{k} = \tau_y(B)$), the total drawing force per unit width of the drum can be calculated using Equation (4.67),

$$F_{draw} = qr_{arc}(1 - \cos \alpha) + \frac{\pi}{2} r_{arc} \bar{k} (\cos \alpha - 1) - c\alpha r_{arc} \bar{k} + \frac{\pi}{2} r_{arc} \bar{k} c \ln \left(\frac{c - \cos \alpha}{c - 1} \right) + \frac{2r_{arc} \bar{k} c^2}{\sqrt{(c-1)(c+1)}} \tan^{-1} \left(\sqrt{\frac{c+1}{c-1}} \tan \frac{\alpha}{2} \right) \quad (4.67)$$

Here,

$$c = \left(\frac{g}{r_{arc}} + 1 \right) \quad (4.68)$$

$$q = \left(\frac{\pi}{2} - \alpha \right) \bar{k} + \frac{\pi}{2} \bar{k} \ln \left(\frac{r_{arc} (c - \cos \alpha)}{g} \right) + \frac{2c\bar{k}}{\sqrt{(c-1)(c+1)}} \tan^{-1} \left(\sqrt{\frac{c+1}{c-1}} \tan \frac{\alpha}{2} \right) \quad (4.69)$$

The second component is due to the hydrodynamic resistance forces which act when the MR fluid prevents the arc from moving inside it. A Bingham plastic model for the MR fluid is assumed with the following characteristic stress-strain relation.

$$\tau = \tau_y(B) + \eta \dot{\gamma} \quad (4.70)$$

Here, $\tau_y(B)$ is the magnetic flux dependent yield stress, η is the plastic viscosity and $\dot{\gamma}$ is the shear rate. For a single arc on the rotor, the resistance force due to Coulomb and viscous shear stress (per unit width) can be calculated using the Equations (4.71) and (4.72) respectively.

$$F_\tau = \tau_o(B) l_{max} \quad (4.71)$$

$$F_\eta = 16\eta r_{arc} r_1 \omega \left[\frac{1}{\sqrt{A_1}} \tan^{-1} \left(\frac{l_{max}}{\sqrt{A_1}} \right) \right] - 12\eta r_{arc} r_1 \omega A \left[\frac{l_{max}}{2AA_2} + \frac{1}{2A_1^{1.5}} \tan^{-1} \left(\frac{l_{max}}{\sqrt{A_1}} \right) \right] \quad (4.72)$$

Here, ω is the rotational speed. The parameters, l_{\max} , A_1 , A_2 and A are defined by Equations (4.73) to (4.76) respectively.

$$l_{\max} = r_{arc} \sin \alpha \quad (4.73)$$

$$A_1 = 2r_{arc} g \quad (4.74)$$

$$A_2 = 2r_{arc} g + l_{\max}^2 \quad (4.75)$$

$$A = \frac{\left[\frac{l_{\max}}{2A_1 A_2} + \frac{1}{2A_1^{3/2}} \tan^{-1} \left(\frac{l_{\max}}{\sqrt{A_1}} \right) \right]}{\left[\frac{3l_{\max}}{8A_1^2 A_2} + \frac{l_{\max}}{4A_1 A_2^2} + \frac{3}{8A_1^{5/2}} \tan^{-1} \left(\frac{l_{\max}}{\sqrt{A_1}} \right) \right]} \quad (4.76)$$

The total resistance force per unit width produced by a single annular arc is the sum of drawing and the hydrodynamic forces given by Equation (4.77),

$$F = F_{draw} + F_{\tau} + F_{\eta} \quad (4.77)$$

The total braking torque produced by the annular gap region can be calculated using Equation (4.78),

$$T_A = \varepsilon w_{arc} N_{arc} r_1 F \quad (4.78)$$

Here, ε is the effective coefficient and w_{arc} is the total width of the annular pole region, which is equal to $2L_1$. The effective coefficient is the percentage of hardened MR fluid in the MR zone which contributes to the resistance force. A value of 0.8 is considered, which is shown to produce good correlation between the experimental and the analytical results (Mousavi and Sayyaadi 2018; Nam and Ahn 2009).

The torque due to the radial surface on either side of the drum brake can be derived in a manner similar to that in previous studies (Nguyen et al. 2015; Nguyen and Choi 2010). The on-state torque on each radial surface is given by Equation (4.79).

$$T_{rad} = \frac{2\pi}{3} (r_1^3 - r_0^3) \tau_r (B) + \frac{\pi\omega\eta}{2g_1} (r_1^4 - r_0^4) \quad (4.79)$$

Here, $\tau_r(B)$ is the average magnetic field in the radial gap. The total on-state resisting torque produced by the brake can be calculated using Equation (4.80),

$$T_{total_ON} = T_A + 2T_{rad} + T_b + T_O \quad (4.80)$$

Here, T_b is the friction in the bearings and T_O is the friction torque due to seals. At a design speed of 8.4 rpm, the torque due to bearings and seals is chosen as 0.8 Nm each (Gudmundsson et al. 2010). In the off-state, when no current is supplied to the brake, the total torque produced can be calculated using Equation (4.81),

$$T_{total_OFF} = w_{arc} N_{arc} r_1 F_\eta + 2 \times \left[\frac{\pi \omega \eta}{2g_1} (r_1^4 - r_0^4) \right] + T_b + T_O \quad (4.81)$$

Weight of the MR brake is another important feature which affects the prosthetic device's ability to assist the amputee. Since the complete assembly contains various other important components such as batteries, electronic circuits, shank and foot assembly etc., the weight of the MR brake should be kept as low as possible. The weight of the proposed brake includes the weight of the rotary drum, MR fluid, outer casing and the coil. To simplify calculation of weight, the waveform arcs on the rotary drum are neglected and a smooth radius of r_1 is assumed. The volume of the rotary drum, MR fluid, outer casing and the coil can be calculated using Equations (4.82) – (4.85) respectively.

$$V_{rotarydrum} = \pi r_1^2 (2L_1 + h) + \pi r_0^2 (2t_1) - \pi h \left[r_1^2 - (r_1 - w)^2 \right] \quad (4.82)$$

$$V_{MR} = 2g_1 \pi \left[(r_1 + g)^2 - r_0^2 \right] + \pi \left[(r_1 + g)^2 - r_1^2 \right] (2L_1 + h) \quad (4.83)$$

$$V_{coil} = \pi h \left[r_1^2 - (r_1 - w)^2 \right] \quad (4.84)$$

$$V_{casing} = \pi (r_1 + g + t_2)^2 \left[2L_1 + h + 2(g_1 + t_1) \right] - V_{rotarydrum} - V_{MR} - V_{coil} \quad (4.85)$$

The total mass of the proposed brake can be calculated using Equation (4.86),

$$M = \rho_c V_{casing} + \rho_r V_{rotarydrum} + \rho_{MR} V_{MR} + \rho_{coil} V_{coil} \quad (4.86)$$

Here, ρ_c is the density of the casing material, ρ_r is the density of the rotary drum material, ρ_{MR} is the density of MR fluid, and ρ_{coil} is the density of the coil. The maximum electrical power consumed by the brake can be calculated using Equation (4.87).

$$P_e = \frac{4I^2 N \bar{d}_c r_c}{d_c^2} \quad (4.87)$$

Here, N is the number of turns of coil, \bar{d}_c is the average diameter of the coil cross-sectional area, r_c is the resistivity of coil and d_c is the diameter of the coil.

4.5.3 Optimization Problem Formulation

The proposed MR brake is designed for a prosthetic knee application. Previous studies based on design optimization of semi-active devices for prosthetic knee application used various combinations of objectives which are on-state torque, off-state torque, dynamic range, power consumption and mass. Since design speeds are low in the prosthetic domain and also since the current design has very low shearing area compared to other multi-plate brakes, there was no significant change observed in off-state torque within the proposed design bounds. In this design, maximization of total on-state torque and minimization of the mass of the brake are chosen as the two objectives. Since the proposed MOPSO algorithm is developed for a minimization problem, the overall minimization optimization problem is defined as follows:

$$\text{Minimize: } \frac{1}{1 + T_{total_ON}} \text{ and } M \quad (4.88)$$

Subjected to constraints:

$$B_{\max} \leq 1.8 \text{ T} \quad (4.89)$$

$$M \leq 1 \text{ kg} \quad (4.90)$$

$$T_{total_OFF} \leq 2 \text{ Nm} \quad (4.91)$$

The chosen design variables are $\{w, h, L_1, r_1, t_1, t_2, N_{arc}\}$ and are listed in Table 4.7 along with the bounds. The bounds are chosen such that the overall brake lies within

the envelope of a normal human knee. The materials chosen for the individual components are listed in Table 4.8. The core material will be subjected to larger magnetic flux densities compared to MR fluid and thus may reach saturation. Therefore, a saturation limit constraint of 1.8 T is imposed on the problem. Further, the total mass of the brake and the total off-state torque are constrained to lie within 1 kg and 2 Nm respectively. These values are set to make the device suitable for a prosthetic knee application. It should be noted that mass is applied as a constraint too so as to obtain the specific part of the Pareto front. The constant design parameters are listed in Table 4.9. A larger radial gap, g_1 is considered to reduce the off-state torque produced by the brake.

4.5.4 Finite Element Method Magnetics

The constrained MDPL-MOPSO code is implemented in MATLAB software and FEMM is communicated for all the non-dominated solutions found at each iteration using OctaveFEMM interface (Meeker 2010). The geometry of the cross-section of the brake at the largest rotor radius as shown in Figure 4.18 (a) is parameterized in terms of optimization design variables. The boundary radius, L_T is considered as the maximum of $\{r_2 + 10 \text{ mm}, L + 10 \text{ mm}\}$. The material properties of SAE 1020, SS 304 stainless steel, air and copper are invoked from FEMM’s material library and for MRF – 132DG, they are supplied using the manufacturer’s data (“Lord Corporation” 2001).

Table 4.7: Design variables and their bounds

Parameter	Name	Bounds	
		Lower	Upper
w	Width of coil (mm)	4	15
h	Height of coil (mm)	4	20
L_1	Pole length (mm)	3	20
r_1	Radius of rotor (mm)	20	40
t_1	Axial thickness of casing (mm)	2	10
t_2	Radial thickness of casing (mm)	3	10
N_{arc}	Number of waveform arcs	10	25

Table 4.8: Materials of the components

Component	Material
Inverted drum rotor, Casing	SAE 1020
Shaft	SS 304 steel
Coil	24 AWG copper coil
MR fluid	Lord MRF – 132 DG

Table 4.9: Constant design parameters

Parameter	Name	Value (units)
r_0	Shaft radius	4 (mm)
g	Annular fluid gap	0.2 (mm)
g_1	Radial fluid gap	1 (mm)
μ_0	Permeability of air	$4\pi \times 10^{-7}$ (H/m)
μ_{1020}	Magnetic permeability of 1020 steel	$760\mu_0$ (H/m)
μ_{MRF}	Magnetic permeability of MR fluid	$3.9\mu_0$ (H/m)

The number of turns of coil is calculated using Equation (4.92).

$$N = \frac{4p_f wh}{\pi d_c^2} \quad (4.92)$$

Here, p_f is the packing factor. The diameter of the copper coil of 24 AWG gage is around 0.511 mm.

In each function call, FEMM determines the average magnetic flux densities in radial and annular gaps. Magnetic flux densities at each node are calculated and a maximum value is found. To reduce the computational load, nodes on only the top half of the axisymmetric model are considered. Further, the maximum flux density is expected to occur in the core material and thus nodes with their Cartesian coordinates in the range of $x \leq (r_1 + g + t_2)$ and $y \leq (L_1 + h + g + t_1)$ are only considered. Each call to FEMM module ends with the return of the three required flux densities to the main MOPSO function.

4.5.5 Equivalent Magnetic Circuit Method

An equivalent magnetic circuit model of the axisymmetric model of the brake is shown in Figure 4.18 (b). Applying Ohm's law around the three loops in Figure 4.18 (c) and also considering the flux conservation rule, Equation (4.93) can be obtained.

$$R\Phi = F \quad (4.93)$$

Here, R is the reluctance matrix, Φ is the magnetic flux vector and F is the equivalent electro motive force vector and are evaluated using Equations (4.94) – (4.96).

$$\Phi = \{\phi \quad \phi_1 \quad \phi_2 \quad \phi_3 \quad \phi_4\}^T \quad (4.94)$$

$$F = \{Ni \quad 0 \quad 0 \quad 0 \quad 0\}^T \quad (4.95)$$

$$R = \begin{bmatrix} R_1 + R_5 & 0 & \begin{pmatrix} R_9 + R_{10} \\ +R_{14} \end{pmatrix} & \begin{pmatrix} R_{12} + R_{11} \\ +R_{15} \end{pmatrix} & 0 \\ 0 & \begin{pmatrix} R_{13} + R_2 + \\ R_3 + R_4 \end{pmatrix} & -\begin{pmatrix} R_9 + R_{10} \\ +R_{14} \end{pmatrix} & 0 & 0 \\ 0 & 0 & 0 & -\begin{pmatrix} R_{12} + R_{11} \\ +R_{15} \end{pmatrix} & \begin{pmatrix} R_6 + R_7 + \\ R_8 + R_{16} \end{pmatrix} \\ 1 & -1 & -1 & 0 & 0 \\ 1 & 0 & 0 & -1 & -1 \end{bmatrix} \quad (4.96)$$

The reluctance of the links in the vertical direction can be calculated using Equation (4.97),

$$R_i = \frac{a_i}{\pi b_i \mu_i}, \quad i = 1, 2, 4, 5, 6, 8, 13, 16 \quad (4.97)$$

The values of a_i , b_i and μ_i can be determined against the link, i from Table 4.10. The reluctances of the links in the horizontal direction can be calculated using Equation (4.98),

$$R_j = \frac{\ln\left(\frac{a_j}{b_j}\right)}{2\pi c_j \mu_j}, \quad j = 3, 7, 9, 10, 11, 12, 14, 15 \quad (4.98)$$

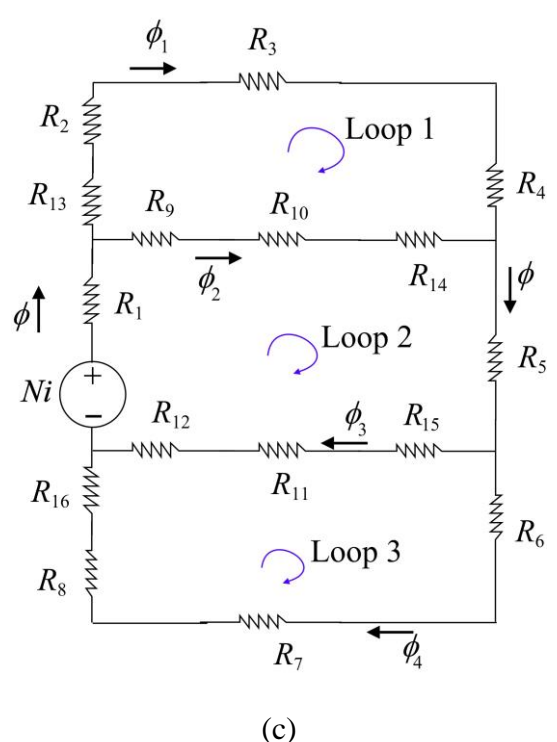
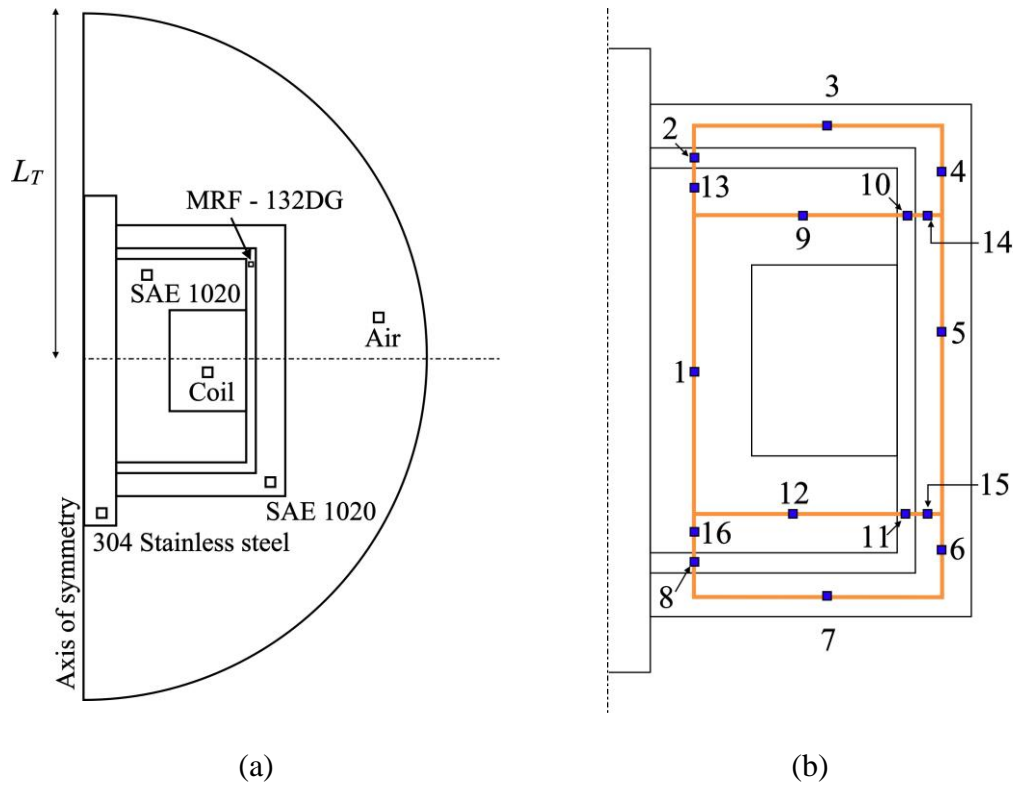


Figure 4.18 (a) FEMM model, (b) axisymmetric model with equivalent links and (c) lumped parameter equivalent magnetic circuit model

The values of a_j, b_j, c_j and μ_j can be determined against the link, j from Table 4.11. Solving Equation (4.93), the flux in the circuit can be determined. Subsequently, the magnetic flux densities in the annular and the radial MR gaps can be calculated using Equations (4.99) - (4.100) respectively,

$$B_2 = \frac{\phi_1}{A_2} \quad (4.99)$$

$$B_{10} = \frac{\phi_2}{A_{10}} \quad (4.100)$$

Here, A_2 and A_{10} are cross-sectional areas of links 2 and 10 respectively. The maximum flux density can be calculated using Equation (4.101),

$$B_{\max} = \max \{B_m\}, \quad m = 1, 2, 3, \dots, 16 \quad (4.101)$$

Table 4.10: Variables for vertical equivalent links.

Link	a_i	b_i	μ_i
1	$L_1 + h$	$(r_1 - w)^2 - r_0^2$	μ_{1020}
2	g_1	$(r_1^2 - r_0^2)$	μ_{MRF}
4	$0.5(L_1 + t_1) + g_1$	$(r_1 + g + t_2)^2 - (r_1 + g)^2$	μ_{1020}
5	$L_1 + h$	$(r_1 + g + t_2)^2 - (r_1 + g)^2$	μ_{1020}
6	$0.5(L_1 + t_1) + g_1$	$(r_1 + g + t_2)^2 - (r_1 + g)^2$	μ_{1020}
8	g_1	$(r_1^2 - r_0^2)$	μ_{MRF}
13	$0.5L_1$	$(r_1^2 - r_0^2)$	μ_{1020}
16	$0.5L_1$	$(r_1^2 - r_0^2)$	μ_{1020}

Table 4.11: Variables for horizontal equivalent links

Link	a_j	b_j	c_j	μ_j
3	$r_1 + g + 0.5t_2$	$r_0 + 0.5(r_1 - w - r_0)$	t_1	μ_{1020}
7	$r_1 + g + 0.5t_2$	$r_0 + 0.5(r_1 - w - r_0)$	t_1	μ_{1020}
9	r_1	$r_0 + 0.5(r_1 - w - r_0)$	L_1	μ_{1020}
10	$r_1 + g$	r_1	L_1	μ_{MRF}
11	$r_1 + g$	r_1	L_1	μ_{MRF}
12	r_1	$r_0 + 0.5(r_1 - w - r_0)$	L_1	μ_{1020}
14	$r_1 + g + 0.5t_2$	$r_1 + g$	L_1	μ_{1020}
15	$r_1 + g + 0.5t_2$	$r_1 + g$	L_1	μ_{1020}

4.5.6 Results and Discussion

With the proposed methodology, the optimization of the MR brake with waveform is performed. The parameters chosen are a population count of 50, number of generations as 100, external archive population of 30 and number of grids as 50. The Pareto front in objective workspace is shown in Figure 4.19.

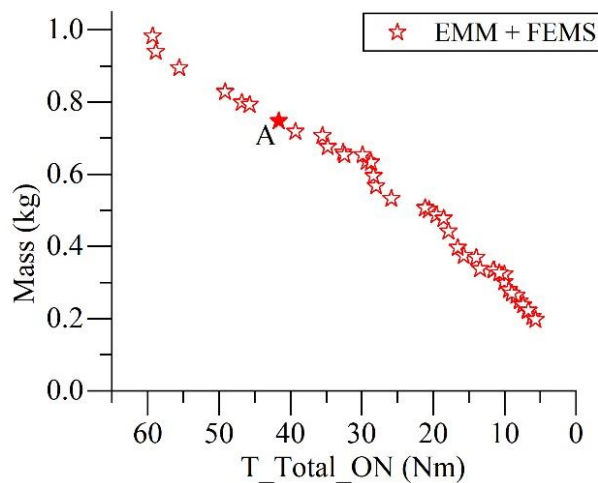


Figure 4.19 Pareto front showing non-dominated solutions

The conflicting nature of the objectives is clearly visible in the front and point A is chosen as the optimal individual among all the feasible points. The optimal

dimensions of the waveform arc rotary brake are listed in Table 4.17. The optimized values of objectives are an on-state braking torque of 41.9 Nm, mass of 0.76 kg. The power dissipation for the selected design calculated using Equation (4.86) is 1.23 W.

Table 4.12: Optimal dimensions of waveform inverted rotary brake

Parameter	Name	Optimal dimensions
w	Width of coil (mm)	10.9
h	Height of coil (mm)	3.7
L_1	Pole length (mm)	6
r_1	Radius of rotor (mm)	35
t_1	Axial thickness of casing (mm)	2
t_2	Radial thickness of casing (mm)	3
N_{arc}	Number of waveform arcs	25

The optimization process was repeated considering power consumption as the third objective, however since no significant reduction in objective values (total on-state torque and mass) was observed. Therefore, the optimal design of MR brake can produce an on-state braking torque of 41.9 Nm with a mass of 0.76 kg and is found to be suitable to satisfy the knee braking torque requirements of an amputee. However, the least fluid gap tolerance in this design configuration is 0.2 mm which may result in relatively higher shear rates as compared to other two selected design configurations (twin rod MR damper and rotary vane MR damper). Further, in the study by Nam and Ahn (2009), they have proposed the mathematical modeling of the waveform arc MR brake and have assumed many parameters such as arc ratio and effective coefficient, ε . The selection of values for effective coefficient and arc ratio needs further research. Also, it is expected that the unconventional fluid mode of operation, which is crushing of magnetic fibrils, may cause particle distortion due to the assumed deformation of metal mechanism. Therefore, this design has many issues to be addressed before it actually can be considered for an optimal design. However, the present design configuration of inverted drum type results in the reduction of electromagnetic coils which further reduces the power dissipation and also generates higher braking torque compared to the T shaped rotor design by Mousavi and Sayyaadi (2018).

4.6 SUMMARY

In the present chapter, four design configurations namely, multi-pole MR brake, twin rod MR damper, rotary vane MR damper and inverted drum MR brake with waveform boundary are considered for a preliminary design task. The multi-pole MR brake was designed using optimization based on data driven modeling methodology. The twin rod MR damper and rotary vane MR damper are designed using O-EMM methodology and the inverted drum MR brake was designed using O-COM methodology. Table 4.13 lists the various parametric comparisons for the preliminary design configurations.

Table 4.13: Preliminary design configuration assessment

Variable	Braking torque ($T > 35$ Nm)	Mass ($m < 1$ kg)	Status
Twin rod MR damper	Yes	Yes	Accepted for further testing
Inverted waveform MR brake	Yes	Yes	Requires further research to determine effect of various design parameters and thus is rejected for further testing.
Rotary vane damper	Yes	Yes	Accepted for further testing
Multi-pole MR brake	No ($T = 14$ Nm)	No ($m > 2$ kg)	Rejected

Based on the results, the multi-pole MR brake and the inverted waveform MR brake are rejected for further optimal design and experimentation.

CHAPTER 5

DESIGN, FABRICATION AND CHARACTERIZATION OF TWIN ROD MR DAMPER

5.1 INTRODUCTION

A twin rod MR damper is a type of linear damping device with piston rods on both ends of the piston. This configuration compensates for the volumetric changes occurring in the cylinder due to the movement of the piston, thus avoiding the use of an accumulator. Also, removal of the accumulator reduces the damper size, complexity and weight. Before considering an optimal design, an initial prototype of a twin rod MR damper has been fabricated and tested so as to obtain a few insights into the working of the damper.

5.2 INITIAL PROTOTYPE OF TWIN ROD MR DAMPER

A twin rod MR damper operating in shear mode is fabricated first. Shear mode as the initial design prototype is considered primarily due to its simplicity. This configuration allows the piston and piston rod to be fabricated out of a single block. The MR damper consists of inner and outer cylinders, piston, piston sleeve, copper coil, piston rods and seals of various kinds. A copper coil is wound on the web of the piston and is protected by a thin aluminum sleeve on the outside. The sleeve protects the coil from getting in contact with the fluid and also prevents leakages through the piston through-hole. Aluminum as a material for the sleeve is chosen because of its low permeability. The piston is connected to piston rods on both sides and the terminals of the coil are extracted from the hole in one of the piston rods. The piston is contained inside the inner cylinder which is filled with an MR fluid. To prevent leakage of the fluid, piston and cylinder seals are accommodated on the cylinder cap. The outer cylinder is simply an attachment used for further characterization of the damper, while it also helps provide free space for one of the piston rods to move. The geometric variables and the cross-section of the MR damper are shown in Figure 5.1.

A damper is fabricated using the parameters listed in table 5.1. A total of 500 turns of copper coil of wire gauge 24 are wound on the web of the piston and the sleeve is press-fit. The outer dimensions of the damper are selected based on the normal human knee size and shape constraints and the dependent variables such as number of turns of coil, wire gage of coil, gap size, etc. are determined based on the outer geometry of damper and also using the previously published literature. The fabricated prototype damper components are shown in Figure 5.2.

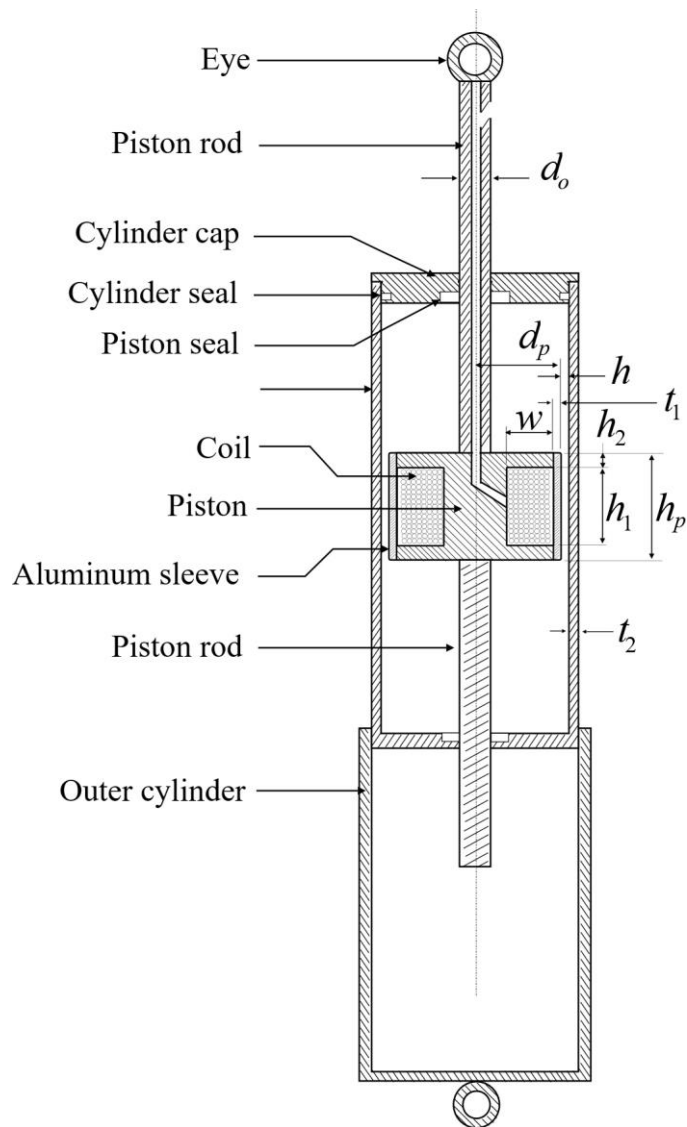


Figure 5.1 Cross-section of twin rod MR damper

Table 5.1: Parameters of twin rod MR damper

Parameter	Description	Value (mm)
d_o	Piston rod diameter	12
d_p	Piston diameter	31.5
t_1	Thickness of sleeve	1
t_2	Thickness of inner cylinder	3.5
w	Width of the coil	6
h	Height of coil	30
h_1	Shear gap for MR fluid	0.75
h_2	Flange width of piston	5
h_p	Total height of piston	40

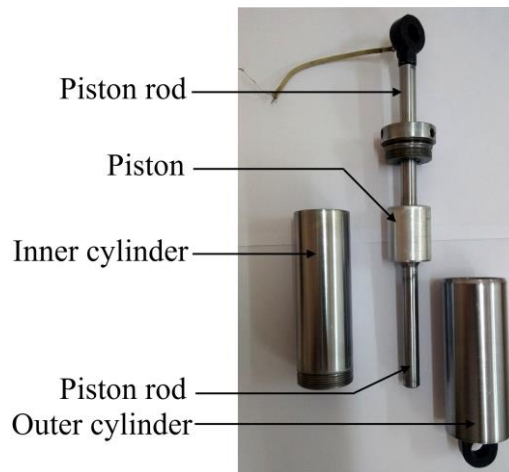


Figure 5.2 Fabricated prototype damper components

5.2.1 Experimental Test Rig

To characterize the twin rod damper, a damper testing machine facility which is available at National Institute of Technology Karnataka, Surathkal was used. The schematic of the machine is shown in Figure 5.3. The setup consists of a hydraulic actuator (Type: double acting, Capacity: ± 20 kN, Stroke: 150 mm) which is powered by a servo controlled valve. The actuator can supply varied input excitations such as ramp, sinusoidal, sine on sine, etc. A hydraulic power pack backs the servo controlled valve with a pressurized hydraulic oil. The temperature of the hydraulic oil is regulated using a radiator system, not shown in the schematic. The actuator is fixed on the cross-

head whose relative position can be adjusted depending on the overall length of the damper. One end of the damper is fixed to the actuator using a U-shaped jaw, while the other end is fixed to the base of the machine along with a force transducer (Capacity: ± 30 kN, Resolution: 0.001 kN). A DC power supply external to the whole setup is used to supply power to the twin rod MR damper. A displacement sensor (Make: GEFRAN, Range: 200 mm) is placed on the other side of the actuator which measures the vertical displacement of the actuator piston. The displacement and force data are collected using a data acquisition system and can be used for continuous online monitoring along with a logging facility. The detailed specifications related to individual units in the experimental setup are provided in the Appendix I.

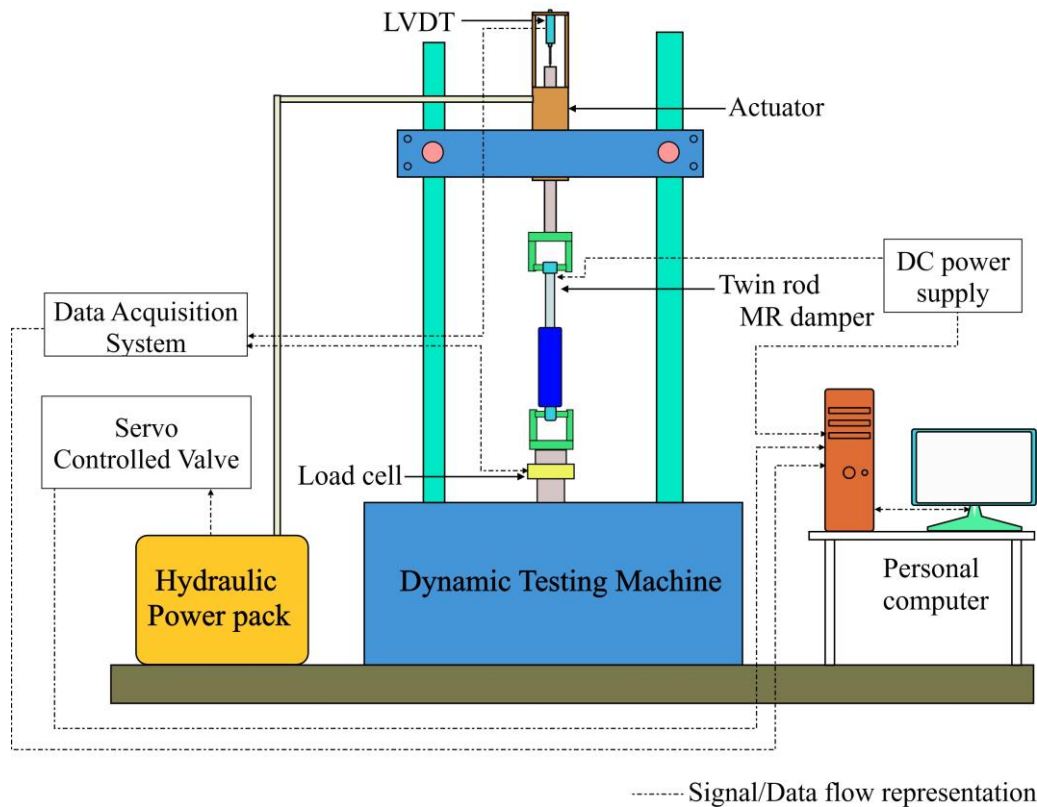


Figure 5.3 Schematic of damper testing machine

5.2.2 Characterization of MR Damper

Experimental testing of the MR damper was performed using the damper testing machine shown in Figure 5.4. The tests were conducted at varying amplitudes, frequencies and currents. Amplitudes of 5 to 10 mm in steps of 5 mm, frequencies of 0.5 to 2.5 Hz in steps of 0.5 Hz and currents of 0 to 1.2 A in steps of 0.4 A were

considered for the experiments. The selected amplitude and frequency sets yield velocities ranging from 0.0157 to 0.235 m/s. In normal human walking, the knee joint reaches a maximum speed of 60 rpm. Assuming a moment arm of 35 mm, this results in a maximum speed of 0.22 m/s. Therefore, the selected amplitudes and frequency data sets cover the entire range of normal human walking.

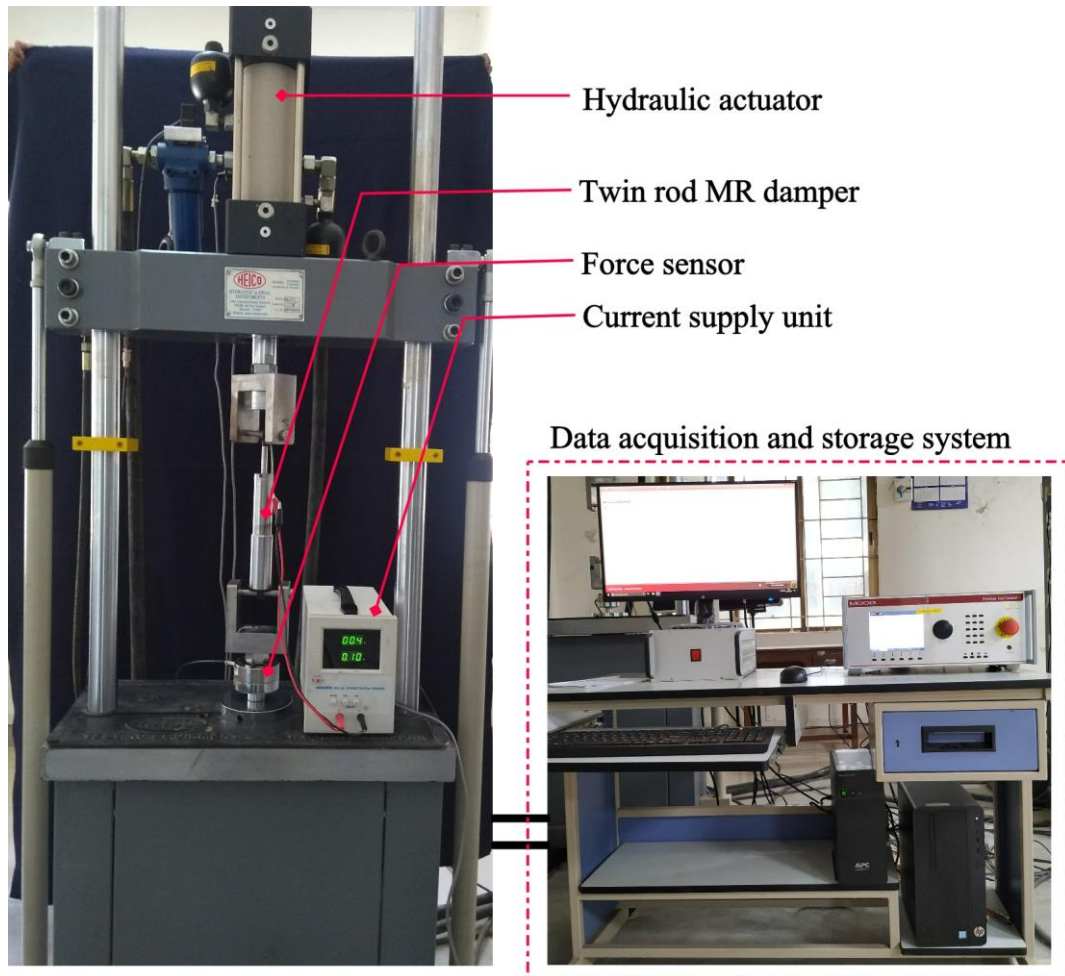


Figure 5.4 Experimental testing of fabricated MR damper

For the given range of amplitudes, frequencies and current, a full factorial experiment considering all possible combinations is selected resulting in a total of 60 experiments. Experimental results for a sample of data sets are shown in Figure 5.5. The effect of varying amplitudes, frequencies and current on damping force can be clearly noticed. The results are grouped into varying currents, frequencies and amplitudes considering other parameters as constant.

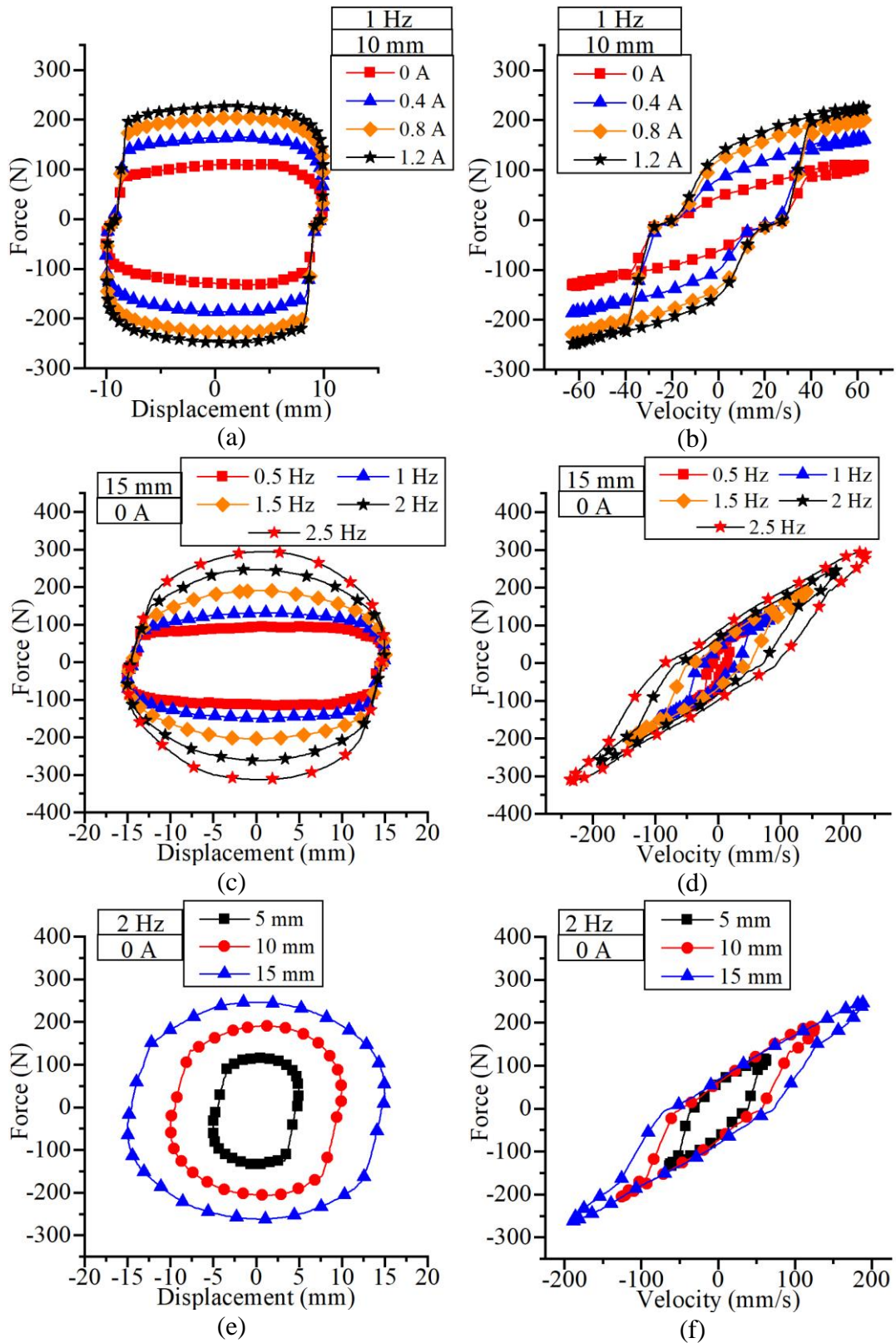


Figure 5.5 Force-displacement and force-velocity curves at varying (a) – (b) currents, (c) – (d) frequencies and (e) – (f) displacements respectively

The following are a few of the observations noticed in the prototype fabrication and testing.

1. The dynamic range of the damper is very low (around 2).
2. The aluminum sleeve on the piston core creates a very high reluctance in the magnetic circuit path. The primary intention of this arrangement was to avoid fluid leakages from the piston rod through-hole.
3. There were fluid leakages through the hole in the piston rod and the sleeve arrangement was not quite effective.
4. The number of turns of coil wounded on the piston is around 500. However, theoretical calculations using a packing factor of 0.7 would result in around 600 turns. Therefore, the packing factor during optimal design procedures needs to be modified to a value of 0.6 for a more reasonable estimation.

5.3 OPTIMAL DESIGN OF TWIN ROD MR DAMPER

Keeping in mind the various shortcomings associated with the prototyping and testing, the piston core assembly has been modified as shown in Figure 5.6. The piston rod is modified into a stepped shaft. An electromagnetic core with coil wound on it is placed inside a hollow outer core. To avoid direct contact between the outer core and the inner core, aluminum washers have been placed between them. Aluminum, being a paramagnetic material, increases the magnetic reluctance between the inner and outer core. MR fluid flows through the annular fluid gap between the outer and inner core. A small slot has been created in the piston inner core which enables the electromagnetic coil terminals to be easily accessed out of the damper. The ensemble of outer core, aluminum washer, inner core, washer in the same order is placed against the step on the piston rod. The threaded joint at the end holds the piston core blocks together and also creates a tight seal to avoid any fluid leakages from the piston through-hole. The inner cylinder design is maintained similar to the initial prototype design.

The total damping force can be calculated using the Equation (5.1).

$$F_{Total} = \frac{12\eta QL_t A_p}{w_t g^3} + \left[2.07 + \frac{12Q\eta}{12Q\eta + 0.4w_t g^2 \tau_y} \right] \frac{\tau_y (2L_a) A_p}{g} \quad (5.1)$$

Here, w_t is the average circumference of the fluid gap, g is the fluid gap, Q is the flow velocity, A_p is the piston cross-sectional area, L_a is the active pole length, η is the fluid viscosity, and τ_y is the fluid yield stress. The first part of Equation (5.1) represents the viscous force, F_{vis} and the second part of the equation represents the controllable MR force, F_{MR} .

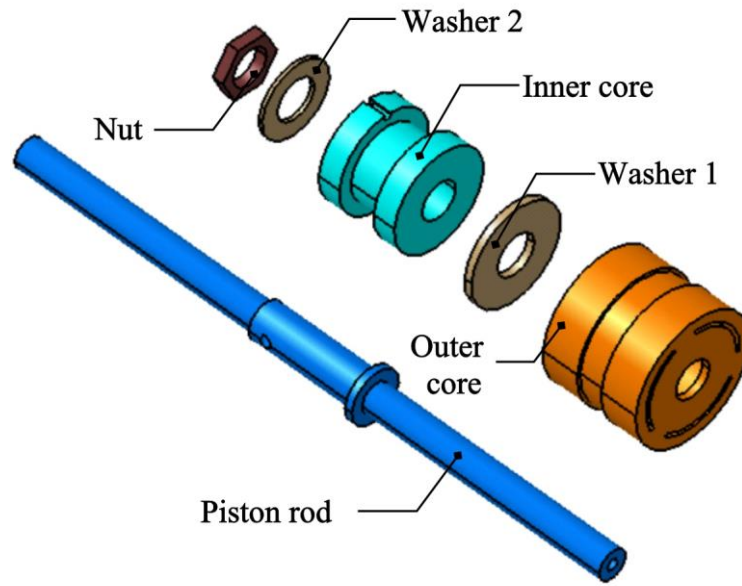


Figure 5.6 Piston core assembly

A few of the dependent variables are given by Equations (5.2) – (5.4).

$$w_t = 2\pi(r_c + w + 0.5g) \quad (5.2)$$

$$A_p = \pi[R^2 - r_0^2] \quad (5.3)$$

$$Q = A_p \dot{u} \quad (5.4)$$

Here, r_0 is the piston rod radius and \dot{u} is the velocity of the piston. In this optimal design, a piston rod radius of 4 mm and a design velocity of 0.1 m/s is chosen.

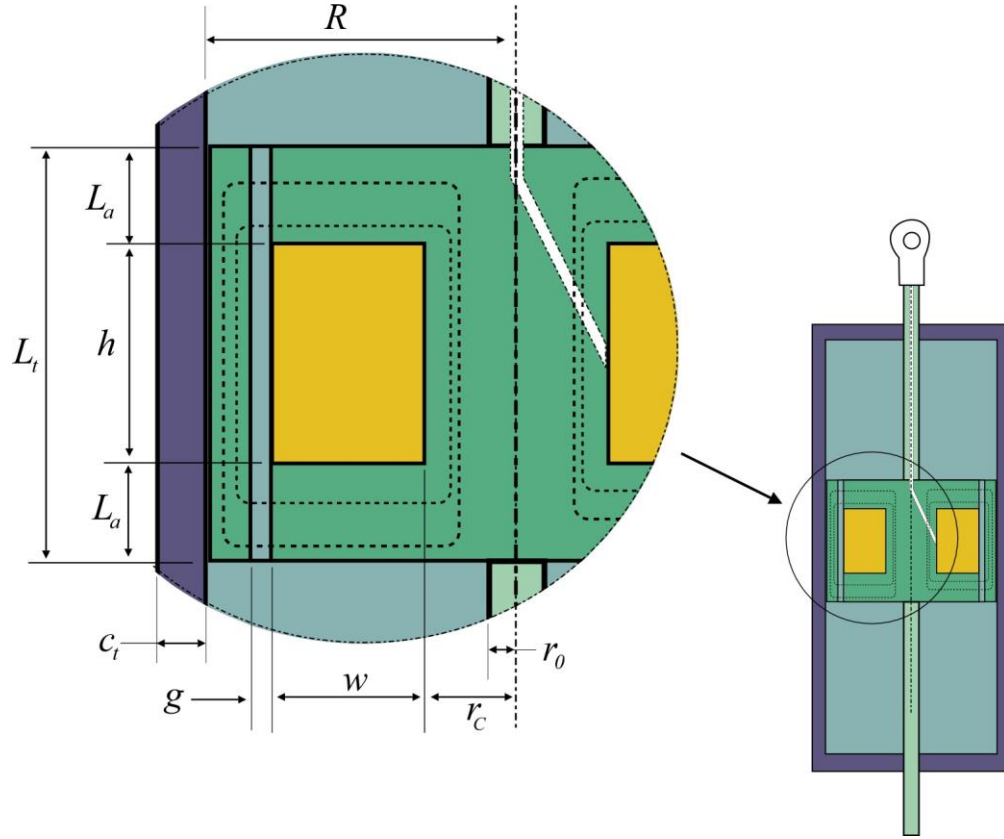


Figure 5.7 Geometry of twin-rod MR damper in flow mode configuration

The volumes of the coil, piston rod, MR fluid, inner core and outer core in the piston rod assembly are calculated by Equations (5.5) – (5.9).

$$V_{Coil} = \pi \left[(r_c + w)^2 - r_c^2 \right] h \quad (5.5)$$

$$V_{rod} = \pi r_0^2 L_t \quad (5.6)$$

$$V_{MRF} = \pi \left[(r_c + w + g)^2 - (r_c + w)^2 \right] L_t \quad (5.7)$$

$$V_{Core} = \pi \left[(r_c + w)^2 - r_0^2 \right] L_t - V_{Coil} \quad (5.8)$$

$$V_{OuterCore} = \pi \left[(r_c + w + g + c_t)^2 - (r_c + w + g)^2 \right] L_t \quad (5.9)$$

The mass of the piston rod assembly can be calculated using Equation (5.10).

$$m_P = \rho_{coil} V_{Coil} + \rho_{core} (V_{Core} + V_{OuterCore} + V_{rod}) + \rho_{MRF} V_{MRF} \quad (5.10)$$

Here, ρ_{coil} , ρ_{core} and ρ_{MRF} are the densities of the coil, core and MR fluid materials respectively. Further, the overall mass of the twin rod MR damper, M is

calculated assuming a cylinder cap thickness of 15 mm and a stroke length of 55 mm. Also, 1018 steel is selected as the magnetic core material due to its high magnetic permeability, low cost and availability. The piston rod is assumed to be made of stainless steel and the outer cylinder is of mild steel. MRF-132 DG (Make: Lord Corporation) is selected as the MR fluid. A packing factor of 0.6 was considered to calculate the number of turns of coil.

An optimal design of twin rod MR damper is performed considering maximization of the total damping force and reduction of mass as the objectives. The design variables and bounds are shown in Table 5.2. An optimization problem of the twin rod MR damper is formulated as follows:

Objective function: Minimization of $[-F_{Total}, M]$

Constraints: $M < 1$ kg, $B_{max} < 1.8$ T and $F_{vis} < 80$ N

Along with saturation constraints and off-state viscosity constraint, mass constraint has also been applied so as to obtain the required part of the Pareto optimal frontal solutions.

Table 5.2: Variables, bounds and optimized values of twin rod MR damper

Variables	Name	Bounds (mm)		Optimized values (mm)
		Lower	Upper	
r_c	Piston core radius	6	16	9.8
w	Coil width	2	10	3.4
h	Coil height	2	10	10
g	Fluid gap	0.5	1.2	0.67
L_a	Active pole length	3	10	6
c_t	Thickness of outer cylinder	3	10	3

An equivalent magnetic model is developed for the axisymmetric model of the piston blocks. Further, FEMM model has also been parameterized to evaluate the magnetostatic analysis given the design variables. The optimization is performed using the O-COM methodology detailed in Chapter 3. The Pareto optimal front of the twin rod MR damper is shown in Figure 5.8(a). Also, magnetostatic analysis of the axisymmetric model of optimal twin rod damper is shown in Figure 5.8(b).

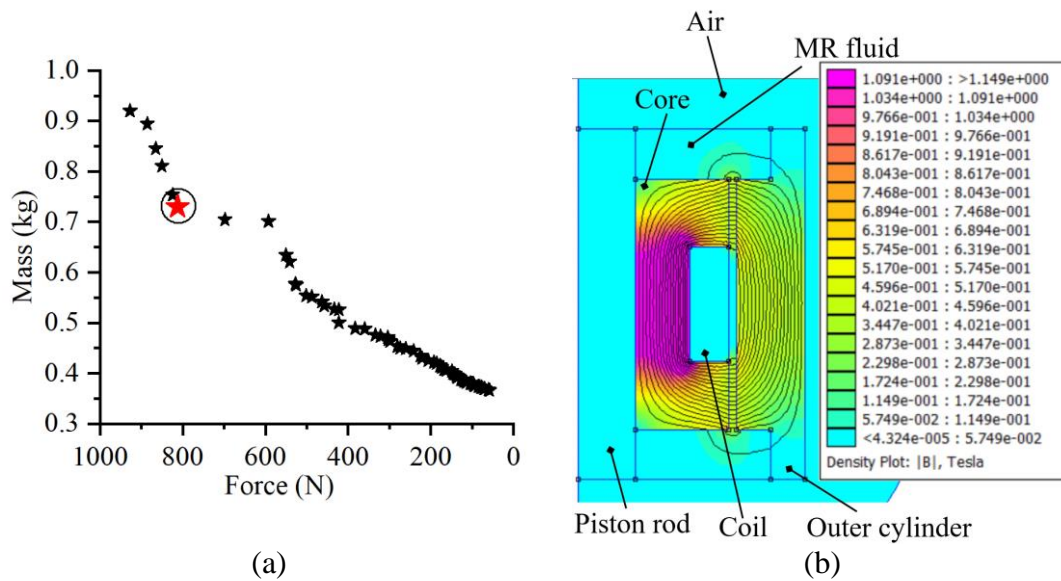


Figure 5.8 (a) Pareto front of twin rod flow mode damper and (b) Magnetostatic analysis of optimal design

A design point which provides a damping force of more than 800 N and is of least possible weight is chosen as the optimal point (colored in red in Figure 5.8 (a)). The dimensions of the optimal point are also listed in Table 5.1. The optimal design point produces a damping force of 812 N with a mass of 0.73 kg. The fabricated components of the optimal twin rod MR damper are shown in Figure 5.9. Also, the piston core assembly is shown in Figure 5.10.

5.4 CHARACTERIZATION OF TWIN ROD MR DAMPER

Due to the unavailability of sufficient quantity of Lord MRF-132DG fluid (to conduct multiple experiments on both linear twin rod and rotary vane MR damper) in the experimental stage, an in-house prepared MR fluid is chosen as an alternative. The properties of the fluid were selected from study by Acharya et al. (2020) which focuses on determination of optimal composition of MR fluids for MR brake application. In that study, MR fluids of various combinations of mean particle sizes, particle fractions and base oil viscosity were synthesized. A design of experiments approach was considered and fluid compositions were optimized for minimum off state and maximum on state braking torques using a multi-objective genetic algorithm. The optimization resulted in an optimal composition of MR fluid with 2.91 microns mean particle size,

mass fraction of 80.95% and a base oil viscosity of 50 cSt. Additionally, on-state braking torque of the optimal composition is 29.2% higher than those compared with Lord MRF-132DG. However, off-state braking torque is 27.3 % higher compared to MRF-132DG, suggesting a higher viscosity of optimal composition. More information on various characterization results of fluid compositions can be found in Acharya et al. (2020).

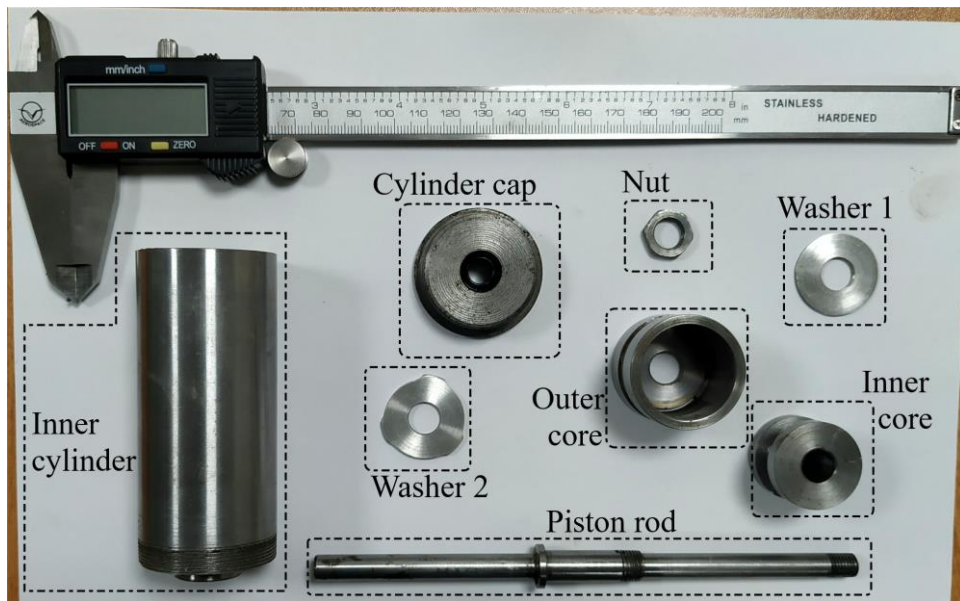


Figure 5.9 Twin-rod damper fabricated components

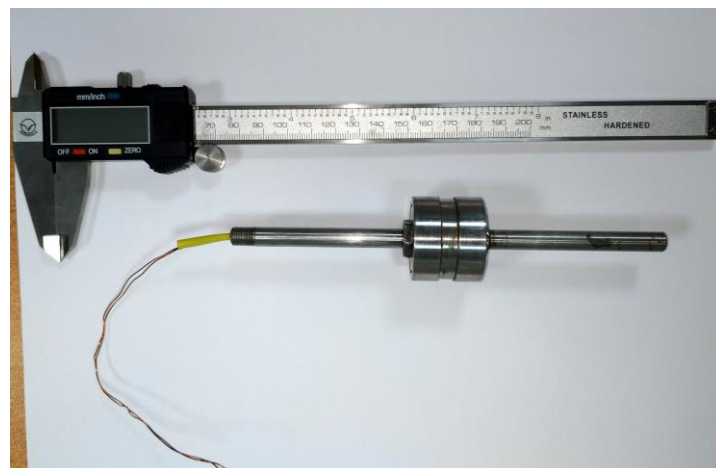


Figure 5.10 Piston core assembly

The selected fluid composition uses silicone oil (viscosity: 50 cSt) as the base fluid with a mass fraction of 19.05% and carbonyl iron particles (mean particle diameter: 2.91 microns) with a mass fraction of 80.95%. Bentonite clay is used as a

thixotropic agent for suspension stability and aluminum distearate to improve redispersibility of iron particles in the MR fluid. Both the additives used are 5% mass of the base oil. Initially, all required components are weighed using an electronic weighing balance. At first, bentonite clay is added to silicone oil and mixed for roughly 1 hour at a speed of 400 rpm. Later, aluminum distearate is added and stirred for another 1 hour at the same speed. Finally, carbonyl iron particles are added in two stages with an interval of 4 hours. The final sample is stirred for another 8 hours at the same speed. Prior to use, the MR fluid was de-gassed in a vacuum chamber to remove the air bubbles trapped due to stirring process. The twin rod MR damper is filled with in-house prepared MR fluid. Care has been taken while filling the liquid to avoid any trapped air bubbles inside the damper.

The experimental tests were performed for an amplitude variation of 5, 10 and 15 mm and frequency variations of 0.5, 1, 1.5, 2, 2.5 Hz and current variation of 0, 0.25, 0.5 and 1 A. Therefore, a total of 75 experiments have been performed on the twin rod MR damper. A sample of the characteristic curves showing variation of force with displacements and velocities at various amplitudes, currents and frequencies are shown in Figure 5.11.

5.5 DESIGN VALIDATION

Theoretically, the optimal design of the twin rod MR damper is capable of producing a damping force of around 812 N at a design speed of 0.1 m/s and at a current of 1 A. The off-state damping force of damper is around 82 N. Figure 5.11 shows the experimental results of force-displacement and force-velocity obtained at varying amplitudes, frequencies and currents. As can be noticed from figures 5.11(a)-(b), the off-state damping force is 132 N at a velocity of 0.1 m/s. The increase in the off-state damping force is due to the use of wiper seals at the two ends of the damper and also due to the difference in off-state viscosity from the design fluid and in-house prepared fluid. This increase in off-state force along with the slight manufacturing deviations from the theoretical design might have contributed to the increase in the total damping force. As shown in figure 5.11(a), the maximum on-state damping force is 1020 N at a

velocity of 0.1 m/s and current of 1 A. Figures 5.11(b), (d) and (f) shows that the hysteresis is enlarged with varying amplitudes, frequencies along with currents.

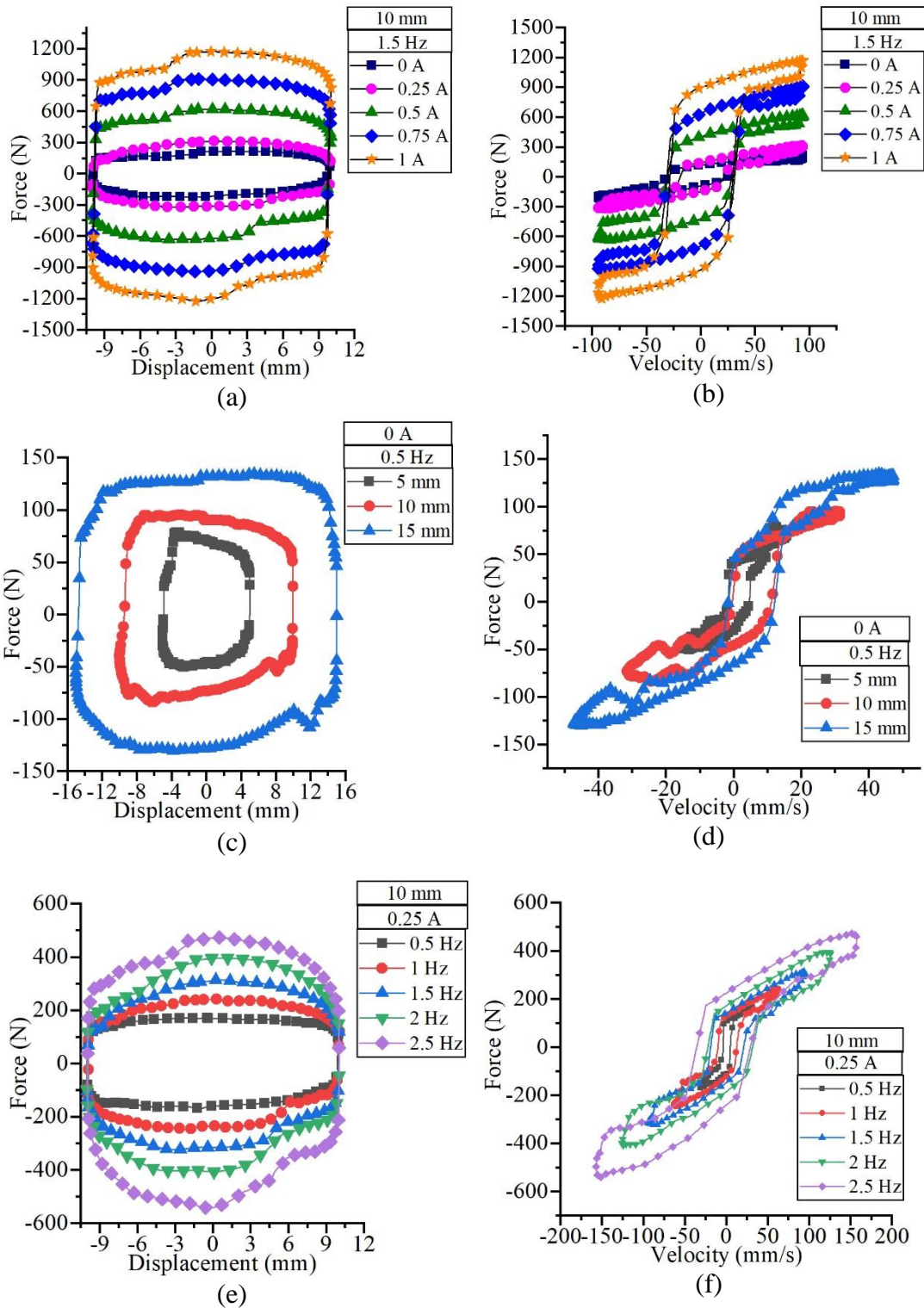


Figure 5.11 Force-displacement and force-velocity curves at varying (a) – (b) currents, (c) – (d) displacements and (e) – (f) frequencies respectively

However, the total damping force is higher than the designed value and thus the design can be suitably applied for a prosthetic knee device. The off-state damping force can be further reduced by employing piston rod coatings, which were not performed during the optimal design prototype fabrication.

The total design mass of twin rod MR damper was 0.73 kg, whereas the actual obtained value is around 0.71 kg. The factors such as material density differences, piston rod through-hole are a few of the possible reasons for this reduction. However, the reduction in overall mass can be considered as a positive indicator for this application.

5.6 SUMMARY

In this chapter, a design optimization of the twin rod MR damper was considered using O-COM methodology. An initial prototype was fabricated and tested for preliminary analysis. Based on the shortcomings noticed during the operation of the initial prototype, the optimal damper design was suitably altered. After the optimization process, the damper was fabricated and characterized using a linear damper testing machine. The experimental results showed an increase in the off-state damping force and the total on-state damping force at 1 A. The probable reasons for an increase in the off-state damping force are the piston rod seals and viscosity of in-house prepared MR fluid.

CHAPTER 6

DESIGN, FABRICATION AND CHARACTERIZATION OF ROTARY VANE MR DAMPER

6.1 INTRODUCTION

A rotary vane damper is a device which generates braking torque by displacing the volume of fluid from one chamber to another chamber. Use of an MR valve arrangement between the two fluid chambers will allow conversion of this passive device into a semi-active device. In the previous studies, various coil arrangements have been considered in the rotary and the static vanes. These coil arrangements inside the vanes will require the core material to be made of higher permeable magnetic materials. This arrangement also increases the outermost diameter of the rotary chamber which further increases the weight of the device, making it unsuitable for prosthetic knee application. Therefore, in this study, an external MR valve is considered. Before considering an optimal design, an initial prototype of the vane type damper has been fabricated to provide a few insights into the working of the vane damper and also to facilitate any design improvements.

6.2 INITIAL PROTOTYPE OF ROTARY VANE MR DAMPER

A rotary vane damper with an MR valve operating in flow mode is fabricated initially. The geometry of the vane type MR damper is shown in Figure 6.1. The rotary chamber accommodates a fixed static vane while the rotary vane is attached with the rotary shaft. The MR fluid inside the rotary chamber is contained using two cover plates on either side of the rotary chamber. This arrangement was considered initially as the device would be easier to manufacture using wire electrical discharge machining (EDM) process. The MR valve houses a core material wound with an electromagnetic coil of 24 AWG copper coil. The core is attached to the valve cap which helps maintain a concentric fluid gap between the core and the valve cylinder. Since no moving faces are involved in the MR valve, flow mode of the MR fluid is realized. The rotary

chamber and the MR valve are connected via hydraulic ports and cables, which are not shown in Figure 6.1.

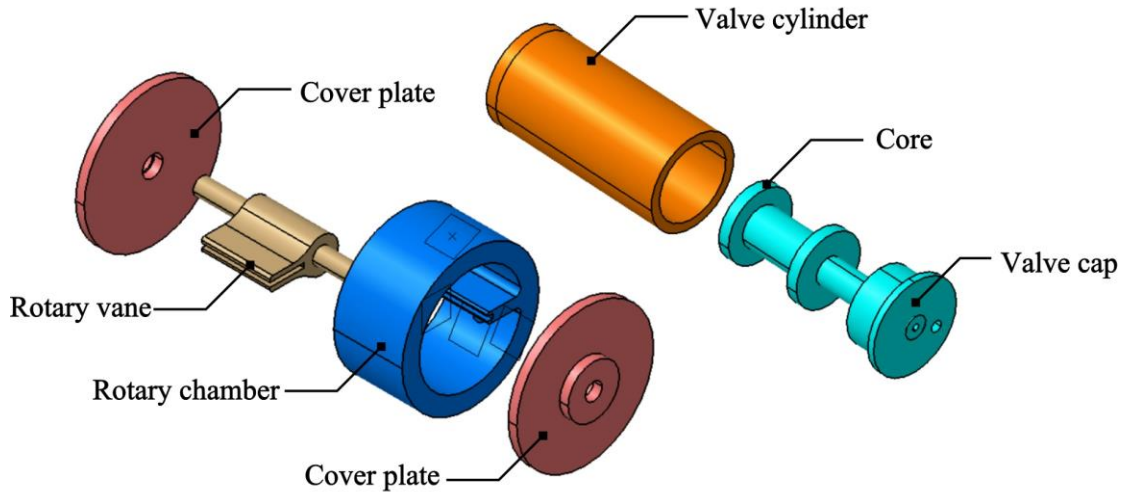


Figure 6.1 3D model of rotary vane damper prototype

Mild steel material was selected to fabricate all components as it is easily available, manufacturable and cheap. The fabricated components of the rotary vane damper are shown in Figure 6.2. To characterize the rotary damper, an experimental test rig has also been developed, which is described in the next section.

Due to the large torque requirements, the experimental test rig was found to be insufficient to characterize this prototype. However, the prototype provided useful insights which helped to develop the final optimal vane type MR damper. The following are a few of the observations noticed during prototype handling.

1. A large quantity of MR fluid, more than 200 ml, is needed to completely fill the rotary and MR valve setup.
2. The static vane plays no role in the development of damping torque and therefore, use of lighter materials can lead to better weight minimization.
3. The use of an aluminium sleeve on the copper coil was to avoid any leakages through the MR valve. Since no moving elements are involved in the MR valve, the design can be simplified by using seals at the piston through-hole and completely eliminating the aluminium sleeve.
4. The elimination of aluminium sleeve also improves the magnetic field in the fluid gap.

- Rotary cylinder and the static vane are made out of a single block using wire EDM techniques; however, this resulted in multiple openings in rotary chamber.

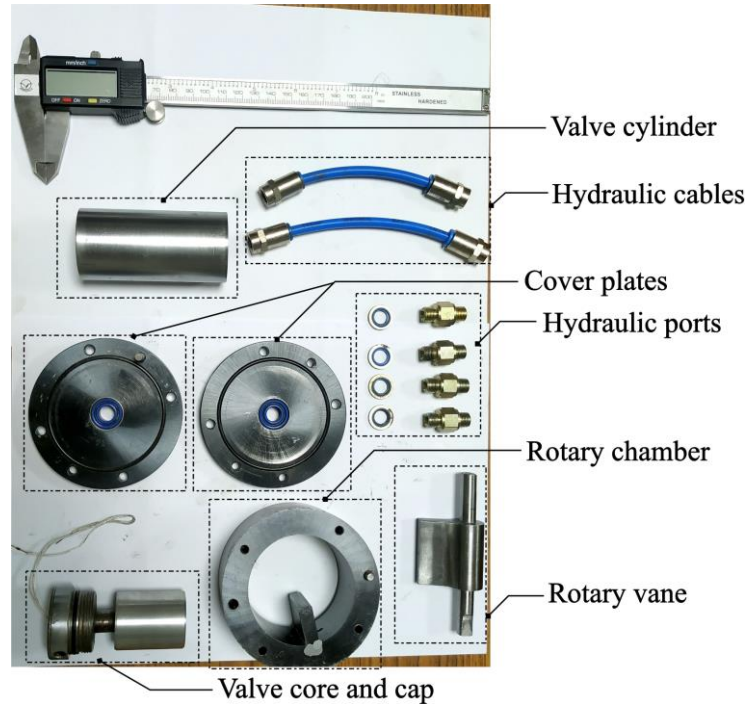


Figure 6.2 Fabricated components of initial rotary vane type MR damper

6.3 OPTIMAL DESIGN OF ROTARY VANE MR DAMPER

The following modifications have been made on the initial prototype to address the issues.

- The bottom cover plate of the rotary cylinder is completely eliminated and the static vane is fabricated separately.
- Since the prosthetic knee rotary motions are limited to 130 degrees, the static vane is made to cover half the portion of the rotary chamber to reduce the amount of MR fluid usage. Although, this component may be completely avoided and the rotary chamber can be made in semi-circular cross-section shape, for ease of manufacturing and to reduce the cost of initial design prototype, the shape of rotary cylinder is retained as circular.
- The aluminium sleeve on the MR valve core has been avoided and instead the piston through-hole is covered with sealant once the electromagnetic coil is wound.

Keeping in mind the above points, the optimal design of the rotary vane MR damper has been performed. The modified design of the rotary vane MR damper is shown in Figure 6.3. Also, the vane type MR damper with various geometric variables is shown in Figure 6.4.

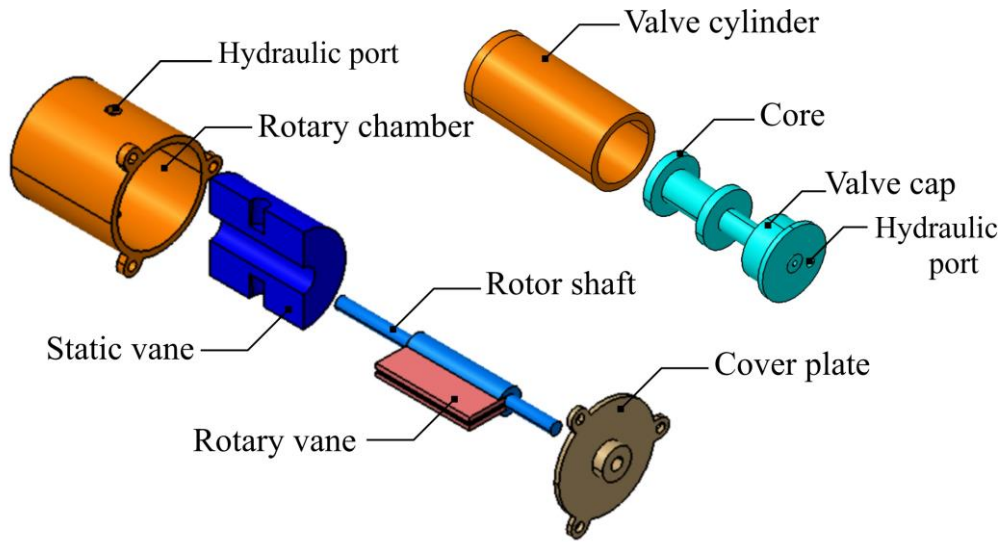


Figure 6.3 Modified rotary vane MR damper

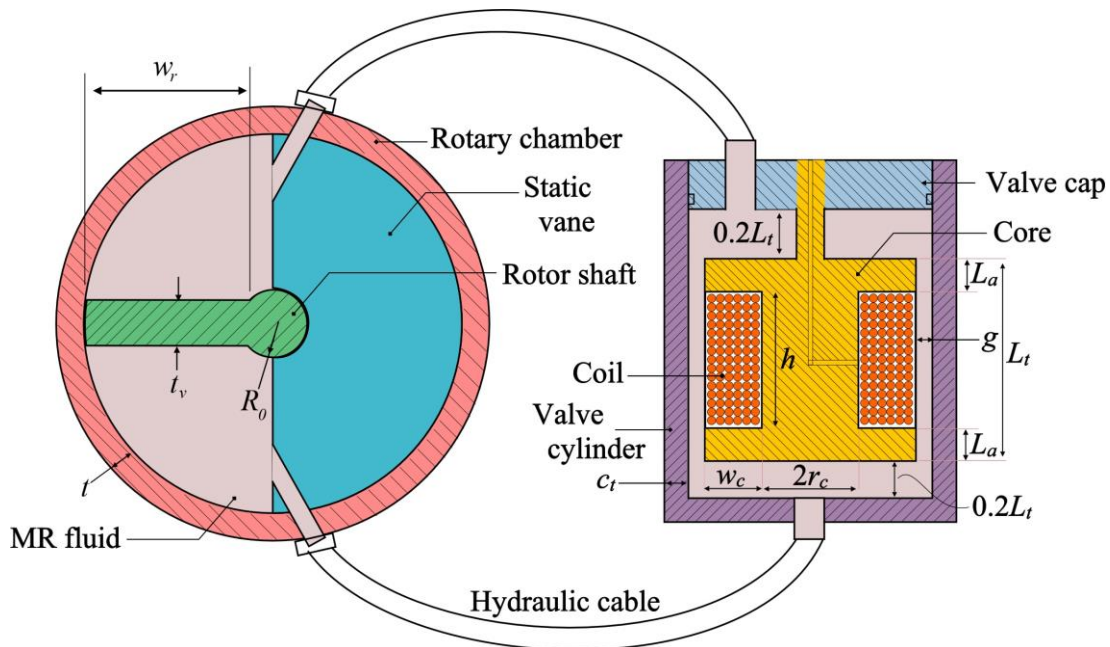


Figure 6.4 Geometric variables of rotary vane MR damper

The total damping torque produced by the vane damper can be calculated using the equation,

$$T = \frac{12\eta QL_t}{g^3 w} (L_r w_r R_r) + \left[\left(2.07 + \frac{12Q\eta}{12Q\eta + 0.4wg^2\tau_y} \right) \frac{2\tau_y L_a}{g} \right] (L_r w_r R_r) \quad (6.1)$$

Here, L_r is the height of the rotary vane in the axial direction along the shaft, w_r is the width of rotary vane along the radial direction, R_r is the radial distance from the shaft axis to the centroid of rotary vane, r_c is the radius of the MR valve core, w is the average circumference of the MR flow channel, w_c is the width of the coil, h is the height of the coil, g is the fluid gap, L_a is the pole length of the MR valve and c_t is the outer cylinder thickness. The average flow rate of the MR fluid and the radial distance can be calculated using Equations (6.2) – (6.3).

$$Q = L_r w_r R_r \omega \quad (6.2)$$

$$R_r = R_0 + 0.5w_r \quad (6.3)$$

Here, ω is the design speed taken as 8.6 rpm, R_0 is the radius of the rotor shaft taken as 4 mm. Also, the parameters such as cover plate thickness, rotor cylinder thickness and MR valve thickness are set to 4 mm. These parameters are required to calculate the overall mass of the braking torque and are estimated based on the previous studies. The first part of Equation (6.1) represents the viscous or off-state damping torque, T_{vis} and the second part of the equation represents the controllable damping torque, T_{MR} . The approximate volumes of coil, rod, MR fluid, inner core, outer core and cap of the MR valve can be calculated using Equations (6.4) – (6.9).

$$V_{Coil} = \pi \left[(r_c + w_c)^2 - r_c^2 \right] h \quad (6.4)$$

$$V_{rod} = 1.2\pi r_0^2 L_t \quad (6.5)$$

$$V_{MRF} = \pi \left[(r_c + w_c + g)^2 - (r_c + w)^2 \right] L_t + 0.4\pi L_t \left[(r_c + w_c + g)^2 - r_0^2 \right] \quad (6.6)$$

$$V_{Core} = \pi \left[(r_c + w_c)^2 - r_0^2 \right] L_t - V_{Coil} \quad (6.7)$$

$$V_{OuterCore} = 1.4\pi L_t \left[(r_c + w_c + g + c_t)^2 - (r_c + w_c + g)^2 \right] \quad (6.8)$$

$$V_{cap} = \pi (r_c + w + g + c_t)^2 t_c \quad (6.9)$$

The mass of the MR valve can be calculated using Equation (6.10),

$$m_{valve} = \left\{ \begin{array}{l} \rho_{Coil} V_{Coil} + \rho_{Core} (V_{Core} + V_{OuterCore} + V_{rod} + V_{cap}) \\ + \rho_{MRF} V_{MRF} + \rho_{Al} \rho_{Cap} \end{array} \right\} \quad (6.10)$$

Here, ρ_{Al} is the density of aluminium. The cap of the MR valve is assumed to be made of aluminium material to prevent flux leakage between the inner and outer core directly via the piston rod. The core and cylinder are assumed to be made of 1018 steel and other components are assumed to be made of aluminium material. The mass of the rotary vane, MR fluid in the rotary chamber and the rotary enclosure can be calculated using Equations (6.11) – (6.13).

$$m_{RVane} = \rho_{Al} \left[\pi R_0^2 (L_r + 2t) + L_r w_r t_v \right] \quad (6.11)$$

$$m_{RMRF} = \rho_{MRF} \left\{ 0.5\pi \left[(R_0 + w_r)^2 - R_0^2 \right] - L_r w_r t_v \right\} \quad (6.12)$$

$$m_{Renc} = \rho_{Al} \left(\pi L_r (R_0 + w_r + t)^2 - (R_0 + w_r)^2 \right) + 2\pi t_c (R_0 + w_r + t)^2 \quad (6.13)$$

The overall mass of the rotary vane MR damper can be calculated using Equation (6.14),

$$m_{Total} = m_{valve} + m_{RVane} + m_{RMRF} + m_{Renc} \quad (6.14)$$

An optimization problem of rotary vane MR damper is formulated as follows:

Objective function: Minimization of $[-T, m_{Total}]$

Constraints: $m_{Total} < 1$ kg, $B_{max} < 1.8$ T and $T_{vis} < 2.5$ Nm

The parameters of optimization are maintained similar as in the earlier case. The design variables and bounds are listed in Table 6.1. The Pareto optimal front showing various design points of the rotary vane damper is shown in Figure 6.5(a). Also, the magnetostatic analysis of an axisymmetric model of an MR valve is shown in Figure 6.5(b).

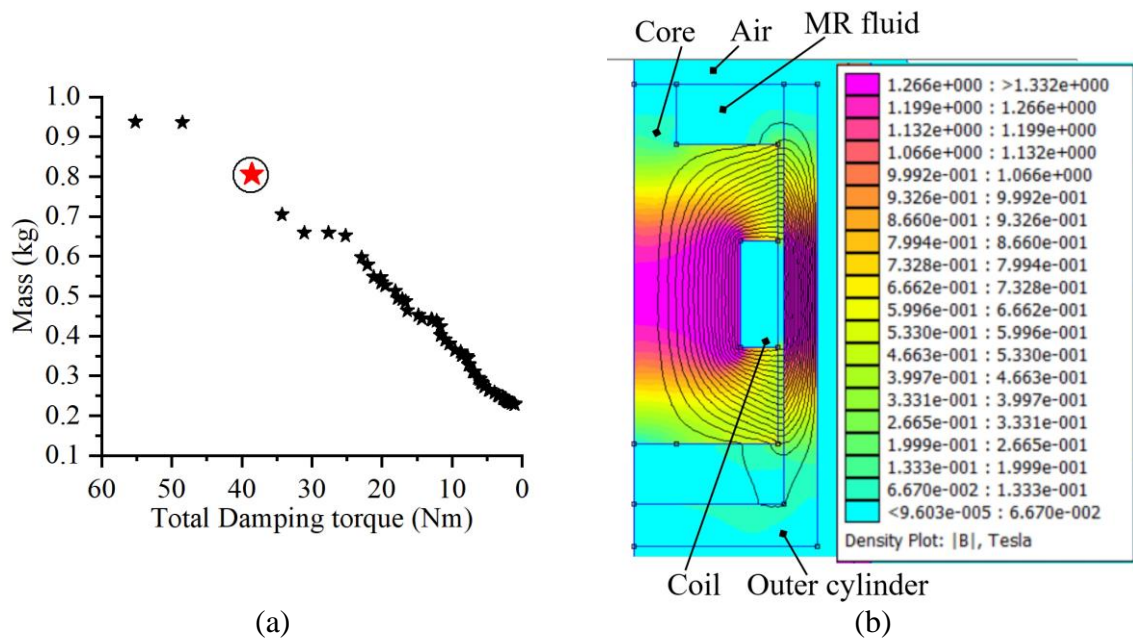


Figure 6.5 (a) Pareto front of rotary vane MR damper and (b) Magnetostatic analysis of MR valve

Among the design points, the optimal design point with a braking torque of more than 35 Nm and which offers least mass is selected as the optimal design. The optimal design is capable of producing a braking torque of 37 Nm and has a total mass of around 0.8 kg. For manufacturing ease, the dimensions were rounded off to the nearest realizable value. Further, the rotor shaft was slightly modified so as to allow the rotary vane to be connected easily using screws. This modified design is capable of producing 35 Nm with a total mass of around 0.82 kg. The optimal values of the rotary vane damper are listed in Table 6.1. The mass of the static vane, hydraulic ports, cables along with MR fluid occupying these components were not considered due to uncertainty. Using the dimensions listed in Table 6.1, the components of the vane type MR damper are fabricated. The fabricated components along with the hydraulic ports, cables are shown in Figure 6.6.

Table 6.1. Bounds and optimum values of design variables

Variables	Bounds		Optimum values (mm)
	Lower (mm)	Upper (mm)	
L_r	40	80	65
w_r	15	35	25
r_c	5	14	9.8
w	2	10	3
h	2	10	10
g	0.5	1.2	0.56
L_a	3	10	8
c_t	3	10	3.2

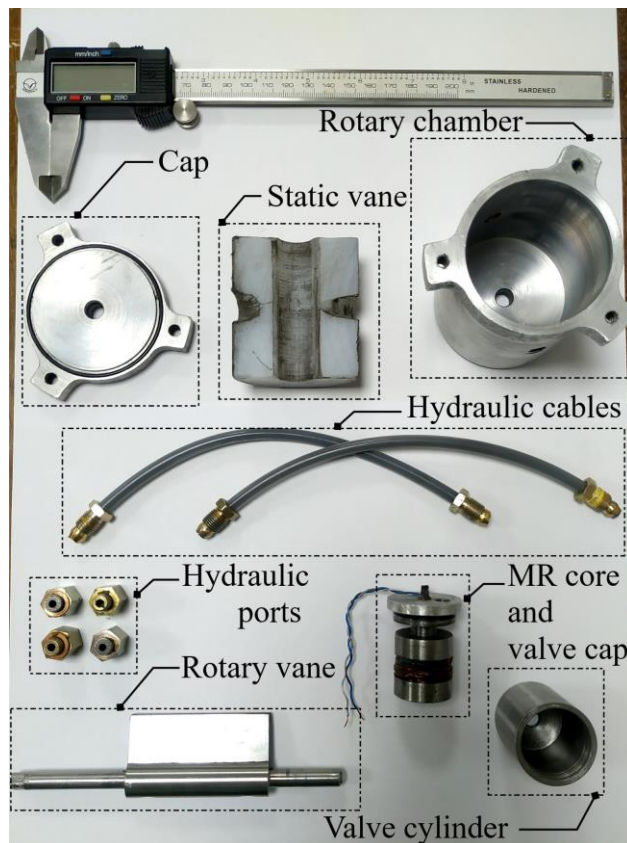


Figure 6.6 Fabricated components of optimal design of rotary vane damper

6.4 DEVELOPMENT OF EXPERIMENTAL TEST RIG

A test facility to generate harmonic excitations in rotary motion was developed to characterize the vane damper. The schematic of the rotary test setup is shown in

Figure 6.7. A hybrid stepper motor (Make: Rhino Motions, Model: RMCS-1056) is used to provide the required angular displacements. A Leadshine servo drive (Model: ES-D1008) is used to drive the stepper motor. The motor was coupled with a planetary gear box (Gear ratio 10:1) to reduce the speed and also to increase the torque capacity of characterization setup. A torque transducer (Make: Datum Electronics; Model: M425) is coupled in line with the rotary system with one end connected to the gear box shaft. The other end of the transducer is connected to the rotary damper. Various sub-systems are interconnected using suitable flexible shaft couplers. An encoder (Make: Rhino Motions, Model: RMCS-5102) is connected at the far end of the rotary damper to measure angular displacement. Bearing block supports are provided at various places to support individual subsystems and also to effectively transfer the motion from the motor to the rotary damper. Detailed specifications of individual subsystems are provided in Appendix I.

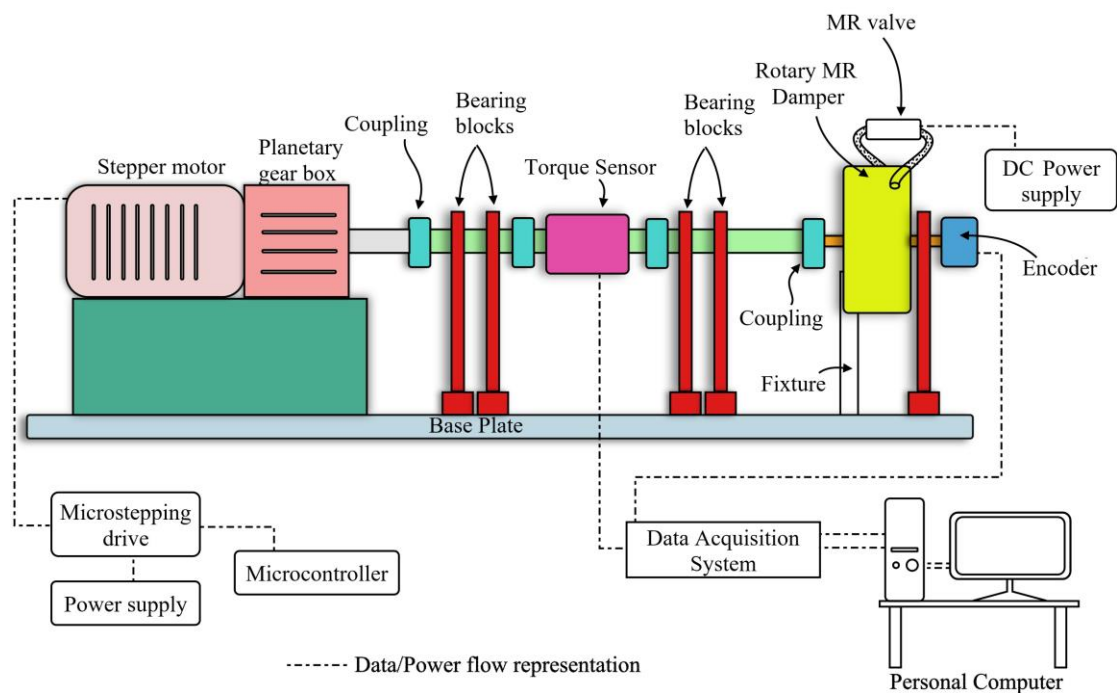


Figure 6.7 Schematic of Rotary damper experimental test setup

The stepper motor system is actuated independently using a microcontroller. The microcontroller is preloaded with the time steps of harmonic excitation profiles with varying displacement amplitudes and frequencies during each cycle of experiments. The rotary damper is supported using a fixture so as to restrict the relative

motion of the outer cylinder of the rotary chamber. The torque sensor display unit provides an analog output signal in the range of 0 to 10 V. This signal is acquired using an analog input module (Make - National Instruments; Model – NI 9205) connected to the chassis (Make – National Instruments; Model – cDAQ 9174). The torque and encoder signals are acquired using a LabVIEW program, which allows continuous monitoring along with data logging for subsequent analysis. The fabricated setup along with the rotary vane MR damper is shown in Figure 6.8. Sequential installation of individual subsystems in the order of motor, gearbox, torque transducer, rotary vane damper and encoder has been performed and alignment issues have been corrected carefully.

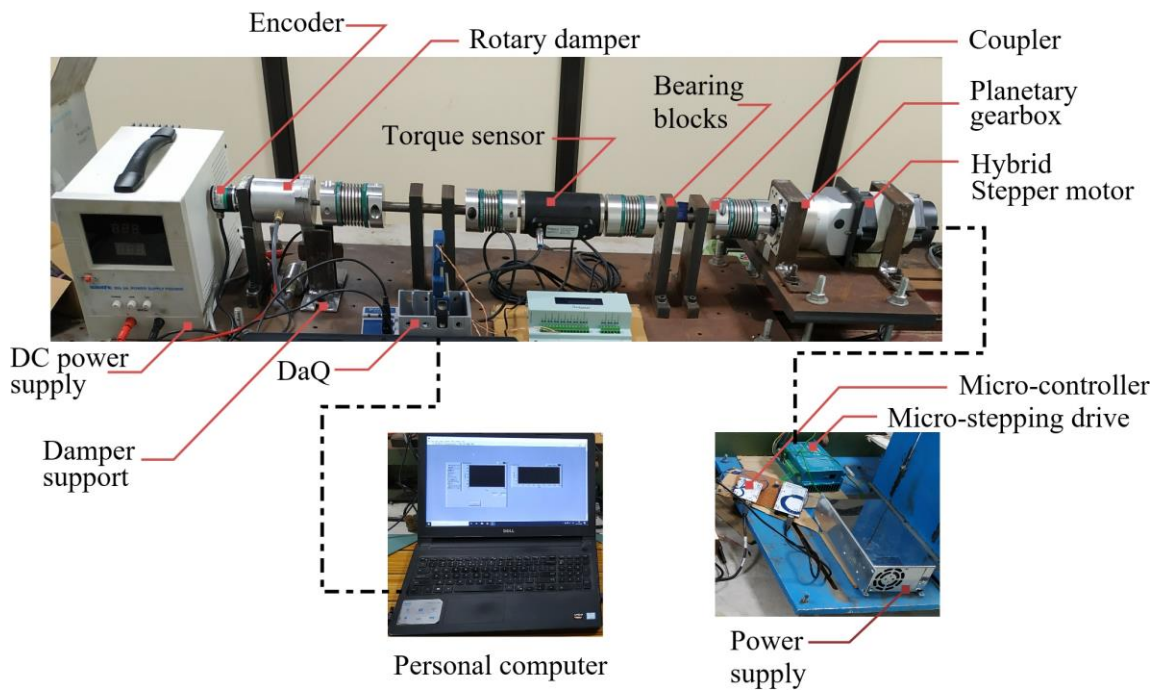


Figure 6.8 Rotary damper experimental test setup

6.5 CHARACTERIZATION OF ROTARY VANE DAMPER

Before performing experiments, the rotary damper has been carefully filled with MR fluid. The device involves intricate dimensional changes; thus the fluid filling using a vacuum pump arrangement is employed. The vacuum pump is connected to the rotary damper device as shown in Figure 6.9. One side of the rotary chamber is maintained with MR fluid till level B during the entire process. A bypass MR valve is assembled

using the individual components i.e., valve core, cylinder and cylinder cap. One of the ports of the MR valve is connected to the rotary cylinder while the other port is connected to the vacuum pump. The pump is switched on until the MR fluid reaches level A in Figure 6.9. The MR valve and the hydraulic cables are constantly tapped to remove any trapped air bubbles. Later, the vacuum pump is disconnected and the other port of MR valve is connected back to the rotary chamber. The rotary chamber filled with MR fluid is shown in Figure 6.10. The same composition of in-house MR fluid used in the experimentation of linear twin rod MR damper is used to test the rotary vane MR damper too.

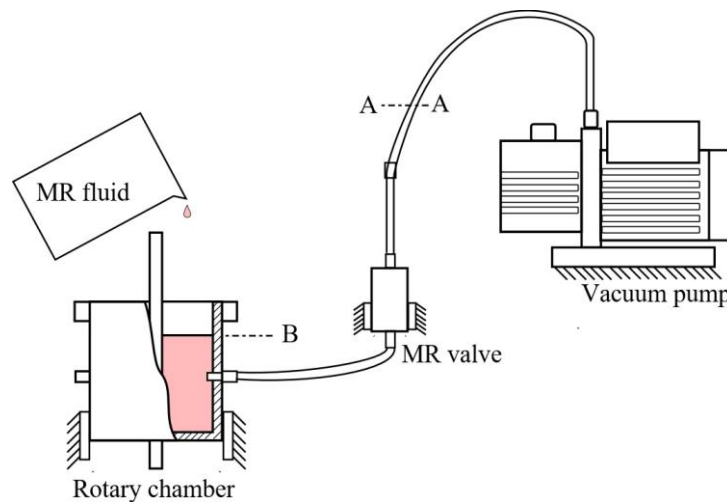


Figure 6.9 MR fluid filling process

Once the rotary chamber is filled with the MR fluid, the lid is tightened. The device is carefully fixed in the experimental test rig and the bearing blocks are adjusted to take care of any small misalignments. The microstepping driver is adjusted for 1600 steps per revolution. The planetary gear box has a gear ratio of 10:1. Therefore, 1600 time steps to the stepper motor will produce an angular displacement of 36° . The time steps for sinusoidal excitation which are to be preloaded in the microcontroller has been calculated for 400, 800, 1200 and 1600 steps which correlate to the amplitudes of 9° , 18° , 27° and 36° respectively. The frequency sets of 0.167, 0.5 and 0.833 Hz are considered for experimentation. The amplitude and frequency set combinations are selected such that they fall within the limits of normal human knee displacements and velocities. The current to the MR valve has been varied from 0 to 1 A in steps of 0.25 A. A total of 60 sets of experimental runs have been performed on the rotary vane MR

damper. A few characteristic curves of the damper showing torque variation with angular displacement, angular velocities and currents are shown in Figure 6.11.



Figure 6.10 Rotary chamber filled with MR fluid

It may be noted from the characteristic curve of Figure 6.11(e) that the displacement amplitude is not constant for all the curves. In the experimental test setup, the stepper motor actuation system is not based on a closed loop tracking control. Thus the high dissipation torque of the damper prevents the motor from carrying out additional time steps necessary to reach the desired amplitude. However, the variation of torque with current for a specific displacement and frequency is clearly visible from the figures. Since the requirement was to demonstrate the proof of concept of the damper device, the experimental test setup serves the purpose.

6.6 DESIGN VALIDATION

Theoretically, the optimal design of rotary vane MR damper can produce a total damping torque of 37 Nm at a design speed of 8.6 rpm (or 0.9 rad/s or 51.6 deg/s) and at a current of 1 A. However, the actual damping torque measured from experiments at a similar design speed and current value was around 20 Nm. Although, the device generated a maximum damping torque of around 33 Nm at a speed of 23.6 rpm and a current of 1 A. The off-state torque also increased from 1.07 Nm from simulation to 5 Nm in experiment. Also, the mass of the device increased from 0.8 kg to 1.1 kg.

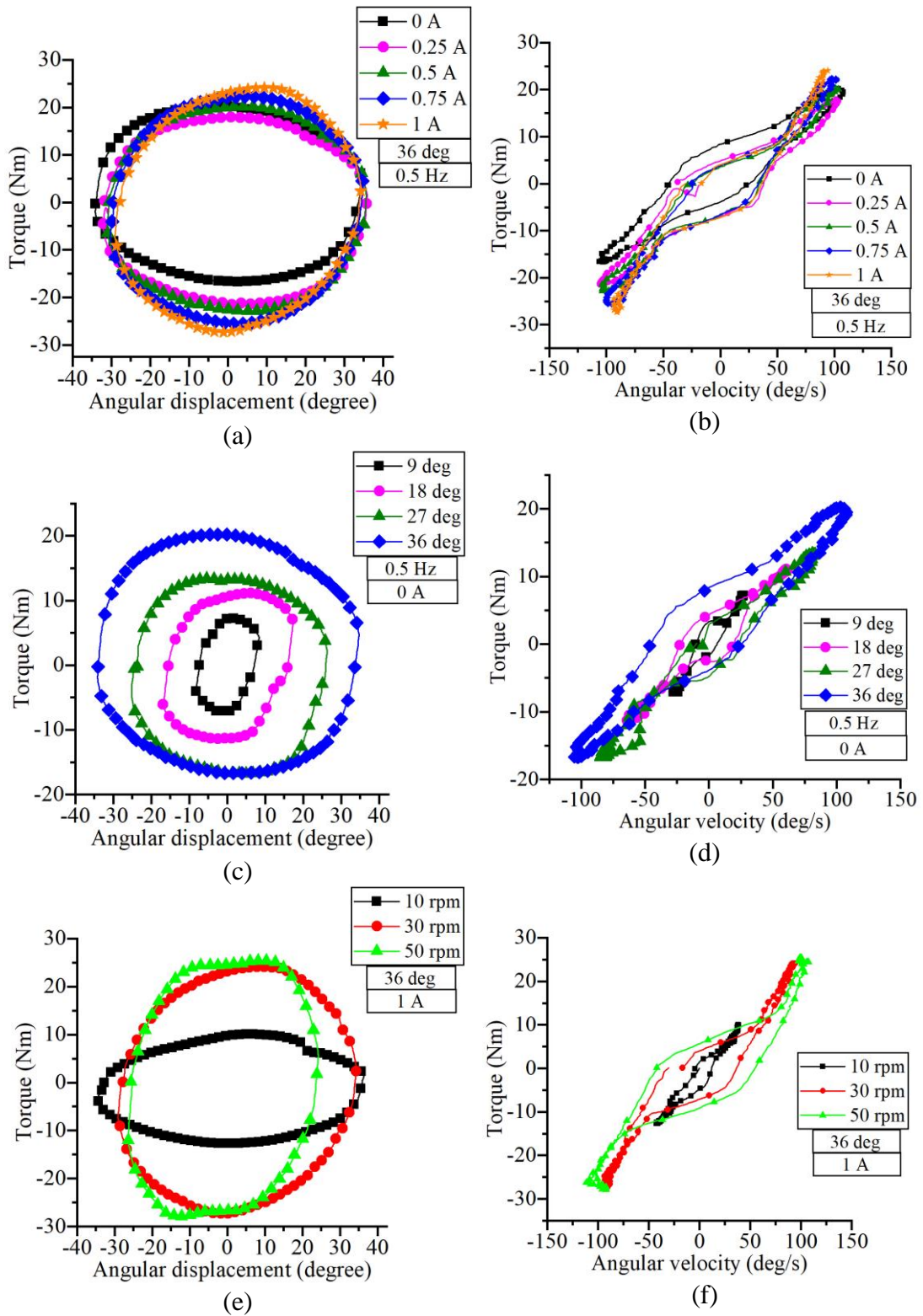


Figure 6.11 Force-displacement and force-velocity curves for varying (a) – (b) currents, (c) – (d) amplitudes and (e) – (f) frequencies respectively.

Considering the magnetostatic analysis results of the axisymmetric cross-section of MR valve in Figure 6.5 (b), the optimal twin rod MR valve also produced similar magnetic flux density distribution in the fluid gap as that of rotary vane MR valve as evident from Figure 6.12. Additionally, other dimensional parameters and material properties are almost similar for both optimal designs as can be verified from Tables 5.2 and 6.1. Since the performance of the MR valve in the twin rod MR damper was in correlation with the theoretical design values, bypass MR valve can be safely neglected as a reason for obtaining low dynamic range in the current design too.

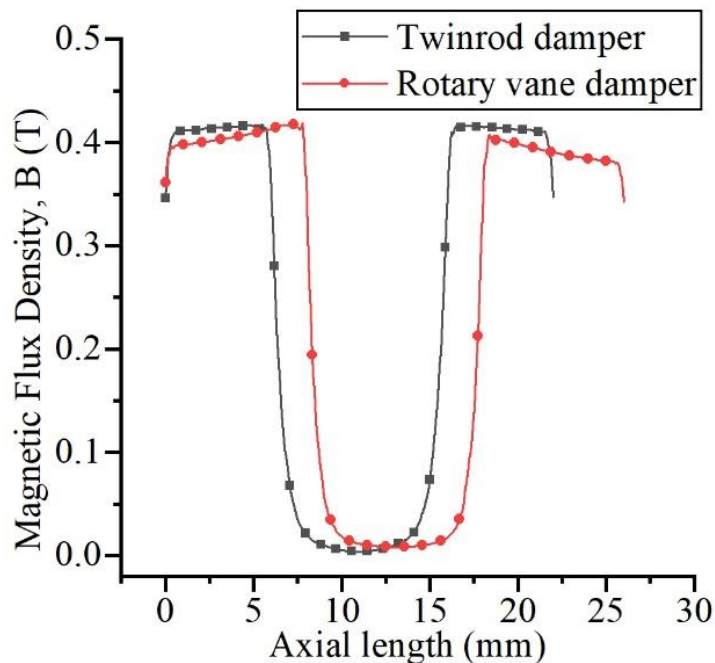


Figure 6.12: Magnetic flux density in fluid gap

A few other possible reasons for the deviation in experimental and theoretical results are:

1. Leakages around the axial or radial faces of the rotary vane and sides of static vane are considered as one of the main reasons for under performance of the design. Therefore, a low dynamic range of 1.4 was obtained due to the presence of leakage paths over high resistance annular channels in MR valve.

2. Use of multiple seals on rotary vane along with shaft seals, frictional losses due to multiple entrances, exits and hydraulic losses contributed to the increase of off-state braking torque.
3. Unaccounted masses of hydraulic ports, cables, MR fluid and static vane led to an increase in overall mass of device.

The rotary vane design by Kim and Oh (2001) consists of a rectangular channel in a bypass MR valve, thus reducing many entrance and exit losses. This configuration resulted in an off-state torque of 1.5 Nm, however, the on-state torque was found insufficient for prosthetic knee application. Previous studies on bypass MR valves (including those using linear MR damper configuration) assumed minimal losses owing to intricate valve dimensional changes. Although the dimensions of the hydraulic connections utilised in previous studies were not explicitly specified, they are noticeably larger than those employed in this investigation. The weight of the device is a significant restriction in this application, and as a result, low density hydraulic cables with an inner diameter of 4 mm were employed, which is believed to be one of the reasons for the large off-state damping torque. Similar differences in off-state damping forces were seen in a study by Idris et al., (2020), in which the researchers evaluated the use of a concentric bypass MR valve in conjunction with a linear damper. Off-state damping forces were found to be tenfold greater in experiments than in simulations identical to the current work. The researchers determined that the probable cause was seal friction. However, in comparison to the present bypass MR valve, the one developed by Idris et al. is concentric in design and involves fewer valve dimensional changes, suggesting that frictional losses associated with these modifications might also possibly account for this difference.

It should be noted that the static vane can be completely avoided and the rotary chamber can be made into a semi-circular cross-section. However, the additional mass due to hydraulic ports, cables and MR fluids cannot be avoided. Since the vane damper design is the lowest possible mass design which can produce a required braking torque of more than 35 Nm, these additional units will further increase the mass of the vane damper even if they are specifically designed for this device. Also, they contribute for an increase in off-state braking torque.

6.7 COMPARISON OF VARIOUS PROSTHETIC KNEE SYSTEMS

Table 6.2 shows a comparison of various dampers applied for prosthetic knee systems along with two damper designs from the present work. A force arm length of 40 mm was chosen to convert the dynamic force into knee torque. It can be observed that the twin rod MR damper can provide the required braking torque at the knee joint and has performance indices much better than those of the commercial MR brake model. However, it has a higher off-state braking torque. It should be noted that the off-state force for linear dampers was calculated at a design speed of 0.1 m/s. Considering the assumed arm length of 40 mm, this corresponds to a rotational speed of 2.5 rad/s, whereas the design speed of rotary brakes is around 0.84 rad/s (8 rpm). From the first part of equation (5.1), it can be stated that the viscous force of a linear damper varies proportionally to the velocity and thus a reduced off-state damping force can be expected for lower speeds. Also, employing a chromium coating similar to the ones used in commercial designs is believed to further reduce the off-state damping force of the linear twin rod MR damper.

The mass of the twin rod damper is less than that compared to all other devices applied for prosthetic applications, apart from the hybrid waveform boundary MR brake. The low dynamic range of the damper is due to the high off-state force of the MR damper. On the other hand, the rotary vane damper in the current work performs better than the rotary vane MR damper designed in the study by Kim and Oh (2002). However, it fails in supplying the required knee braking torque and also has a very high mass in comparison with other dampers applied for prosthetic knee applications. The vane damper requires many modifications in terms of design before it can be considered for prosthetic knee application. The mass of the damper can be reduced by eliminating the static vane completely and by considering a semi-circular cross-sectional design. The MR valve design can be modified into a design which can gradually lead the flow to the fluid gap, rather than the sudden step reduction in the present design. However, this may further increase the mass of the damper and an optimal design procedure may be followed.

Another factor in the prosthetic knee damper design is the degree of deterioration of the MR fluid. This can be evaluated based on an ad-hoc measure, lifetime dissipated energy (LDE) given by the following equation (Carlson 2005).

$$LDE = \frac{1}{V} \int_0^{life} P dt \quad (6.15)$$

Here, V is the volume of the MR fluid in the device and P is the instantaneous mechanical power converted to heat. Note from Table 6.2 that the maximum damping torque of the twin rod damper from the current work is almost similar to the commercial brake model. Thus, mechanical power calculated using the mechanical torque and angular speed for the commercial model in the study by Hreinsson (2011) during each walking cycle can be assumed to be similar in both the cases. The LDE measure is thus scaled based on the volume of the MR fluid, which is around 1.2 ml for the commercial brake model and around 60 ml for the current twin rod MR damper. Therefore, the twin rod damper is expected to produce much lower LDE values for similar cycles.

Although higher MR fluid usage increases the cost of the device, the comparatively larger fluid gap tolerance in current damper design allows the use of larger sized iron particles as opposed to bimodal MR fluids in commercial brake model. Also, larger fluid gap clearances allow for lower shear rates, which in turn reduces MR fluid degradation. Therefore, considering the present design configurations, it can be stated that the twin rod MR damper from the present work can sufficiently produce the necessary damping force required during normal human walking and also is an optimal design for prosthetic knee application. Further experiments are required on the twin rod MR damper to be able to comment on durability, structural stability and other aspects of the overall prosthetic knee system integrated with the damper from the present work.

Table 6.2. Comparison of prosthetic knee MR devices

	Current work		Linear dampers			Rotary dampers/ MR brakes		
	Rotary damper	Linear damper	MR damper (Gao et al. 2017)	MR damper (Park et al. 2016)	LORD RD-8040 - 1	Össur brake (Mousavi and Sayyaadi 2018)	MR brake with waveform boundary (Mousavi and Sayyaadi 2018)	Vane type MR damper (Kim and Oh 2002)
Design	Rotary vane type	Twin rod MR damper	Twin rod damper	Twin rod damper	Mono tube	Multi plate	T-shaped rotor with waveform boundary	Rotary vane damper with MR valve
Fluid regime	Flow mode	Flow mode	Flow mode	Flow mode	Flow mode	Shear mode	Hybrid mode	Flow mode
Mass (kg)	1.1	0.71	0.74	-	0.89	0.8	0.7	-
MR gap	0.56 mm	0.67 mm	1.1 mm	1 mm	0.2 – 1 mm	30 -35 μm	0.2 mm	1.4 mm
Maximum On-state Torque (Nm)	33 @ 1 A	40.8 Nm @ 1 A	24 @ 0.8 A	6 @ 90 mA	~ 48.9 Nm @ 1 A	38	38.5 @ 1.2 A	23
Off-state torque (Nm)	5 @ 8.4 rpm	~ 5.2	3.8	0.44	~ 2.4	2.4 @ 8 rpm	2.1 @ 5 rpm	1.5 Nm @ 10 rpm
TMR (Nm/kg)	~ 30	57.46	32.43	-	54.94	47.5	55	-
Dynamic range	6.6	7.84	6.31	13.6	20.37	15.83	18.33	15.33

6.8 SUMMARY

In the present chapter, optimal design of a rotary vane MR damper is considered using the O-COM methodology with maximizing on-state braking torque and minimizing mass as the objective functions. A few design modifications are performed based on the prototype handling. A rotary equivalent of a damper testing machine is developed which can produce harmonic excitations with variable amplitudes and frequencies to characterize the vane damper. After characterization of the vane damper, it is observed that the present design configuration has high off-state damping torque and also cannot adequately produce the required maximum knee braking torque. A comparative study is performed on the twin rod MR damper and vane type MR damper design, along with many designs from literature and two commercial models. Considering the present design configurations, it can be stated that the twin rod MR damper from the present work can sufficiently produce the necessary damping force required during normal human walking and also is an optimal design for prosthetic knee application.

In the next chapter, a mathematical model of this optimal damper is performed which is later considered for a closed loop control study of a semi-active prosthetic knee model.

CHAPTER 7

SEMI-ACTIVE PROSTHETIC KNEE MODEL – A CLOSED LOOP CONTROL STUDY

7.1 INTRODUCTION

The development of accurate dynamic models of prosthetic devices can be used to predict kinetic or kinematic performances of an amputee by incorporating the prosthetic model with the musculoskeletal model (Chien et al. 2014). Further, the performances can be easily evaluated and the effect of parameters on the prosthetic device can be studied and altered suitably. A qualitative evaluation of amputee gait conducted by Bae et al. (2007) involved performing gait tasks for normal and stair ascent-descent. The kinetic data further coupled with musculoskeletal models revealed that the high power and moment at the knee joint of amputees' sound limbs compensated for the lack of prosthetic limbs. Their study involved clinical trials conducted on the amputees themselves and for prosthetic devices which are still in prototype stages, clinical trials may prove quite risky. Thus a dynamic model of the prosthetic device may help a great deal in not only obtaining the kinematic performances, but also in evaluating kinetic performances and muscle forces at the design stage itself.

In the present chapter, a mathematical model is developed for the twin rod MR damper (optimal design configuration among the four studied designs). An inverse model is also proposed based on the forward dynamic model of the damper. A PD plus CT torque controller, along with the forward and inverse models are applied to a single axis prosthetic knee model to realize a closed loop semi-active prosthetic knee model. The closed loop dynamic model of the prosthesis is analyzed for the swing phase of the gait cycle and the kinematic performances are evaluated.

7.2 MATHEMATICAL MODELING OF TWIN ROD MR DAMPER

Hysteresis and non-linearity are two inherent characteristics of an MR damper and many dynamic models have been proposed in literature to characterize them. Theoretical models of the MR damper can be derived for the given damper geometry based on parallel plate or axisymmetric models using the Bingham fluid model, Herschel-Bulkley model, etc. (Goldasz and Sapiński 2015). These models are easy to implement in numerical simulation, but they cannot predict well the non-linearity of the MR damper. Bouc-Wen operator based models are one of the parametric models well studied in the past and have been known to capture the hysteresis and non-linearity (Rossi et al. 2018; Wang and Liao 2011). Therefore, in the present study, a parametric Bouc-Wen model given by Equation (7.1) is employed. The model parameters are evaluated by minimizing a chosen error function between the experimentally measured damping forces and model-predicted forces.

According to the Bouc-Wen model, damping force of the MR damper is given by Equation (7.1).

$$F_d = Kx + C\dot{x} + \mu z + f_0 \quad (7.1)$$

Here, K is the stiffness and C is the damping coefficient, x is the piston displacement, \dot{x} is velocity, z is the hysteresis variable, μ is the scaling parameter and f_0 is the force offset.

Generally, in the Bouc-Wen model, offset force is included in the spring force itself using the initial deflection variable (Kwok et al. 2007; Spencer et al. 1997), but the considered design of the MR damper has no accumulator and thus the stiffness, K is considered as zero, and further an offset force was included. To accommodate the hysteresis in the off state too, the scaling parameter considered by Mao (2011) was modified as follows.

$$\mu = \alpha_0 + \alpha I^\beta \quad (7.2)$$

Here, α_0 , α and β are the parameters of the MR damper and I is the current supplied to the damper.

The hysteresis operator is defined by Equation (7.3).

$$\dot{z} = -\gamma z |\dot{x}| |z|^{n-1} - \phi \dot{x} |z|^n + \delta \dot{x} \quad (7.3)$$

Here, γ , ϕ , δ and n are hysteresis loop variables. Since the data sets considered are of a single cycle, the initial condition of the hysteresis operator plays an important role in evaluating damping force. According to Ikhoulane and Rodellar (2007), the initial value of hysteresis operator is given by Equation (7.4). This value is also referred to as the ultimate hysteretic strength, Z_u (Spencer et al. 1997).

$$Z_u = \sqrt[n]{\frac{\delta}{\gamma + \phi}} \quad (7.4)$$

7.3 OPTIMIZATION OF BOUC – WEN MODEL PARAMETERS

A total of 9 parameters $\{C, \alpha_0, \alpha, \beta, \gamma, n, \phi, \delta, f_0\}$ are required to estimate the damping force at different displacements and velocities. The stiffness coefficient is neglected since there is no inherent accumulator in the device. An optimization algorithm is used to evaluate these parameters. The error norms for time, displacement and velocity given by Equations (7.5) to (7.7) respectively are used to estimate the deviation of the model from the experimental data (Spencer et al. 1997).

$$E_t = \sqrt{\frac{\int_0^T (F_{\text{exp}} - F)^2 dt}{\int_0^T (F_{\text{exp}} - \bar{F}_{\text{exp}})^2 dt}} \quad (7.5)$$

$$E_x = \sqrt{\frac{\int_0^T (F_{\text{exp}} - F)^2 \left| \frac{dx}{dt} \right| dt}{\int_0^T (F_{\text{exp}} - \bar{F}_{\text{exp}})^2 dt}} \quad (7.6)$$

$$E_v = \sqrt{\frac{\int_0^T (F_{\text{exp}} - F)^2 \left| \frac{d\dot{x}}{dt} \right| dt}{\int_0^T (F_{\text{exp}} - \bar{F}_{\text{exp}})^2 dt}} \quad (7.7)$$

Here, F is the predicted model force value, F_{exp} is the experimentally measured force, and \bar{F}_{exp} is the average experimental force value along the cycle period, T .

A multi objective genetic algorithm as an optimization procedure was used to minimize the error function between the experimental results and the model results. Out of 75 experimental data sets, a total of 20 data sets which include varying frequency, amplitude and current were selected for the optimization process. The cumulative error function vector was modified accordingly as shown in Equation (7.8).

$$e = \left[\frac{\sum_{i=1}^{N_d} (E_t)_i}{N_d}, \frac{\sum_{i=1}^{N_d} (E_x)_i}{N_d}, \frac{\sum_{i=1}^{N_d} (E_v)_i}{N_d} \right] \quad (7.8)$$

Here, N_d is the number of data sets considered. The bounds of the model parameters will have a significant effect on the optimization problem. Assuming zero hysteresis, the upper bound of the damping coefficient, C_{max} for any given experimental cycle can be determined according to Equation (7.9).

$$C_{\text{max}} \leq \frac{F_{\text{max}} - F_{\text{min}}}{\dot{x}_{\text{max}} - \dot{x}_{\text{min}}} \quad (7.9)$$

Here, F_{min} and F_{max} are the minimum and maximum damping forces, \dot{x}_{min} and \dot{x}_{max} are the minimum and maximum velocities in the cycle. For example, considering Figure 7.1(b), the upper bound of damping coefficient for the cycle with amplitude 10 mm, frequency 1.5 Hz and current of 1 A can be calculated as follows.

$$\begin{aligned} C_{\text{max}} \Big|_{10 \text{ mm}, 1.5 \text{ Hz}, 1 \text{ A}} &\leq \frac{1169 - (-1181)}{0.0942 - (-0.0942)} \\ &\leq 12473.46 \text{ N s/m} \end{aligned} \quad (7.10)$$

Since more than a single dataset is involved, the upper bound of damping coefficient is determined using Equation (7.11).

$$C_{\text{max}} \leq \text{maximum of} \left\{ \left(\frac{F_{\text{max}} - F_{\text{min}}}{\dot{x}_{\text{max}} - \dot{x}_{\text{min}}} \right)_{\forall \text{ cycles}} \right\} \quad (7.11)$$

Similarly the offset force range is determined such that $f_0 \in \left[\text{minimum of } \{ \bar{F}_{\nabla \text{ cycles}} \}, \text{maximum of } \{ \bar{F}_{\nabla \text{ cycles}} \} \right]$. Here, \bar{F} is the average damper force for each cycle. The remaining parameters directly influence the nonlinearity and shape of the hysteresis loop (Ikhouane and Rodellar 2007). The bounds of remaining parameters shown in Table 7.1 are obtained after conducting repeated trial and error simulation runs. A multi objective optimization problem is formulated with the objective function being minimization of the error vector, e and the variables with the bounds defined as in Table 7.1.

Table 7.1: Parameter bounds and optimized values of the mathematical model of MR damper

Parameter (units)	Bounds		Optimized values
	Lower	Upper	
$C \left(\text{N} \cdot \text{s} \cdot \text{m}^{-1} \right)$	1500	55000	2257.4
$f_0 \text{ (N)}$	- 82	59	5.52
$\alpha_0 \left(\text{N} \cdot \text{m}^{-1} \right)$	100	1000	303.93
α	1000	10000	9370.7
β	0.1	2	1.663
γ	2000	6000	5933.4
n	0.7	2	1.48
ϕ	1000	100000	27431
δ	100	1000	907

The optimized values of parameters are also shown in Table 7.1. The experimental and model-generated results for varying amplitude, frequencies and currents are shown in Figure 7.1. The analytical model captures the hysteresis accurately even with off-state. The mathematical model in the present study is compared using the error norms similar to that in the study by Rossi et al. (2018). The optimization algorithm reported average values of 0.2158, 0.0467 and 0.2224 for time, displacement and velocity error norms. The error norms reported for the Bouc – Wen model in the study by Spencer et al. (1997) are 0.167, 0.0585 and 0.135 for time, displacement and velocity error norms.

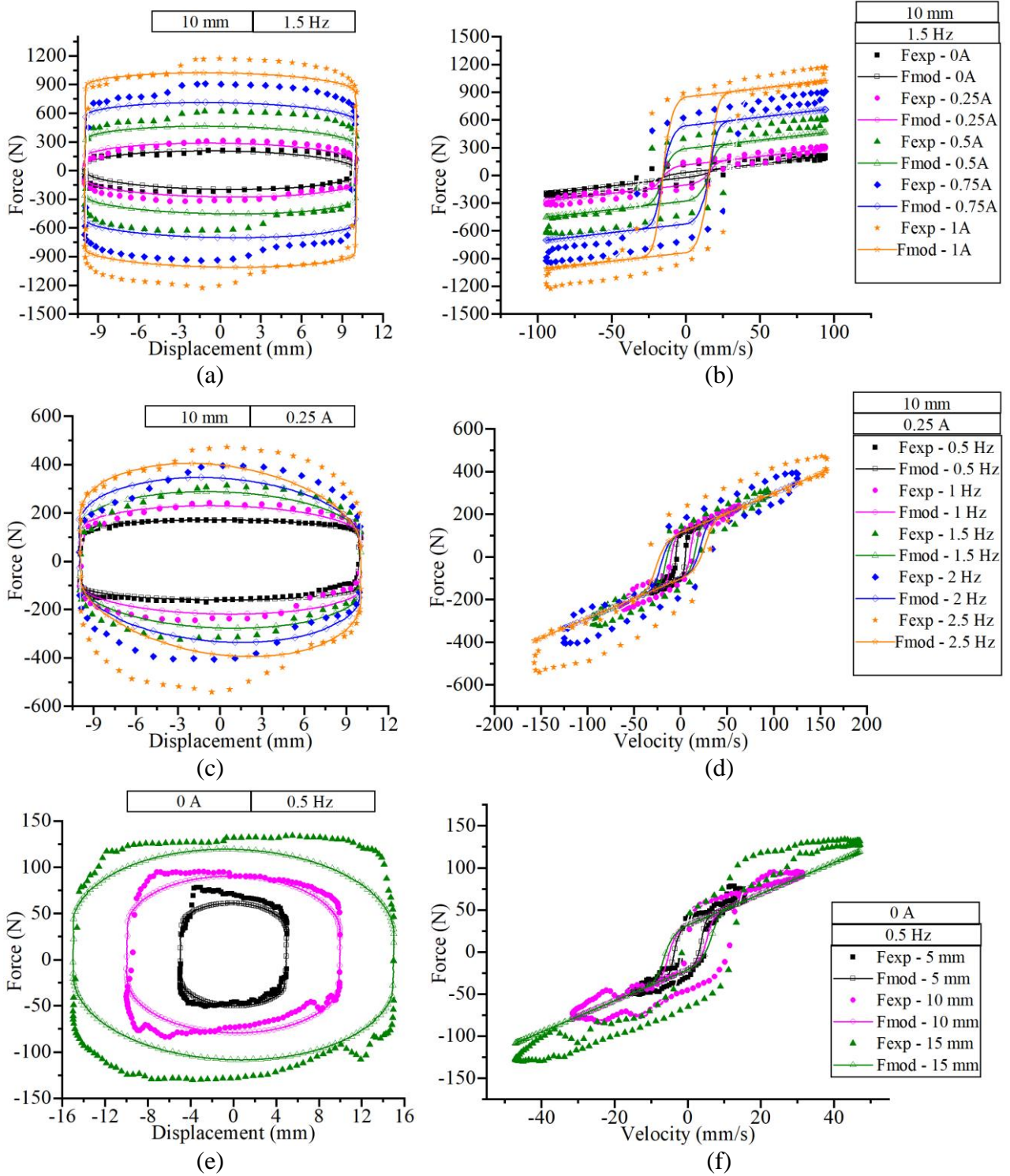


Figure 7.1 Force – displacement and force – velocity curves for experimental and model-predicted values for varying (a) – (b) currents, (c) – (d) frequencies and (e) – (f) displacements respectively (Similar legends for (a)-(b), (c)-(d) and (e)-(f))

It should be noted that the reported error norms in the study by Spencer et al. (1997) were considered for a single cycle, while the values reported in the present study are averaged across 20 data sets used in the optimization algorithm. Table 7.2 lists the error norms for the data sets used in the optimization algorithm and it can be noticed that the values are in accordance with the previous studies with a few deviations for higher frequency data sets.

Table 7.2: Error norms of data sets used in optimization problem

Sl. No.	Parameters			E_t	E_x	E_v
	Amplitude (mm)	Frequency (Hz)	Current (A)			
1	5	0.5	0	0.1574	0.0222	0.0307
2	5	0.5	0.25	0.1463	0.0203	0.029
3	5	0.5	0.5	0.1323	0.0195	0.0249
4	5	0.5	0.75	0.1934	0.0251	0.0416
5	5	0.5	1	0.1974	0.0282	0.0417
6	10	1.5	0	0.2174	0.0435	0.1846
7	10	1.5	0.25	0.1409	0.0292	0.1191
8	10	1.5	0.5	0.2338	0.0457	0.2005
9	10	1.5	0.75	0.2341	0.0428	0.2045
10	10	1.5	1	0.2164	0.032	0.1967
11	15	2.5	0	0.2738	0.0971	0.4644
12	15	2.5	0.25	0.2819	0.0937	0.4975
13	15	2.5	0.5	0.274	0.0835	0.4896
14	15	2.5	0.75	0.2921	0.0806	0.5271
15	15	2.5	1	0.2886	0.0656	0.536
16	10	0.5	0	0.2091	0.0297	0.0595
17	10	1	0	0.1826	0.0329	0.1012
18	10	2	0	0.2104	0.0471	0.2428
19	10	2.5	0	0.2699	0.0717	0.3964
20	15	0.5	0	0.1642	0.0233	0.0604

Further, the model is verified across all the experimental data sets and the calculated error norms are listed in Table 7.3. The error norms are averaged across all the current data sets. For instance, cell 1 of Table 7.3 represents the error norms at amplitude 5 mm, frequency of 0.5 Hz averaged across current data sets from 0 A to 1 A in steps of 0.25 A. The data shows that the model parameters depend on amplitude

and frequency too, apart from the current. Furthermore, the phenomenological modified Bouc-Wen model too which is believed to capture hysteresis well also shows a lot of deviation for random displacement data when the model parameters evaluated using a single cycle experimental data set were used. For this reason, large data sets were used in this study to obtain the model parameters and the average error norms across all the experimental data sets were found to be 0.2092, 0.0428 and 0.1897 for time, displacement and velocity respectively. The average error norms across all experimental data sets are similar to those of datasets used during the optimization process. Therefore, this model can be perceived as a good fit of experimental data and will be used in the semi-active closed loop study.

Table 7.3: Error norms averaged across varying currents

Frequency (Hz)	Error	Amplitude (mm)		
		5	10	15
0.5	E_t	0.1653	0.1604	0.1899
	E_x	0.0231	0.023	0.0315
	E_v	0.0336	0.0452	0.0664
1	E_t	0.1744	0.1764	0.222
	E_x	0.0259	0.0306	0.0431
	E_v	0.0678	0.0985	0.1565
1.5	E_t	0.1872	0.2085	0.2275
	E_x	0.0321	0.0387	0.0507
	E_v	0.1076	0.1811	0.2424
2	E_t	0.2137	0.2257	0.2588
	E_x	0.0426	0.048	0.0665
	E_v	0.162	0.2625	0.3692
2.5	E_t	0.1921	0.2533	0.2821
	E_x	0.0408	0.0615	0.0841
	E_v	0.1796	0.3697	0.5029

7.4 MATHEMATICAL MODELING OF PROSTHETIC LIMB

Dynamic analysis of a prosthetic limb requires a mathematical model of the MR damper incorporated in a lower limb model. The differential equations of motion of the lower limb are formulated using a two segment single axis knee joint, assuming a fixed ankle joint. The free body diagram of a lower limb model in swing phase is shown in Figure 7.2. Here, θ_1 represents the absolute angular displacement of the hip, θ_2 is the absolute angular displacement of the knee, L_1 is the thigh segment length, L_2 is the shank segment length, r_1 is the distance from the hip to the mass center of the thigh, r_2 is the distance from the knee to the mass center of the shank, m_1 is the thigh mass, m_2 is the shank mass including the foot, τ_1 is the torque applied at the hip, τ_2 is the torque applied at the knee, I_1 and I_2 are the moments of inertia of the thigh and shank-foot segments about axes passing through their respective mass centers. Also, (x_h, y_h) are the coordinates of the hip with respect to the global reference frame XY ; F_{xh} and F_{yh} are the forces acting at the hip joint.

The convention followed in this study is that the angular displacements, knee and hip joint torques are all considered positive in the counterclockwise direction.

Following the present convention, and assuming that the hip can be actively controlled by the patient, the differential equations of motion considering only the knee joint and neglecting the ground reaction forces thus are in the following form (Borjian 2008).

$$I_\phi \ddot{\theta}_2 + V(\theta_1, \theta_2) = \tau_2 \quad (7.12)$$

where,

$$I_\phi = I_2 + m_2 r_2^2 \quad (7.13)$$

$$V(\theta_1, \theta_2) = m_2 g r_2 \sin \theta_2 - m_2 r_2 \left\{ \begin{array}{l} L_1 \dot{\theta}_1^2 \sin(\theta_1 - \theta_2) - L_1 \ddot{\theta}_1 \cos(\theta_1 - \theta_2) \\ -\ddot{x}_h \cos \theta_2 - \ddot{y}_h \sin \theta_2 \end{array} \right\} \quad (7.14)$$

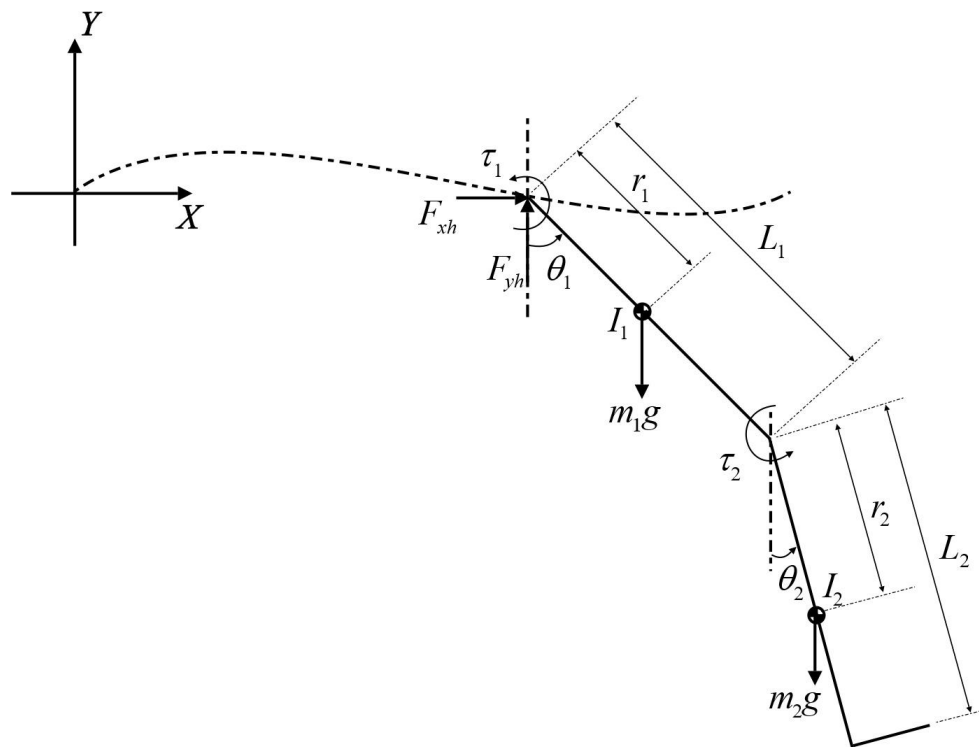


Figure 7.2 Free body diagram of lower limb model in swing phase

The inputs to the model such as thigh displacements and their derivatives, as well as hip joint accelerations are obtained from Winter (2009). The weight of the semi-active prosthesis reported in literature varies distinctly with a few of them higher than their anthropological counterparts (Park et al. 2016) and others lower than them (Herr and Wilkenfeld 2003; Ochoa-Diaz et al. 2014). The total mass of the semi-active prosthesis including knee mechanism, solid ankle cushioned heel (SACH) foot, installed electronics, and excluding the mass of the damper is around 1.75 kg as reported by Pandit et al. (2018). The fabricated damper in the present study has a mass of 0.71 kg, bringing the whole weight of the prosthesis to around 2.5 kg, assuming the rest of components to be similar to those in their study. Further, the study performed by Narang et al. (2016) on the effect of inertial properties on knee prosthesis revealed that reducing the prosthetic mass by 25% of the physiological leg mass decreases peak swing knee moment. Thus, in any case, it is always better that the prosthesis mass is similar to or less than that of the physiological leg. In the current study, the inertial properties of the physiological leg will be considered for further analysis of the prosthetic leg. The parameters of the subjects' lower limb are given in Table 7.4. A

subject of mass 56.7 kg is considered for the study and the inputs are scaled anthropometrically.

Table 7.4: Parameters of subjects' lower limb (Winter 2009)

Parameter	Value
m_2	3.46 kg
I_2	0.108 kg · m ²
L_1	0.314 m
L_2	0.425 m
r_2	0.2576 m

7.5 SEMI-ACTIVE KNEE WITH TWIN ROD MR DAMPER

The length of the damper keeps varying with the knee and so does the damping force, which in turn, controls the torque at the knee joint. The upper part of the damper is connected to the thigh by extending a small perpendicular pin of length s from the knee joint and the other end of the damper is linked to the shank at a distance of b from the joint, K as shown in Figure 7.3.

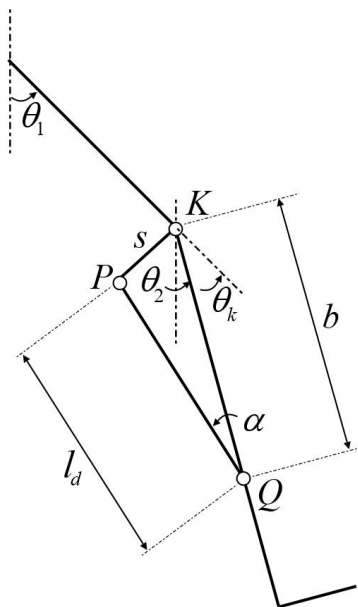


Figure 7.3 Knee joint line diagram

The torque at the knee joint is related to the damping force by Equation (7.15). The angular displacement is positive in the counterclockwise direction and thus the

damping force always acts opposite to the motion which explains the negative sign in the torque equation.

$$\tau_k = -F_d b \sin \alpha \quad (7.15)$$

Considering the triangle PQK in Figure 7.3, the angle α can be calculated using the set of Equations (7.16) and (7.17).

$$l_d = \sqrt{s^2 + b^2 - 2bs \sin \theta_k} \quad (7.16)$$

$$\alpha = \sin^{-1} \left(\frac{s \cos \theta_k}{l_d} \right) \quad (7.17)$$

The fabricated damper in this study has a fully extended length of 0.24 m and a stroke of 50 mm. Thus the value of b in Figure 7.3 is fixed to 0.22 m such that the damper can safely reach full knee extension and maximum knee flexion during walking. Similarly, the value of s is taken as 0.035 m based on the initial structural design carried out in a previous study (Seid 2017). Further, initial computational studies conducted using just the knee joint damper showed that the shank does not reach full knee extension at this phase end. The use of a spring in compressed form can store some energy in the stance phase and assist the shank to full extension. Current prostheses such as stabilized knee, Rheo knee also use springs for active knee extension (Wentink et al. 2013). Further, off the shelf MR dampers by Lord Corporation used previously in studies (Carlson et al. 2001; Pandit et al. 2018) of prosthetic devices used an accumulator in their design, providing compliance to the device and thus did not require any other form of energy storage element. Since in the present study, a twin rod MR damper is considered which does not require an accumulator at least for volume compensation, a spring is modeled in parallel to the damper to assist in full knee extension. The knee torque given by Equation (7.15) is modified to include the spring stiffness and is shown in Equation (7.18).

$$\tau_k = -[F_d + k_s (l_d - x_0)] b \sin \alpha \quad (7.18)$$

Here, k_s is the spring stiffness and x_0 is the initial length of the spring.

7.6 PD PLUS CT CONTROL

A PD plus CT controller is employed in this study. The CT term is initialized to cancel out the nonlinear terms and thus the equations of motion are linearized and a PD controller acts on the linear part of the dynamic equation. The control input torque is given by Equation (7.19) (Park et al. 2016).

$$\tau_c = I_\phi \ddot{\theta}_{2d} + K_p (\theta_{2d} - \theta_2) + K_d (\dot{\theta}_{2d} - \dot{\theta}_2) + V(\theta_1, \theta_2) \quad (7.19)$$

Here, K_p is the proportional and K_d is the derivative gain, θ_{2d} is the desired knee angle, $\dot{\theta}_{2d}$ is the desired knee angle velocity and $\ddot{\theta}_{2d}$ is the desired knee angle acceleration. Substituting the control torque input given by Equation (7.19) in place of the knee torque in Equation (7.12) helps obtain Equation (7.20). This equation represents the error dynamic equation of the PD controller.

$$I_\phi \ddot{e} + K_d \dot{e} + K_p e = 0 \quad (7.20)$$

The controller remains stable as long as the poles of the system remain on the left half of the s plane. The output of the controller is a control torque input that can be converted to damping force by using Equation (7.18). An inverse model is necessary to calculate the driving current to be supplied to the damper which generates the required amount of force. Substituting Equation (7.2) in Equation (7.1) and eliminating the stiffness K since it is set to zero and after suitable rearrangement, the driving current input can be expressed as,

$$I = \left\{ \left[\frac{(F_d - C\dot{x} - f_0)}{z} - \alpha_0 \right] \frac{1}{\alpha} \right\}^{1/\beta} \quad (7.21)$$

By estimating the parameter z as $Z_u \operatorname{sgn}(\dot{x})$, where Z_u represents the ultimate hysteretic strength given by Equation (7.4), the input current can be estimated by modifying Equation (7.21) as,

$$I = \left\{ \left[\frac{(F_d - C\dot{x} - f_0)}{Z_u \operatorname{sgn}(\dot{x})} - \alpha_0 \right] \frac{1}{\alpha} \right\}^{1/\beta} \quad (7.22)$$

Since the MR damper cannot supply positive power and can only dissipate energy, the passivity constraints given by Equation (7.23), and the limitation constraints given by Equation (7.24) should be satisfied (Tsang et al. 2006).

$$F(t) = \begin{cases} F_{optimal}(t), & F_{optimal}(t) \cdot v(t) > 0 \\ 0, & F_{optimal}(t) \cdot v(t) \leq 0 \end{cases} \quad (7.23)$$

Here, $F_{optimal}(t)$ is the optimal force given by the PD plus CT control algorithm and $v(t)$ is the damper velocity.

$$|F_{min}(t)| \leq |F_{optimal}(t)| \leq |F_{max}(t)| \quad (7.24)$$

Here, $|F_{min}(t)|$ and $|F_{max}(t)|$ are the magnitudes of the minimum and maximum forces that can be produced by the damper at the given instant of time t .

Substituting Equation (7.2) in Equation (7.1) and assuming the hysteretic parameter as the ultimate hysteretic strength, the maximum and minimum damping forces can be evaluated as follows,

$$F_{min} = C\dot{x} + \alpha_0 Z_u \operatorname{sgn}(\dot{x}) + f_0 \quad (7.25)$$

$$F_{max} = C\dot{x} + (\alpha_0 + \alpha I_{max}^\beta) Z_u \operatorname{sgn}(\dot{x}) + f_0 \quad (7.26)$$

Here, I_{max} is the maximum value of current that can be allowed in the damper. Based on the optimal design current, a value of 1 A is taken for I_{max} .

Thus if the conditions given by Equations (7.23) and (7.24) are satisfied, the current is supplied according to Equation (7.22), otherwise, a value of 0 A or 1 A is decided based on the limiting constraints.

7.7 RESULTS AND DISCUSSION

The literature provides a large repository of gait data normalized to body weight. The thigh angular displacements and their derivatives, along with the desired knee angle trajectories and their derivatives for normal human walking are provided as inputs to the model from Winter (2009). Using the anthropometric data from Table 7.3 and

Equation (7.19), the control torque input is calculated. Equation (7.15) converts the control torque to the damping force required and Equation (7.22) provides the current input required to the model. The forward dynamic model represented by the Bouc - Wen model given by Equation (7.1) is utilized to calculate the effective damping force. This is later used in the differential equation of motion given by Equation (7.12) and the knee angle trajectories are evaluated. The PD plus CT controller minimizes the error difference between the desired and the actual knee angular displacements. The structure of the model employed in Simulink is shown in Figure 7.4.

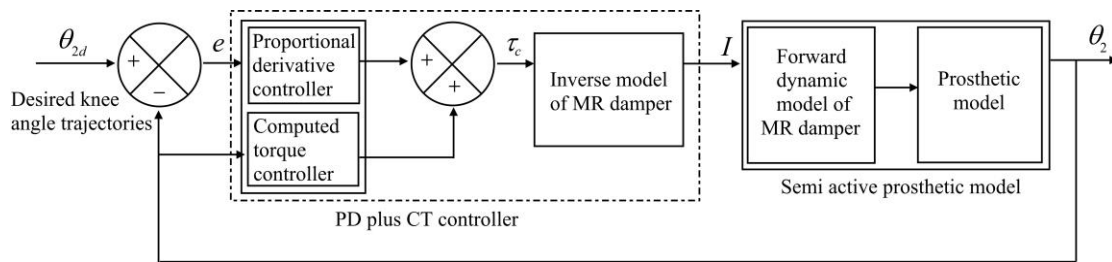


Figure 7.4 Block diagram of the simulation model

The structure shown in Figure 7.4 is implemented in Simulink software. For the prosthetic limb to reach full extension, the spring stiffness, k_s and the initial length of the spring are set to 2000 N/m and 0.27 m respectively. The total length PQ in Figure 7.3 in fully extended knee position is 0.2227 m, which is below the assumed initial length of the spring; thus the spring remains in the compressed state till the end of the swing phase. The control parameters, K_p and K_d are tuned to reduce the error difference between the controller-estimated torque and the desired knee torque. The controller-estimated torque and the desired torque are shown in Figure 7.5. The achievable range is defined as the range in which both the passivity and limitation constraints defined by Equations (7.23) - (7.24) are satisfied.

Upon trial and error and based on the criteria of minimizing the error between the controller-estimated and the desired torque, the proportional and derivative gain values are taken as 1.48 and 1.18 respectively. The poles of the system remain on the left half of the s -plane for the selected values of control parameters. The desired and the obtained knee angle trajectories are plotted in Figure 7.6. As seen in the figure, the model tracks the desired knee angular displacements with excellent accuracy. The knee

reaches a maximum knee flexion angle of 59.25° at a similar gait state and also reaches full extension at the end of swing phase.

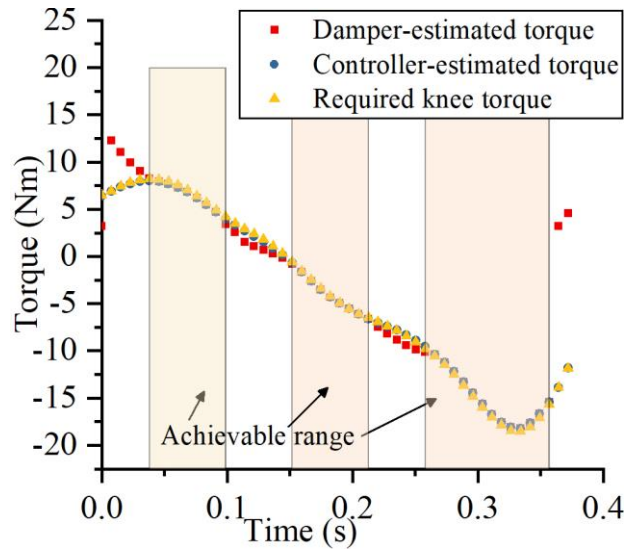


Figure 7.5 Estimated and obtained torque curves

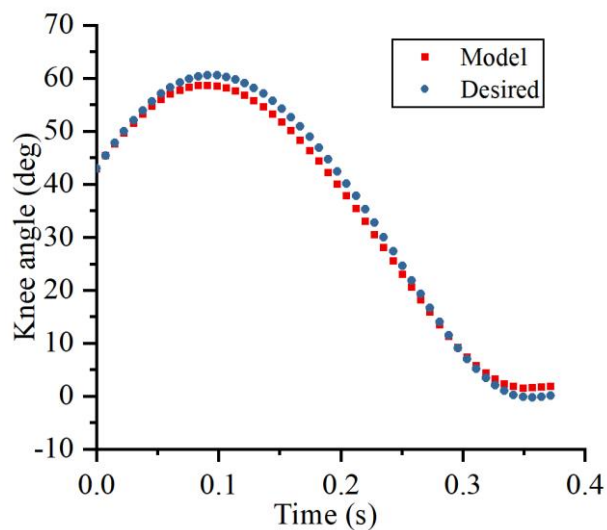


Figure 7.6 Desired and simulated knee angle trajectories

Figure 7.7 shows the power at the knee joint and Figure 7.8 shows the current to be supplied to the damper. The power dissipation in the swing phase of the gait cycle is dissipative in nature, except at the end of the swing phase and at the position where the knee reaches a maximum flexion. Both the model and the desired values match to a good extent except in the non-achievable range. The model predicts a positive power right after the knee reaches maximum flexion angle at 0.1 s. This is because of the

potential energy stored in the spring which assists the device in early knee extension, thus supplying positive power. During this phase, the spring force dominates the damping force and the damper supplies the least amount of force. Also, the current supplied to the damper is zero during that phase as can be verified in Figure 7.8. Further, as the simulation proceeds, the damping force starts to be modulated and the knee traces the desired angle.

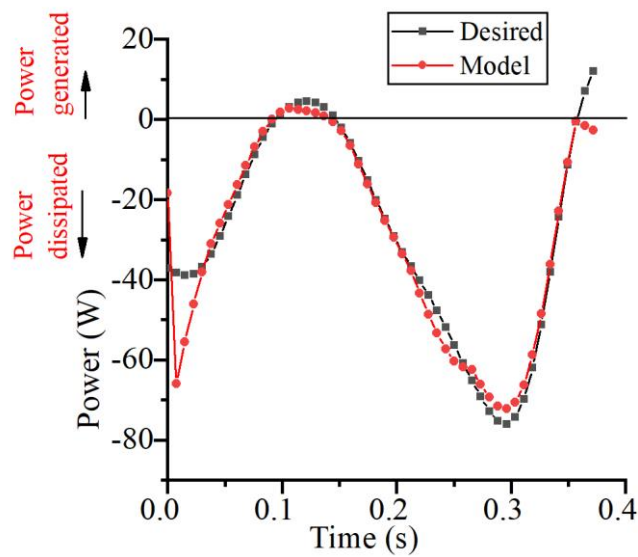


Figure 7.7 Power generated and power dissipated at knee joint

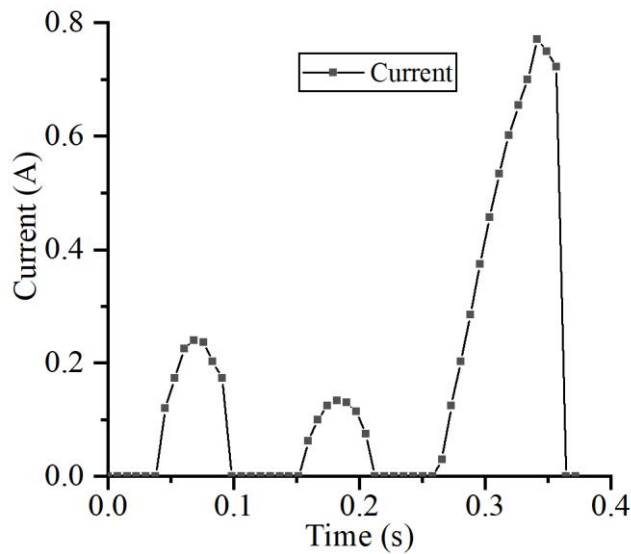


Figure 7.8 Current input supplied to the MR damper

In figure 7.8, there are three different current peaks observed. They are typically equivalent to the three phases of swing phase of gait cycle which are initial swing, mid swing and terminal swing. Initial swing corresponds to 60 – 73% of gait cycle (0 – 0.1s) and begins with a lift off and ends when the swinging foot is opposite to stance foot. At the end of this phase, knee angular velocity becomes zero and the shank begins to move in the opposite direction. In the present model, spring constant has been used which serves as a positive power to the prosthetic at the terminal stance phase and thus the controller adjusts the current such that the knee angular velocity becomes zero at the end of first phase. The second phase, mid-swing corresponds to 73% to 87% of gait cycle (0.1 – 0.25 s) and ends when the swinging limb is forward and shank is almost perpendicular to ground. Since the knee observes a large angular displacement of approximately 50° , current supplied is minimal. In the terminal swing phase which corresponds to 87 – 100 % of gait cycle (0.25s – 0.38 s), shank prepares itself for foot strike and knee comes to a complete stop. Therefore, a peak value of 0.8A of current supplied is observed in this phase to reduce the knee angular speed.

The current levels shown in Figure 7.8 vary between 0 A and the maximum allowable value of 1 A. Thus, a passive damper with a constant equivalent damping coefficient cannot mimic the normal human knee displacement. Further, different levels of damping by using finite state controllers with only one state for the whole of the swing phase may not capture the knee angle trajectories well.

7.8 VALIDATION OF THE INVERSE MODEL

Tsang et al. (2006) derived simple inverse dynamic models based on the Bingham and modified Bouc-Wen models. Two types of feedback, such as position feedback and force feedback methods were proposed. But the inverse model using modified Bouc-Wen model was not used; rather a form of the exponential function relating the yield force to the current supplied was characterized specific to the damper and was further used as an inverse model. The reason was that in the modified Bouc-Wen model, three parameters were assumed to be current dependent, and even after assuming the hysteresis parameter z as the constant ultimate hysteretic strength, the model results in a polynomial in the current parameter (Attia et al. 2016). Solving the

polynomial model requires a large computational effort at each time step and therefore, the exponential form of yield force given by Equation (7.27) was used.

$$F_{\tau} = k_4 - k_5 e^{-k_6 i} \quad (7.27)$$

Here, F_{τ} is the yield force, i is the current supplied to the damper, k_4 , k_5 and k_6 are the parameters specific to each damper configuration (Tsang et al. 2006; Yang et al. 2002).

Using Equation (7.27), the current to be supplied to the damper can be estimated if the controller predicts the required optimal yield force. Since in the present study, Bouc-Wen model with only one current dependent parameter is considered, current can be easily estimated using Equation (7.22) with no requirement of solving for any roots of the polynomial. Equation (7.22) can only be used provided the limiting and the passivity constraints are satisfied at that time instant. Figure 7.9 shows the comparison between the PD plus CT controller-estimated damping force and the MR damper output force, thus showing the validity of the considered inverse model. The range of values shown in Figure 7.9 is the damper realizable force range at that particular instant. If the controller-estimated force falls within this range, the inverse model calculates the current using Equation (7.22) and passes it to the prosthetic model. If the controller-estimated damping force does not fall in this range, then depending on the limiting constraints, the damper is supplied with either a 0 A or a maximum current of 1 A.

From the beginning till 0.03796 s the passivity and/or the limitation constraints are not satisfied; thus the damper is supplied with a zero current. From 0.09869 s to 0.1518s, the limitation constraints are not satisfied since the controller-estimated force is less than the damper achievable force range. Therefore, the damper is supplied with no current. The same is reflected in Figure 7.8 too. Therefore, the inverse model can be justified if the two plotted forces match in the achievable force ranges shown in figure which are 0.03796 s – 0.09869 s, 0.1518 s – 0.2126 s and 0.2581 s – 0.3568 s. Figure 7.9 shows that the damper output force and the controller-estimated force match excellently in the provided ranges, thus justifying the validity of the assumed inverse model.

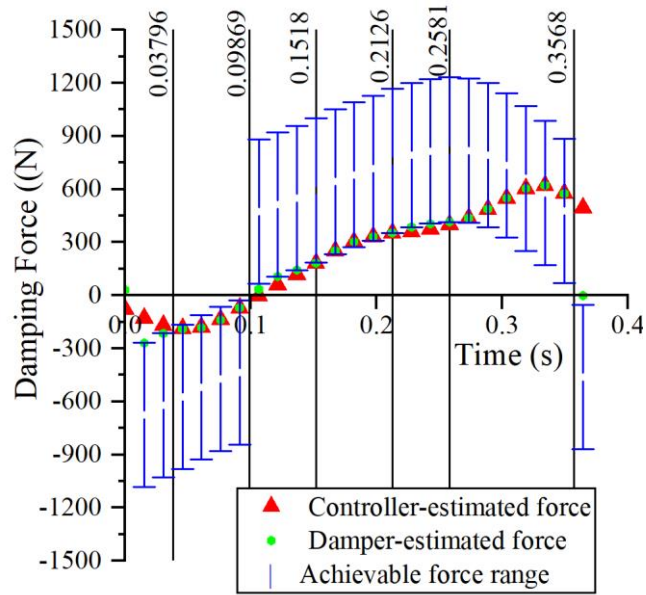


Figure 7.9 Estimated and obtained damping force curves

7.9 SUMMARY

In the present chapter, a dynamic analysis of knee prosthesis was performed using an inverse dynamic model based on Bouc-Wen parametric model. Two parts of experimental data sets were considered, one in the use of an optimization algorithm to obtain the model parameters of the simple Bouc-Wen model and the other data set to determine the accuracy with which the parameters are fit. The average error norms are found to perform well over the selected ranges of experimental data. Further, to capture the hysteresis in the off state also, the current dependent function was modified accordingly. The characterized mathematical model of the damper was used in the single axis two segment prosthetic model. A PD plus CT controller was used and the parameters of the controller were tuned based on the criteria of minimizing the error difference between the controller-estimated torque and the desired torque. An inverse model based on Bouc-Wen model with an upper bound of the hysteresis parameter was used. The dynamic analysis of the prosthetic model was performed with inputs of thigh motion and desired knee motion. The controller with the designed parameters traces the desired angular displacement reasonably well. The maximum knee angle flexion is reached at the same time as that of normal walking and also the knee extends into a full extension with a terminal velocity of 0.9 rad/s which is small enough to be stopped by

a rubber stopper. The inverse model used in this study is simple, yet accurate enough in predicting the desired current to the damper. This inverse model can be extended with different kinds of controllers other than PD plus CT and variable damping can be effectively achieved. The accuracy of the inverse model depends on the accuracy with which the selected damper is characterized, since the inverse model and the forward dynamic model are based on the same parameters.

CHAPTER 8

SUMMARY AND CONCLUSIONS

8.1. SUMMARY

This dissertation presents various design configurations which have a potential for being used in a semi-active prosthetic knee device. The present study aims to obtain an optimal design configuration of an MR damper among the various design configurations available in literature and also a few intuitive designs. Based on an extensive literature survey, an intuitive design of multi-pole MR brake which will provide a uniform magnetic field on the rotor was selected. Also, to reduce the number of electromagnetic coils on the T-shaped rotor configuration which ultimately leads to a very compact design, an inverted drum brake rotor with waveform arc boundary is selected as the second design configuration. Furthermore, because of very limited studies on rotary vane MR damper and owing to its high damping torque to weight ratio, this is selected as the third design configuration. Finally, due to use of suboptimal design methodologies in the design of twin rod MR damper and also to develop an improved design, twin rod MR damper is selected as the fourth design configuration.

Since many studies including the same design objectives and constraints are available on multi-plate MR brake design, this has been omitted for optimal design in this work. Instead, this design is used in performing a comparative study along with many design configurations from literature. A preliminary design optimization is performed on the selected devices which resulted in elimination of two designs on the basis of their insufficiency in producing the required braking torque for prosthetic knee and also due to their large weight. Based on comparative studies, twin rod MR damper and rotary vane MR damper are selected for further optimal design and experimentation.

A combined magnetostatic approach was proposed which is capable of producing accurate design points with highly reduced optimization time as compared to optimization algorithms with state-of-the-art magnetostatic approaches. To evaluate the performance of the proposed combined magnetostatic approach, the two most

commonly used design problems from literature are selected. Hypervolume indicator is calculated for each of the optimization algorithms. Based on the statistical comparison, it was found that the proposed methodology produces similar design optimal points compared to optimization methodology based on finite element method and also reduces the computational time substantially.

An initial prototype of both twin rod and rotary vane damper was fabricated which could provide sufficient insights related to the operation, fluid filling process, etc. followed by an optimal designs using the proposed methodology. The fabricated models of the dampers were experimentally characterized. To characterize rotary vane damper, an experimental test facility was developed, whereas the twin rod MR damper was characterized using the available damper test machine facility. The selected dampers were compared with commercially available MR brake and also with other optimal designs available in literature. The performance indices suggest that the twin rod MR damper can produce the required braking forces for prosthetic knee application. One of the limitations of the present design is that it has high off-state braking force. The mass of the optimal damper is around 0.71 kg, which is less than those of the commercial MR brake and also the commercial MR damper. The present damper also reduces the design complexity associated with the commercial brake by reducing the number of parts and higher fluid gap tolerances.

Finally, a mathematical modeling of twin rod MR damper is performed using the simple Bouc-Wen model. The mathematical model of the MR damper has been coupled with a semi-active prosthetic model and dynamic analysis has been performed for the swing phase of the gait cycle. The results predict that the MR damper can sufficiently reproduce the knee kinematics. An inverse model has been developed by estimating only one current dependency parameter among all parameters of the Bouc-Wen model. As opposed to most used finite state controllers for prosthetic knee application which can only supply damping force in limited bands, this approach can supply variable damping force within the dynamic range of the damper.

8.2. CONTRIBUTIONS

The main contributions of this work can be summarized as follows:

- The novel approach in design optimization of the MR damper can be employed in designing other semi-active devices based on MR fluids. The optimization code can be suitably modified by developing the relevant EMM and FEM models specific to other applications.
- Based on the comparative results of various optimization algorithms, suitable methodology can be employed at various stages of design of MR damper. For instance, initial design can be performed using O-EMM methodology whereas, an optimal design can be performed using O-COM. Further, sensitivity analysis around optimal design points can be performed using FEM analysis.
- The optimal designs of twin rod MR damper presented in this study can be fabricated and be subjected to further experimentation by coupling the damper with a semi-active knee system.
- The rotary vane MR damper can be modified for weight reduction and also to increase the dynamic range based on the conclusions presented in this study.
- The dynamic model of the twin rod MR damper, along with the inverse dynamic modeling approach developed in this study, can be subjected to further numerical simulation studies using various semi-active prosthetic knee parameters and analyzed before proceeding for actual clinical trials.

8.3. CONCLUSIONS

The following conclusions can be directly derived from the work.

- Based on the quantitative comparison of various magnetostatic approaches, it can be concluded that O-COM methodology produces design solutions with comparable accuracy to O-FEM and also reduces computational cost substantially.
- The multi-pole MR brake design generates a uniform magnetic field distribution on the rotor face as compared to a single pole brake design, but is insufficient in its current form to produce the required braking torque within constrained mass.

- Based on the characterization results of optimal twin rod MR damper, it is found that the device can produce a damping force of 1020 N at 1 A, equivalent to a torque of 40.8 Nm (at 40 mm moment arm). The mass of the damper is found to be 0.71 kg and is less than that of commercially available MR brake and MR damper.
- The optimal design of the rotary vane MR damper is capable of producing a maximum damping torque of 33 Nm. However, the mass of the damper is evaluated to be 1.1 kg which is much higher than that of the commercial counterparts.
- The simple inverse model based on the forward Bouc-Wen model of the MR damper can produce the required current inputs for the given force, displacement and velocity of damper accurately.
- The dynamic analysis of the semi-active prosthetic knee coupled with the Bouc-Wen MR damper model has predicted that the damper can be suitably used for prosthetic knee applications.

8.4. SCOPE OF FUTURE WORK

- Further research on waveform arc boundary brake can be considered and effects of design parameters on the braking torque produced by the device can be studied.
- A hollow core design for the multi-pole MR brake can be considered as another alternative design to reduce the mass of the device.
- To reduce the mass of the rotary vane damper, a rotary chamber of semi-circular cross-section can be considered. Also, to increase the dynamic range of the device and to reduce the off-state dynamic torque, alternative configurations for MR valves can be considered.
- The twin rod MR damper can be subjected to further experimentations to comment on durability.
- The developed mathematical model of the twin rod MR damper can be used in simulation studies to develop the prosthetic knee structure, including thigh sockets, shank and foot segments.

- A complete semi-active prosthetic knee system can be fabricated based on the optimal design in this study and can be studied for the whole gait cycle using gait motion simulators or able-bodied adapter studies before it can be actually tested on amputees.

REFERENCES

- Acharya, S., Saini, T. R. S., Sundaram, V., and Kumar, H. (2020). "Selection of optimal composition of MR fluid for a brake designed using MOGA optimization coupled with magnetic FEA analysis." *J. Intell. Mater. Syst. Struct.*
- Andrade, R. M., Filho, A. B., Vimieiro, C. B. S., and Pinotti, M. (2018). "Optimal design and torque control of an active magnetorheological prosthetic knee." *Smart Mater. Struct.*, 27(10), 105031.
- Arteaga, O., Terán, H. C., Morales V., H., Argüello M., E., Erazo, M. I., Ortiz, M., and Morales, J. J. (2020). "Design of human knee smart prosthesis with active torque control." *Int. J. Mech. Eng. Robot. Res.*, 9(3), 347–352.
- Assadsangabi, B., Daneshmand, F., Vahdati, N., Eghtesad, M., and Bazargan-Lari, Y. (2011). "Optimization and design of disk-type MR brakes." *Int. J. Automot. Technol.*, 12(6), 921–932.
- Attia, E. A., Abd El-Naeem, M. A., El-Gamal, H. A., Awad, T. H., and Mohamed, K. T. (2016). "2179. Simulation of the motion of a four bar prosthetic knee mechanism fitted with a magneto-rheological damper." *J. Vibroengineering*, 18(6), 4051–4068.
- Avraam, M., Horodincea, M., Romanescu, I., and Preumont, A. (2010). "Computer controlled rotational MR-brake for wrist rehabilitation device." *J. Intell. Mater. Syst. Struct.*, 21(15), 1543–1557.
- Bae, T. S., Choi, K., Hong, D., and Mun, M. (2007). "Dynamic analysis of above-knee amputee gait." *Clin. Biomech.*, 22(5), 557–566.
- Bahiuddin, I., Mazlan, S. A., Shapiai, M. I., Imaduddin, F., Ubaidillah, and Choi, S. B. (2019). "A new platform for the prediction of field-dependent yield stress and plastic viscosity of magnetorheological fluids using particle swarm optimization." *Appl. Soft Comput. J.*, 76, 615–628.
- Batdorff, M. A., and Lumkes, J. H. (2009). "High-fidelity magnetic equivalent circuit model for an axisymmetric electromagnetic actuator." *IEEE Trans. Magn.*, 45(8), 3064–3072.
- Bellmann, M., Köhler, T. M., and Schmalz, T. (2019). "Comparative biomechanical evaluation of two technologically different microprocessor-controlled prosthetic knee joints in safety-relevant daily-life situations." *Biomed. Tech.*, 64(4), 407–420.
- Bellmann, M., Schmalz, T., and Blumentritt, S. (2010). "Comparative biomechanical analysis of current microprocessor-controlled prosthetic knee joints." *Arch. Phys. Med. Rehabil.*, 91(4), 644–652.
- Bompos, D. A., and Nikolakopoulos, P. G. (2011). "CFD simulation of magnetorheological fluid journal bearings." *Simul. Model. Pract. Theory*, 19(4), 1035–1060.

- Borjian, R. (2008). "Design, modeling, and control of an active prosthetic knee." M.Sc. Thesis, University of Waterloo.
- Brandt, A., Wen, Y., Liu, M., Stallings, J., and Huang, H. H. (2017). "Interactions between transfemoral amputees and a powered knee prosthesis during load carriage." *Sci. Rep.*, 7(1), 1–12.
- C-Leg. (2016). "OttoBock C-Leg." <<http://www.ottobockus.com/media/local-media/prosthetics/lower-limb/c-leg/files/cleg4brochure.pdf>> (Nov. 24, 2020).
- Carlson, J. D. (2002). "What makes a good MR fluid?" *J. Intell. Mater. Syst. Struct.*, 13(7–8), 431–435.
- Carlson, J. D. (2005). "MR fluids and devices in the real world." *Int. J. Mod. Phys. B*, 19(7–9), 1463–1470.
- Carlson, J. D., Matthis, W., and Toscano, J. R. (2001). "Smart prosthetics based on magnetorheological fluids." *Smart Struct. Mater. 2001 Ind. Commer. Appl. Smart Struct. Technol.*, 308–316.
- Chen, C., Hanson, M., Chaturvedi, R., Mattke, S., Hillestad, R., and Liu, H. H. (2018). "Economic benefits of microprocessor controlled prosthetic knees: a modeling study." *J. Neuroeng. Rehabil.*, 15(S1), 62.
- Chien, M. S. C. H., Erdemir, A., Bogert, A. J. van den, and Smith, W. A. (2014). "Development of dynamic models of the Mauch prosthetic knee for prospective gait simulation." *J. Biomech.*, 47(12), 3178–3184.
- Chugh, T., Chakraborti, N., Sindhya, K., and Jin, Y. (2017). "A data-driven surrogate-assisted evolutionary algorithm applied to a many-objective blast furnace optimization problem." *Mater. Manuf. Process.*, 32(10), 1172–1178.
- Coello, C. A. C., Lamont, G. B., Veldhuizen, D. A. Van, Goldberg, D. E., and Koza, J. R. (2007). *Evolutionary Algorithms for Solving Multi-Objective Problems*. *Evol. Algorithms Solving Multi-Objective Probl.*, Genetic and Evolutionary Computation Series, Boston, MA: Springer US.
- Coello, C. A. C., Pulido, G. T., and Lechuga, M. S. (2004). "Handling multiple objectives with particle swarm optimization." *IEEE Trans. Evol. Comput.*, 8(3), 256–279.
- Creylman, V., Knippels, I., Janssen, P., Biesbrouck, E., Lechler, K., and Peeraer, L. (2016). "Assessment of transfemoral amputees using a passive microprocessor-controlled knee versus an active powered microprocessor-controlled knee for level walking." *Biomed. Eng. Online*, 15(3), 53–63.
- Cristian, A. (2005). *Lower Limb Amputation - Guide to live a quality life*. New York: Demos Medical Publishing.

Deffenbaugh, B., and Herr, H. (2004). “Electronically controlled prosthetic knee.” *US Pat. 6,764,520*, 2(19).

Díaz-Manríquez, A., Toscano, G., Barron-Zambrano, J. H., and Tello-Leal, E. (2016). “A review of surrogate assisted multiobjective evolutionary algorithms.” *Comput. Intell. Neurosci.*, 2016, Article ID 9420460.

Ekkachai, K., Tantaworrasilp, A., Nithi-Uthai, S., Tungpimolrut, K., and Nilkhamhang, I. (2014). “Variable walking speed controller of MR damper prosthetic knee using neural network predictive control.” *Proc. SICE Annu. Conf.*, 513–518.

Erol, O., and Gurocak, H. (2011). “Interactive design optimization of magnetorheological-brake actuators using the Taguchi method.” *Smart Mater. Struct.*, 20(10), 105027.

Fan, Z., Wang, T., Cheng, Z., Li, G., and Gu, F. (2017). “An improved multiobjective particle swarm optimization algorithm using minimum distance of point to line.” *Shock Vib.*, 2017, 1–16.

Fluit, R., Prinsen, E. C., Wang, S., and Kooij, H. Van Der. (2020). “A comparison of control strategies in commercial and research knee prostheses.” *IEEE Trans. Biomed. Eng.*, 67(1), 277–290.

Flynn, L. L., Geeroms, J., Hoeven, T. Van Der, Vanderborght, B., and Lefeber, D. (2018). “VUB-CYBERLEGS CYBATHLON 2016 Beta-Prosthesis: Case study in control of an active two degree of freedom transfemoral prosthesis.” *J. Neuroeng. Rehabil.*, 15(1), 1–16.

Fu, Q., Wang, D.-H., Xu, L., and Yuan, G. (2017). “A magnetorheological damper-based prosthetic knee (MRPK) and sliding mode tracking control method for an MRPK-based lower limb prosthesis.” *Smart Mater. Struct.*, 26(4), 045030.

Gao, F., Liu, Y. N., and Liao, W. H. (2017). “Optimal design of a magnetorheological damper used in smart prosthetic knees.” *Smart Mater. Struct.*, 26(3), 035034.

García, S., Molina, D., Lozano, M., and Herrera, F. (2009). “A study on the use of non-parametric tests for analyzing the evolutionary algorithms’ behaviour: A case study on the CEC’2005 Special Session on Real Parameter Optimization.” *J. Heuristics*, 15(6), 617–644.

Gavin, H., Hoagg, J., and Dobossy, M. (2001). “Optimal design for magnetorheological dampers.” *Proc. U.S.-Japan Work. Smart Struct. Improv. Seism. Perform. Urban Reg.*, (August), 225–236.

Ghaffari, A., Hashemabadi, S. H., and Ashtiani, M. (2015). “A review on the simulation and modeling of magnetorheological fluids.” *J. Intell. Mater. Syst. Struct.*, 26(8), 881–904.

Giorgetti, A., Baldanzini, N., Biasiotto, M., and Citti, P. (2010). “Design and testing of

a MRF rotational damper for vehicle applications.” *Smart Mater. Struct.*, 19(6), 065006.

Goldasz, J., and Sapiński, B. (2015). *Insight into Magnetorheological Shock Absorbers. Insight into Magnetorheol. Shock Absorbers*, Cham: Springer International Publishing.

Gudmundsson, K. H., Jonsdottir, F., and Thorsteinsson, F. (2010). “A geometrical optimization of a magneto-rheological rotary brake in a prosthetic knee.” *Smart Mater. Struct.*, 19(3), 035023.

Gudmundsson, K. H., Jonsdottir, F., Thorsteinsson, F., and Gutfleisch, O. (2011). “An experimental investigation of unimodal and bimodal magnetorheological fluids with an application in prosthetic devices.” *J. Intell. Mater. Syst. Struct.*, 22(6), 539–549.

Hadadian, A. (2011). “Optimal design of magnetorheological dampers constrained in a specific volume using response surface method.” M.Sc. Thesis, Concordia University.

Hayashi, Y., Tsujiuchi, N., Koizumi, T., and Matsuda, Y. (2014). “Comparative verification into gait motion of healthy subjects and trans-femoral amputee based on singular value decomposition.” *5th IEEE RAS/EMBS Int. Conf. Biomed. Robot. Biomechatronics*, IEEE, 1022–1027.

Henrikson, N., Hafner, B. J., Dettori, J., Norvell, D. C., Raich, A., Brodt, E., and Skelly, A. (2011). *Microprocessor-controlled Lower Limb Prostheses*.

Herr, H., and Wilkenfeld, A. (2003). “User-adaptive control of a magnetorheological prosthetic knee.” *Ind. Rob.*, 30(1), 42–55.

Hreinsson, E. (2011). “Durability of a Magnetorheological Fluid in a Prosthetic Knee Joint.” M.Sc. Thesis, University of Iceland.

Idris, M. H., Imaduddin, F., Ubaidillah, Mazlan, S. A., and Choi, S. B., “A concentric design of a bypass magnetorheological fluid damper with a serpentine flux valve”, *Actuators*, 9(1), pp. 1–21 (2020).

Ikhouane, F., and Rodellar, J. (2007). *Systems with Hysteresis*. West Sussex: John Wiley & Sons Ltd.

Imaduddin, F., Mazlan, S. A., and Zamzuri, H. (2013). “A design and modelling review of rotary magnetorheological damper.” *Mater. Des.*, 51, 575–591.

Imaduddin, F., Mazlan, S. A., Zamzuri, H., and Azizi Abdul Rahman, M. (2014). “Bypass rotary magnetorheological damper for automotive applications.” *Appl. Mech. Mater.*, 663, 685–689.

Jaegers, S. M. H. J., Arendzen, J. H., and Jongh, H. J. de. (1995). “Prosthetic gait of unilateral transfemoral amputees: A kinematic study.” *Arch. Phys. Med. Rehabil.*, 76(8), 736–743.

Johansson, J. L., Sherrill, D. M., Riley, P. O., Bonato, P., and Herr, H. (2005). “A clinical comparison of variable-damping and mechanically passive prosthetic knee devices.” *Am. J. Phys. Med. Rehabil.*, 84(8), 563–575.

Jonsdottir, F., Thorarinsson, E. T., Palsson, H., and Gudmundsson, K. H. (2009). “Influence of parameter variations on the braking torque of a magnetorheological prosthetic knee.” *J. Intell. Mater. Syst. Struct.*, 20(6), 659–667.

Kalyanmoy, D. (2001). *Multi-Objective Optimization using Evolutionary Algorithms*. John Wiley & Sons Ltd.

Kendell, C., Lemaire, E. D., Kofman, J., and Dudek, N. (2016). “Gait adaptations of transfemoral prosthesis users across multiple walking tasks.” *Prosthet. Orthot. Int.*, 40(1), 89–95.

Keshav, M., and Chandramohan, S. (2019). “Geometric optimisation of magnetorheological valve using feedforward neural networks for distribution of magnetic flux density inside the valve.” *Smart Mater. Struct.*, 28(10), 105018.

Kim, J. H., and Oh, J. H. (2001). “Development of an above knee prosthesis using MR damper and leg simulator.” *Proc. - IEEE Int. Conf. Robot. Autom.*, 4, 3686–3691.

Kim, J. H., and Oh, J. H. (2002). “Design and analysis of rotary MR damper using permanent magnet.” *IFAC Proc. Vol.*, 35(2), 823–827.

Kirtley, C. (2006). *Clinical gait analysis: Theory and practice*. Elsevier Ltd.

Knowles, J. D., Thiele, L., and Zitzler, E. (2006). “A Tutorial on the Performance Assessment of Stochastic Multiobjective Optimizers.” *TIK-Report*, 214.

Kwok, N. M., Ha, Q. P., Nguyen, M. T., Li, J., and Samali, B. (2007). “Bouc-Wen model parameter identification for a MR fluid damper using computationally efficient GA.” *ISA Trans.*, 46(2), 167–179.

Lara-Barrios, C. M., Blanco-Ortega, A., Guzmán-Valdivia, C. H., and Bustamante Valles, K. D. (2018). “Literature review and current trends on transfemoral powered prosthetics.” *Adv. Robot.*, 32(2), 51–62.

Lawson, B. E., Mitchell, J., Truex, D., Shultz, A., Ledoux, E., and Goldfarb, M. (2014). “A robotic leg prosthesis: design, control, and implementation.” *IEEE Robot. Autom. Mag.*, 21(4), 70–81.

Lawson, B. E., Varol, H. A., Huff, A., Erdemir, E., and Goldfarb, M. (2013). “Control of stair ascent and descent with a powered transfemoral prosthesis.” *IEEE Trans. Neural Syst. Rehabil. Eng.*, 21(3), 466–473.

“Lord Corporation.” (2001). *Smart Mater. Bull.*

Lura, D. J., Wernke, M. W., Carey, S. L., Kahle, J. T., Miro, R. M., and Highsmith, M.

- J. (2017). “Crossover study of amputee stair ascent and descent biomechanics using Genium and C-Leg prostheses with comparison to non-amputee control.” *Gait Posture*, 58(July), 103–107.
- Ma, H., Chen, B., Qin, L., and Liao, W.-H. (2017). “Design and testing of a regenerative magnetorheological actuator for assistive knee braces.” *Smart Mater. Struct.*, 26(3), 035013.
- Manjeet, K., and Sujatha, C. (2019). “Magnetorheological valves based on Herschel–Bulkley fluid model: modelling, magnetostatic analysis and geometric optimization.” *Smart Mater. Struct.*, 28(11), 115008.
- Mao, M. (2011). “Adaptive magnetorheological sliding seat system for ground vehicles.” Ph.D. Thesis, University of Maryland.
- Martínez, S. Z., and Coello, C. A. C. (2011). “A multi-objective particle swarm optimizer based on decomposition.” *Genet. Evol. Comput. Conf. GECCO’11*, 69–76.
- Mauch, H. A. (1968). “Stance control for above-knee artificial legs-design considerations in the SNS knee.” *Bull. Prosthet. Res.*, 10(10), 61–72.
- Meeker, D. (2009). “FEMM 4.2.” *User’s Manual, Virginia*.
- Meeker, D. (2010). “OctaveFEMM.”
- Mitsoulis, E. (2007). “Flows of viscoplastic materials: models and computations.” *Rheol. Rev.*, 135–178.
- Mousavi, S. H., and Sayyaadi, H. (2018). “Optimization and testing of a new prototype hybrid MR brake with arc form surface as a prosthetic knee.” *IEEE/ASME Trans. Mechatronics*, 23(3), 1204–1214.
- Nam, T. H., and Ahn, K. K. (2009). “A new structure of a magnetorheological brake with the waveform boundary of a rotary disk.” *Smart Mater. Struct.*, 18(11), 115029.
- Narang, Y. S., Arelekatti, V. N. M., and Winter, A. G. (2016a). “The effects of prosthesis inertial properties on prosthetic knee moment and hip energetics required to achieve able-bodied kinematics.” *IEEE Trans. Neural Syst. Rehabil. Eng.*, 24(7), 754–763.
- Narang, Y. S., Murthy Arelekatti, V. N., and Winter, A. G. (2016b). “The effects of the inertial properties of above-knee prostheses on optimal stiffness, damping, and engagement parameters of passive prosthetic knees.” *J. Biomech. Eng.*, 138(12).
- Nguyen, P.-B., and Choi, S.-B. (2011). “A new approach to magnetic circuit analysis and its application to the optimal design of a bi-directional magnetorheological brake.” *Smart Mater. Struct.*, 20(12), 125003.
- Nguyen, Q.-H., and Choi, S.-B. (2009). “Optimal design of MR shock absorber and

application to vehicle suspension.” *Smart Mater. Struct.*, 18(3), 035012.

Nguyen, Q. H., and Choi, S. B. (2010). “Optimal design of an automotive magnetorheological brake considering geometric dimensions and zero-field friction heat.” *Smart Mater. Struct.*, 19(11), 115024.

Nguyen, Q. H., Choi, S. B., Lee, Y. S., and Han, M. S. (2009). “An analytical method for optimal design of MR valve structures.” *Smart Mater. Struct.*, 18(9), 095032.

Nguyen, Q. H., Choi, S. B., and Wereley, N. M. (2008). “Optimal design of magnetorheological valves via a finite element method considering control energy and a time constant.” *Smart Mater. Struct.*, 17(2), 025024.

Nguyen, Q. H., Han, Y. M., Choi, S. B., and Wereley, N. M. (2007). “Geometry optimization of MR valves constrained in a specific volume using the finite element method.” *Smart Mater. Struct.*, 16(6), 2242–2252.

Nguyen, Q. H., Lang, V. T., and Choi, S. B. (2015). “Optimal design and selection of magneto-rheological brake types based on braking torque and mass.” *Smart Mater. Struct.*, 24(6), 067001.

Nguyen, Q. H., Lang, V. T., Nguyen, N. D., and Choi, S. B. (2014). “Geometric optimal design of a magneto-rheological brake considering different shapes for the brake envelope.” *Smart Mater. Struct.*, 23(1), 015020.

Ochoa-Diaz, C., Rocha, T. S., Levy Oliveira, L. De, Paredes, M. G., Lima, R., Padilha, A., Bó, L., and Borges, G. A. (2014). “An above-knee prosthesis with magnetorheological variable-damping.” *Proc. IEEE RAS EMBS Int. Conf. Biomed. Robot. Biomechatronics*, 108–113.

Omidbeygi, F., and Hashemabadi, S. H. (2012). “Experimental study and CFD simulation of rotational eccentric cylinder in a magnetorheological fluid.” *J. Magn. Mater.*, 324(13), 2062–2069.

Pandit, S., Godiyal, A. K., Vimal, A. K., Singh, U., Joshi, D., and Kalyanasundaram, D. (2018). “An affordable insole-sensor-based trans-femoral prosthesis for normal gait.” *Sensors (Switzerland)*, 18(3), 10–12.

Papanastasiou, T. C., and Boudouvis, A. G. (1997). “Flows of viscoplastic materials: Models and computations.” *Comput. Struct.*, 64(1–4), 677–694.

Park, E. J., Luz, L. F. da, and Suleman, A. (2008). “Multidisciplinary design optimization of an automotive magnetorheological brake design.” *Comput. Struct.*, 86(3–5), 207–216.

Park, J., and Choi, S.-B. (2015). “A prosthetic knee using magnetorheological fluid damper for above-knee amputees.” *Act. Passiv. Smart Struct. Integr. Syst. 2015*, W.-H. Liao, ed., 943108.

- Park, J., Yoon, G. H., Kang, J. W., and Choi, S. B. (2016). “Design and control of a prosthetic leg for above-knee amputees operated in semi-active and active modes.” *Smart Mater. Struct.*, 25(8), 1–13.
- Parlak, Z., Engin, T., and Çalli, I. (2012). “Optimal design of MR damper via finite element analyses of fluid dynamic and magnetic field.” *Mechatronics*, 22(6), 890–903.
- Paul, J. P. (2005). “The history of musculoskeletal modelling in human gait.” *Theor. Issues Ergon. Sci.*, 6(3–4), 217–224.
- Power knee. (2011). “Össur - Power Knee.” <https://media.ossur.com/image/upload/v1573569995/product-documents/en-us/PN20033/catalogs/PN20033_Power_Knee.pdf> (Nov. 24, 2020).
- Radcliffe, C. W. (1977). “The Knud Jansen Lecture: above-knee prosthetics.” *Prosthet. Orthot. Int.*, 1(January), 146–160.
- Rheo Knee. (2011). “Össur - Rheo Knee.” <https://media.ossur.com/image/upload/v1598437046/product-documents/en-us/PN20224/catalogs/PN20224_RHEO_Knee.pdf> (Nov. 24, 2020).
- Rossi, A., Orsini, F., Scorza, A., Botta, F., Belfiore, N., and Sciuto, S. (2018). “A review on parametric dynamic models of magnetorheological dampers and their characterization methods.” *Actuators*, 7(2), 16.
- Rutkowska-Kucharska, A., Kowal, M., and Winiarski, S. (2018). “Relationship between asymmetry of gait and muscle torque in patients after unilateral transfemoral amputation.” *Appl. Bionics Biomech.*, 2018, 1–9.
- Sawers, A. B., and Hafner, B. J. (2013). “Outcomes associated with the use of microprocessor-controlled prosthetic knees among individuals with unilateral transfemoral limb loss: A systematic review.” *J. Rehabil. Res. Dev.*, 50(3), 273–314.
- Schmalz, T., Blumentritt, S., and Jarasch, R. (2002). “Energy expenditure and biomechanical characteristics of lower limb amputee gait: the influence of prosthetic alignment and different prosthetic components.” *Gait Posture*, 16(3), 255–63.
- Seid, S. (2017). “Optimal Design of a Magnetorheological (MR) Damper for Prosthetic Knee Application.” Ph.D. Thesis, Indian Institute of Technology Madras.
- Seymour, R., Engbretson, B., Kott, K., Ordway, N., Brooks, G., Crannell, J., Hickernell, E., and Wheeler, K. (2007). “Comparison between the C-leg® microprocessor-controlled prosthetic knee and non-microprocessor control prosthetic knees: A preliminary study of energy expenditure, obstacle course performance, and quality of life survey.” *Prosthet. Orthot. Int.*, 31(1), 51–61.
- Spanias, J. A., Simon, A. M., Finucane, S. B., Perreault, E. J., and Hargrove, L. J. (2018). “Online adaptive neural control of a robotic lower limb prosthesis.” *J. Neural Eng.*, 15(1), 016015.

Spencer, B. F., Dyke, S. J., Sain, M. K., and Carlson, J. D. (1997). “Phenomenological model for magnetorheological dampers.” *J. Eng. Mech.*, 123(3), 230–238.

Sudeesh, S., Sujatha, S., and Shunmugam, M. S. (2020). “On the possibility of achieving near-normal swing phase of walking with passive single-axis and polycentric knees.” *J. Prosthetics Orthot.*, 32(2), 121–133.

Taheri, A., and Karimi, M. T. (2012). “Evaluation of the gait performance of above-knee amputees while walking with 3R20 and 3R15 knee joints.” *J. Res. Med. Sci.*, 17(3), 6–11.

Thiele, J., Schöllig, C., Bellmann, M., and Kraft, M. (2019). “Designs and performance of three new microprocessor-controlled knee joints.” *Biomed. Tech.*, 64(1), 119–126.

Thorarinsson, E. T., Jonsdottir, F., and Palsson, H. (2006). “Design of a magnetorheological prosthetic knee.” *Proc. Nord. 2006 Conf.*, 382–392.

Torrealba, R. R., Fernández-López, G., and Grieco, J. C. (2008). “Towards the development of knee prostheses: Review of current researches.” *Kybernetes*, 37(9–10), 1561–1576.

Tsang, H. H., Su, R. K. L., and Chandler, A. M. (2006). “Simplified inverse dynamics models for MR fluid dampers.” *Eng. Struct.*, 28(3), 327–341.

Tschiedel, M., Russold, M. F., and Kaniusas, E. (2020). “Relying on more sense for enhancing lower limb prostheses control: a review.” *J. Neuroeng. Rehabil.*, 17(1), 1–13.

Wang, D. H., and Liao, W. H. (2011). “Magnetorheological fluid dampers: a review of parametric modelling.” *Smart Mater. Struct.*, 20(2), 023001.

Wang, Q. (2013). *Practical Design of Magnetostatic Structure Using Numerical Simulation*. Singapore: John Wiley & Sons (Asia) Pte Ltd.

Weaver, K. F., Morales, V. C., Dunn, S. L., Godde, K., and Weaver, P. F. (2017). *An Introduction to Statistical Analysis in Research With Applications in the Biological and Life Sciences*. John Wiley & Sons, Inc.

Wentink, E. C., Koopman, H. F. J. M., Stramigioli, S., Rietman, J. S., and Veltink, P. H. (2013). “Variable stiffness actuated prosthetic knee to restore knee buckling during stance: A modeling study.” *Med. Eng. Phys.*, 35(6), 838–845.

Whittle, M. W. (2007). *Gait Analysis. Gait Anal.*, Elsevier Ltd.

Winter, D. A. (2009). *Biomechanics and Motor Control of Human Movement. Biomech. Mot. Control Hum. Mov. Fourth Ed.*, Hoboken, NJ, USA: John Wiley & Sons, Inc.

Woldesenbet, Y. G., Yen, G. G., and Tessema, B. G. (2009). “Constraint handling in multiobjective evolutionary optimization.” *IEEE Trans. Evol. Comput.*, 13(3), 514–

525.

Wolf, E. J., Everding, V. Q., Linberg, A. A., Czerniecki, J. M., and Gambel, C. J. M. (2013). "Comparison of the Power Knee and C-Leg during step-up and sit-to-stand tasks." *Gait Posture*, 38(3), 397–402.

Xia, B., Liu, R., He, Z., and Seop, C. (2020). "A single - and multi - objective optimization algorithm for electromagnetic devices assisted by adaptive kriging based on parallel infilling strategy." *J. Electr. Eng. Technol.*, (0123456789).

Xu, L., Wang, D.-H., Fu, Q., Yuan, G., and Hu, L.-Z. (2016). "A novel four-bar linkage prosthetic knee based on magnetorheological effect: principle, structure, simulation and control." *Smart Mater. Struct.*, 25(11), 115007.

Xu, Z. D., Sha, L. F., Zhang, X. C., and Ye, H. H. (2013). "Design, performance test and analysis on magnetorheological damper for earthquake mitigation." *Struct. Control Heal. Monit.*, 20(6), 956–970.

Yang, G., Spencer, B. F., Carlson, J. D., and Sain, M. K. (2002). "Large-scale MR fluid dampers: Modeling and dynamic performance considerations." *Eng. Struct.*, 24(3), 309–323.

Yilmaz, A., and Orhanli, T. (2015). "Gait motion simulator for kinematic tests of above knee prostheses." *IET Sci. Meas. Technol.*, 9(3), 250–258.

Younis, A., Karakoc, K., Dong, Z., Park, E., and Suleman, A. (2011). "Application of SEUMRE global optimization algorithm in automotive magnetorheological brake design." *Struct. Multidiscip. Optim.*, 44(6), 761–772.

Zhang, J. Q., Feng, Z. Z., and Jing, Q. (2009). "Optimization analysis of a new vane MRF damper." *J. Phys. Conf. Ser.*, 149, 012087.

Zhang, W., Huang, X., Gao, X. Z., and Yin, H. (2015). "A constrained multi-objective particle swarm optimization algorithm based on adaptive penalty and normalized non-dominated sorting." *Int. J. Innov. Comput. Inf. Control*, 11(6), 1835–1853.

Zitzler, E., Knowles, J., and Thiele, L. (2008). "Quality assessment of pareto set approximations." *Lect. Notes Comput. Sci. (including Subser. Lect. Notes Artif. Intell. Lect. Notes Bioinformatics)*, 5252 LNCS, 373–404.

Appendix I

Instrument and Material specifications

The following are the list of instruments as well as material specifications used in this research work. A few technical specifications are listed, while other details can be easily obtained using the name, model number and other details of the concerned item.

1. Lord MRF – 132DG

Table 1: Typical Properties of Lord MRF – 132DG

Parameter	Specification
Appearance	Dark Gray Liquid
Viscosity, Calculated as slope 800-1200 sec ⁻¹ , Pa-s @ 40°C (104°F)	0.112 ± 0.02
Density, g/cm ³ (lb/gal)	2.95-3.15 (24.6-26.3)
Solids Content by Weight, %	80.98
Flash Point, °C (°F)	>150 (>302)
Operating Temperature, °C (°F)	-40 to +130 (-40 to +266)

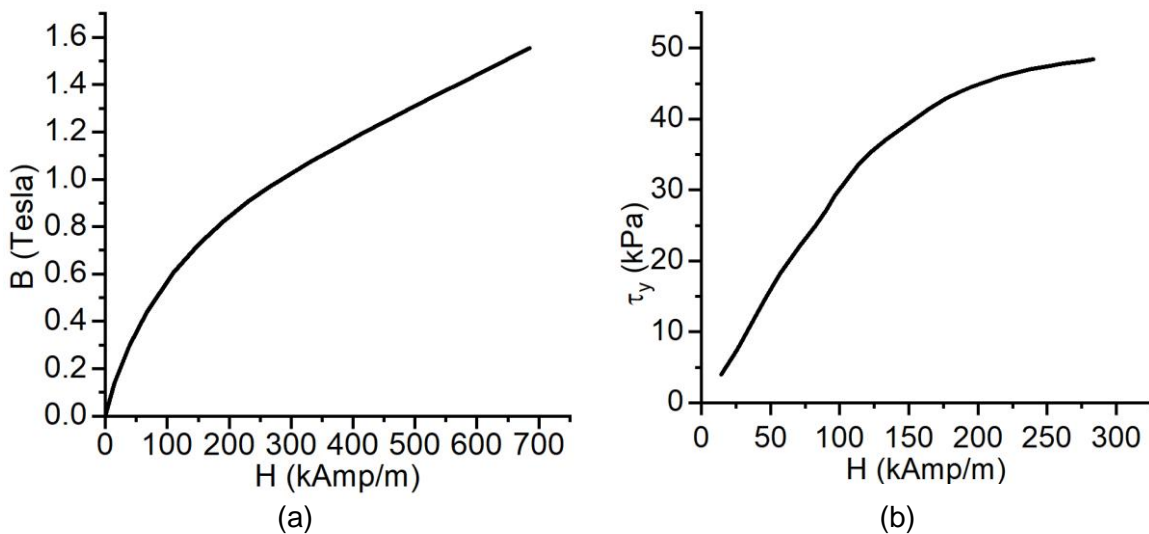


Figure 1: (a) Yield Stress vs. Magnetic field strength and (b) Magnetic flux density vs. Magnetic field strength for Lord MRF – 132DG

2. Lord MRF – 140CG

Table 2: Typical Properties of Lord MRF – 140CG

Parameter	Specification
Appearance	Dark Gray Liquid
Viscosity, Calculated as slope 800-1200 sec ⁻¹ , Pa-s @ 40°C (104°F)	0.280 ± 0.070
Density, g/cm ³ (lb/gal)	3.54 – 3.74 (29.5 – 31.2)
Solids Content by Weight, %	85.44
Flash Point, °C (°F)	>150 (>302)
Operating Temperature, °C (°F)	-40 to +130 (-40 to +266)

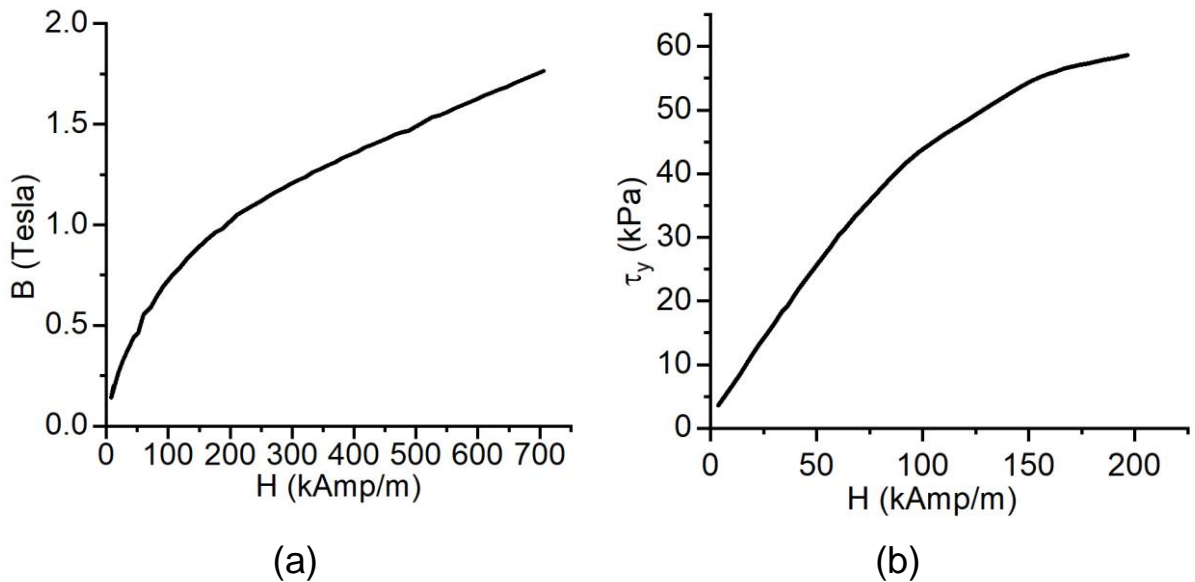
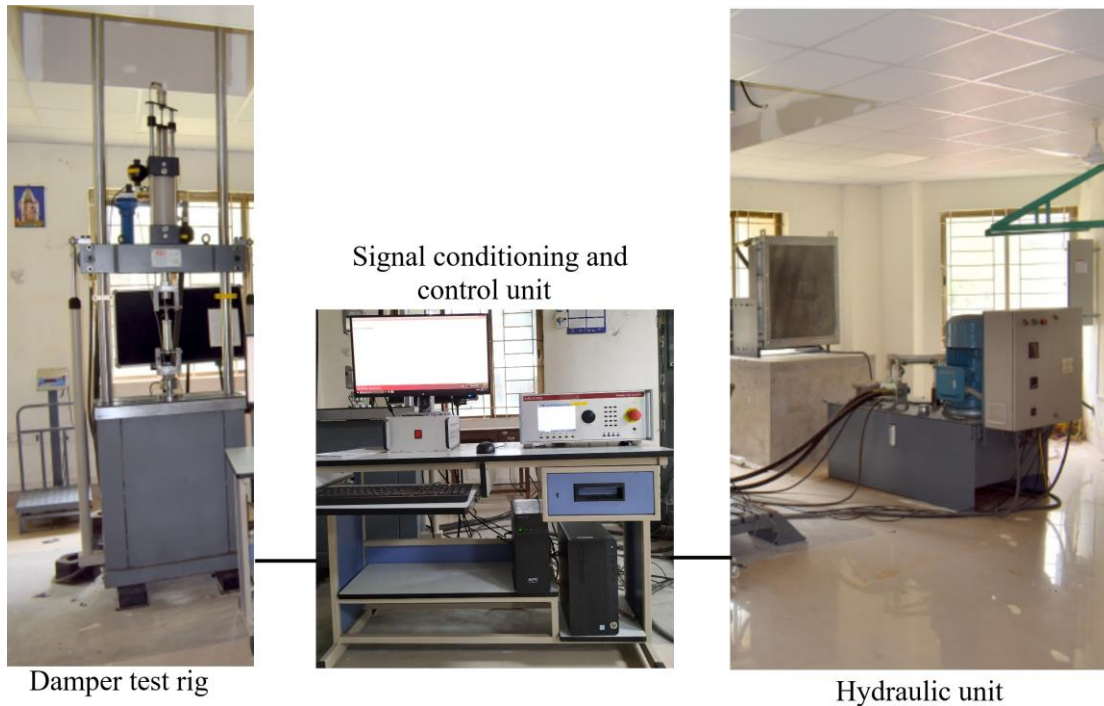


Figure 2: (a) Yield Stress vs. Magnetic field strength and (b) Magnetic flux density vs. Magnetic field strength for Lord MRF – 140CG

3. Linear Damper Testing Machine (Make: HEICO)



Signal conditioning and control unit

Damper test rig

Hydraulic unit

Figure 3: Linear damper testing machine

Specifications of individual subsystems:

A. Hydraulic power pack



Parameter	Specification
Flow of the pump	64 LPM
Max. Operating Pressure	210 bar
Oil tank capacity	200 L
Power rating of motor	40 HP
Length of hoses	5 m (each)
Electric power supply	440V, 3 phase (AC supply)

B. Hydraulic actuator



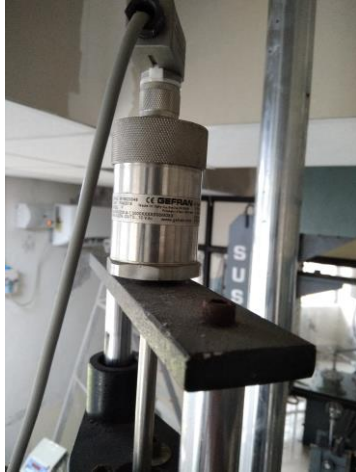
Parameter	Specification
Type	Double acting double ended
Capacity	± 20 kN
Stroke	150 mm (± 75 mm)
Max. working pressure	210 bar
Max. sustained velocity	0.8 m/s
Peak velocity	1.2 m/s
Servo valve	63 LPM
Pressure line filter	180 LPM with 3 microns filtration
Accumulator (2 No.)	0.36 L capacity

C. Force Transducer



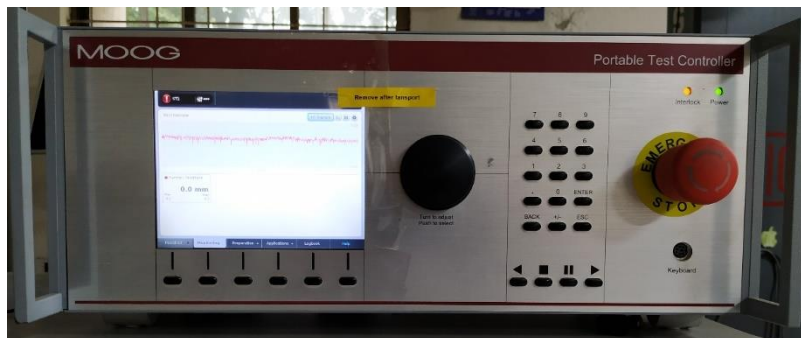
Parameter	Specification
Capacity	± 30 kN
Resolution	0.001 kN
Full scale output	2 mV/V
Excitation Voltage	10 Volts DC
Non-linearity	$< \pm 0.15$ % FSO
Safe overload	150 %
Operating temperature	0 to + 60 deg. C
Accuracy	0.5% of indicated value as per ISO7500-1

D. Displacement Transducer



Parameter	Specification
Range	200 mm
Make	Gefran/Balluff
Full scale output	10 volts
Repeatability	< 0.01 mm
Pressure withstand	Upto 600 bar
Excitation voltage	24 volts DC
Sampling rate	2 kHz
Operating temperature	-30 to + 75 deg. C

E. Signal conditioning and control unit



Specifications of controller:

- Auto PID operation with auto zeroing, auto tuning and auto-adjustment feature servo operation.
- Digital signal processing (DSP) based closed loop servo controller with closed loop update rate of 10 kHz.
- Number of control channels - 4 (Load/Displacement/External channel strain 1 and strain2).
- Demand wave generation - Sine, Triangular, Square and ramp signal.
- High speed 32 bit data acquisition with 6 kHz sampling rate on all primary channels.
- Auto calibration and digital auto zero capability.

4. DC Power Supply



Parameter	Specification
DC output	0 to 30V / 5A
Settling resolution	V: 10 mV, I : 5 mA
Load Regulation	$\leq \pm (0.05\% + 10 \text{ mV})$
Input Supply	230 AC \pm 10% / 50-60 Hz
Internal resistance	≤ 10 milli Ohms

5. Rotary Damper Testing Machine

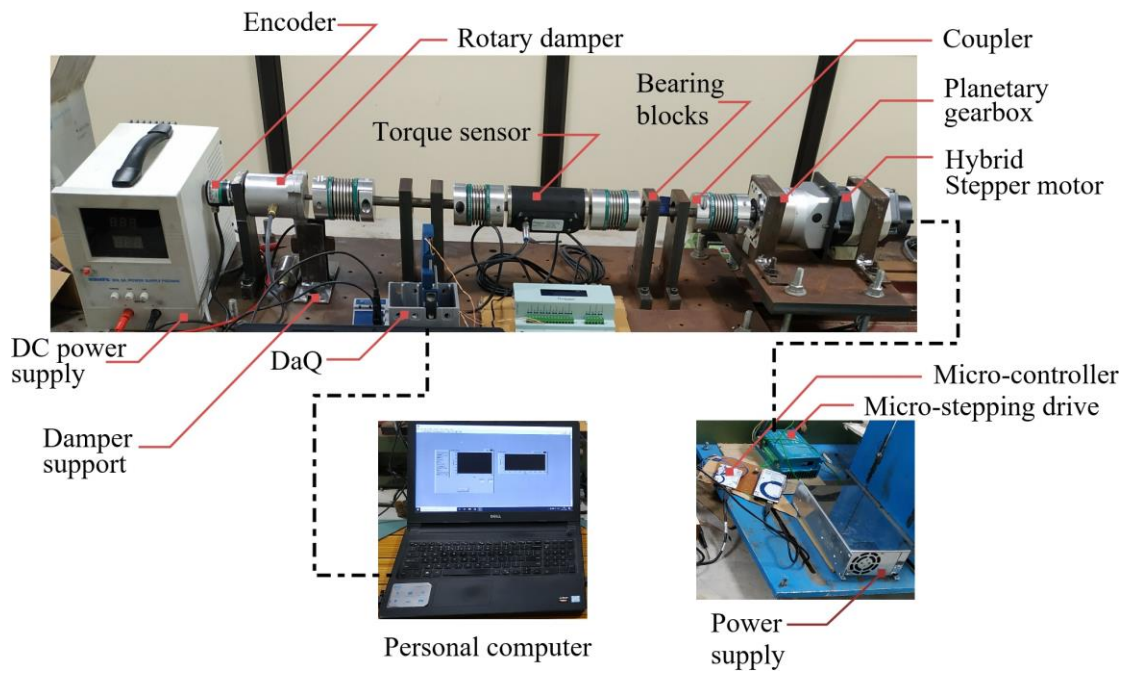


Figure 4: Rotary vane damper characterization test setup

Specifications of individual subsystems:

A. Hybrid Stepper Motor (Model: RMCS - 1056)



Parameter	Specification
Step angle	1.8
Number of phase	2
Shaft diameter (mm)	14
Encoder resolution (CPR)	1000
Rated voltage (V)	3.2
Rated current (A)	4.2
Holding torque (kg.cm)	85

B. Micro-stepping drive (Model: ES – D1008)



Parameter	Specification
Input voltage	20 – 70 VAC 30 – 100 VDC
Output current	0.5 – 8.2 A
Pulse input frequency	0 – 200 kHz
Logic signal current	7 – 16 mA
Isolation resistance	500 M Ohms

C. DC power supply (Model: RMCS-4037)



Parameter	Specification
Input voltage	230 V AC
Power rating	500 W
Output rating	48V 10.4 A

D. Planetary gearbox (Model: PLF90-L1-10-S2-P2)



Parameter	Specification
Gear ratio	10
Gear box mounting type	Inline
Backlash	12 Arc min
Rated output torque	39.5 Nm

E. Torque sensor (Model: M425, Make: Datum Electronics)



Parameter	Specification
Torque range	0 – 100 Nm
Accuracy	0.1%
Non-linearity	0.1%
Repeatability	0.05%
Sample rate	1 to 4000 samples/s

F. Encoder (Model: RMCS – 5102)



Parameter	Specification
Torque range	0 – 100 Nm
Accuracy	0.1%
Non-linearity	0.1%
Repeatability	0.05%
Sample rate	1 to 4000 samples/s

G. Analog input module NI 9205



Parameter	Specification
Signal levels	+/- 200 mV, +/-1 A, +/-5 V, +/-10 V
Channels	32 Single ended, 16 differential
Sample rate	250 kS/s
Resolution	16 bit
Connectivity	Spring terminal DSUB

H. Chassis – cDAQ 9174



Parameter	Specification
Input FIFO size	127 samples per slot
Max. update rate	1.6 MS/s (onboard regeneration)
No. of counters/timers	4
Resolution	32 bits

I. Micro-controller (Arduino Mega)



Parameter	Specification
Clock speed	16 MHz
Operating voltage	5 V
Input pins (Digital/Analog)	54 / 16
Flash memory	256 KB
Input voltage (recommended)	7 – 12V

Appendix II

1 General Multi-Objective Optimization Problem Definition

As opposed to single objective optimization problem, a multi-objective optimization problem (MOOP) consists of a vector of objectives to be maximized or minimized. Without loss of generality, a minimization problem is assumed and the constrained MOOP can be defined as follows:

For $x = (x_1, x_2, x_3, \dots, x_n)$ bounded by $[x_i^{\min}, x_j^{\max}]$, $i = 1, 2, 3, \dots, n$

$$\begin{aligned} \text{Minimize: } f(x) &= [f_1(x) \ f_2(x) \ f_3(x) \ \dots \ f_l(x)]^T \\ \text{subject to } g_j(x) &\leq 0, \quad j = 1, 2, 3, \dots, q \end{aligned} \quad (1)$$

where, n is the number of decision variables, l is the number of objective functions, q is the number of non-linear constraints. Only inequality constraints are shown, an equality constraint defined as $h_p = 0$ can be converted into an inequality constraint, $|h_p - \varepsilon| \leq 0$. Here, ε is a small quantity.

1.1 Multi-objective Particle Swarm Optimization (MOPSO) Algorithm

PSO is an algorithm based on the movement of a flock of birds. The algorithm incorporates social and cognitive behavior of these birds motion towards their aim to find food, in this case approaching a global minimum of the problem. The definition of global minimum for a single objective problem is rather obvious while for a MOOP, there exists a vector of optimized values that represents a trade-off between the objectives. The particle's flight in the n -dimensional decision space is updated using the following set of equations (Martínez and Coello 2011).

$$v_{t+1}(i) = \omega v_t(i) + c_1 R_1 (P_{best,t}(i) - X_t(i)) + c_2 R_2 (G_{best,t}(i) - X_t(i)) \quad (2)$$

$$X_{t+1}(i) = X_t(i) + v_{t+1}(i) \quad (3)$$

Here, ω is the damping coefficient considered to reduce the effects of particle inertia and is generally set to vary linearly from 0.9 to 0.4, t is the time step assumed as unity, $v_t(i)$ is the i^{th} particle velocity, $X_t(i)$ is the i^{th} particle displacement, c_1 and c_2

are the cognitive and the social learning factors respectively, R_1 and R_2 are the random numbers in the range of $[0,1]$, $P_{best,t}(i)$ is the personal best of the particle, and $G_{best,t}(i)$ is the global best of the particle over all time steps. A MOPSO differs from a single objective PSO in its way of handling the objectives and constraints, selection of personal best, selection of global best and way of choosing an elite population.

In the study by Fan et al. (2017), a novel way of choosing a global leader using a minimum distance of point to line method was described and its performance on the unconstrained test functions was compared with other optimization algorithms. Later, the method was applied to a practical vehicle dynamic optimization problem and the results were compared with advanced evolutionary algorithms proving the superiority of their method. In the present study, this algorithm is extended for a constrained multi-objective problem using an adaptive constraint handling technique, which was initially developed for evolutionary algorithm (Woldesenbet et al. 2009). Although this technique was extended to PSO in the study by Zhang et al. (2015), the method of selecting the global best was randomly chosen based on crowding distance. In the present study, the adaptive constraint handling method and the MDPL method are combined and used together to develop a constrained minimum distance of point to line multi-objective particle swarm optimization (CMDPL-MOPSO) method. A flowchart of the proposed algorithm is shown in Figure 1. The following are the features used in the present algorithm.

1.2 Constraint handling

The adaptive constraint handling technique determines an adaptive penalty for each of the objective functions of every individual. First, the objective functions are normalized according to equation (4),

$$\tilde{f}_i(x) = \frac{f_i(x) - \min\{f_i(x)\}}{\max\{f_i(x)\} - \min\{f_i(x)\}}, \quad i = 1, 2, \dots, l \quad (4)$$

Here, $\min\{f_i(x)\}$ and $\max\{f_i(x)\}$ represent the minimum and the maximum values in the i^{th} dimension of the objective space respectively. The new objective

function, $F_i(x)$ is a sum of two components: adaptive component, $p_i(x)$ and the distance measure, $d_i(x)$ as given by equation (5),

$$F_i(x) = d_i(x) + p_i(x) \quad i = 1, 2, \dots, l \quad (5)$$

Both the components are based on the proportion of feasible solutions obtained in the current population given by equation (6),

$$\gamma_f = \frac{\text{number of feasible solutions in current population}}{\text{population size}} \quad (6)$$

An individual constraint violation term, $v(x)$ is defined by equation (7),

$$v(x) = \frac{1}{q} \sum_{j=1}^q \frac{c_j(x)}{c_j^{\max}} \quad (7)$$

where, $c_j(x) = \max(0, g_j(x))$, $j = 1, 2, 3, \dots, q$.

The distance measure in equation (5) can be calculated using equation (8),

$$d_i(x) = \begin{cases} v(x) & \text{if } \gamma_f = 0 \\ \sqrt{\tilde{f}_i(x)^2 + v(x)^2} & \text{otherwise} \end{cases} \quad (8)$$

The penalty function in equation (5) can be calculated using equation (9).

$$p_i(x) = (1 - \gamma_f) X(x) + \gamma_f Y_i(x) \quad (9)$$

where, $X(x) = \begin{cases} 0 & \text{if } \gamma_f = 0 \\ v(x) & \text{otherwise} \end{cases}$, and $Y_i(x) = \begin{cases} 0 & \text{if } x \text{ is feasible} \\ \tilde{f}_i(x) & \text{otherwise} \end{cases}$.

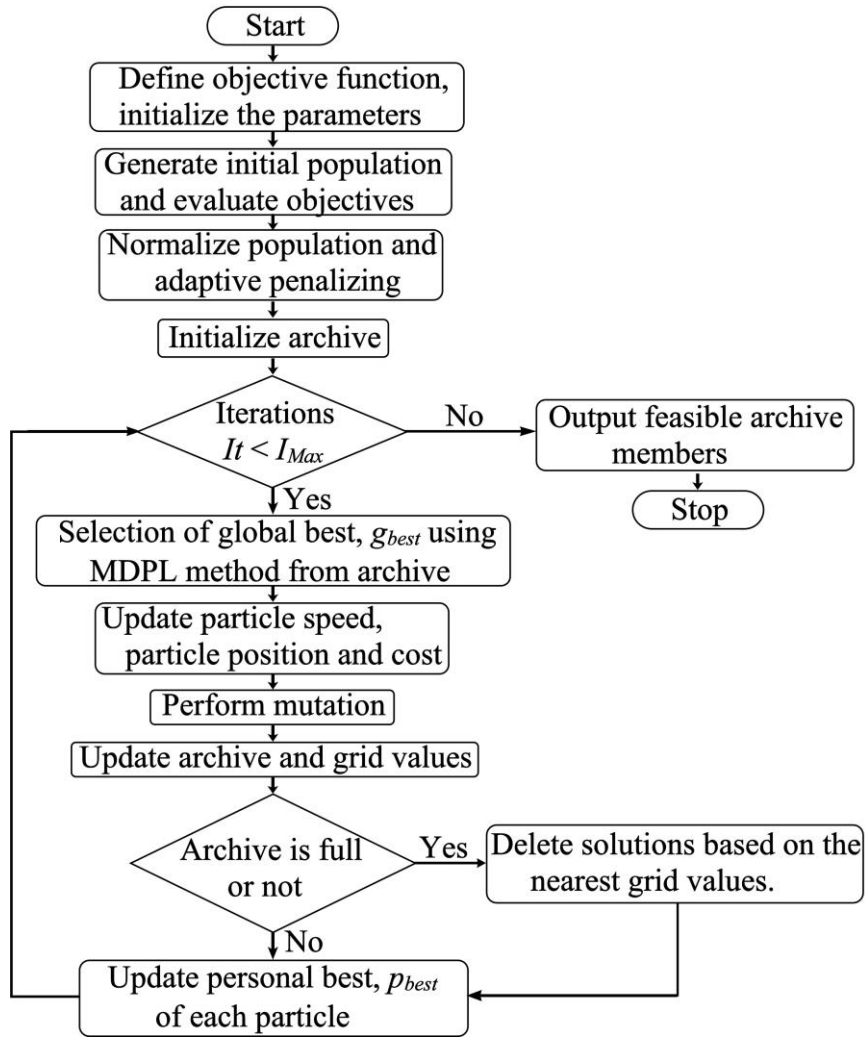


Figure 1 Flowchart of the proposed algorithm

In the current population, if all the solutions are feasible then the new objective function returns the normalized objective function values. Any violation of constraints results in adjusting a penalty value proportional to its constraint violation degree and the violating individual is pushed away from the Pareto front.

1.3 Personal best selection

The selection of personal best for an individual is performed using the Pareto-dominance concept. In this concept, “an individual x_p is said to be dominating the individual x_q if $f_i(x_p) < f_i(x_q)$ for all objective functions. Further, if $f_i(x_p) \leq f_i(x_q)$ for all objectives, then the individual p is said to be strictly dominating

the individual q ". If dominance cannot be asserted, then one of them is chosen randomly.

1.4 Global best selection

One of the key differences between the crowding distance MOPSO and the MDPL-MOPSO is the method of maintaining diversity among the Pareto fronts. In crowding distance MOPSO, the global best selection method itself ensures that the whole population is pushed towards an individual with largest crowding distance, in an attempt to improve spacing among the Pareto front individuals. Whereas in MDPL-MOPSO, the global best selection method ensures the individuals move towards the nearest Pareto front individual, thus guiding each particle directly towards the Pareto front. The diversity among the Pareto front particles is taken care of by the grid controller and the archive update mechanism.

In this algorithm, the selection of global best is performed in the objective space. Since an external archive containing all the non-dominated particles is maintained, the global leader for each particle will be selected from this archive. First, the task of determining a global best using the MDPL method will be explained using a two objective minimization problem. Assume P , Q and R to be some of the non - dominated points till current generation and point A to be the one for which global best is to be determined. The line L_1 from the origin to the point, $P(f_{11}, f_{21})$ is defined using equation (10),

$$\frac{x}{f_{11}} = \frac{y}{f_{21}} \quad (10)$$

The shortest distance from point $A(f_{1i}, f_{2i})$ to the line L_1 can be calculated using equation (11),

$$d_{i1} = \frac{|f_{21}f_{1i} - f_{11}f_{2i}|}{\sqrt{f_{11}^2 + f_{21}^2}} \quad (11)$$

A vector of distances from point A to the lines joining the origin and all the points in the external archive can be calculated and a particle $X(k)$ is defined as the global best for A if the distance, d_{ik} is defined as follows:

$$d_{ik} = \min \{d_{ij} | j = 1, 2, 3, \dots, m\} \quad (12)$$

Here, m is the number of non-dominated solutions in the external archive. Thus in Figure 2, if the external archive consists of just P , Q and R particles, the global best for particle A can be determined as particle Q (assuming $d_{i2} < d_{i3} < d_{i1}$). Similarly, in a three objective optimization problem, the distance from point $A(x_0, y_0, z_0)$ to the line joining origin, O and Pareto front particle $P(a, b, c)$ can be calculated using equation (13),

$$d = \frac{|\overrightarrow{OA} \times \overrightarrow{OP}|}{|\overrightarrow{OP}|} \quad (13)$$

$$= \frac{\sqrt{(cy_0 - bz_0)^2 + (cx_0 - az_0)^2 + (bx_0 - ay_0)^2}}{\sqrt{a^2 + b^2 + c^2}}$$

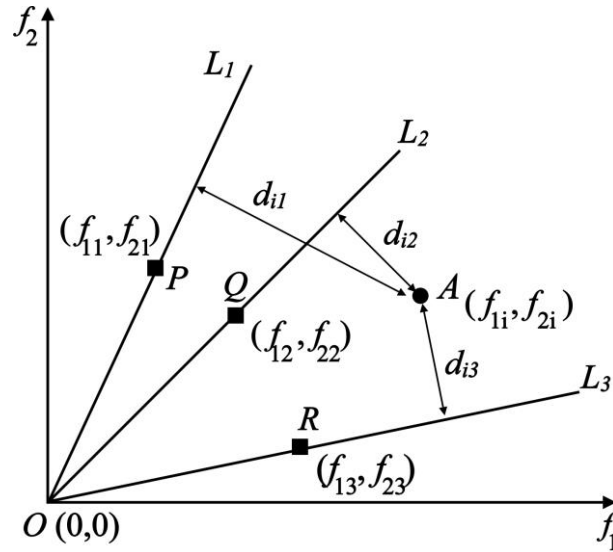


Figure 2 Distance of point to line in 2D objective space

Determining all the distances, a global best guide can be chosen based on the minimum distance value. For more than 3 objectives, an objective aggregation technique to reduce the objectives to 2 or 3 can be applied (Fan et al. 2017). The results of the study were compared with advanced evolutionary algorithms proving their superiority over them. In crowding distance value method, a global best particle is chosen based on the largest crowding distance. Although this may encourage the

algorithm towards less dense regions of the front, a random selection still exists. Contrary to this, since particles in external archive constitute a Pareto front, choosing a global best using MDPL method pushes the particle directly towards the Pareto front.

1.5 External repository

This repository maintains a record of all the non-dominated solutions found so far in the optimization process. The number of records is usually restricted to a pre-set allowable value. Further, to store and promote diversity among the non-dominated solutions, the two components namely archive control and grid control are invoked (Coello Coello et al. 2004).

1.5.1 Archive control

- (i) This component is mainly concerned with the decision of adding a new particle to the archive. The following set of rules are followed in order to make the decision:
- (ii) Only the non-dominated vectors in the current population are compared with the ones already existing in the external archive.
- (iii) At the beginning of the algorithm, the external archive is directly populated with all the non-dominated vectors found in the first generation.
- (iv) In the later stages, if any new particle from the current population dominates an individual(s) from the external repository, then the new particle replaces the dominated individual(s) in the archive.
- (v) Otherwise, if the new particle is dominated by any individual from the external repository, then the new particle is discarded.
- (vi) If the external archive reaches its allowable capacity, then the adaptive grid method described in next section is invoked.

1.5.2 Grid control

A hypercube with sides composed of all objectives is generated and each dimension of the objective vector is divided into equal spaces with width varying by a value of $\frac{f_{\max}^i - f_{\min}^i}{n_{grid}}$. Here, n_{grid} is the number of grids that needs to be pre-defined,

f_{\max}^i and f_{\min}^i are the maximum and minimum values of the objective in the i^{th} dimension of the objective vector. Based on the values of non-dominated vectors, each vector is provided with a coordinate in the grid. If the external archive reaches its maximum allowable capacity, individuals with the same grid coordinates are deleted randomly. The grid is updated at each iteration to accommodate newly incorporated solutions in the external archive.

1.6 Mutation

Mutation is a mechanism used by many PSO algorithms to remove the tendency of local minima trap and further to improve the exploratory abilities of the algorithm. In this study, a mutation operator is used which selects the individual particle vectors at random and replaces any one variable value in the given ranges of values. The probability of mutation is set to decrease along the progression of the algorithm.

2 Comparison

The MDPL method to determine the global best and the other features in the present algorithm were compared with the unconstrained test functions in a study by Fan *et al* (Fan et al. 2017). Further, the same algorithm was extended to accommodate the constraints in an optimization problem and an adaptive penalty method was applied. It can be noticed from equations (4) to (9) that when no constraints exist in the optimization problem, the algorithm resorts to simple MDPL-MOPSO proposed in the study by Fan et al. (2017). The metrics such as generational distance and the spacing were already shown to perform well when compared to crowding distance PSO and other evolutionary algorithms. Hence, in the present study, only unconstrained test functions are chosen for performance evaluation.

2.1 Test functions

To evaluate the performance of the proposed algorithm, four representative test functions listed in table 1 are chosen.

Table 1: Constrained test functions

Problem	No. of objectives	No. of decision variables	Comments on Pareto front connectivity
CONSTER (Woldesenbet et al. 2009)	2	2	Continuous
Srinivas (Kalyanmoy 2001)	2	2	Continuous
Tanaka (Kalyanmoy 2001)	2	2	Disconnected
BINH4 (Kalyanmoy 2001)	3	2	Connected

2.2 Performance Metrics

The following are the performance metrics defined to compare the algorithm proposed in this study.

2.2.1 Generational Distance

This metric requires a true Pareto front of the problem at hand. The Euclidean distances between the Pareto individuals found in the optimization problem and their nearest true Pareto front individuals are calculated. The generational distance can be calculated using equation (14),

$$GD = \frac{\sqrt{\sum_{i=1}^n d_i^2}}{n} \quad (14)$$

Here, n is the number of non-dominated solutions found, d_i is the distance between the Pareto individual and the nearest true Pareto front individual. A lower value indicates that the non-dominated solutions are approaching the Pareto optimal set.

2.2.2 Spacing

This metric reflects the spread of the non-dominated solutions found. The spacing can be calculated using equation (15),

$$SP = \sqrt{\frac{1}{n-1} \sum_{i=1}^n (\bar{d} - d_i)^2} \quad (15)$$

$$\text{Here, } d_i = \min_{\substack{j=1,2,\dots,n \\ j \neq i}} \left\{ \sum_{k=1}^l |f_k(x_i) - f_k(x_j)| \right\}, \quad i=1,2,3, \dots, n \text{ denotes the L1}$$

distance between the solution x_i and its nearest objective, x_j and \bar{d} is the average of d_i . A lower value of spacing is desired which reflects the non-dominated solutions to be spread evenly across the front.

2.3 Performance comparison using test functions

As commonly found in literature, each algorithm is repeated 30 times and an average value and standard deviations of the performance metrics are calculated (Martínez and Coello 2011; Woldesenbet et al. 2009). Further, the population size is set to 100, external archive size to 50, maximum number of generations to 100 and number of grid dimensions to 100. The performance metrics for various test functions are shown in the tables 2 and 3. Calculation of generational distance requires a true Pareto front and an enumerative approach is used to obtain the true Pareto front of all test functions. A null hypothesis is formulated stating that the mean of the performance metric obtained from the proposed algorithm is greater than or equal to the performance metric obtained from previous study (Zhang et al. 2015).

Table 2. Generational distance metric

Algorithm	CONSTER	Srinivas	Tanaka	BINH4
CMPSO (Zhang et al. 2015)	0.0025	0.0012	0.0023	0.0151
Proposed algorithm	0.0005 $p < 0.05$	0.0018 $p > 0.05$ No significant reduction	0.00198 $p < 0.05$	0.0059 $p < 0.05$

Table 3. Spacing metric

Algorithm	CONSTER	Srinivas	Tanaka	BINH4
CMPSO (Zhang et al. 2015)	0.1165	0.074	0.0125	0.1612
Proposed algorithm	0.022914 $p < 0.05$	0.021116 $p < 0.05$	0.019075 $p > 0.05$ No significant reduction	0.036609 $p < 0.05$

From the above results, it can be concluded that the proposed CMDPL-MOPSO algorithm shows a significant reduction in performance metrics apart from a few deviations. The Pareto fronts of the test functions are plotted against their respective true Pareto fronts as shown in Figure 3.

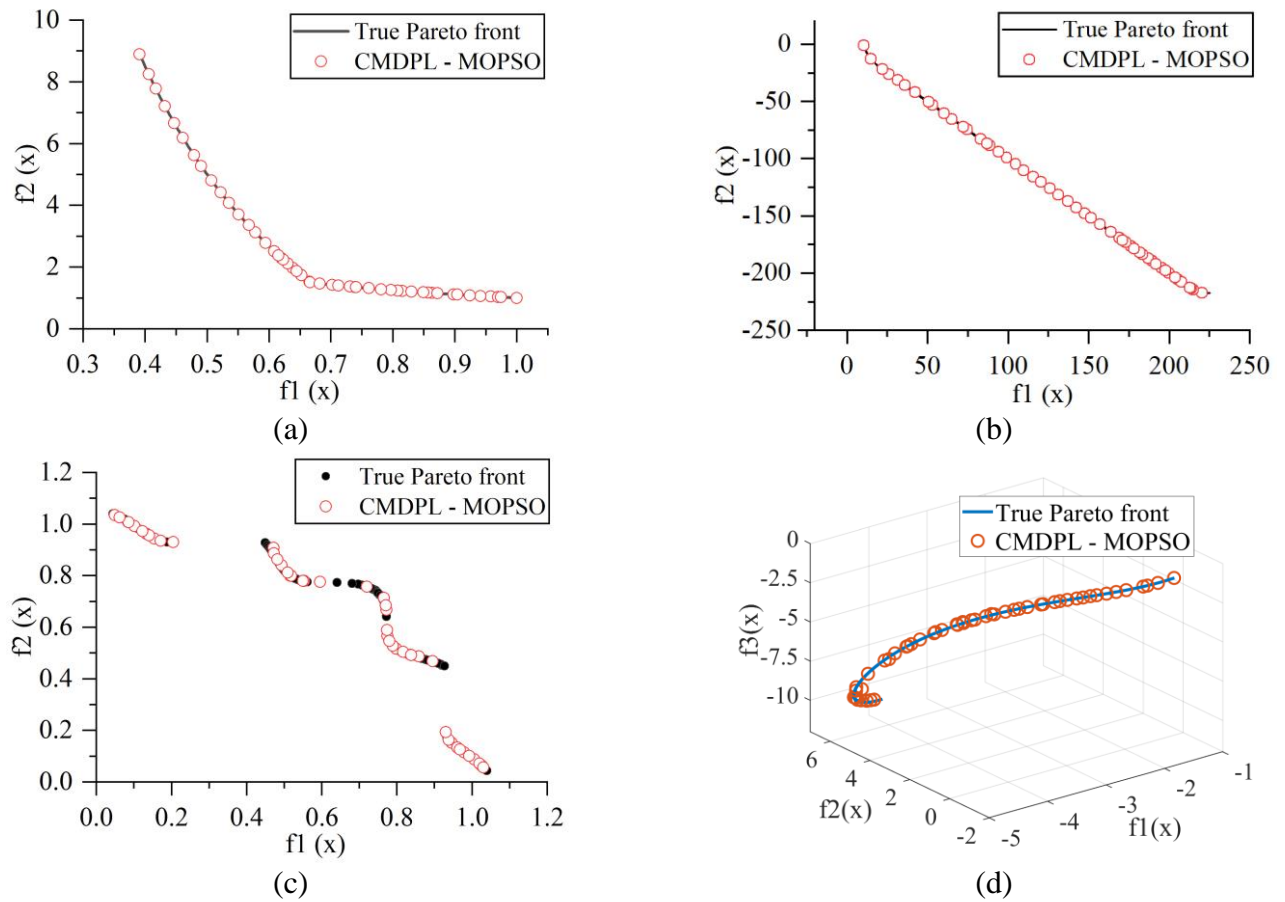


Figure 3. Comparison of True Pareto front and computed front from proposed algorithm for (a) CONSTER (b) Srinivas (c) Tanaka and (d) BINH4 test functions.

Appendix III

In the dissertation O-COM methodology has been applied at various places. The objective function in each application is almost similar with a minor changes in variables, geometry etc. Therefore, to avoid repeating similar code multiple times, an example objective function is provided next. The following function is an objective function which calculates the dynamic range and time constant as the output. It also evaluates two constraints which are saturation and the off-state force constraint. This function corresponds to O-COM methodology from Chapter 3 DP1.

```
%% The following function calculates the dynamic range and time
constant
% as the costs for the given geometry and also evaluates constraints
% Save the following as ObjectiveDamper_J3.m

function [cost, c0] = ObjectiveDamper_J3(param, arg)
%% Initialization
rc = param(1)/1000;
wc = param(2)/1000;
h = param(3)/1000;
la = param(4)/1000;
I = param(5);
R = 30/1000;
L = 50/1000;
r0 = 5/1000;
d_avg = 2*(rc + 0.5*wc);           % Average diameter of coil cross-section
u = 0.1;                          % design speed
n = 0.112;                         % off-state viscosity of MRF
resistivity = 0.01726e-6;
Coil_dia = 0.51/1000;
pf = 0.6;
Coil_area = pi*Coil_dia^2/4;
N_turns = pf*(wc*(L-2*la))/Coil_area;
switch arg
    case "EMM"
        [B, B_max] = Model_EMM_Damper(param);
    case "FEMM"
        [B, B_max] = Model_FEMM_Damper(param);
    case "NN"
        [B, B_max] = Model_NN_Damper(param);
end
ty = 1000*(52.962*B^4-176.51*B^3+158.79*B^2+13.708*B+0.1442);
% Design equations
w = 2*pi*(rc+wc+0.5*h);
Ap = pi*(R^2-r0^2);
Q = Ap*u;

%% Objectives
% Damping force
F_Vis = 12*n*Q*L*Ap/(h^3*w);
```

```

c1 = 2.07+12*Q*n/(12*Q*n+0.4*w*h^2*ty);
F_MR = c1*ty*(2*la)*Ap/h;
Dynamic_Range = (F_MR + F_Vis)/F_Vis;

phi = B*la*2*pi*(rc+wc+0.5*h);
L_in = N_turns*phi/I;
R_w = N_turns*pi*d_avg*resistivity/Coil_area;

Time_Constant = L_in/R_w*1000;
cost = [-Dynamic_Range Time_Constant];

%% Non Linear Constraints - Penalty rule
c0 = [];
c0(1) = max(0,B_max - 1.5);
c0(2) = max(0,F_Vis - 100);

%% The following function uses EMM modelling to solve for magnetic
variables
% in the geometry
% Save the following as Model_EMM_Damper.m

function [B, B_max] = Model_EMM_Damper(param)
rc = param(1)/1000;
wc = param(2)/1000;
h = param(3)/1000;
la = param(4)/1000;
I = param(5);
R = 30/1000;
L = 50/1000;
pf = 0.6;
dw = 0.51/1000;
N_turns = pf*4*(wc*(L-2*la))/(pi*dw*dw);

mu_0 = 4*pi*10^(-7);           % vacuum permeability
mu_steel = 1600*mu_0;         % SAE 1020 permeability
mu_mrf = 4*mu_0;              % MRF permeability

%% Magnetic circuit equations
R1 = (L-la)/(pi*mu_steel*(rc^2));
R2 = log((rc+wc)/(0.5*rc))/(2*pi*mu_steel*la);
R3 = log((rc+wc+h)/(rc+wc))/(2*pi*mu_mrf*la);
R4 = (L-la)/(pi*mu_steel*((R)^2-(rc+wc+h)^2));

Rt = R1+2*R2+R4+2*R3;
phi = N_turns*I/Rt;

B1 = phi/(pi*rc^2);
B2 = phi/(2*pi*la*(0.75*rc+0.5*wc));
B4 = phi/(pi*((R)^2-(rc+wc+h)^2));
B = phi/(2*pi*(rc+wc+0.5*h)*la);
B_max = max([B1 B2 B4]);

%% The following function uses FEM modelling to solve for magnetic
variables
% in the geometry. This function uses OctaveFEMM interface to call
FEMM

```

```

% module from MATLAB
% Save the following as Model_FEMM_Damper.m

function [B, B_max] = Model_FEMM_Damper(param)

rc = param(1);
wc = param(2);
h = param(3);
la = param(4);
current = param(5);

R = 30;
L = 50;
pf = 0.6;
dw = 0.51;
N_turns = pf*4*(wc*(L-2*la))/(pi*dw*dw);

extra_len = 10;
Rmax = 60;

% Opens FEMM
openfemm;
% We need to create a new Magnetostatics document to work on.
newdocument(0);
% Define the problem type. Magnetostatic; Units of mm; Axisymmetric;
% Precision of 10(-8) for the linear solver; a placeholder of 0 for
% the depth dimension, and an angle constraint of 30 degrees
mi_probdef(0, 'millimeters', 'axi', 1.e-8, 0, 30);

% Draw the outer sketch
mi_drawrectangle([0 -0.5*L-extra_len; R 0.5*L+extra_len]);
mi_drawrectangle([0 -0.5*L; rc+wc 0.5*L]);
mi_drawrectangle([rc -(0.5*L-la); rc+wc 0.5*L-la]);
mi_drawrectangle([rc+wc+h -0.5*L; R 0.5*L]);

% Draw a half-circle to use as the outer boundary for the problem
mi_drawarc([0 -Rmax; 0 Rmax], 180, 2.5);
mi_addsegment([0 -Rmax; 0 Rmax]);

% Add block labels, one to each the steel, coil, and air regions.
mi_addblocklabel(0.5*rc, 0) % Core
mi_addblocklabel(rc+0.5*wc, 0) % Coil
mi_addblocklabel(rc+wc+0.5*h, 0.55*L) % MRF
mi_addblocklabel(0.9*R, 0) % Outercore
mi_addblocklabel(1.1*R, 0) % Air

% Define an "asymptotic boundary condition" property. This will
mimic
% an "open" solution domain
muo = pi*4.e-7;
mi_addboundprop('Asymptotic', 0, 0, 0, 0, 0, 0, 0, 1/(muo*0.2), 0, 2);

% Apply the "Asymptotic" boundary condition to the arc defining the
% boundary of the solution region
mi_selectarcsegment(1.1*R, 0);
mi_setarcsegmentprop(2.5, 'Asymptotic', 0, 0);

% Add some materials properties

```

```

mi_getmaterial('Air');
mi_getmaterial('24 AWG');

% A more interesting material to add is the iron with a nonlinear
% BH curve. First, create a material in the same way as if we
% were creating a linear material, except the values used for
% permeability are merely placeholders.
mi_addmaterial('MRF', 2100, 2100, 0, 0, 0, 0, 0, 1, 0, 0, 0);
mi_addmaterial('SiliconSteel', 2100, 2100, 0, 0, 0, 0, 0, 1, 0, 0,
0);

% A set of points defining the BH curve is then specified.

bhcurve = [0.14 0.3 0.44 0.6 0.72 0.83 0.91 0.97 1.08 1.14 1.19 1.25
1.31 1.36 1.41 1.46 1.55;
14284.48 38554.55 66533.46 109402.33 150383.19 191350.94 232308.88
265813.66 332815.8 373757.36 ...
414698.11 453570.36 498065.46 538911.52 577626.65 610089.33
685142.11]';

bhcurve1 = [0.38, 0.75, 1.05, 1.1, 1.3, 1.4, 1.465, 1.49, 1.51;
130, 260, 400, 430, 1000, 2000, 4000, 6000, 11000]';
% plot(bhcurve(:,2),bhcurve(:,1))
% Another command associates this BH curve with the Iron material:
mi_addbhpoints('MRF', bhcurve);
mi_addbhpoints('SiliconSteel', bhcurve1);

% Add a "circuit property" so that we can calculate the properties of
the
% coil as seen from the terminals.
mi_addcircprop('Current', current, 1);

% Apply the materials to the appropriate block labels
mi_selectlabel(0.5*rc, 0);
mi_setblockprop('SiliconSteel', 0, 1, '<None>', 0, 0, 0);
mi_clearselected

mi_selectlabel(rc+wc+0.5*h, 0.55*L);
mi_setblockprop('MRF', 0, 1, '<None>', 0, 0, 0);
mi_clearselected

mi_selectlabel(rc+0.5*wc, 0);
mi_setblockprop('24 AWG', 0, 1, 'Current', 0, 0, N_turns);
mi_clearselected

mi_selectlabel(0.9*R, 0);
mi_setblockprop('SiliconSteel', 0, 1, '<None>', 0, 0, 0);
mi_clearselected

mi_selectlabel(1.1*R, 0);
mi_setblockprop('Air', 0, 1, '<None>', 0, 0, 0);
mi_clearselected

% Now, the finished input geometry can be displayed.
mi_zoomnatural

% We have to give the geometry a name before we can analyze it.
mi_saveas('Test.fem');

```

```

% Now,analyze the problem and load the solution when the analysis is
finished
mi_analyze
mi_loadsolution

% Get B values in MR fluid
mo_addcontour(rc+wc+0.5*h,0.5*L);
mo_addcontour(rc+wc+0.5*h,0.5*L-la);
temp = mo_lineintegral(0);
mo_clearcontour;
B = temp(2);

% Get B_max values. take average of 10 maximum values.
count_femm = 0.5*mo_numnodes;
for j = 1:count_femm
    Node = mo_getnode(j);
if Node(:,1) < R && (Node(:,2)) < 0.6*L
    try
        b1(j,:) = mo_getb(Node);
    catch
        b1(j,:) = [NaN NaN];
    end
else
    b1(j,:) = [NaN NaN];
end
end

b1 = b1(any(~isnan(b1),2),:);
B11 = sort(sqrt(b1(:,1).^2+b1(:,2).^2));
B_max = sum(B11((length(b1)-9):length(B11)))/10;
closefemm

%% The following function uses NN model to solve for magnetic
variables
% Before using this, a Neural network model has to be saved in the
working directory
% Save the following as Model_NN_Damper.m

function [B, B_max] = Model_NN_Damper(param)

load('Bmax_NN_mod.mat');
load('Bmr_NN_mod.mat');

B_max = sim(Bmax_NN_mod, param');
B = sim(Bmr_NN_mod, param');

```

The above codes are suitably modified for various applications on which O-COM methodology has been performed in this research work. This work can be extended to other semi-active models such as MR brakes, MR dampers, MR valves etc.

LIST OF PUBLICATIONS

INTERNATIONAL JOURNALS

1. Radhe Shyam Tak Saini, Hemantha Kumar and Sujatha Chandramohan, “Optimal design of inverted rotary MR brake with waveform boundary using a novel combined magnetostatic approach”, *Smart Materials and Structures*, 29, 105014, 2020. IOP Publishing (SCI, SCIE and Scopus Indexed, Impact Factor: 3.585).
2. Radhe Shyam Saini Tak, Sujatha Chandramohan, Sujatha Srinivasan, Hemantha Kumar, “Design of bypass rotary vane magneto rheological damper for prosthetic knee application”, *Journal of Intelligent Material Systems and Structures*, 2020. DOI: 10.1177/1045389X20942577. SAGE Publisher (SCIE and Scopus Indexed, Impact Factor: 2.569).
3. Radhe Shyam Tak Saini, Hemantha Kumar and Sujatha Chandramohan, “Semi-active control of a swing phase dynamic model of transfemoral prosthetic device based on inverse dynamic model”, *Journal of the Brazilian Society of Mechanical Sciences and Engineering* 42(6), 294, 2020, Springer Publishers. (SCIE and Scopus Indexed, Impact Factor: 2.220).
4. Radhe Shyam Tak Saini, Manjeet Keshav, Hemantha Kumar and Sujatha Chandramohan, “A comparative study on magnetostatic approaches in design optimization of magnetorheological dampers”, *Engineering optimization*, Taylor and Francis Publisher. (SCIE and Scopus indexed. Impact factor: 3.230) (*Under Review*).
5. Radhe Shyam Tak Saini, Hemantha Kumar and Sujatha Chandramohan, “Optimal design of flow mode semi-active prosthetic knee dampers”, *Scientia Iranica*, Publisher: Sharif University of Technology. (SCIE and Scopus Indexed, Impact Factor: 1.435) (*Under review*).

INTERNATIONAL CONFERENCES

1. Radhe Shyam Saini Tak, Sujatha Chandramohan, Sujatha Srinivasan, Hemantha Kumar, “Design of bypass rotary vane magneto rheological damper for prosthetic knee application”, *30th International Conference on Adaptive Structures and Technologies*, Concordia University, Montreal, Canada, October 7 – 13, 2019.

2. Radhe Shyam Tak Saini, Hemantha Kumar, Sujatha Chandramohan and Sujatha Srinivasan (2020). “Optimal design of Rotary magneto-rheological drum brake for transfemoral prosthesis”, *7th International Congress on Computational Mechanics and Simulation, IIT Mandi, Himachal Pradesh, India, December 11 – 13, 2019.*

3. Radhe Shyam Tak Saini, Hemantha Kumar, Sujatha Chandramohan and Sujatha Srinivasan (2019). “Design of twin rod flow mode magnetorheological damper for prosthetic knee application”, *1st International Conference on Manufacturing, Material Science and Engineering, CMRIT Hyderabad, Andhra Pradesh, India, August 16-17, 2019.*

BIODATA

NAME: RADHE SHYAM TAK SAINI

DATE OF BIRTH: 06 – 04 – 1991

Mobile No.: +91 9491694102

Email: radhe.chandu@gmail.com



ADDRESS: D NO. 63-2-108,
Indira Colony,
Sriharipuram,
Visakhapatnam – 530011.

QUALIFICATION:

Examination	Institute/University	University/Board	Year	Percentage/ CGPA
Ph. D	National Institute of Technology Karnataka, Surathkal	National Institute of Technology Karnataka, Surathkal	2021	9.5 (Course work)
M. Tech (Machine design)	Chaitanya Engineering College	Jawaharlal Nehru Technological University Kakinada	2017	74.5 %
B.E. (Mechanical Engg)	MVGR College of Engineering	Jawaharlal Nehru Technological University Kakinada	2014	73.3 %

I hereby declare that the above information is true and correct to the best of my knowledge.

- Radhe Shyam Saini